

NSK Technical Journal

Motion & Control

No. 34 June 2023



ISSN1342-3630

NSK

MOTION & CONTROL No. 34

NSK Technical Journal

Printed and Published: June 2023

ISSN1342-3630

Publisher: NSK Ltd., Ohsaki, Shinagawa, Tokyo, JAPAN

Public Relations Department

TEL +81-3-3779-7050

FAX +81-3-3779-7431

Editor: Hayato OHMI

Managing Editor: Shunya MORIKAWA

Design, Typesetting & Printing: Kuge Printing Co., Ltd.

© NSK Ltd.

The contents of this journal are the copyright of NSK Ltd.

Contents

Technical Papers

NSK's Automotive Products and Technologies	<i>H. Ohmi</i>	1
Development of Bearings with Insulating Coating to Resist Electrical Corrosion in HEV/EV Units	<i>S. Katto</i>	2
How Hub Unit Bearings Contribute to Carbon Neutrality	<i>M. Kato</i>	8
Development of Magnetostrictive Torque Sensor	<i>T. Odera, K. Fukuda, J. Ono</i>	17
Evaluation of Steering Feel in the Off-Center Range Using Physiological Characteristics	<i>M. Miyake, A. Kanbe, K. Suzuki, M. Nishio</i>	24

New Products

Ball Bearings with Labyrinth Seal for Transmission Applications		38
BOC Bearings with Resistance to Wear from Creep		40
Development of Gen 4 High-Speed Ball Bearings for HEVs/EVs		42
Large-Size T-HUB 1 Bearings for Trucks		44
Next-Generation Long-Life Planetary Shafts (SHJ7)		46
Drawn Cup Needle Roller Bearings with Large Diameter for Electric/Hybrid Vehicles		48
Column EPS with Steering Wheel Angle Detection		50

Technical Papers

Trends in Bearings for Steelmaking Equipment	<i>T. Nomura</i>	52
QuickStopBearing™ for Dental Air Turbines	<i>Y. Okazaki, M. Shirai</i>	64
Evaluation of Lubrication Performance in Ball Screws and Linear Guides by the Electrical Impedance Method	<i>J. Aoyama, A. Tsutsui</i>	70
NSK VIRTUAL EXPO	<i>Y. Yano</i>	79
Study on Simple Vibration Prediction Method for Permanent Magnet Synchronous Motors and Applications	<i>I. Nitta</i>	84
Establishment of an Integrated Automated Embryonic Manipulation System for Producing Genetically Modified Mice	<i>H. Ueda, T. Eto, N. Tanaka</i>	95

New Products

NSK Verify (Bearing Information Acquisition Service Using 2D Barcode)		110
Bioplastic Cage for Deep Groove Ball Bearings		112
High Load Capacity Angular Contact Ball Bearings with Pressed Steel Cage (BEAW)		114

NSK's Automotive Products and Technologies

Hayato Ohmi

Automotive Business Headquarters

Automotive Technology Development Center Managing Executive Officer

Thank you for reading *NSK Technical Journal: Motion & Control*. This issue presents products for automobiles and mini features on NSK's latest technologies.

The world of automobiles is currently undergoing a once-in-a-century revolution, with drive units using electric systems under active development and a large variety of electric vehicles (EVs) appearing on the market. EVs have come into focus and are expected to become more widespread as carbon-neutral vehicles that do not emit carbon dioxide. However, extending continuous operation time (cruising distance) remains a challenge. Various solutions are being considered and developed, including increasing motor output. There are also growing calls to reduce energy losses in EVs to zero, echoing the need to reduce fuel consumption in vehicles with conventional internal combustion engines. By refining NSK's fundamental technologies and applying them to new core functions required for electrification, we are working to enhance system efficiency and performance while improving vehicle safety and comfort.

We hope you enjoy reading about these exciting developments and look forward to your continued guidance and support.



Hayato Ohmi

Development of Bearings with Insulating Coating to Resist Electrical Corrosion in HEV/EV Units

Satoshi Katto

Automotive Technology Development Center, Automotive Bearing Technology Center, Powertrain Bearing Technology Department

Abstract

As environmental issues such as global warming continue to grow in importance, the automotive industry is actively making efforts to reduce environmental impacts through the release of hybrid electric vehicles (HEVs) and electric vehicles (EVs). The high-speed, high-efficiency, and high-output bearings that support HEV/HV drive motors can be easily damaged by the flow of high-frequency current through the bearing. In addition, damage from electrical corrosion (electrical erosion) is becoming more frequent, increasing the need for solutions.

Ceramic balls are highly insulating and already widely used; however, their low availability, high price, and replacement requirements have stifled demand in recent years. In response, NSK has been developing low-cost electrically conductive grease and seals, but maintaining high conductivity to further suppress damage has remained an issue.

Here, we introduce the development of a specialized insulating coating that aims to replace high-cost ceramic balls.

1. Foreword

In light of environmental problems such as global warming, efforts are being made around the world to achieve carbon neutrality, including with HEVs and EVs, which are becoming increasingly popular because of their low environmental impact¹⁾. Critical issues electric vehicles face in becoming more popular are extension of driving range and reduction of recharging time, requiring drive motors that allow for higher speeds, higher efficiency, and higher output. Reducing motor power loss requires the output of an ideal sine waveform, so a high inverter control frequency (carrier frequency) is needed. The energy handled by automobiles is increasing every year, and the voltage/current is increasing accordingly. Furthermore, the need for rapid charging is driving the growing trend toward higher voltages. The combined need for a higher frequency and higher voltage/current results in high-frequency currents flowing inside the bearings that support the drive motors for HEVs and EVs.

This has in turn dramatically increased the number of cases of electrical corrosion damage to bearings in recent years. Electrical corrosion-resistant items are needed to suppress this electrical corrosion damage. Ceramic balls, which exhibit high insulation properties, have been widely used due to their high resistance to electrical corrosion. However, the high demand for ceramics in recent years has led to a shortage of materials and rise in material costs, thus increasing the demand for an alternative to ceramic balls that is highly resistant to electrical corrosion. NSK has developed conductive grease and conductive seals that are resistant to electrical corrosion. However, it has yet to ensure sufficient conductivity to suppress the electrical corrosion damage in bearings for HEV and EV drive motors and is therefore currently unable to provide a complete preventive measure.

This paper introduces our efforts to develop bearings with an insulating coating that exhibit electrical corrosion resistance and cost less than ceramic balls.

2. Electrical Corrosion

Electrical corrosion occurs when the insulating oil film formed between the raceway surfaces and rolling elements of a rotating bearing undergoes dielectric breakdown. The resultant discharge locally melts and disfigures the raceway surfaces and rolling elements. The most prominent are the ridge marks in Photo 1, indicating a wavy wear aspect. Figure 1 shows the voltage/current waveforms during discharge, where the breakdown of the oil film triggers the current flows, and the voltage waveform collapses.

The electrical corrosion is caused by a portion of the shaft voltage generated by the pulse width modulation (PWM) control of the inverter equipment being applied between the inner and outer rings of the bearing, and this voltage causes the breakdown of the oil film. Preventing the breakdown of the insulation is therefore effective for preventing electrical corrosion in the bearing, which can be achieved by reducing the voltage applied between the inner and outer rings of the bearing to less than the breakdown voltage of the oil film or by applying a material with high insulation properties to the bearing to suppress the current flow between the bearing's inner and outer rings.

3. Criteria for Electrical Corrosion Damage

When electrical corrosion causes severe damage, ridge marks form on the raceway surfaces and rolling elements, as described above. In electric cars, for which a high degree of quietness is required, abnormal sliding noise on the raceway surfaces caused by ridge marks is a bearing damage problem.

Although the criteria for bearing sound pressure in HEV and EV units vary from one unit to another, NSK evaluates the increase in sound pressure of a single bearing as the criterion for abnormal noise generation due to electrical corrosion damage. The control values are set based on the experience of detecting abnormal noise after the endurance evaluation test of motor support bearings and the database of bearing sound pressure of products subjected to electrical corrosion.

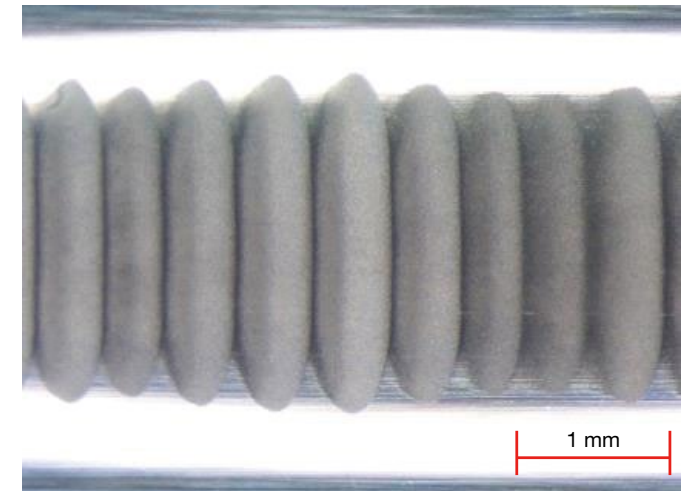


Photo 1 Ridge marks on a 6206 ball bearing outer ring raceway



Fig. 1 Voltage/current waveform during discharge

To confirm the validity of one of the criteria, specifically the amount of sound pressure increase, an evaluation of the difference in electrical corrosion damage was conducted at different current values for each oil film parameter (Λ), shown in Figure 2. A 6206 bearing (inner diameter: 30 mm, outer diameter: 62 mm) was used as the evaluation bearing. The oil film parameter (Λ) was varied by changing the oil temperature, and the discharge current value was varied. The results show that the larger the oil film parameter and the higher the discharge current value, the greater the electrical corrosion damage.

The relationship between the discharge current value and sound pressure increase for each oil film parameter (Λ) is shown in Figure 3. Figure 3 shows that the amount of sound pressure increase also grows under high electrical corrosion damage conditions. This indicates that the amount of sound pressure increase is one of the criteria for electrical corrosion damage.

4. Insulating Coating with Calcinated Coating

NSK uses a calcinated coating of resin for the insulating. The characteristics of the coating products we developed are described as follows.

4.1 Insulating coating location

When applying an insulating coating to the bearing outer ring, reliable insulation requires applying the coating to all contact areas between the bearing outer ring and the mating member. The coating must therefore be applied to the outer ring's outer diameter surface and end faces. Although NSK has mass-produced bearings with calcinated coating in the past, only the outer ring outer diameter surface has been coated, and not the end face. Since the coating must be applied to the finished bearing for ease of assembly, it must also be applied evenly to the end faces to prevent paint splattering onto the bearing raceway surfaces, which requires difficult masking techniques. When the bearing is used with a press-fitted outer ring, the inner ring's inner-diameter surface and end faces must be coated, which makes the coating more difficult compared to that of the outer ring. The new insulating coating has been developed for compatibility with the inner and outer rings (Photo 2).

4.2 Insulating coating paint

Additives are commonly added to paints to improve such areas as stabilizing quality, making painting work more efficient, and protecting the paint afterward. Since additives enhance various functions of paint, optimal amounts of additives are mixed in. The insulating coating should have high insulation properties, although the optimal amount of additives should be mixed with the developed insulating coating paint and used in the coating

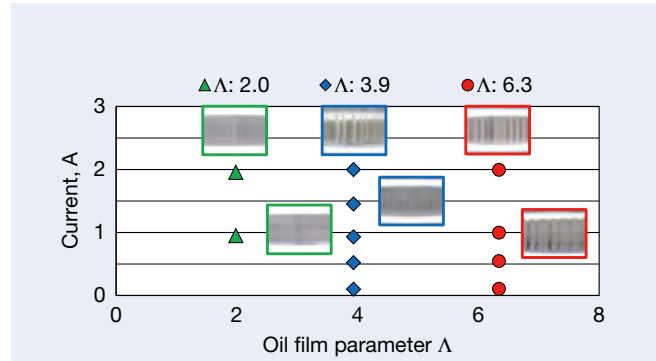


Fig. 2 Relationship between current values and electrical corrosion damage by oil film parameter (Λ)

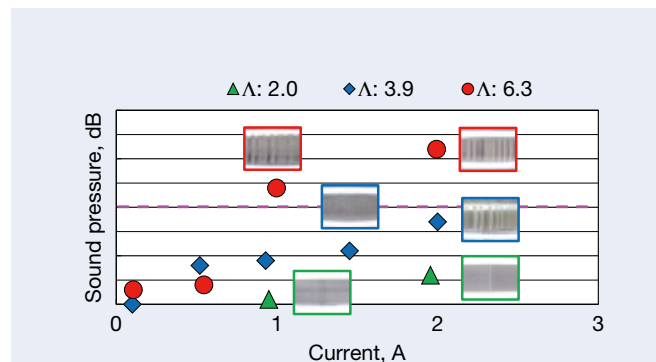


Fig. 3 Relationship between current values and increase in sound pressure by oil film parameter (Λ)



Photo 2 Bearings with insulating coating to resist electrical corrosion

process. There is a limit to the amount of additives that can be used because those with excellent coating stability counteract the insulation properties. Therefore, the impossibility of using the amount of additives considered optimal for coating stability to ensure insulation leads to the use of paints with lower viscosity than ordinary paints by solvent dilution. For paints with low viscosity, the picture-frame effect, shown in Figure 4, occurs on the outer ring outer-diameter surface during painting. The picture-frame effect is an increased coating thickness at the edges due to an imbalance between fluidity and surface tension. This occurs when solvent dilution increases the fluidity, and the surface tension raises the paint at the edges. The picture-frame effect would destabilize the dimension after the coating, and the coating peels off when the housing is inserted, degrading the insulation property. As a result, insulating coatings that cannot use optimal amounts of additives are more difficult to paint with.

4.3 Insulation properties and coating thickness

Since the voltage generated between the inner and outer rings of the bearings in the HEV/EV unit is an AC voltage, a small amount of capacitor current flows even if the bearings are insulated. This capacitor current is confirmed to cause minute electrical discharges in the bearing raceway surfaces and rolling elements. The capacitor current can be calculated using Equation (1) and is determined by the inverter control frequency and the insulating bearing's capacitance.

$$I_c = 2\omega f \times CV \dots \text{Equation (1)}$$

I_c : Capacitor current [Arms]

f : Frequency [Hz]

C : Capacitance of coating bearing [F]

V : Electric potential [Vrms]

The thickness of the developed insulating coating is several tens of micrometers. Some capacitor current flows at the voltage and frequency expected in bearings for drive motors for HEVs and EVs. For this reason, the thickness of the insulating coating is set in the range where the capacitor current saturates, as shown in Figure 5. It has been confirmed that electrical corrosion damage can be suppressed to a level that does not affect bearing function at the capacitor current level.

The insulation properties of the developed product were confirmed as follows. A 6206 bearing (inner diameter: 30 mm, outer diameter: 62 mm) was used as the evaluation bearing, and a sine wave of voltage $50 V_{p-p}$ and frequency 100 kHz was applied between the inner and outer rings of the bearing for 20 hours. For comparison, a 6206 standard bearing was tested with a voltage of $3 V_{p-p}$, a frequency of 1 kHz, and a duration of 20 hrs. Figure 6 shows the results. The standard bearing tested under mild conditions exhibited ridge marks on the outer ring raceway surfaces. The sound pressure increase of the bearing alone was above the control value. Still, the bearing with the insulating coating showed no abnormal

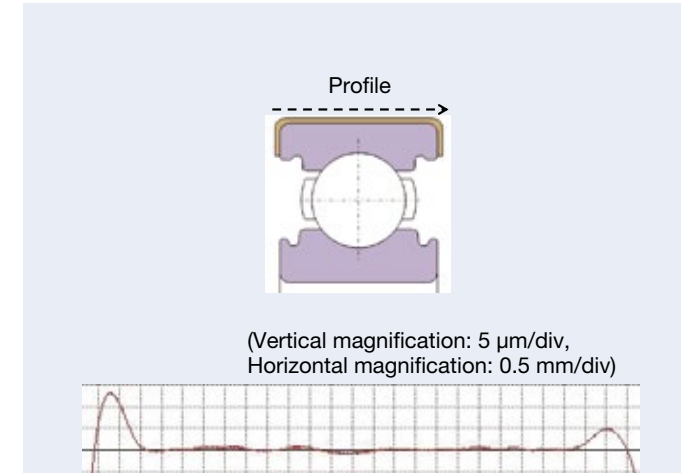


Fig. 4 Picture framing effect on outside diameter surface of outer ring

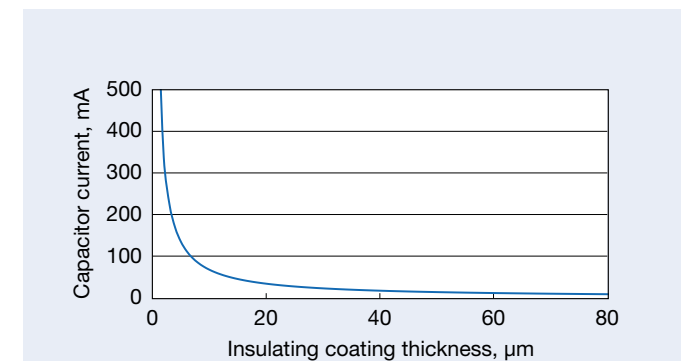
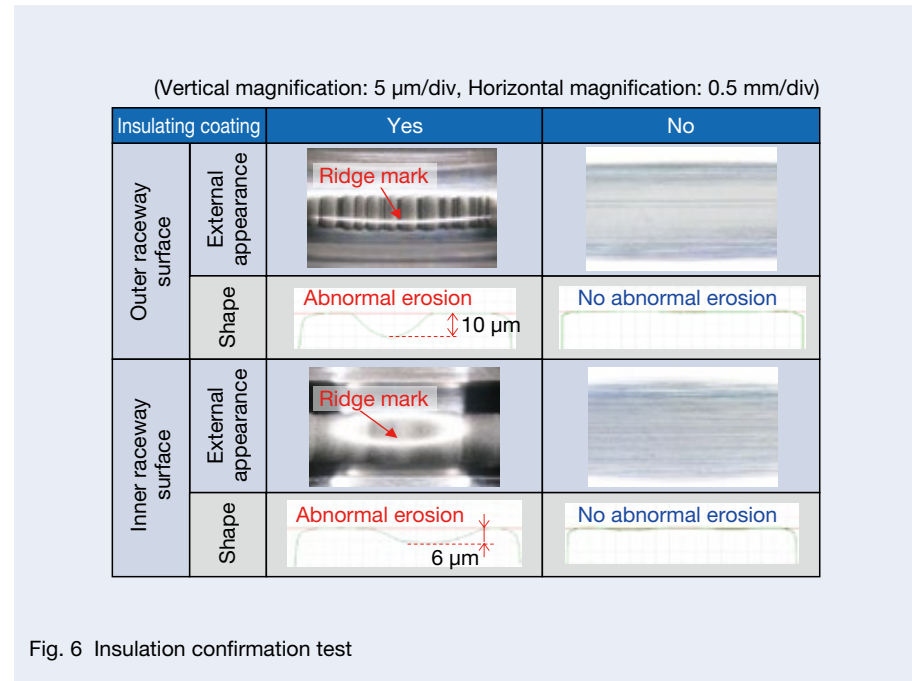


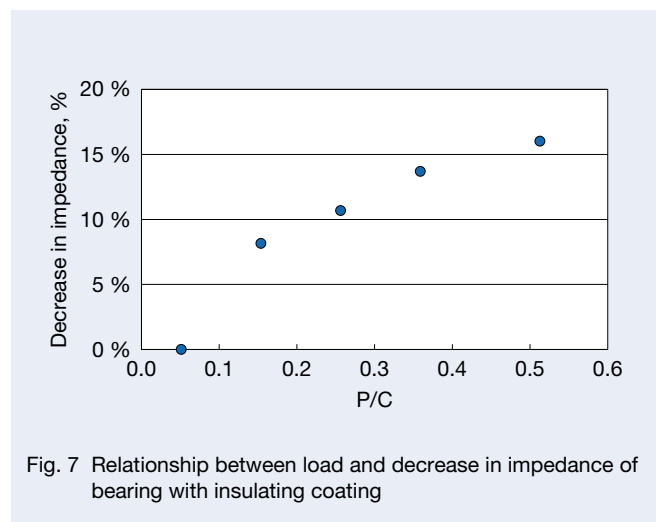
Fig. 5 Relationship between insulating coating thickness and capacitor current



wear due to electrical corrosion damage on the inner and outer ring raceway surfaces despite the harsher conditions compared to those of the standard bearing. The sound pressure increase was less than the control value, and the electrical corrosion damage was suppressed to a level that did not affect the bearing function.

4.4 Heavy load capacity

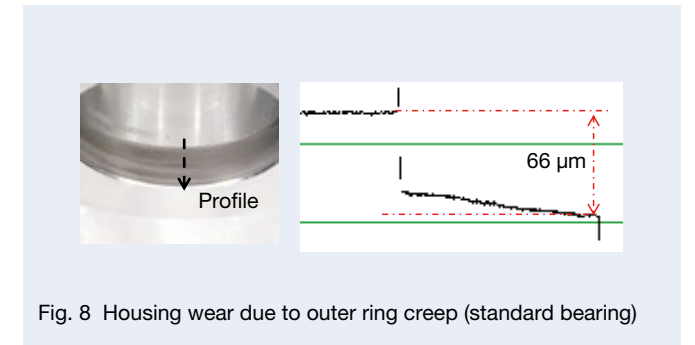
The bearings with insulating coating are being developed to withstand drive motor support bearings for HEVs and EVs and support bearings subjected to gear loads. Therefore, the rate of impedance reduction of the bearings with insulating coating due to load loading was evaluated. A 6206 bearing (inner diameter: 30 mm, outer diameter: 62 mm) was used as the evaluation bearing, and radial loads of 5 to 50% of the basic dynamic load rating of the evaluation bearing were used. The rate of impedance reduction under each radial load was measured relative to the impedance when applying the radial load, which was 5% of the basic load rating. The measurement was performed as a static evaluation in order to eliminate the influence of the impedance of the dynamically formed oil film. The results are shown in Figure 7. The rate of impedance reduction was less than 20%, and the developed product was deemed to have sufficient impedance, even at 50% of the basic load rating.



4.5 Insulation persistence in creep environment

When the outer ring of a drive motor bearing for HEVs and EVs uses a running fit, the whirling radial load (eccentric load) of the motor rotor causes the outer ring, which should not rotate, to do so due to the difference in circumference between the outer ring outer diameter and housing inner diameter, a phenomenon known as creep¹⁾. The insulating coating of the developed product must maintain its insulation properties even in a creep environment. Therefore, the following evaluations were conducted to confirm the insulation durability of the insulating coating.

A 6206 bearing (inner diameter: 30 mm, outer diameter: 62 mm) was used for the evaluation. The bearing was subjected to a whirling radial load, and the outer ring was kept creeping during the evaluation. A voltage was applied between the inner and outer rings of the bearing to confirm whether the insulation property was maintained. As shown in Figure 8, it was confirmed in advance that the aluminum housing wears about 60 μm with the outer ring creeping at 20 000 rpm when the same conditions were evaluated with the 6206 standard bearings. This amount of wear is generally considered abnormal, so the conditions of this evaluation are sufficiently harsh. The results of electrical corrosion damage to the raceway surface after 30 000 rpm creep are shown in Figure 9. The bearings with an insulating coating maintained their insulation properties without causing large current discharges, despite harsher conditions than those of the standard bearings. Abnormal wear due to electrical corrosion damage was not observed on the inner and outer ring raceway surfaces, and electrical corrosion damage was suppressed to a level that does not affect the functions of the bearing.



5. Afterword

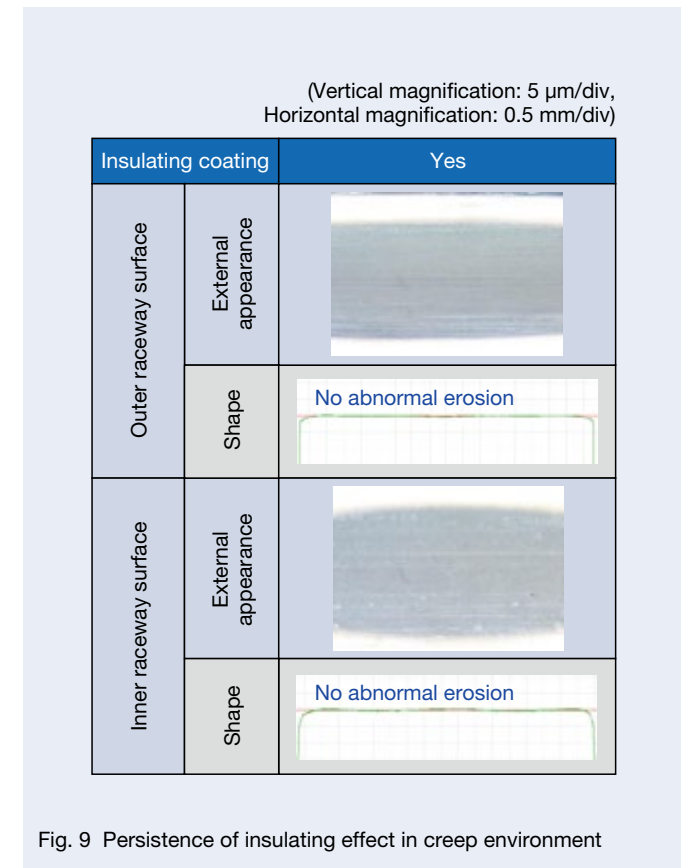
This paper describes NSK's efforts to develop bearings with an insulating coating, one of the items developed by NSK to resist electrical corrosion in bearings for drive motors for HEVs and EVs.

In addition to the insulating coating, an anti-electrical corrosion item described in this paper, NSK is also developing insulation measures by applying resin molding to the raceway rings. Along with the insulation countermeasures, we are also improving conductive grease and conductive seals that are conventional conductive countermeasures and developing new alternative conductive countermeasures. We aim to manage electrical corrosion resistance from both insulating and conducting.

Electric vehicles such as HEVs and EVs will clearly and rapidly become more popular as society strives to realize a future that is carbon neutral. Since the requirements for bearings are changing every day, NSK will improve the reliability of HEVs and EVs with a comprehensive understanding of the user's operating environment and by continuously promoting and proposing product development that meets the market's needs.

Reference

- 1) Yasuhiro Iwanaga, "Latest Technical Trends for HEV/EV Powertrain Bearings," *Monthly Tribology* (Oct. 2019).



Satoshi Katto

How Hub Unit Bearings Contribute to Carbon Neutrality

Meiji Kato
Automotive Powertrain Bearing Technology Center, Chassis Bearing Technology Department

Abstract

Global warming continues to progress year by year, making countermeasures urgently needed. Carbon neutrality is a crucial first step in reducing the percentage of greenhouse gases in the atmosphere that cause global warming. It is achieved by balancing carbon dioxide emissions from human activities with their removal from the air. As automobiles are a major source of emissions, improving their energy efficiency is a major area of focus.

Here, we describe how hub unit bearings, as critical components that support the wheels of automobiles, help to realize carbon neutrality.

1. Introduction

Reducing CO₂ emissions and improving fuel and electricity costs have in recent years become significant issues for the automotive industry as countermeasures to global environmental problems such as air pollution and global warming.

In October 2020, the Japanese government declared its goal of carbon neutrality, which means zero overall greenhouse gas emissions by 2050¹⁾.

Electric vehicles (EVs) such as BEVs, HVs, PHVs, and FCVs are rapidly becoming popular, and the Japanese government is aiming for 100% of new vehicle sales to be electric by 2035, while other nations are working to achieve this by 2030 to 2040.

An EV uses a battery or fuel cell as its energy source to drive its wheels with a motor. Since electricity distributed from power plants to households and businesses is used to recharge batteries, improvements are needed in regard to fossil fuel use for power generation. Renewable energies such as wind and hydropower have limitations in terms of how much electricity they can generate. Reducing power consumption therefore requires improved energy efficiency.

Furthermore, batteries can be recharged overnight if recharging facilities are available at homes or businesses, but continuous driving requires 30 minutes of charging, even with a quick charge, which is longer than refueling with gasoline or diesel. In this context, extending the cruising range for travel on a single charge is essential.

There are two main ways of improving the cruising range (km): increasing the battery capacity (kWh) and reducing battery consumption (km/kWh). Increasing the battery capacity is not a good idea since it consumes resources and energy in battery production while also making the vehicle heavier and electricity costs worse.

One way to improve energy efficiency to enhance cruising range is regenerative braking. In conventional internal combustion engine vehicles, kinetic energy is converted to heat energy as braking or friction losses during deceleration and dumped into the air. A regenerative brake uses the motor as a generator during deceleration, converting the kinetic energy of a running vehicle into electrical energy to charge the battery. Therefore, in addition to reducing fuel and battery consumption during driving by reducing rolling resistance, there is an even greater need for lower friction to increase the amount of kinetic energy recovered through regeneration.

NSK has set the goal of achieving carbon neutrality by reducing Scope 1 and 2 CO₂ emissions to virtually zero by FY2035. As shown in Figure 1, CO₂ emissions are reduced from the following perspectives: manufacturing = technological development and production, and use = products and services.

NSK manufactures bearings for automobiles, including hub unit bearings that support wheels, bearings for transmissions and other drive trains, and bearings used in engine accessories and motors for EVs. In this paper, we discuss the development of environmentally friendly products in hub unit bearings.

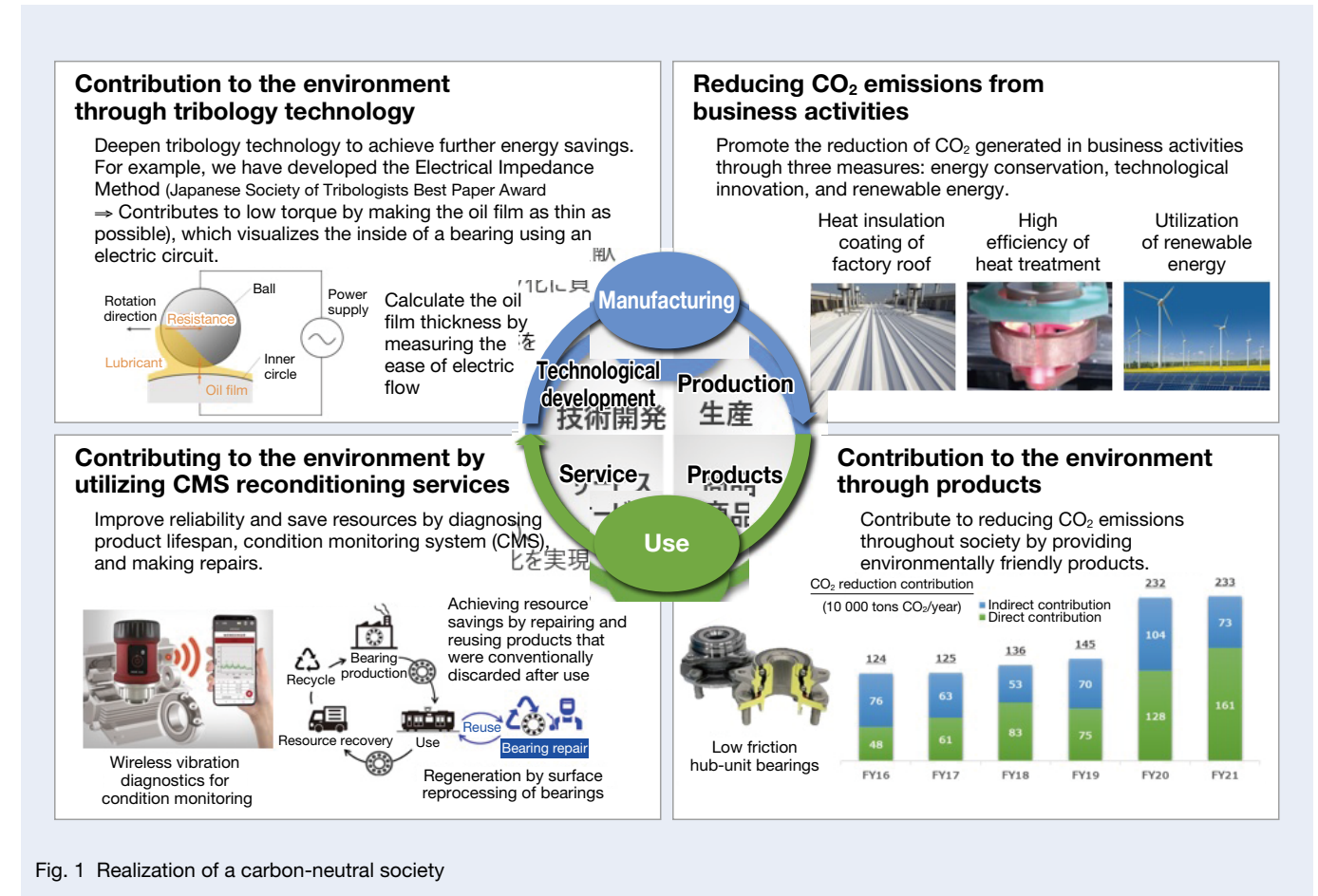


Fig. 1 Realization of a carbon-neutral society

2. Friction of Hub Unit Bearings

Figure 2 shows the functions required of hub unit bearings. In recent years, there has been a growing demand for even higher reliability, rigidity, lower friction, and lighter weight. On the other hand, high reliability conflicts with low friction, while high rigidity conflicts with low friction and light weight.

Here we also describe efforts to reduce friction while maintaining reliability and high rigidity.

As shown in Figure 3, friction in hub unit bearings can be divided into internal friction caused by balls, raceway surfaces, cages, internal grease and seal friction; seals are necessary to prevent muddy water ingress. The friction of the bearing is approximately 50% internal friction and 50% seal.

Items that reduce internal friction and seal friction are described as follows.

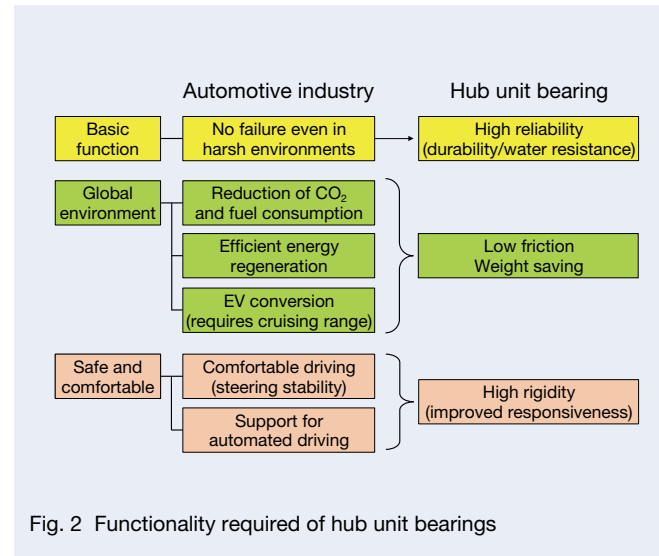


Fig. 2 Functionality required of hub unit bearings

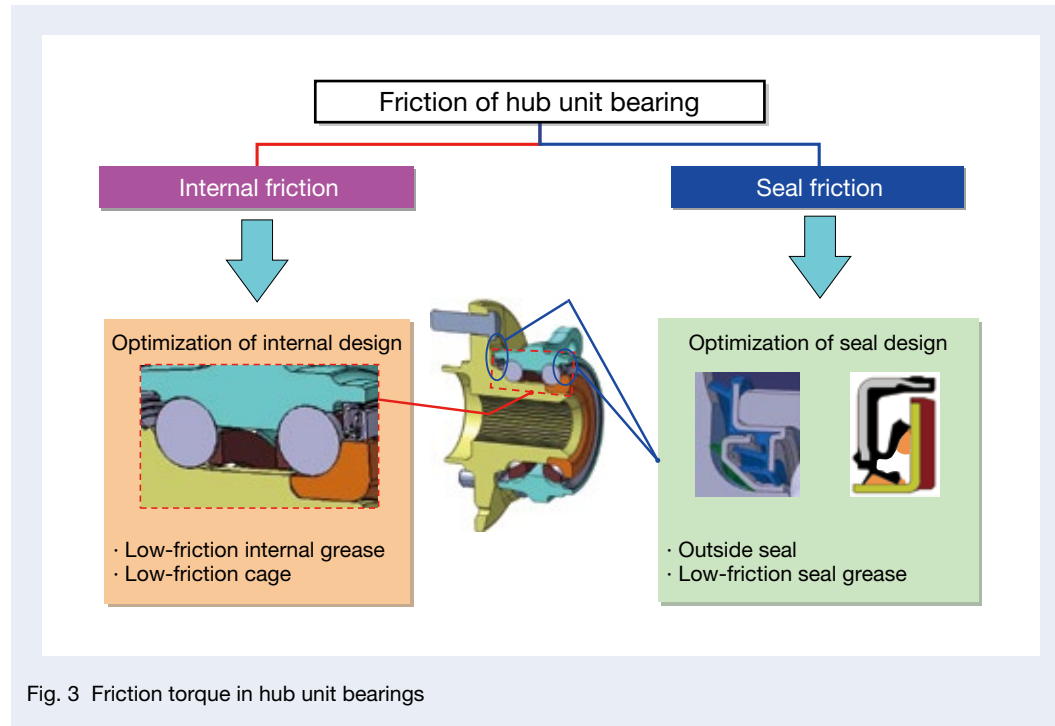


Fig. 3 Friction torque in hub unit bearings

3. Reduction of Internal Friction of Bearings

As shown in Figure 4, rolling elements (balls or rollers), raceway surfaces, cages, and grease are inside the hub unit bearing. Internal friction of a bearing can be divided into rolling resistance and stirring resistance.

Rolling resistance is caused by the shear of the base oil at the contact surface between the balls and the raceway surface. Rolling resistance is the dominant internal friction in hub unit bearings used at low speeds and high loads.

Stirring resistance is generated by the grease being pushed around by the balls and cage as they rotate. The lower viscosity of the base oil reduces rolling resistance, which increases the stirring resistance ratio, and the new internal bearing grease reduces stirring resistance.

3.1 Bearing internal grease Second-generation low-friction grease

Grease mainly consists of three components: base oil, thickener, and additives. Base oil forms an oil film between rolling elements and raceway surfaces for lubrication and is classified into mineral oil and synthetic oil according to the manufacturing method. In the past, greases using inexpensive mineral oil were mainly used. In recent years, however, synthetic oil with less viscosity change relative to temperature has been increasingly used to achieve low friction.

Thickeners hold the base oil, making it semi-solid like a sponge. The thickener keeps the grease in place so that it does not drain out, and it provides base oil for lubrication between the rolling elements and raceway surfaces.

Additives include antioxidants, rust inhibitors, anti-wear agents, friction reducers, and water-resistant prescriptive additives, which are blended to improve the various functions of the grease.

Although lowering the viscosity of the grease base oil is effective in reducing rolling resistance, there is a concern that lowering the viscosity of the base oil will cause the oil film to become thin when the bearing is subjected to large loads and high temperatures, resulting in metallic contact between the balls and the raceway surface.

To achieve both low torque at 40–50°C outer ring surface temperature in everyday driving and durability at high temperatures (outer ring surface temperature of 80°C or higher), the first and second-generation low friction greases use chemically synthesized base oils with small viscosity change (high viscosity index) with temperature.

Soft grease (with a considerable consistency) gives the impression of low resistance to the touch. In reality, the grease is pushed off the rolling surface by the balls and cage during running, then returns to its original position (churning property) and continues to generate resistance by contacting the balls and cage. On the other hand, hard grease (with a little consistency) has high resistance to the touch, but grease pushed out of the rolling surface by the balls and cage stays there (channeling property), so the grease is not pushed out again, and stirring resistance can be reduced.

The internal grease of conventional hub unit bearings has a urea thickener with high heat resistance. The second-generation low-friction grease has a thickener with finer fibers to increase the retention capacity of the base oil, thereby reducing the amount of thickener while maintaining grease hardness and achieving reduced stirring resistance.

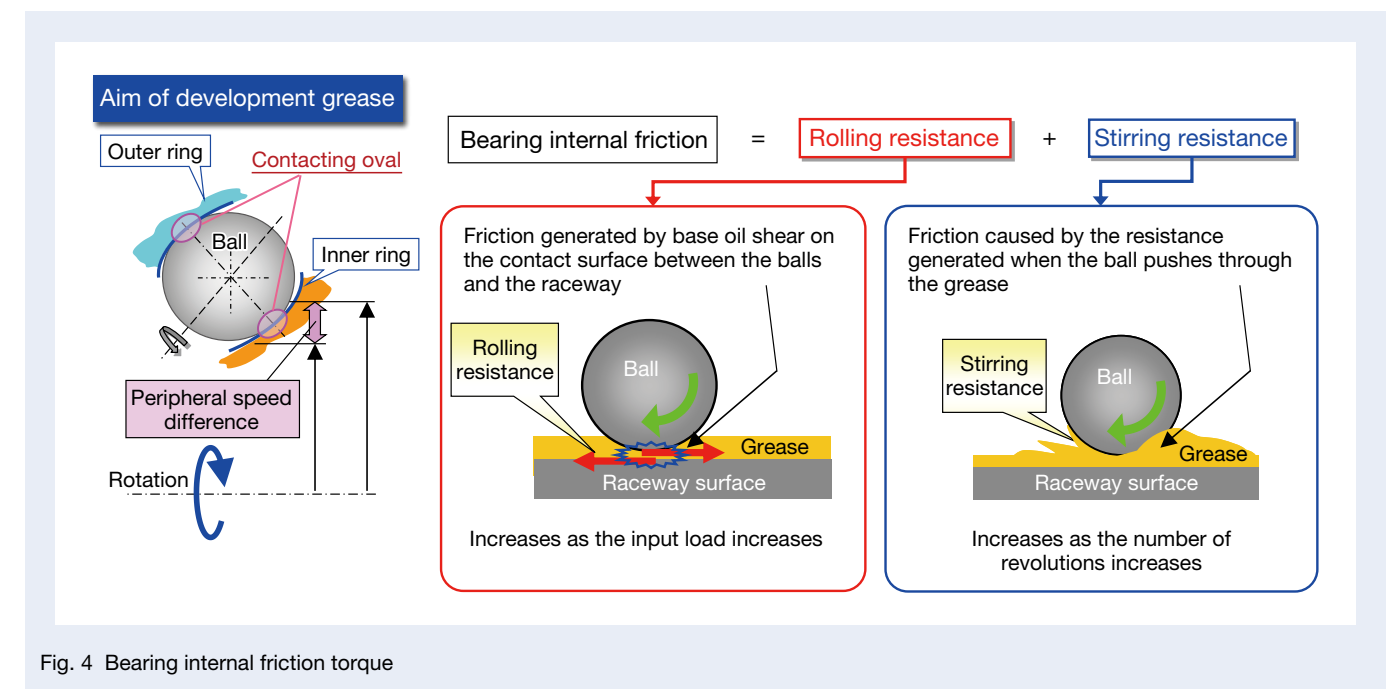


Fig. 4 Bearing internal friction torque

A performance comparison of the first and second-generation low-friction greases is shown in Figure 5. The second-generation low-friction grease has achieved a 30% reduction in friction while maintaining high-speed, high-load endurance, as well as low-temperature fretting resistance*.

*Fretting of hub unit bearings is a phenomenon in which micro-wear occurs due to metallic contact between the rolling elements of the bearing and the raceway surface due to oil film loss caused by vibration without tire rotation when automobiles are transported by freight train or truck. This is particularly problematic during long-distance transportation in cold regions in winter.

3.2 Low-friction cages

Conventional and low-friction cages are shown in Figure 6. Conventional cages have a column between the balls, which causes grease-stirring resistance between the balls and the cage. In addition, stirring resistance occurs between the cage outer diameter and outer ring inner diameter as well as between the cage inner diameter and shaft outer diameter.

The new low-friction cage can reduce bearing internal friction by:

- Reducing stirring resistance by removing the columns between the pockets
- Reducing stirring resistance by changing the outer and inner diameter dimensions

Figure 7 shows the friction reduction effect of the low-friction cage. An 11% reduction in internal torque was achieved by removing the columns between the ball pockets and changing their dimensions.

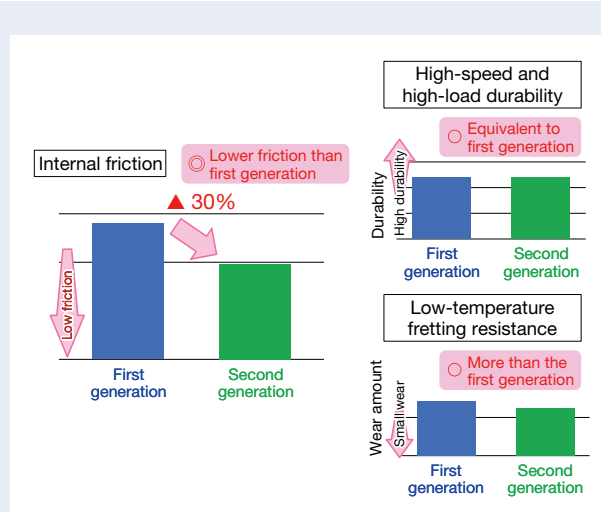


Fig. 5 Performance of second generation low friction grease

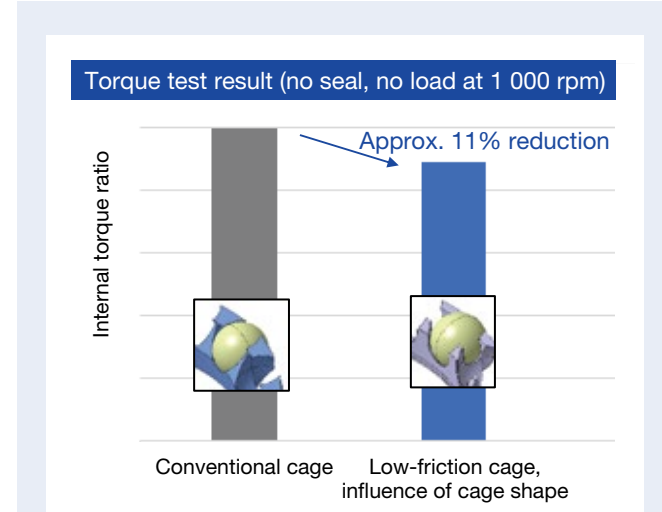


Fig. 7 Reduction in friction from low-friction cage

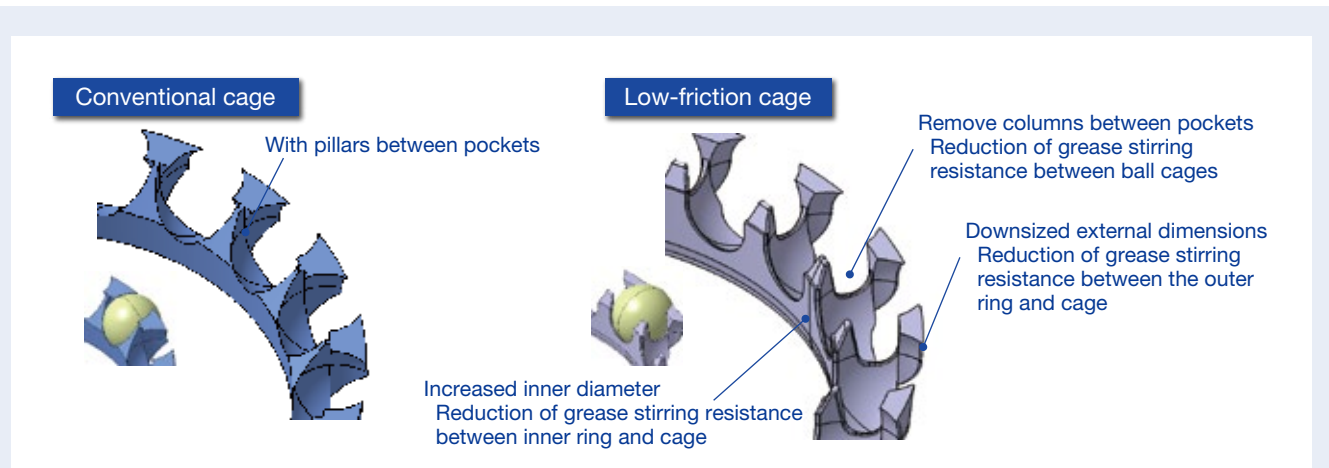


Fig. 6 Conventional cage and low-friction cage

4. Reducing Seal Friction

Hub unit bearings support the wheels of automobiles. They are used in harsh environments where the hub unit bearings are subjected to muddy water splashed up by tires, so preventing muddy water from entering the hub unit bearings is the most crucial function of seals.

Nevertheless, increasing the number of contact lips to increase mud resistance and increasing the contact force of the lips will increase the friction of the seal, making both mud resistance and low friction a technical challenge in terms of seals. The friction torque of the seal is the sum of the frictional force F_1 at the sliding seal lip and the grease stirring resistance F_2 (Figure 8).

The friction force F_1 on the sliding part can be obtained by $F_1 = \mu N$, where the seal rubber material, grease, and surface properties of the sliding surface determine the coefficient of friction μ . In contrast, the seal rubber material and shape determine the lip reaction force N .

Grease stirring resistance is affected by grease viscosity, channeling characteristics, and grease quantity. Focusing on these factors, we are working to reduce seal friction.

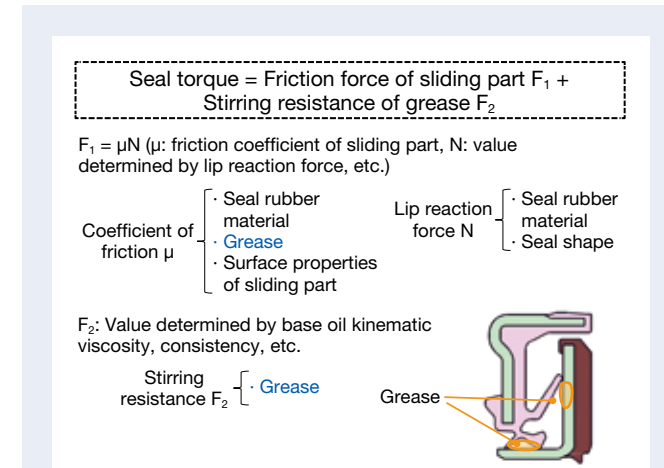


Fig. 8 Components of seal friction torque

4.1 New seal grease

Seal grease lubricates the lip and sliding surfaces, and seal grease significantly affects the coefficient of friction in the above equation. Decreasing the kinematic viscosity of the grease base oil can reduce the coefficient of friction. However, because base oil with a small kinematic viscosity has a high fluidity with little interaction between base oil molecules, the oil film tends to break easily, and mud can penetrate through the seal.

The new grease has a lower base oil viscosity to reduce the coefficient of friction and is blended with polar polymers in the base oil.

Figure 9 shows the action of polar polymers. The entanglement of polymer chains holds back base oil molecules and prevents oil film rupture when exposed to muddy water. The excellent compatibility and wettability of polar polymers as well as the sliding surfaces of the seal lip rubber material facilitate oil film and grease to intervene in the sliding parts.

Figure 10 shows the torque reduction effect of the new seal grease. A 25% reduction in seal friction and a 50% improvement in sealing performance could be achieved simultaneously.

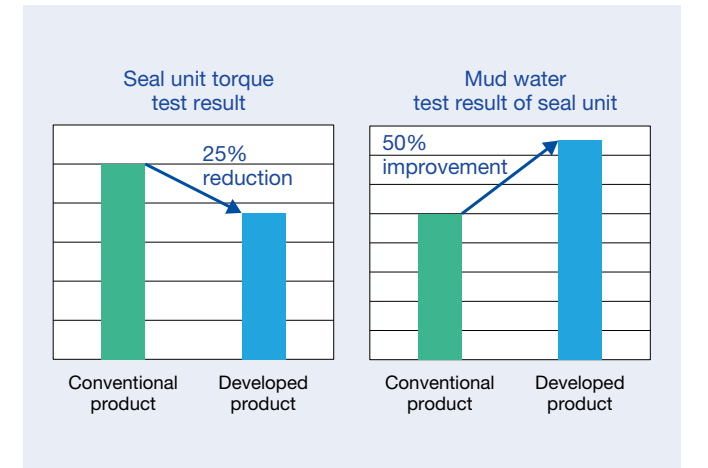


Fig. 10 Friction reduction and sealing performance of new seal grease

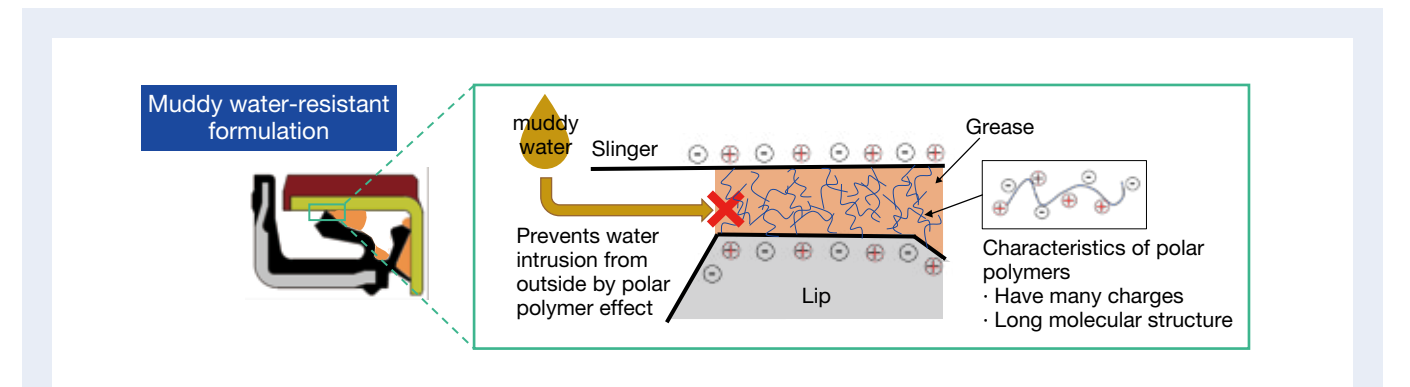


Fig. 9 Function of polymer in new seal grease

4.2 Slinger seal

Conventional third-generation hub unit bearings use a seal structure in which the seal lip of the vehicle's outer seal slides directly on the shaft's outer diameter. On the other hand, a magnetic encoder that generates wheel rotation speed signals for vehicle control systems such as ABS and anti-skid devices is fitted to the inner ring on the seal inside the vehicle, and the seal lip slides on the surface of the slinger, the core of the magnetic encoder.

NSK has also developed a structure that uses slingers for outside seals (Figure 11). The use of slingers for outside seals has the following advantages.

- Complicating the labyrinth structure can keep muddy water away from the seal lip.
- Reducing the amount of muddy water reaching the seal lip can reduce the number of contact lips on the seal from three to two, for example.
- Reducing the number of contact lips allows for lower friction.

Figure 12 shows a torque comparison between the conventional and slinger seals. A 40% reduction in torque was achieved while maintaining sealing performance.

5. Effect of Internal Friction Reduction and Seal Friction Reduction

Incorporating all internal friction reduction and seal friction reduction items is expected to reduce friction by approximately 30% compared to the current product.

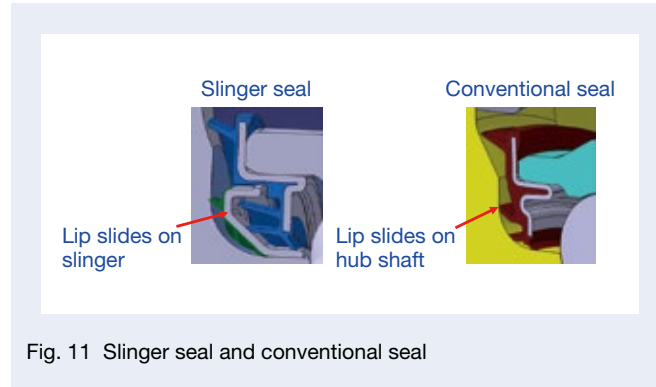


Fig. 11 Slinger seal and conventional seal

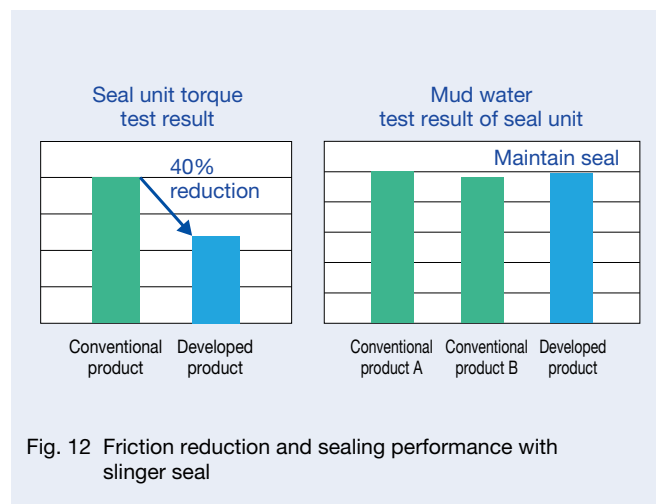


Fig. 12 Friction reduction and sealing performance with slinger seal

6. Other Methods of CO₂ Reduction

Efforts to reduce CO₂ emissions from hub unit bearings include reducing the use of raw materials, extending service life by improving reliability, and developing biomass materials that are directly related to carbon neutrality, in addition to reducing losses by lowering friction.

For example, we have completed the development of a cage made of biomass plastic. Conventional cages for hub unit bearings are made of polyamide 66, derived from fossil fuels. On the other hand, biomass plastic is made from plants that have grown by absorbing CO₂ from the atmosphere, so it does not increase the CO₂ concentration in the atmosphere when incinerated and thus contributes to carbon neutrality. Figure 13 shows the difference between fossil-derived plastics and biomass plastics.

NSK selected polyamide 410, a 100% plant-derived biomass plastic with a chemical structure similar to polyamide 66. Material characterization and bearing rotation tests confirmed that polyamide 410 performs similarly to polyamide 66. Using polyamide 410 can reduce CO₂ emissions by 90% over the entire life cycle compared to polyamide 66.

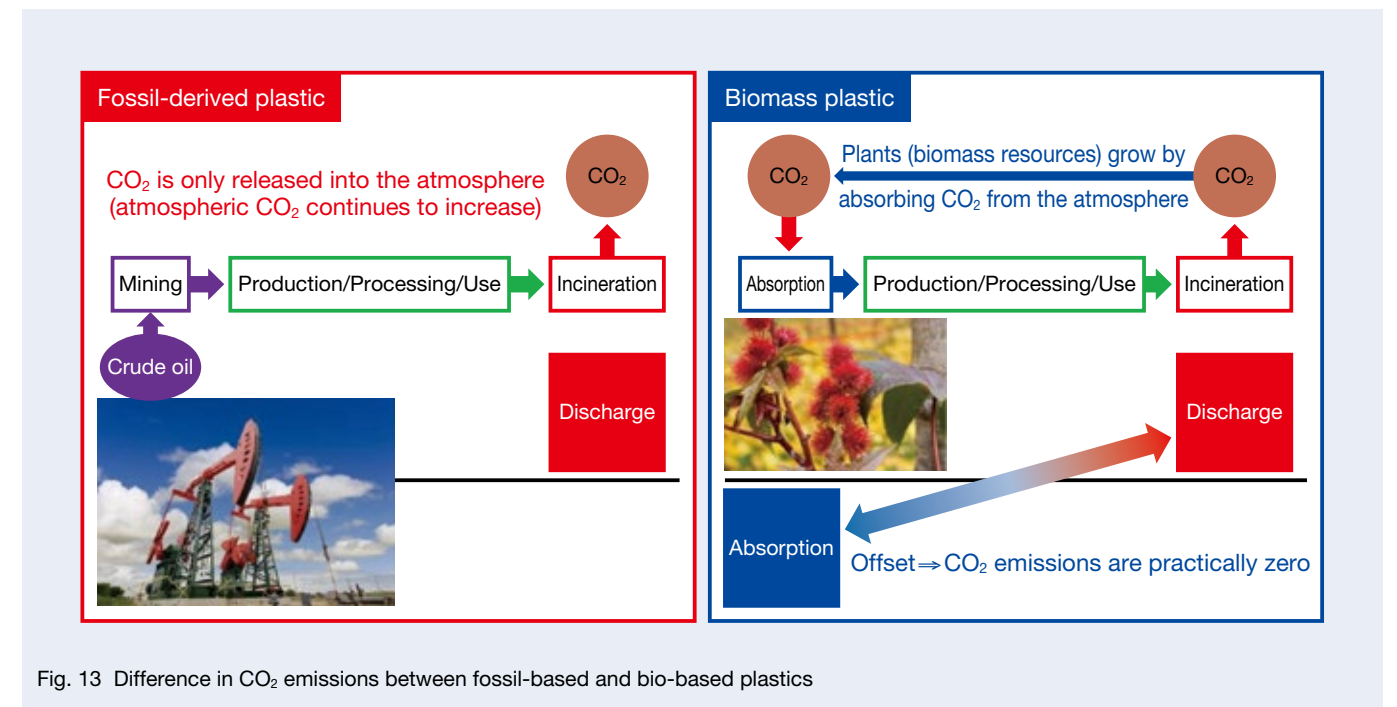


Fig. 13 Difference in CO₂ emissions between fossil-based and bio-based plastics

7. CO₂ Reduction Effect

This section summarizes the CO₂ reductions for the low-friction items presented so far. Based on the results for FY2021, the total CO₂ reduction of NSK's hub unit bearings with low-friction items is 330 kt/year.

Reducing the use of raw materials due to lighter weight bearings can reduce CO₂ emissions by 5 kt/year. Reducing the number of parts replaced in the market by applying water-resistant grease can reduce CO₂ emissions by 6 kt/year. Therefore, an overall reduction of 341 kt/year in CO₂ emissions for hub unit bearings is achieved.

Let us consider the implications of a 341 kt/year reduction in CO₂. Since the annual CO₂ emissions of Japanese households is 2.88 t²⁾, a reduction of 341 kt/year of CO₂ emissions is equivalent to the CO₂ emissions of about 118 000 households.

Since approximately 71 cedar trees absorb 1 ton of CO₂ annually, a reduction of 341 kt/year of CO₂ is equivalent to 24 million cedar trees. Assuming 900 cedar trees per hectare of forest, this corresponds to a forest area of about 26 900 hectares (269 km²), or about 43% of the 23 wards of Tokyo.

8. Conclusion

We have explained the technology of hub unit bearings and how they contribute to carbon neutrality. The leading cause of global warming is believed to be the increase in the concentration of CO₂ in the air. To stop global warming, it is necessary to reduce CO₂ emissions and achieve carbon neutrality.

NSK provides environmentally friendly products through its tribology and manufacturing technologies and promotes efforts to reduce CO₂ emissions by reducing the use of fuel and electricity, technological innovation, and the use of renewable energy.

Furthermore, developing and adopting environmentally friendly materials, distribution with less environmental impact, and using and disposing of NSK products will reduce CO₂ emissions throughout the supply chain.

References

- 1) Ministry of the Environment, "What is carbon neutral?" (Apr. 26, 2022), https://ondankataisaku.env.go.jp/carbon_neutral/about/
- 2) Ministry of the Environment, "Statistical survey on CO₂ emissions in the household sector in 2020 (confirmed value)," https://www.env.go.jp/earth/ondanka/ghg/kateiCO2_R2_1_1.pdf



Meiji Kato

Development of Magnetostrictive Torque Sensor

Takahiro Odera, Kota Fukuda

NSK-Warner K. K., Products Development Department

Junji Ono

Automotive Technology Development Center, Automotive New Product Development Department

Abstract

The drive shaft of a vehicle transmits not only torque from the engine or motor but also reaction torque from the wheel. If accurately measured, information on the torque of the drive shaft could be utilized in powertrain control and vehicle condition monitoring to extend cruising range, increase ride comfort, and ensure vehicle safety.

Here, we introduce a developed contactless torque sensor that uses inverse magnetostriction. With a compact and robust structure for powertrain applications, the developed torque sensor offers superior mountability. The sensor demonstrated accurate torque measurements for $\pm 1\,000$ Nm of torque input on a shaft with an outer diameter of 40 mm within a 4% error.

1. Introduction

In recent years, the automotive industry has undergone a technological revolution known as CASE, accelerating progress in automated driving technology and toward electrification to comply with environmental regulations. In order to improve safety and comfort and reduce environmental impact, automobiles are now equipped with a variety of sensors, and the information from these sensors is used for vehicle control.

NSK focused on the torque transmitted through the drive shaft as automobile control information. The transmission or reduction gear transmits the power generated by the engine or motor as torque to the tires. Conversely, the reaction force received by the tires from

uneven road surfaces is transmitted to the transmission and reduction gear. Understanding and utilizing these torques for control and condition monitoring is expected to improve cruising range, comfort, and safety. Commercial torque sensors are systems designed for bench use and are not suitable for mass-production applications in automobiles. However, NSK has developed a magnetostrictive torque sensor system mountable in the powertrain. This torque sensor is in non-contact with the drive shaft of the powertrain and has a compact and robust structure, making it easy to mount.

This paper presents an overview of the magnetostrictive torque sensor system developed by NSK, its detection principle, and performance verification.

2. System Overview

2.1 System configuration

Photo 1 and Figure 1 show the configuration of the torque sensor system. This system consists of three elements: a sensor head, shaft, and arithmetic unit. The sensor head is the ring-shaped component shown in Photo 1, which measures the shaft that goes through it. The sensor head is held out of contact with the shaft, allowing torque detection on a rotating power transmission shaft. Flexible printed circuits (FPCs) are provided inside the sensor head. A coiled copper wire pattern is formed on the FPC, and when current is applied, a magnetic field is generated between the FPC and the shaft.

The arithmetic unit mainly drives the sensor head, converts the signal from the sensor head into a torque value, and outputs the torque value to a higher-level control device such as an in-vehicle controller.

2.2 Torque detection flow

Figure 2 shows the flow of torque detection by this torque sensor system. When detecting torque with the torque sensor system, the arithmetic unit first applies a current to the sensor head (①). The current excites the FPC coil inside the sensor head, generating a magnetic field between it and the shaft, and a magnetic flux passes over the surface of the shaft (②). In this state, when the shaft is twisted (torque is loaded) and stress is generated, the inverse magnetostriction effect occurs¹⁾. The inverse magnetostriction effect is a phenomenon in which the magnetic properties of a magnetic material, such as iron, change when an external force distorts its crystal structure. This inverse magnetostriction effect changes the permeability of the torque-loaded shaft (③). When the permeability of the shaft changes, the magnetic flux generated by the FPC coil inside the sensor head by the excitation current of the arithmetic unit also changes, thereby changing the inductance of the FPC coil (④). Since the change in inductance can be extracted as an electrical signal, it can be output (⑤) as an electrical signal that changes in accordance with torque by applying signal processing, such as signal amplification and filtering in an arithmetic unit.



Photo 1 Magnetostriuctive torque sensor

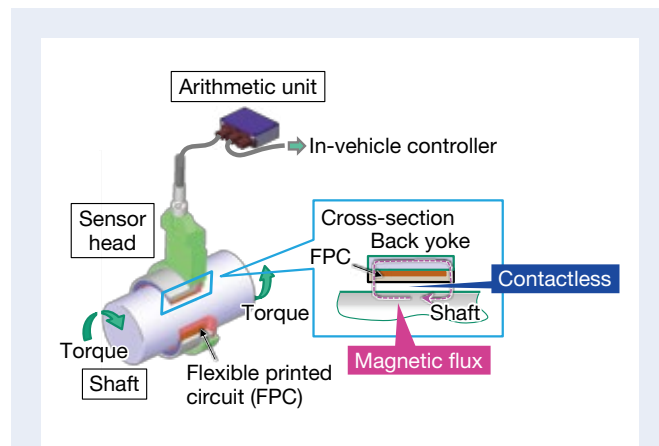


Fig. 1 Configuration of components in the magnetostriuctive torque sensor

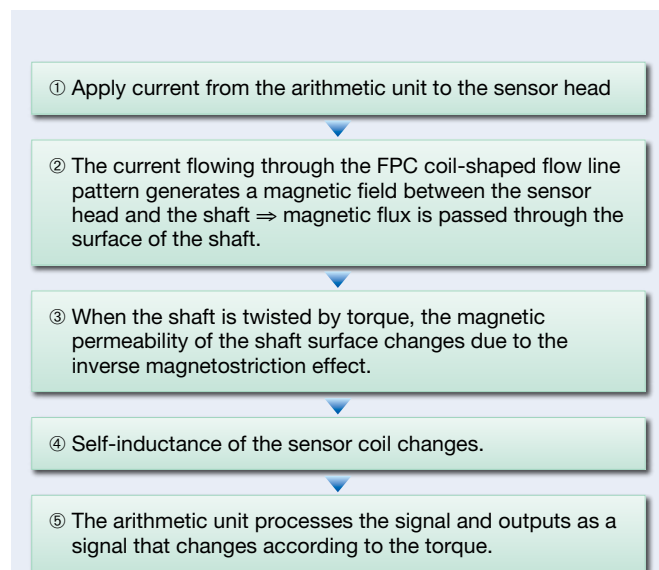


Fig. 2 Flowchart of torque detection by sensor

2.3 Torque detection performance and accuracy

This section describes the torque sensor system's torque detection performance and accuracy. The torque sensor system can output an analog voltage proportional to the detected torque, as described in section 2.2. The higher the "torque sensitivity," the ratio of input torque to sensor output, the less sensitive the sensor is to noise and errors, and the better the detection performance. Achieving high torque sensitivity as a system includes applying surface treatment to the shaft, selecting the steel grade, and optimizing shaft diameter and wall thickness.

Figure 3 also shows the three main errors in torque detection of the torque sensor system. The first error is the output change error due to torque loading, which includes hysteresis and nonlinearity errors, as shown in Figure 3 (1). This hysteresis is considered to be an effect of the magnetostrictive characteristics of the shaft.

The second error occurs during shaft rotation, as shown in Figure 3 (2), where the sensor output signal voltage fluctuates periodically with rotation. This phenomenon occurs when the magnetic permeability of the shaft surface is non-uniform in the circumferential direction.

The third error is the one that occurs when the operating ambient temperature changes, as shown in Figure 3 (3). In the torque sensor system, fluctuations in sensor output due to temperature are inherently unavoidable. This is because copper is used in the coil that produces the magnetic field inside the sensor head, and the electrical resistivity of copper changes with temperature. Therefore, the system has a circuit that estimates the sensor

temperature in the arithmetic unit. The temperature compensation using the signal enabled application of the system to a temperature range of -40°C to 150°C , assumed in automotive applications. However, although the change in electrical resistivity of copper itself can be regarded as linear over a practical temperature range, each component of the FPC coil inside the sensor expands and contracts according to different linear expansion coefficients. The output variation with temperature is therefore not perfectly linear. Hysteresis and nonlinearity errors remain even with the temperature compensation by the arithmetic unit as described above.

In developing the torque sensor system, the sum of these three errors was defined as the total system accuracy.

2.4 System development issues

The development of the torque sensor system aims for its application in an actual equipment environment, assuming an automotive powertrain. This actual equipment environment should include various environmental characteristics. Examples include oil containing foreign matter such as iron powder, wide temperature variations, vibration, shock, electromagnetic compatibility, high load torque, and high shaft speed rotation.

In addition, reducing the errors described in section 2.3 is essential to achieve highly accurate torque measurement. In developing the system, we worked to achieve within 5% of $\pm 1\,000\text{ Nm}$ (maximum shaft stress of 79.6 MPa) on a $\phi 40$ -solid shaft as a tentative target for the overall accuracy defined in section 2.3.

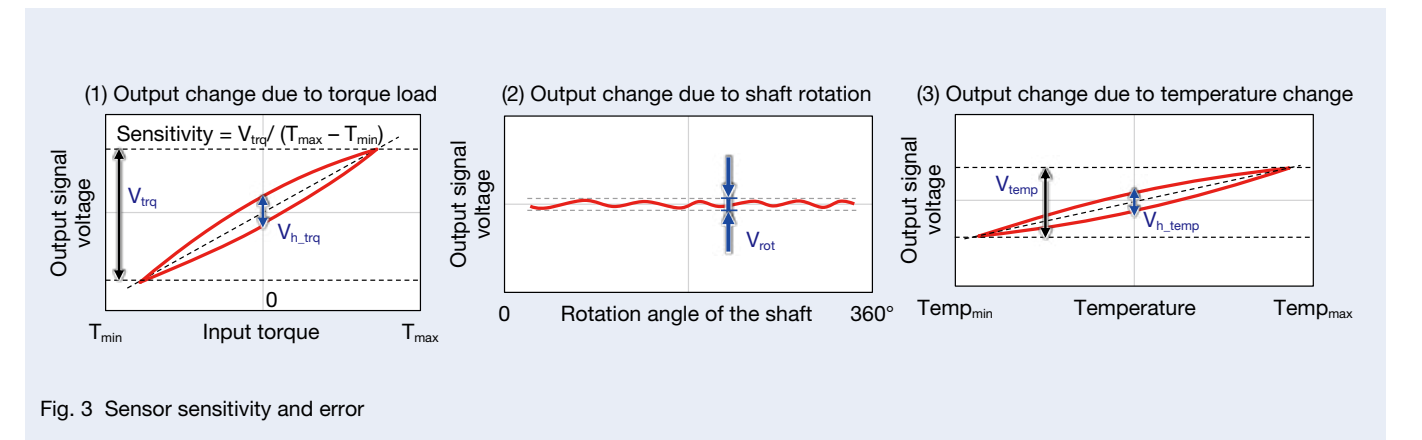


Fig. 3 Sensor sensitivity and error

3. Development of Each Component

3.1 Development of the sensor head

Figure 4 shows the developed sensor head. A plastic bobbin is placed at the innermost part of the sensor head, and an FPC used for torque detection is wound around its outer diameter surface. A back yoke is placed outside the FPC to suppress magnetic flux leakage. It is integrally molded with a plastic outer cover together with a plastic bobbin.

The inner diameter of the sensor head is $\phi 41.5$ mm. A clearance of 0.75 mm on each side was secured for the $\phi 40$ mm outer diameter of the shaft targeted by the torque sensor system to prevent interference due to runout or bending of the actual shaft.

The sensor head is 5 mm thick from the outer diameter of the back yoke to the inner diameter of the bobbin, which serves as the guide surface when mounted on the actual machine to achieve a compact and thin-walled structure. The sensor head is 28 mm wide in the axial direction.

Assuming the use of the developed product in oil containing foreign matter, such as iron powder, a lip-seal sealing structure is applied. Preventing oil and foreign matter from entering between the back yoke and bobbin prevents sensor detection performance degradation.

We evaluated the sensor performance in a box environment with ATF or MTF filled to the shaft center containing foreign matter at an oil temperature of 120°C and a rotation speed of 4 000 rpm for over 1 000 hours in order to confirm the oil resistance and contamination resistance of the product. This test confirmed no difference in sensor performance before or after the test.

Sensor specifications/dimensions

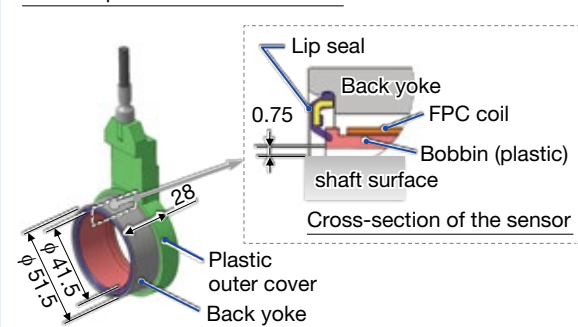


Fig. 4 Structure of sensor head

3.2 Shaft development

As described in sections 2.2 and 2.3, the magnetostrictive characteristics of the shaft affect the sensitivity of the sensor and the hysteresis error to torque in the system. This characteristic is known to vary depending on the steel grade used to make the shaft, heat treatment, and surface treatment²⁾.

Figure 5 shows the relationship between the steel grade and manufacturing method of the shaft and the sensitivity and hysteresis error of the sensor output. Focusing on the hysteresis error, the SCr and SCM materials, which are carburized and hardened, have significantly reduced hysteresis error compared to induction-hardened shafts made of carbon steel. Shot peening of the shaft and selecting a steel grade with a high Ni content effectively improve the sensor's sensitivity. Shot peening treatment on the shaft surface transforms non-magnetic austenite into ferromagnetic martensite, which is one factor that improves sensitivity¹⁾. In addition, using Ni-alloy steel as the steel grade can further improve the sensitivity. Shot peened shafts (SCr420H + SP, SCM420H + SP) were approximately four times more sensitive than untreated shafts (SCr420H, SCM420H). Shafts with SNCM420H (Ni = 1.55 – 2.0%) and SNC815 (Ni = 3.0 – 3.5%) were approximately 1.5 and 1.8 times more sensitive, respectively, than those with SCr420H (Ni \leq 0.25%).

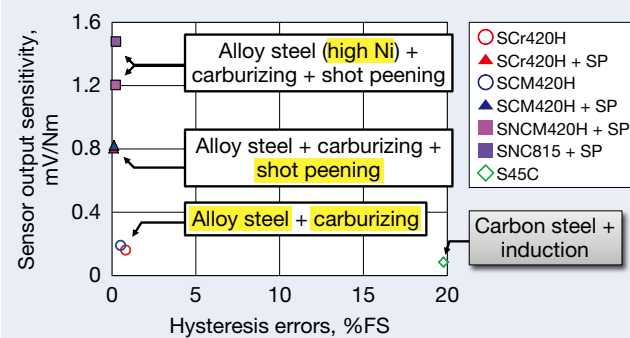
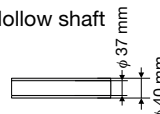


Fig. 5 Relationship between sensor output and shaft specification relative to torque

The evaluation results of the effect of shaft shape on sensitivity are shown in Table 1. Comparing a solid shaft with an outer diameter of $\phi 40$ mm and a hollow shaft with the same outer diameter but an inner diameter of $\phi 37$ mm, the sensitivity was about 4.1 times higher with the hollow shaft. The ratio of the stress generated to the torque is about 3.7 times, suggesting that the stress generated in the shaft should also be considered in the sensitivity design of the system using the sensor.

In addition, as discussed in section 2.3, non-uniformity of permeability in the circumferential direction of the shaft is a factor in errors that occur during rotation. As shown in Figure 6, uniform quality in the circumferential direction during the shaft manufacturing process effectively reduces errors during rotation.

Table 1 Stress on shaft and sensor sensitivity

	Generated stress per 1 Nm, MPa/Nm (calculated value)	Sensitivity of sensor output to input torque, mV/Nm (measured value)
Solid shaft 	0.08	0.66
Hollow shaft 	0.30	2.72
Hollow/solid ratio	3.7	4.1

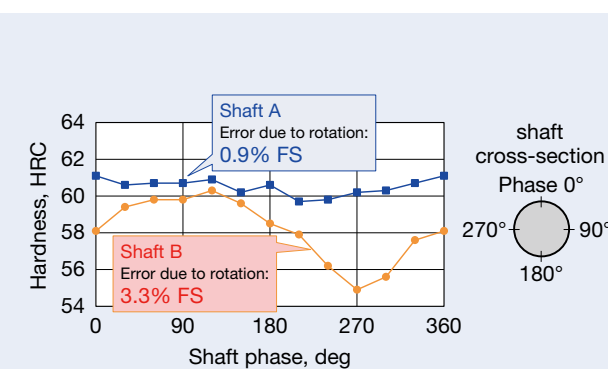


Fig. 6 Error from rotation and hardness around shaft

3.3 Development of the arithmetic unit

Figure 7 shows the arithmetic unit. An external power supply activates the arithmetic unit. Consideration of the actual automobile environment rated the power supply voltage at 12 V.

The arithmetic unit AC excites the sensor head, and the signal from the sensor head received by the arithmetic unit is converted to a torque signal. The arithmetic unit monitors the signal based on the current in the sensor head. It simultaneously performs temperature estimation to temperature compensate for the torque signal. The torque signal thus obtained is converted to an analog voltage or CAN signal and output externally.

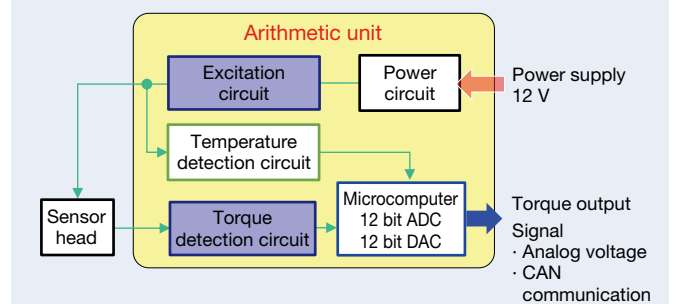
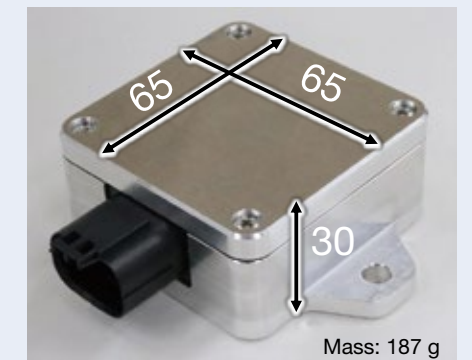


Fig. 7 Processing unit of torque sensor

4. Verification of the Torque Sensor System

We combined the sensor head, shaft, and arithmetic unit described in the previous sections to verify the system's torque measurement performance. Shafts were prepared by carburizing, hardening, and tempering SCr420H of diameter ϕ 40 (solid) and polishing and shot peening the torque measurement surface. The output of the magnetostrictive torque sensor was checked at temperatures of -30°C , 20°C , and 150°C with a torque of $\pm 1\ 000\ \text{Nm}$ applied to the shaft. The output characteristics are shown in Figure 8. The system has high linearity to the input torque (Figure 8 (1)). Furthermore, the temperature compensation function of the arithmetic unit enables output with minimal error (Figure 8 (2)) over the temperature range expected for the actual vehicle operating environment.

The overall accuracy of the output characteristics obtained from these measurements is shown in Figure 9. The overall accuracy of the torque sensor system was confirmed to be approximately 4.0%, which is lower than the target of 5% set in section 2.4.

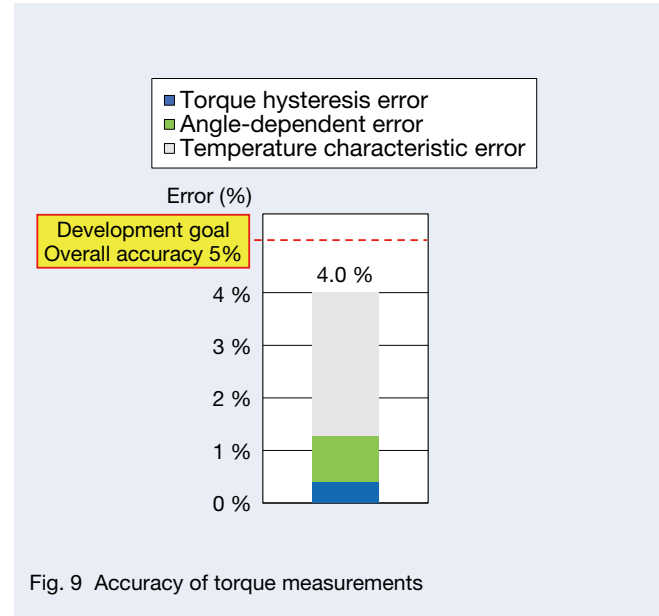


Fig. 9 Accuracy of torque measurements

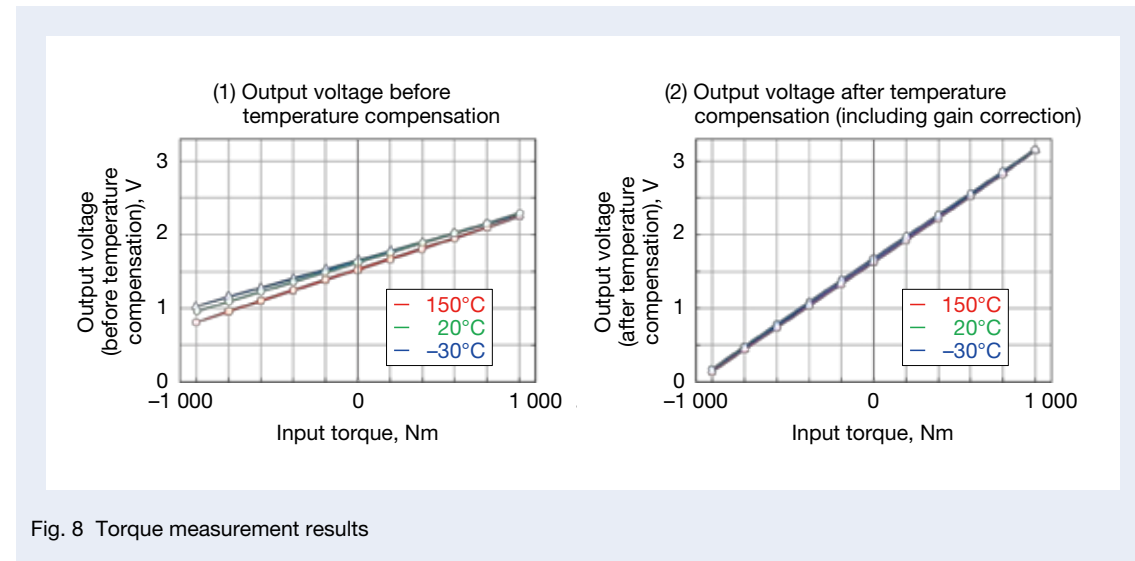


Fig. 8 Torque measurement results

5. Postscript

This paper describes developing a magnetostrictive torque sensor system for automotive powertrains that can be implemented in actual equipment and demonstrates its output characteristics. The demonstration confirmed that the torque sensor system has high linearity to the input torque and that the environmental temperature does not affect the output by applying temperature compensation using an arithmetic unit. Furthermore, an overall accuracy of approximately 4.0% was confirmed in the $\pm 1\ 000\ \text{Nm}$ torque range.

We are currently conducting various reliability evaluations, including durability in an oil environment. We will also expand the sensor head sizes to accommodate various applications.

References

- 1) T. Nakamura, Y. Sugiyama, and H. Shimizu, "Magnetostrictive Torque Sensor for In-Vehicle Transmission," *Hitachi Metals Technical Review*, Vol. 35 (2019), pp. 18–23.
- 2) K. Fukuda, J. Ono, T. Miyazaki, and S. Okada, "Proposal to apply Magnetostrictive Torque sensor in EV—Real time torque measurement of turbine shaft," JSAE Annual Spring Congress, No. 20195291 (2019), pp. 1–6.



Takahiro Odera



Kota Fukuda



Junji Ono

Evaluation of Steering Feel in the Off-Center Range Using Physiological Characteristics

Masaki Miyake

Technology Development Division Headquarters, New Field Products Development Center, Technology Development Department 1

Atsushi Kanbe

Department of Media Informatics, Faculty of Engineering, Aichi University of Technology

Keisuke Suzuki

Kagawa University Faculty of Engineering and Design

Makoto Nishio

This article has been approved for reprint by the Society of Automotive Engineers of Japan, Inc., following preprints of the *Transactions of Society of Automotive Engineers of Japan* (2022) (Vol. 53, No. 2).

Abstract

The purpose of this study is to construct the quantitative evaluation method of steering feel based on the sensitivity evaluation. In this study, we conducted experiments simulating and evaluating steering reaction torque characteristics in the off-center range by a driving simulator. We performed principal component analysis of sensitivity evaluation values and analyzed correlations with physiological indices. The results showed a strong correlation between electrocardiogram LF/HF and LF/(LF+HF), which are a sympathetic nerve activity index, and comfort, which shows the possibilities of more concentrated driving with favorite reaction torque characteristic.

1. Introduction

In addition to safety and security, automakers emphasize mood performance, such as driving enjoyment and comfort. Drivers get a feel from steering reaction force and vehicle behavior¹⁾, and steering feel influences the driver's mood. Therefore, design guidelines for steering feel are required for ensuring a positive mood for the driver²⁾. However, only a few studies have quantitatively analyzed the relationship between steering feel and driver mood. Automakers have been creating a steering feel based on sensory evaluations by test drivers. With regard to steering reaction force and vehicle behavior, changing vehicle behavior is challenging because this depends on vehicle specifications. Electric power steering (EPS) can design the steering reaction force relatively

freely. Furthermore, steer-by-wire systems have increased freedom in designing steering reaction force in recent years. It is considered adequate to design steering reaction force according to the driver's mood to efficiently improve the mood performance of automobiles.

Previous studies on driver mood evaluation have evaluated driving enjoyment³⁾. This evaluation method is valid for evaluating positive sentiments toward steering feel. However, it does not evaluate the driver's overall mood, including negative moods. Also, even in the same psychological state in the sensory evaluation, the physiological state may appear different due to differences in perception of the evaluation terms. It is therefore ideal to objectively confirm the validity of the psychological state with physiological characteristics such as EEG and heartbeat⁴⁾.

On the other hand, previous studies on steering feel using physiological characteristics evaluated the physical burden from muscle potentials during driving and the psychological burden from autonomous nerve activity⁵⁻⁷⁾. However, it was limited to research on the ease and burden of driving. The relationships between steering reaction force and drivers' moods, such as enjoyment and comfort, have not been investigated.

Against this background, the authors have been constructing a quantitative evaluation method for drivers' moods toward steering reaction force to realize a steering feel that can improve driving enjoyment and comfort. In a previous study⁸⁾, the authors showed the possibility of evaluating driver mood toward steering reaction force using mood evaluation and heartbeat-derived physiological characteristics. But because the evaluation environment was one in which discomfort toward reaction force characteristics was strong, enjoyment and comfort were not investigated. Also, because the mood evaluation terms are abstract, they have yet to be utilized in the design guidelines for steering reaction force. This study therefore addressed the following three objectives. The first was to evaluate various drivers' moods about steering feel comprehensively through mood evaluation, such as enjoyment and comfort, in steering. Second, the validity of the mood evaluation results would be objectively supported by physiological characteristics. The third was to extract drivers' characteristics (e.g., preferences for steering feel) from the mood evaluation results supported by physiological characteristics and demonstrate that they can be utilized in design guidelines for steering feel.

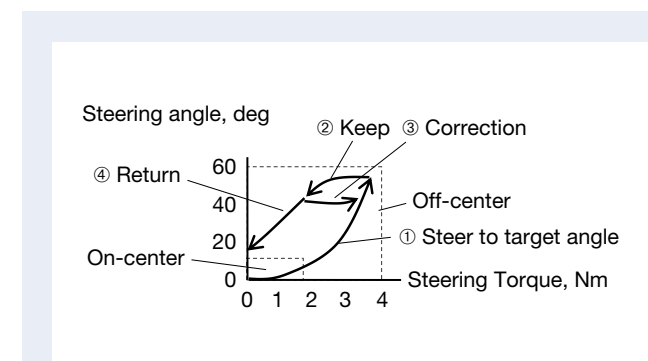


Fig. 1 Driver's steering actions in the off-center area

2. Method for Evaluating Steering Feel Using Physiological Characteristics

2.1 Steering feel in this study

We defined steering feel as the mood a driver feels through the steering reaction force and vehicle response when steering a vehicle. The driver's steering was divided into passive steering to maintain a straight line and active steering for curves. The on-center and off-center ranges were defined based on the difference in the steering angle range. Since drivers perform complex and active steering in the off-center range, such as (1) turning and steering to the target steering angle, (2) steering retention, (3) corrective steering, and (4) returning steering, as shown in Figure 1, we believe that various moods can be induced, and in this study we evaluated steering feel in the off-center range.

2.2 Mood evaluation

A previous study reported a method for evaluating basic moods regarding alertness and comfort/discomfort⁹⁾. This study used the basic mood model assumed in the previous study⁸⁾ to evaluate the driver's mood toward steering feel (Figure 2). The basic mood model allows for a comprehensive evaluation of the driver's moods, such as excitement, enjoyment, boredom, and frustration, based on pleasure/displeasure and alertness levels.

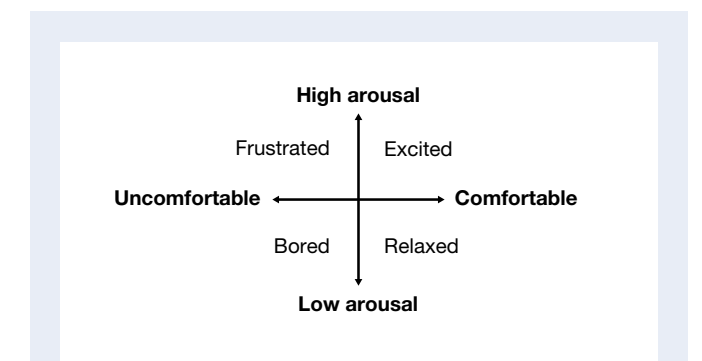


Fig. 2 Basic emotion model⁹⁾

This study evaluated drivers' moods using the basic mood model and the seven-step semantic differential (SD) method with mood evaluation words related to steering feel. A total of 36 mood evaluation words were used (Table 1): 8 words for basic moods, 16 abstract evaluation words that provide supplementary descriptions of basic

moods, and 12 force evaluation words selected to guide the design of the steering feel. Abstract evaluation terms were extracted from the previous study⁸⁾, excluding those with ambiguous meanings. The force evaluation terms related to the off-center range were selected from those used to evaluate automobile steering systems.

Table 1 Sensitivity evaluation words

Basic emotion	Abstract evaluation words	Force-based evaluation words
Comfortable	<ul style="list-style-type: none"> Controllable Frisky Luxurious Cheap 	<ul style="list-style-type: none"> Good Sense of unity with vehicle Increase rate of steering torque is linear Easy to estimate vehicle behavior Lumpy
Uncomfortable		
Awake	<ul style="list-style-type: none"> Active Stretchy Cleared Strong 	<ul style="list-style-type: none"> Steering torque of on-center is heavy/light Steering-retaining torque is heavy/light
Sleepy		
Excited	<ul style="list-style-type: none"> Attractive Sporty Exact Monotonous 	<ul style="list-style-type: none"> Good vehicle reaction Quick vehicle reaction
Bored		
Relaxed	<ul style="list-style-type: none"> Regulated Steady Smooth Delicate 	<ul style="list-style-type: none"> Returns easily Returns quickly Smooth counter steering Steering retaining is easy
Frustrated		

2.3 Physiological indicators

2.3.1 Heartbeat-derived physiological index

The same autonomic indexes as in the previous study⁹⁾ were used to evaluate the comfort/discomfort of the steering feel. Physiological indices related to sympathetic (concentration and stress) and parasympathetic (relaxation) nerve indices were calculated from the R-R interval of heartbeats for six autonomic nervous system indices, shown in Table 2. Note that CSI and CVI are indices proposed in a previous study¹⁰⁾ and are calculated by performing Lorenz plot analysis on time series data of R-R intervals.

2.3.2 EEG-derived physiological indices

The same CNS physiological indices as in the previous study⁹⁾ were used to evaluate the alert state for steering feel. The measured EEG data allowed for the calculation of power spectral integrals at 1 Hz intervals by fast Fourier transform (FFT). Theta waves (4 Hz to less than 8 Hz), alpha waves (8 Hz to less than 13 Hz), and beta waves (13 Hz to less than 30 Hz) were used as physiological indicators.

3. Experimental Environment

3.1 Driving simulator (DS)

We used a DS that uniquely combined an Elsaco shaking device and a Mige reaction force device (90ST-AM04025)

with the DS-nano simulation software from Misaki Design. DS is equipped with a steering system model^{1, 8)} that allows the user to change the reaction force characteristics as desired. Vehicle behavior was calculated using CarSim, and the vehicle model was a D-segment sedan type⁸⁾.

During the experiment, running images and shaking were presented to the participants from three LCD monitors and motion devices via DS-nano. The lighting in the laboratory was turned off because the participants might experience simulator sickness if they could see their surroundings during the shaking. To improve the sense of immersion in the driving experience, the driving sounds of a sedan attached to the DS were played.

3.2 Driving course

The driving course is shown in Figure 3. A circular course with a straight line and five S-curves allowed the experimental participants to actively steer in the off-center range. The entire course was 7 km long. To have the participants concentrate on steering operation, the vehicle speed was fixed at 60 km/h. They were instructed to follow the solid yellow line in the center of the road. Each curve's radius of curvature R was set to $R = 60$ m so that the maximum steering angle at the steering wheel would be 60 degrees. In addition, a relaxation section is provided at the junction of a straight line and a curve to prevent abrupt steering operation.

Table 2 Physiological indices of autonomic nervous system

Physiological indices	Neural activity
CVR-R	Parasympathetic nerve activity (relaxation)
HF	
LF/HF	Sympathetic nerve activity (concentration/stress)
LF/(LF + HF)	
CSI	
CVI	Parasympathetic nerve activity

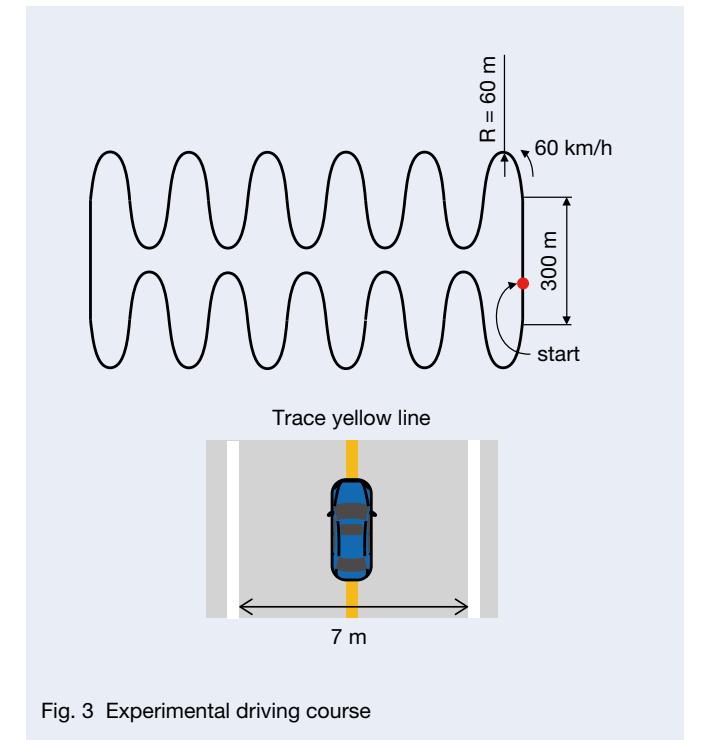


Fig. 3 Experimental driving course

3.3 Reaction force characteristics

In turning and steering in the off-center range, the larger the slope of change in steering torque (T_{sw}) to steering angle (θ_{sw}) ($\Delta T_{sw}/\Delta\theta_{sw}$) in in-center steering, the heavier the response. In addition, a moderate hysteresis of steering torque (T_{hys}) between steering retaining and corrective steering reduces the driving burden. This study set up three reaction force characteristics with different gradients and hysteresis of steering torque change with the steering angle. Figure 4 shows the set reaction force characteristics.

The reaction force characteristic in Figure 4 (a) are designed to have heavy steering torque by increasing the steering torque change gradient ($\Delta T_{sw}/\Delta\theta_{sw}$) compared to other reaction force characteristics (Figure 4 (a) is referred to as the heavy characteristic hereafter). The reaction force characteristic in Figure 4 (b) is designed to allow the

driver to control the vehicle with less operational burden by reducing the steering torque change gradient ($\Delta T_{sw}/\Delta\theta_{sw}$) when turning and steering compared to the heavy characteristic (Figure 4 (b) is from now on referred to as the light characteristic). The light characteristic has a larger hysteresis T_{hys} than the heavy characteristic, reducing the operational burden of steering retention and corrective steering. The heavy and light characteristics were given steering torque vibration corresponding to road surface vibration in order to improve the sense of immersion in driving¹¹⁾. The reaction force characteristic in Figure 4 (c) is based on the light characteristic. It was given a steering wheel vibration that simulates driving on rough roads, resulting in a bumpy, snaggy characteristic that intentionally makes steering difficult (Figure 4 (c) will be referred to as the lumpy characteristic).

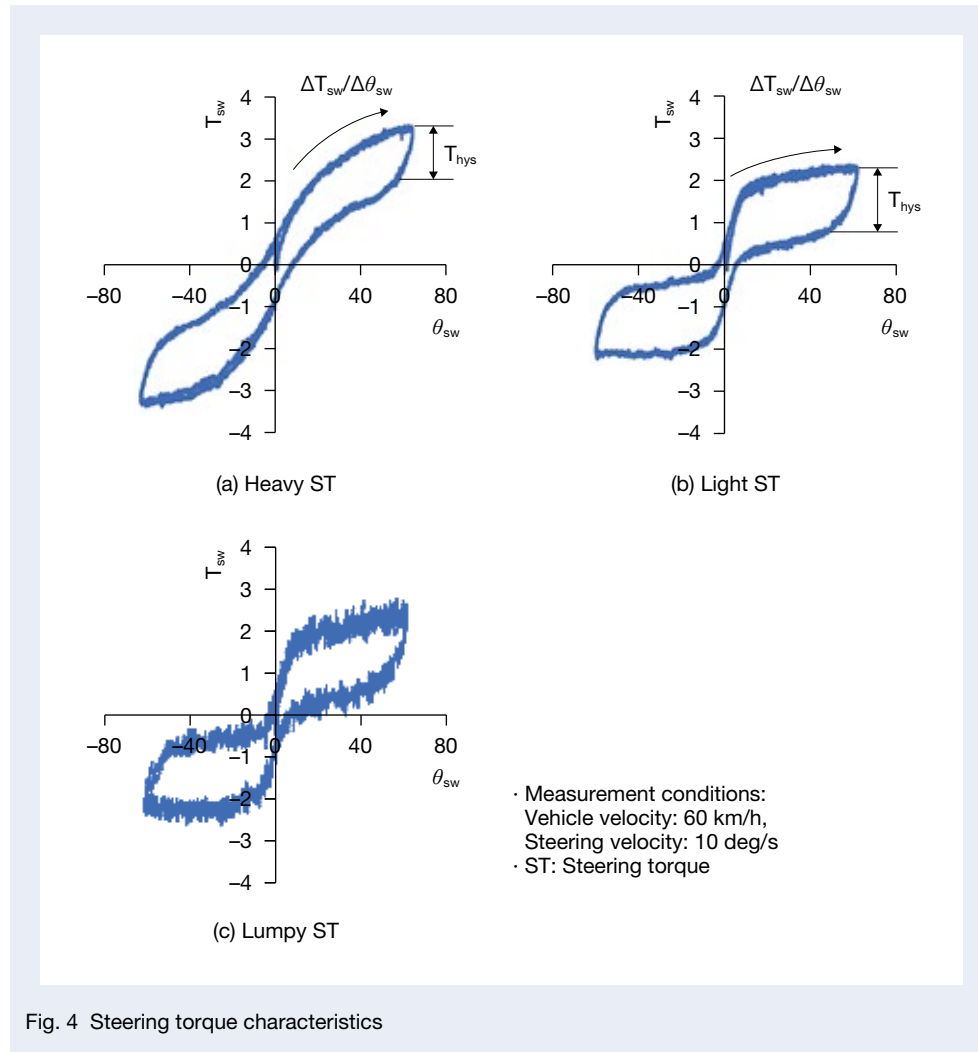


Fig. 4 Steering torque characteristics

3.4 Experimental methods

3.4.1 Participants in the experiment

The experimental participants were 16 males (average age: 35.6 years, standard deviation: 13.5) with regular driver's licenses. Of the participants in the experiment, nine were evaluation drivers involved in the development of car steering systems (average age: 45.2 years, standard deviation: 10.5), and seven were general drivers who drive cars daily (students, average age: 23.1 years, standard deviation: 1.12); the ratio of the number of participants was 6:4. Informed consent, discussed and approved by the Research Ethics Committee of the Faculty of Creative Engineering, Kagawa University, was obtained from the experimental participants.

3.4.2 Driving method

We conducted two runs for the three types of reaction force characteristics: one for mood evaluation and the other for measurement of physiological characteristics. In mood evaluation driving, physiological characteristics were not measured, and the driving time was unlimited to have the experimental participants concentrate on the difference in steering feel. The running order of the three reaction force characteristics was randomized. A practice run (3 min) was conducted before the actual run (unlimited time) to exclude the influence of learning effects, and a mood evaluation (15 min, including breaks) was conducted after the actual run. On the other hand, in the run for the evaluation of physiological characteristics, to stabilize the physiological characteristics before the actual run and to use them as a basis for data analysis, rest with eyes closed (5 min) was added between the practice run and the actual run for the mood evaluation. The actual run time was 10 min.

3.4.3 Methods measuring physiological characteristics

The heartbeat R-R interval was measured using the myBeat WHS-1 heartbeat sensor manufactured by Union Tool Co., the same as in the previous study⁸⁾, and Ambu's SP-00-S, a disposable-type silver chloride electrode. The measurement point was the left chest.

EEG was measured using the DualMind VBPG-01, a simultaneous EEG/pulse wave measuring device manufactured by TAOS Institute, Inc., the same manufacturer as in the previous study⁸⁾. The device was attached to the frontal region of the patient's head. EEG was measured at Fp1 and Fp2 as defined by the ten-twenty electrode system, the international standard for EEG measurement sites.

4. Experimental Results

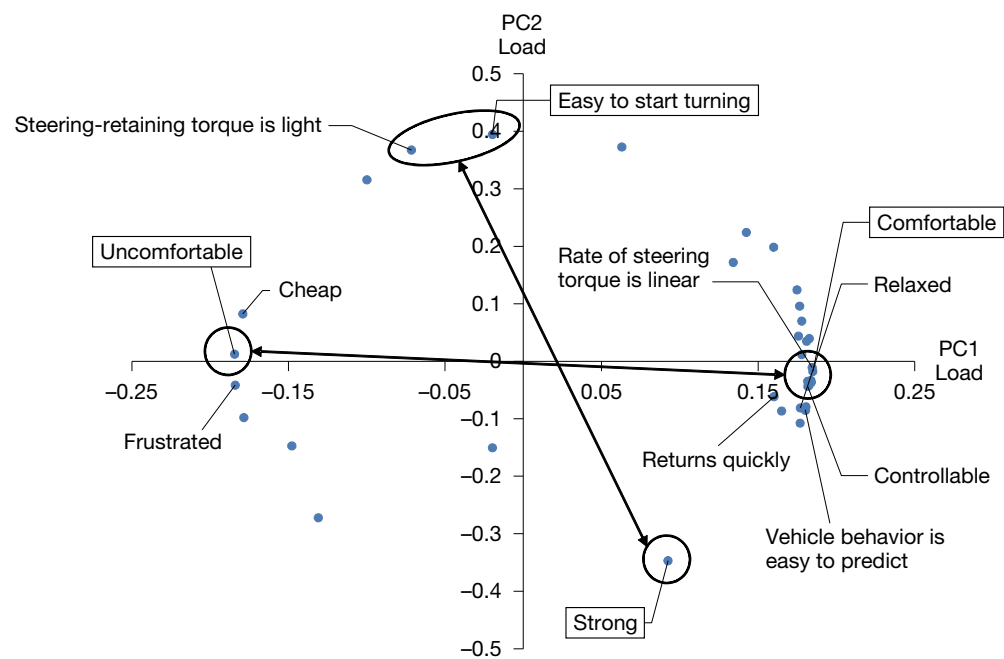
4.1. Results of principal component analysis of mood evaluation

Principal component analysis was performed on the mood evaluation results of 16 experimental participants. Since the results were divided into driver groups that preferred heavy and light characteristics, principal component analysis was performed for each group. Figures 5 and 6 show the results of the principal component analysis for the group that preferred light characteristics (9 people) and the group that preferred heavy characteristics (7 people). The principal component loadings scatter plots shown in Figures 5 (a) and 6 (a) confirmed the evaluation words corresponding to the first Principal Component (PC1) and the second Principal Component (PC2) and found that PC1 was "comfort/discomfort" and PC2 was "heavy/light" for both groups. Preferences for heavy and light characteristics were classified according to PC1 scores, representing "comfort/discomfort." Figure 7 shows PC1 scores for all the experimental participants. The ratio of the number of evaluation drivers and general drivers in each group was 6:4, the same as that of the 16 participants.

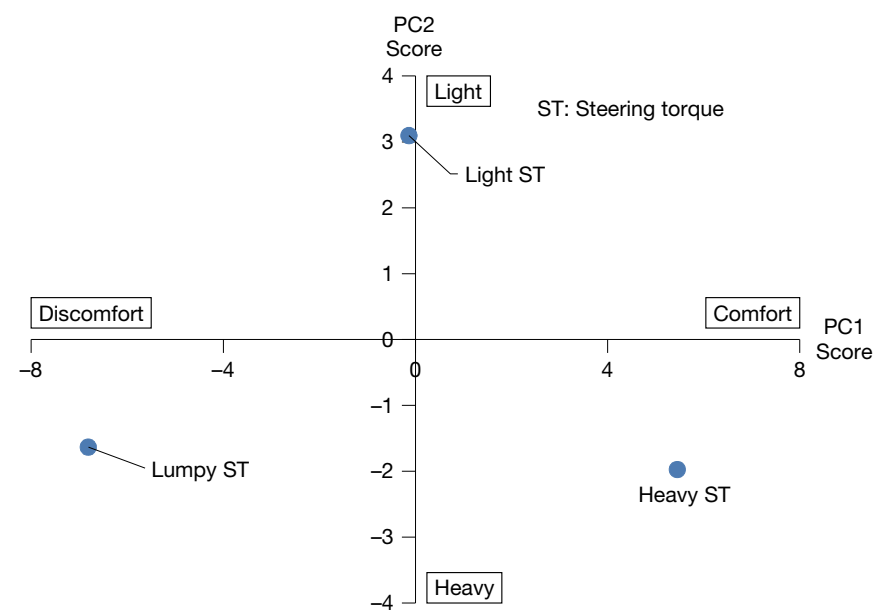
The eigenvalue list in Table 3 shows that the steering feel in the off-center range could be evaluated more than 90% by "comfort/discomfort" and "heavy/light." Furthermore, the principal component score scatter plots shown in Figures 5 (b) and 6 (b) confirm that all experimental participants could clearly distinguish the three reaction force characteristics.

4.2 Results of correlation analysis of basic moods and physiological indices

From 16 experimental participants, the threshold of the correlation coefficient $|R|$ was set at $|R| > 0.6$ to satisfy a t value (2.264) that satisfied the 1% level (one-tailed test) in a t distribution with 16 samples. When we checked the correlation between the results of mood evaluation and physiological indices for the 16 participants, we could not confirm a correlation coefficient of $|R| > 0.6$, so we divided them into two groups, evaluation drivers and general drivers, and conducted a correlation analysis for each group. Table 4 shows the correlation analysis between the evaluation drivers' basic moods and the heartbeat-derived sympathetic nerve indices, LF/HF and LF/(LF + HF). Table 4 confirmed a correlation coefficient of $|R| > 0.6$ for "A: Comfortable," "B: Uncomfortable," and "G: Relaxed." From the above, we could quantitatively evaluate "comfort/discomfort" and "relaxed" among the driver's basic moods toward the steering feel by using mood evaluation and physiological characteristics for the evaluation drivers. We could not confirm a correlation coefficient of $|R| > 0.6$ for general drivers and EEG-derived physiological indices.

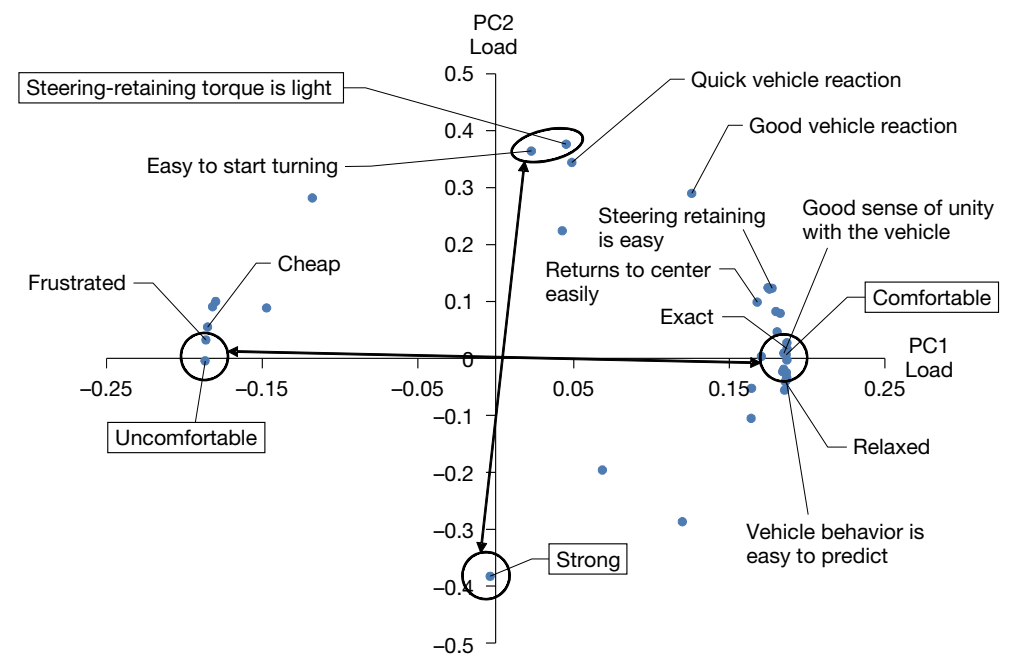


(a) Scatter plot of principal component loads

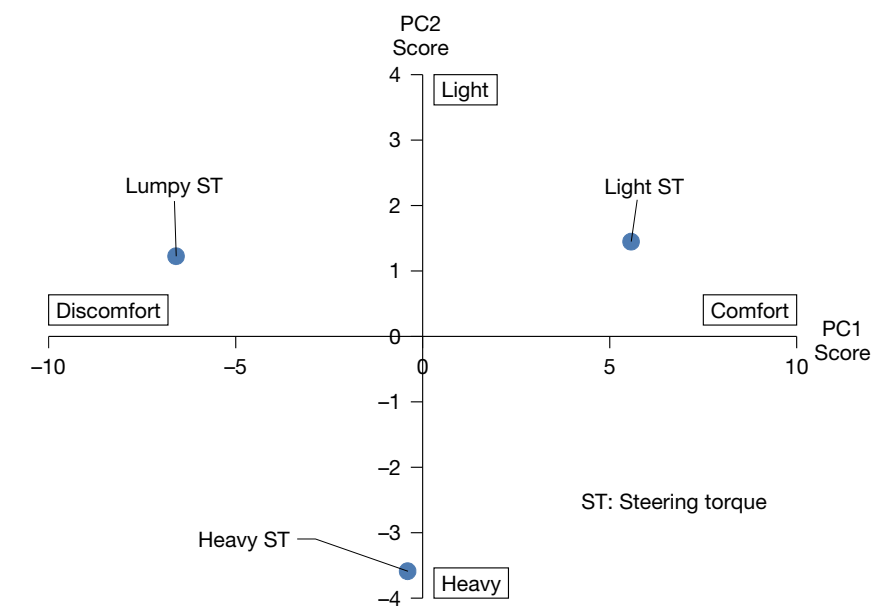


(b) Scatter plot of principal component scores

Fig. 5 Principal component analysis (drivers prefer heavy ST)



(a) Scatter plot of principal component loads



(b) Scatter plot of principal component scores

Fig. 6 Principal component analysis (drivers prefer light ST)

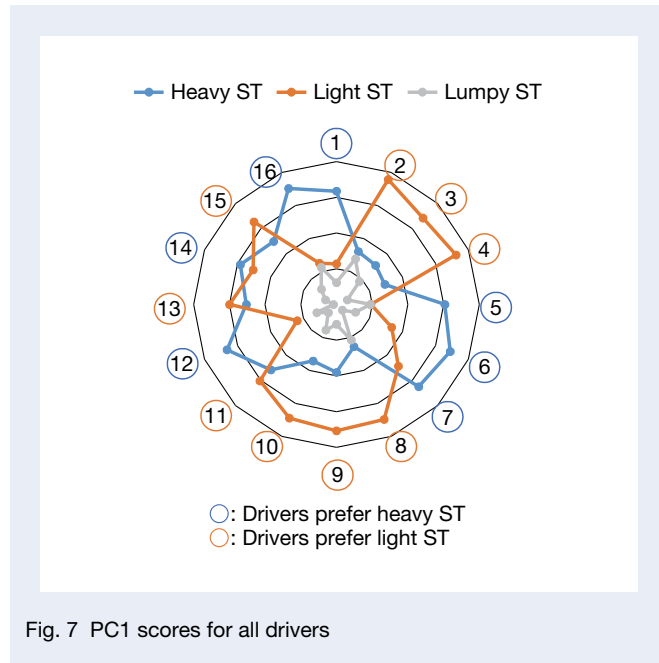


Table 3 Eigenvalue list

	Drivers prefer heavy ST		Drivers prefer heavy ST	
	PC1	PC2	PC1	PC2
Eigenvalue	28.3	6.5	29.1	6.2
Contribution rate (%)	74.4	17.0	76.7	16.3
Cumulative contribution rate (%)	74.4	91.4	76.7	93.0

4.3 Influence of different reaction force characteristics on physiological characteristics

To confirm the effects of the preferred reaction force characteristics on the physiological characteristics of the drivers, an analysis of variance was conducted for the three types of reaction force characteristics using the indicators with the high correlation coefficients among the sympathetic nerve indices that were confirmed to correlate with “comfort/discomfort” for the groups that preferred heavy and light reaction forces, respectively.

LF/ (LF + HF) ($R = 0.59, p = 0.005$) was used for the group that preferred heavy characteristics. First, a test of homogeneity of variance resulted in $p < .05$, and equal variances could not be assumed. Therefore, an analysis of variance using the Welch method confirmed a significant difference ($F(2, 9.84) = 33.209, p < .001$). Therefore, multiple comparisons using the Games-Howell method confirmed significant differences ($p < .001$), as shown in Figure 8.

CSI ($R = 0.49, p = 0.009$) was used for the group that preferred light characteristics. First, a test of homogeneity of variance resulted in $p \geq .05$. Since equal variances could be assumed, a one-way analysis of variance was conducted, confirming a significant difference ($F(2, 24) = 6.045, p = .007$). Multiple Tukey comparisons confirmed a significant difference ($p = .012$), as shown in Figure 9. These results confirmed that the driver’s sympathetic nerve index is significantly greater in the preferred reaction force characteristics. The sympathetic nerve index is an index of concentration and stress, as shown in Table 2. However, as shown in Table 4, the correlation between the sympathetic nerve index, LF/ (LF + HF), and “G: Relaxed” was also confirmed, suggesting that the drivers could concentrate on driving in their preferred reaction force characteristics.

One possible reason for the lack of correlation between LF/LF + HF and “comfort/discomfort” in the group that preferred light characteristics may be the effect of respiratory rhythm. Speeding up breathing decreases the apparent LF component and increases the HF component¹²⁾. On the other hand, CSI is less susceptible to respiratory rhythm fluctuations because Lorenz plot analysis can exclude outliers¹⁰⁾. In addition, in this research, improving the sense of immersion in driving facilitated a sense of tension similar to that of a real car in the experimental environment. From the above, CSI could be applied to the group that preferred light characteristics since tension caused a faster respiratory rhythm.

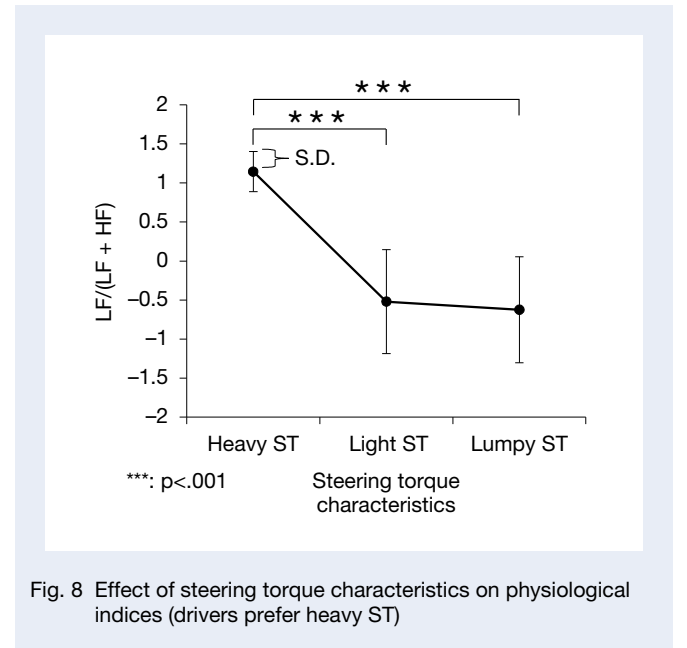


Fig. 8 Effect of steering torque characteristics on physiological indices (drivers prefer heavy ST)

Table 4 Correlation analysis results (only evaluation drivers)

Basic emotion		A	B	C	D
LF/HF	R	0.700	-0.783	-0.043	-0.153
	P value	< .001	< .001	0.831	0.445
LF/(LF + HF)	R	0.632	-0.738	-0.025	-0.243
	P value	< .001	< .001	0.903	0.223
Basic emotion		E	F	G	H
LF/HF	R	0.288	-0.152	0.783	-0.442
	P value	0.145	0.450	< .001	0.021
LF/(LF + HF)	R	0.307	-0.082	0.714	-0.411
	P value	0.120	0.686	< .001	0.033

A: Comfortable B: Uncomfortable C: Awake D: Sleepy E: Excited F: Bored G: Relaxed H: Frustrated

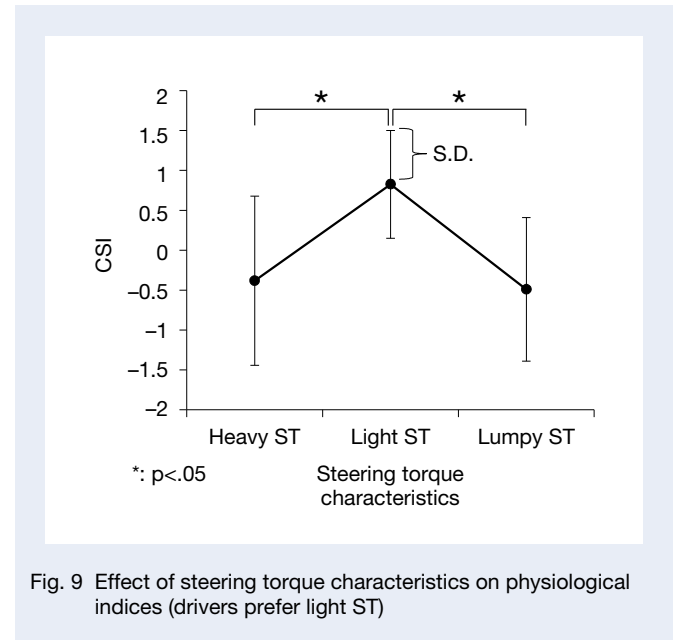


Fig. 9 Effect of steering torque characteristics on physiological indices (drivers prefer light ST)

5. Analysis of driver characteristics

In the previous chapter, dividing the experimental participants into groups of evaluation drivers, general drivers, and drivers who prefer heavy and light characteristics confirmed the correlation between basic moods and mood evaluation results and the effects of steering reaction force on physiological characteristics. However, specific factors that could classify drivers (characteristics common to each driver group) still need to be determined. This chapter analyzes driver characteristics based on driving behavior and mood evaluation results.

5.1 Analysis of driver characteristics by driving behavior

From the steering speed data of the five mid-course S-curves shown in Figure 3, SE values indicating the steering smoothness were calculated using the steering entropy method (SE)¹³⁾ and compared for each participant in the experiment. The bumpy characteristic in Figure 4 (c) was excluded from the analysis because the steering was intentionally set to be difficult, and its SE value was obviously significant. Cluster analysis using Ward's method resulted in three groups, as shown in Figure 10. As shown in Figure 11, the SE values were smaller in the order of Group A, Group B, and Group C. The groups with smaller SE values contained more evaluation drivers.

Therefore, a t-test conducted on the SE values of the evaluation drivers and the general drivers confirmed that the evaluation drivers had significantly smaller SE values than the general drivers ($t(14) = -3.125, p < .01$), as shown in Figure 12. These results suggest that not only the evaluation drivers but also those who steer smoothly are more sensitive to changes in forceful stimuli of steering reaction force, and their physiological characteristics are more likely to be affected. This may be one reason the correlation between the mood evaluation results and physiological characteristics in Section 4.2 could not be confirmed in general drivers.

5.2 Analysis of driver characteristics by mood evaluation

Fourteen mood evaluation values were compared in the driver groups that preferred heavy and light characteristics by adding "e: Strong" and "j: Delicate," which are evaluation words concerning forceful stimuli from among the abstract evaluation words, to the forceful evaluation words (12 words) concerning the steering feel shown in Table 1.

The mean value for each evaluation word was calculated. Figure 13 shows the difference between the means for each group (a group that prefers heavy characteristics – a group that prefers light characteristics). Positive scores in Figure 13 indicate a higher mood evaluation value for the group that prefers heavy characteristics. In comparison, negative

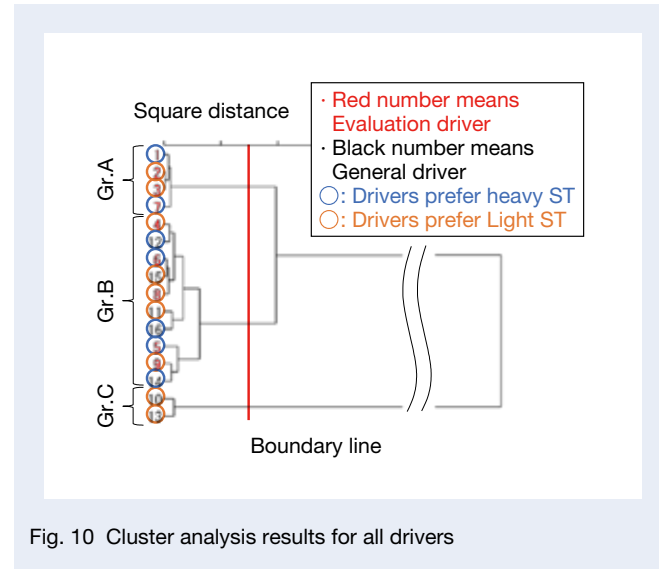


Fig. 10 Cluster analysis results for all drivers

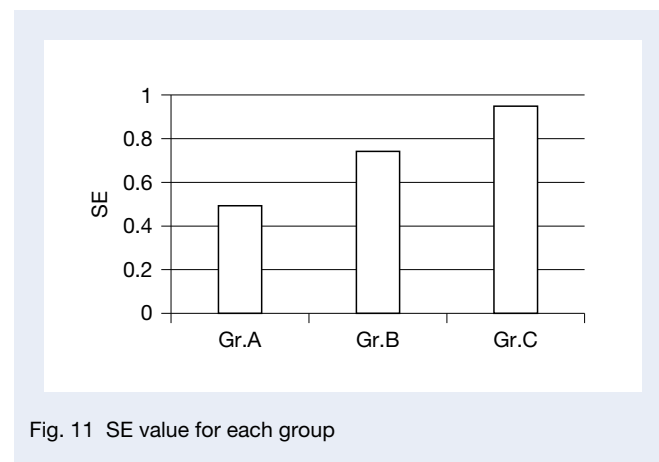


Fig. 11 SE value for each group

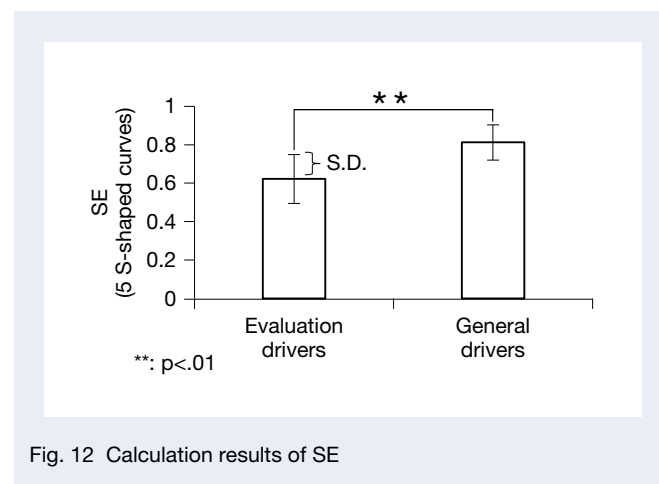


Fig. 12 Calculation results of SE

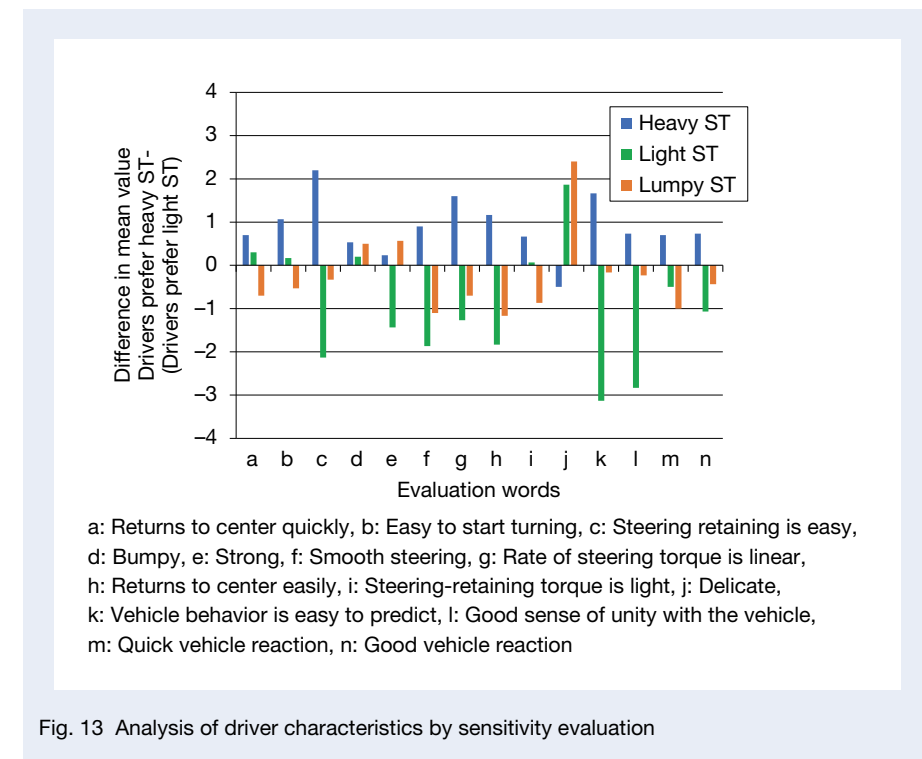


Fig. 13 Analysis of driver characteristics by sensitivity evaluation

scores indicate a higher mood evaluation value for the group that prefers light characteristics.

Also shown in Figure 13, the group that prefers light characteristics has a difference of more than 2 points in mood evaluation values (k: Easy to estimate vehicle behavior, l: Good sense of unity with vehicle) regarding vehicle response in the preferred reaction force, which is more pronounced than the other evaluation words. Thus, the driver group that prefers light characteristics may be more sensitive to the overall steering feel, including vehicle behavior. On the other hand, the group that prefers heavy characteristics has a difference of more than 2 points for "j: Delicate" in the bumpy reaction force characteristic, which is more pronounced than the other evaluation words. This suggests that the driver group that prefers heavy characteristics may be more sensitive to the forceful stimulation of steering reaction force. Based on the mood evaluation results, we could provide a design guideline for the driver's preferred steering feel.

6. Summary

6.1 Evaluation of drivers' moods for steering feel

A mood evaluation based on the basic mood model was performed for the steering feel in the off-center range, and drivers' moods were comprehensively evaluated. The principal component analysis of the mood evaluation showed that the steering feel in the off-center range can be evaluated as "comfort/discomfort" and "heavy/light."

6.2 Corroboration of mood evaluation results by physiological evaluation

Correlation analysis of the results of mood evaluation and physiological characteristics confirmed a correlation between LF and LF/(LF + HF), which are sympathetic nerve indices, and "comfort/discomfort" and "relaxed." Drivers also showed that the sympathetic nerve index LF/(LF + HF) or CSI was activated in their preferred reaction force characteristics, indicating the possibility of more attentive driving.

6.3 Analysis of drivers' characteristics

With regard to the operator's driving behavior and mood evaluation results, classifying the drivers' preferences and sensitivities to the steering feel could indicate design guidelines for the steering feel that drivers prefer.

7. Future Plans

Although this study evaluated drivers' moods toward steering feel in the active off-center range, the possibility of evaluating drivers' moods in the passive on-center range needs to be verified. In addition, a clear classification of drivers' characteristics has yet to be determined. In the future, understanding various drivers' characteristics will enable the design of a steering feel that matches the driver's preferences.

Acknowledgments

We want to express our deepest gratitude to Dr. Miyatake Hiroaki, formerly of Suzuki Laboratory, Kagawa University, for his excellent cooperation in the experiments and data analysis, and Dr. Kushiro Ikuo for his valuable comments on the construction of the experimental environment.

References

- 1) Daisuke Yamada, Ikuo Kushiro, and Yuji Muragishi, "Investigation of the Relationship between Characteristics of Steering Wheel Torque and Behavior of Driver-Vehicle Systems," *Transactions of the Society of Automotive Engineers of Japan*, 44 (2), pp. 459–465, 2013.
- 2) I. Badiru, "Customer Focus in EPS Steering Feel Development," *SAE Int. J.J., Passenger Cars—Mechanical Systems* 7 (3), pp. 1 009–1 015, 2014.
- 3) Katsunori Tanaka, Tsuyoshi Sakuma, Hideaki Misawa, and Yuka Miyashita, "A Study of Driving Pleasure Based on KANSEI Engineering," *Transactions of the Society of Automotive Engineers of Japan*, Vol. 47, No. 05, 2016.
- 4) Sonoko Ishimaru, "Study on the Relationship Between Psychological Condition and Physiological Measurement, and Tactile," *Journal of the Japan Research Association for Textile End-Uses*, Vol. 47, pp. 772–785, 2006.
- 5) H. Krüger, A. Neukum, and J. Schuller, "A Workload Approach to the Evaluation of Vehicle Handling Characteristics," SAE Technical Paper 2000-02-0170, 2000.
- 6) Koji Mikami, Yukiyo Kuriyagawa, and Ichiro Kageyama, "Fundamental Study on Evaluation for Driving-Pleasure Using Biological Reaction," *The Japan Society of Mechanical Engineers*, 14th The Transportation and Logistics Conference, No. 05-52, pp. 291–294, 2005.
- 7) Akira Kuramori, Noritake Koguchi, Masayoshi Kamijo, Tsugutake Sadoyama, and Yoshio Shimizu, "Evaluation Method for Vehicle Handling and Stability Focusing on Muscle Tension of the Driver," *Journal of Japan Society of Kansei Engineering*, Vol. 6, No. 2, pp. 87–92, 2006.
- 8) Atsushi Kanbe, Hiroaki Miyatake, and Keisuke Suzuki, "Physiological Measurement and Kansei Evaluation of Steering Feeling Affected by Steering Wheel Torque," *Journal of Japan Society of Kansei Engineering*, Vol. 19, No. 1, pp. 73–79, 2019.
- 9) J.A. Russell, "A Circumplex Model of Affect," *Journal of Personality and Social Psychology*, 39 (6), pp. 1 161–1 178 (1980).
- 10) Motomi Toichi, Yoko Kamio, Toshiya Murai, Ryo Kubota, Toshihiro Inakuma, and Akira Sengoku, "Changes of Cardiac Autonomic Function in Association with Psychotic Symptoms in Schizophrenia," *Seishin Igaku*, Vol. 40, No. 1, pp. 37–42, 1998.
- 11) Ikuo Kushiro, Daisuke Yamada, Koji Sawamura, Yuji Muragishi, Hiroshi Kuroyanagi, Eiichi Ono, Kenji Konomi, and Takehito Tomita, "Evaluations of road information and stiffness feeling by means of steering vibration," *Transactions of the JSME*, Vol. 84, No. 868, 2018.

- 12) Chizuru Nakagawa, "Special Issues No. 3: Measurement Technique for Ergonomics, Section 4: Measurements and Analyses of Bioelectric Phenomena and Others, (5) Measurement and Analysis of Autonomic Indices," *The Japanese Journal of Ergonomics*, Vol. 52, No. 1, pp. 6–12, 2016.
- 13) Okihiko Nakayama, Tohru Futami, Tomokazu Nakamura, and Erwin R. Boer, "Development of a Steering Entropy Method for Evaluating Driver Workload," SAE Technical Paper 1999-01-0892, 1999.



Masaki Miyake



Atsushi Kanbe



Keisuke Suzuki

Makoto Nishio

Ball Bearings with Labyrinth Seal for Transmission Applications

With the acceleration of electrification in automobiles in recent years, automobile transmissions have been a focus for technological developments aimed at extending cruising range. Besides further advancements in efficiency, there must be reductions in size and weight. Accordingly, there is a growing demand for bearings used in transmissions to have lower losses from friction, to be smaller and lighter, and to offer longer service life. Sealed clean ball bearings are a light and small solution for longer life in conventional manual and dual clutch transmissions.

These bearings use contact seals to prevent the entry of contaminants that can cause premature failure; however, the sliding contact of the seal creates unwanted losses from friction.

NSK has developed a ball bearing with a labyrinth seal for transmissions (Photo 1) that reduces losses from friction and extends service life, contributing to longer cruise ranges in electric vehicles.



Photo 1 Ball bearing with labyrinth seal for transmission applications

1. Product Features

(1) Seal specifications and torque performance

Conventional seals make contact with the inner ring, whereas the newly developed labyrinth seal is a non-contact seal with an improved seal end shape (seal lip) featuring optimized maze-like gaps between the seal and ring. This reduces friction that occurs as the seal moves, cutting bearing torque to nearly half that of conventional products (Figures 1 and 2).

(2) Effect on life

The main cause limiting the life of transmission bearings is flaking caused by contaminants caught in the bearings. The newly developed product has an optimized clearance (labyrinth structure) between the seal and inner ring to prevent the intrusion of contaminants

which can significantly reduce bearing life. Although the clearance between the seal and inner ring is less effective in preventing foreign matter intrusion compared to conventional sealed clean bearings, it provides a clear advantage over open bearings in stopping contaminants from making their way to the bearing interior, allowing for longer life (Figures 3 and 4).

2. Summary

Ball bearings with labyrinth seals for transmissions were developed to help extend the cruising range of electric vehicles. With lower bearing torque and longer life, they are expected to help achieve smaller, lighter, and more efficient automobiles.

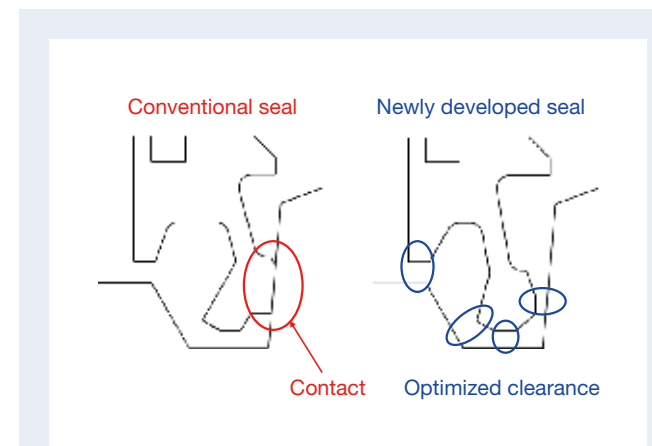


Fig. 1 Comparison of profiles for conventional seal and newly developed seal

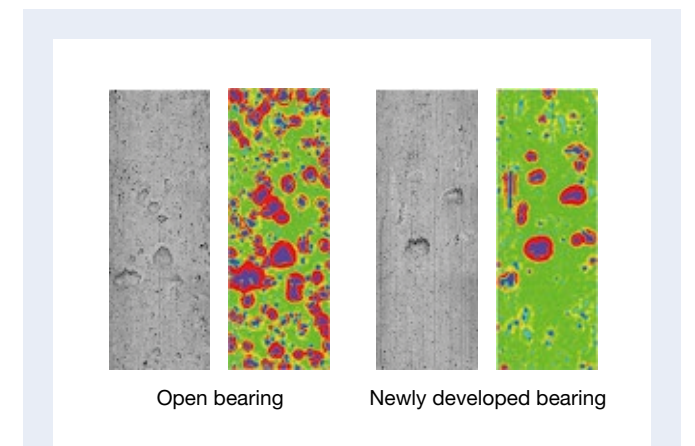


Fig. 3 Comparison of dents from contaminants for open bearing and newly developed bearing

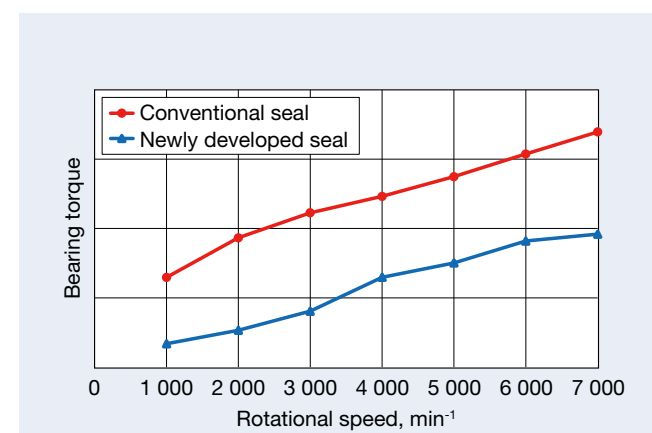


Fig. 2 Comparison of bearing torque for conventional seal and newly developed seal

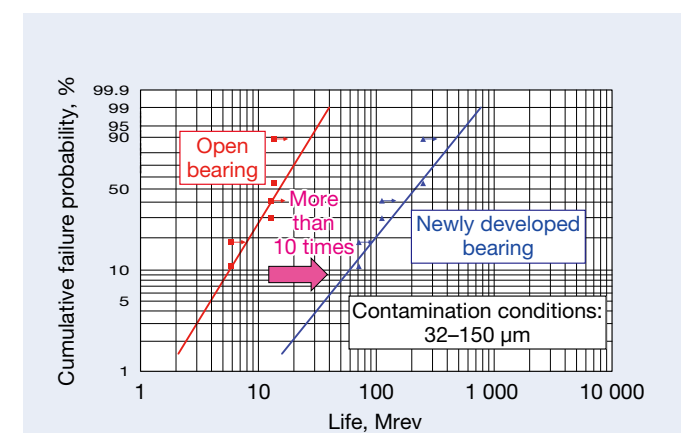


Fig. 4 Results of endurance testing for open bearing and newly developed bearing

BOC Bearings with Resistance to Wear from Creep

Demand has been growing for smaller and lighter HEV/EV motors and reduction gear units to save space and reduce vehicle weight, and as a result, housings and bearings are becoming increasingly thin. However, this thinning has led to increased occurrence of the phenomenon known as creep. Creep occurs when the housing becomes deformed during operation, creating a clearance between the housing and bearing. It can also occur when the outer ring becomes deformed, allowing it to rotate when it should stay stationary.

Creep and progressive wear on the housing in contact with the outer ring can cause increased noise and vibration, poor rotation, and functional deterioration of internal components due to wear debris. These negative effects impact automobile reliability and comfort, making responses to creep a top priority for rolling bearings.

To respond to this need, NSK has developed creep-resistant BOC bearings (Photo 1) featuring a black oxide coating (BOC) on the outer ring that enhances creep-resistance.



Photo 1 BOC bearing

1. Composition, Structure, and Specifications

BOC has been used for purposes other than creep resistance, but in BOC bearings, it is applied to the outer ring to reduce wear from creep (Photo 2).

There is no need to increase the bearing size or change the bearing peripheral structure. Assembly can be performed in the same way as standard products without coatings.

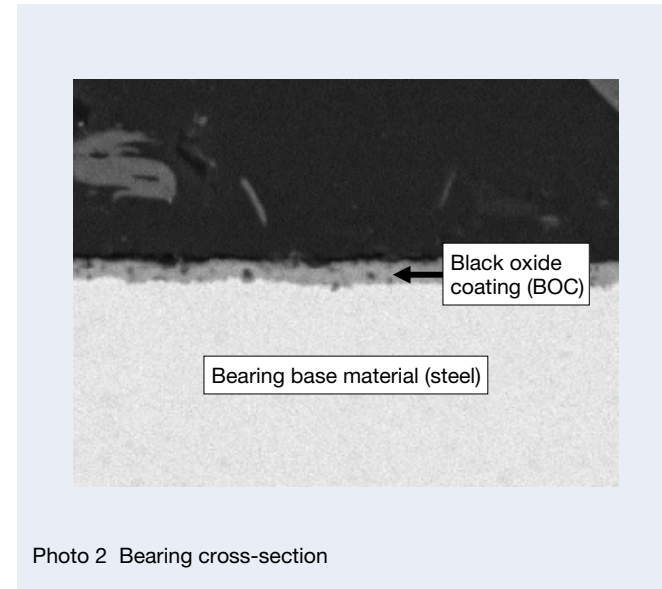


Photo 2 Bearing cross-section

2. Features

Wear from creep can be addressed in two ways: by preventing it from occurring (keeping the outer ring from rotating) or by controlling housing wear if creep occurs. Mechanically fixing the bearing to the housing with a flange, pin, or similar is a well-known way to prevent outer ring creep, but this increases costs and makes assembly more difficult. NSK has developed next-generation creep-free bearings that suppress creep under static and rotational loads. This suppression was possible by increasing the rigidity of the outer ring with a thicker wall and optimizing the characteristics of the O-ring on the outer ring's outside diameter surface.

However, dimensional limitations may prevent the application of such countermeasures, allowing creep to occur. For these cases, we developed bearings that suppress housing wear. The bearings have an outer ring outside diameter surface coated with a low-friction solid lubricant that reduces the friction coefficient between the bearing and housing.

Although BOC bearings are less effective in suppressing housing wear than solid lubrication coatings, they are characterized by low cost. A test under unidirectional load showed that housing wear in BOC bearings was 1/3 that of standard products (Figure 1).

3. Usage

Various countermeasures for creep can be applied according to the factors causing it and the surrounding environment (Figure 2).

Solid lubrication coatings have been applied when there were dimensional limitations. However, BOC bearings are

a less expensive option in environments where some wear is allowed.

BOC bearings have a significant wear suppression effect in automotive powertrains, other automotive applications, and various industrial machinery where creep wear is a problem.

4. Conclusion

BOC bearings do not require an increase in dimensions (outer ring wall thickness). Additionally, they can reduce transmission housing wear caused by creep while keeping costs low.

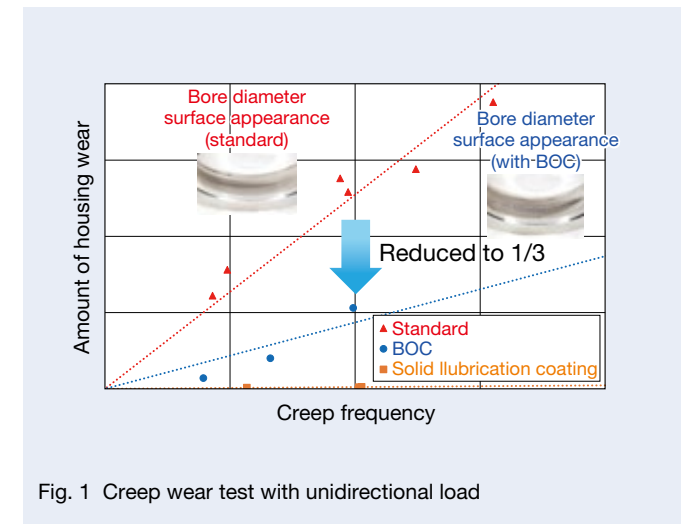


Fig. 1 Creep wear test with unidirectional load

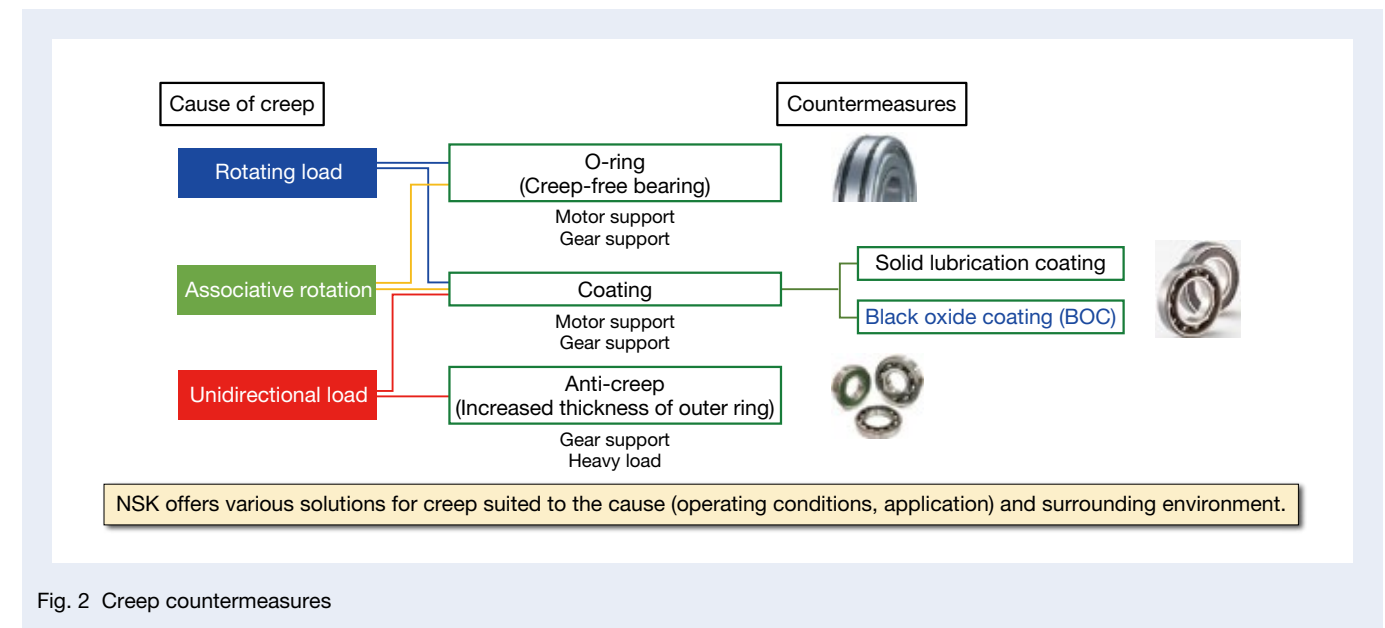


Fig. 2 Creep countermeasures

Development of Gen 4 High-Speed Ball Bearings for HEVs/EVs

To address environmental problems such as global warming, society is making stronger efforts to achieve carbon neutrality, and wider use of HEVs and EVs is expected due to their low environmental impact. Extending cruising range, however, is a critical issue affecting how widely EVs are used in the future, and drive motors for HEVs and EVs will have to be smaller and lighter.

Since torque and rotation rate determine the output of a motor, increasing the rotation rate can reduce torque and rotor size. This means that drive motors for HEVs and EVs are increasing the rotation rate. Recently, the

development of EV units with a maximum drive motor rotation rate exceeding 30 000 rpm has been reported. Ball bearings supporting the drive motor are also required for a high-speed rotation performance of 30 000 rpm or higher.

NSK has developed high-speed ball bearings with high-speed specifications of Gen 2, dmN of over 1.4 million, and Gen 3, dmN of over 1.8 million, by applying original high-speed grease, reducing the weight of the cage, and increasing the rigidity of the materials. This article introduces the Gen 4 high-speed ball bearings with dmN of 2.1 million or more, developed to cope with even higher rotation rates.



Photo 1 Gen 4 high-speed ball bearings for HEVs/EVs

1. Composition, Structure, and Specifications

The Gen 4 high-speed rotating ball bearing is made with a more rigid material than that of the Gen 3 bearing, which reduces stress on the cage and deformation during high-speed rotation while simultaneously achieving an even lighter weight and high rotational speed associated with the optimized shape.

2. Features

To confirm the high-speed rotation performance of the developed Gen 4, high-speed rotation endurance tests were conducted under a grease lubrication environment. Figure 2 shows the structure of the high-speed rotation tester. The shaft is supported by four bearings: two at each end as test bearings and two in the center as support bearings. The test conditions were as follows. The radial load was 10% of the basic dynamic load rating of the bearing. A heater adjusted the outer ring outer diameter temperature to 120°C as the test temperature. The test length was set as one hour.

Figure 3 shows the test results. As shown in Figure 3, Gen 4 achieved the target time without abnormal heat generation under dmN of 2.1 million.

3. Usage

The bearing allowed for the downsizing of the drive motor unit, contributing to better fuel and power consumption, a longer cruising range, and more comfort for EVs.

4. Conclusion

This article has introduced NSK's Gen 4 grease-lubricated high-speed rotating ball bearings for HEV and EV drive motors (achieving dmN of over 2.1 million). The use of HEVs and EVs is expected to spread rapidly as a means of helping to realize a carbon-neutral society. NSK will continue working to understand the user's operating environments and continuously develop products that satisfy the market's needs, contributing to better fuel efficiency, electric power consumption, and reliability of HEVs and EVs.

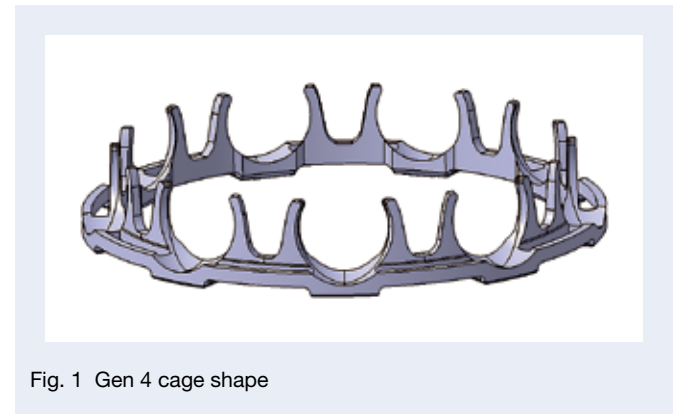


Fig. 1 Gen 4 cage shape

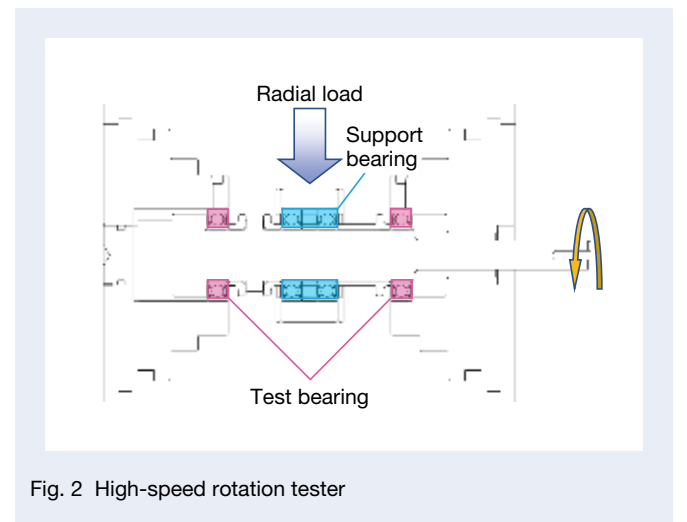


Fig. 2 High-speed rotation tester

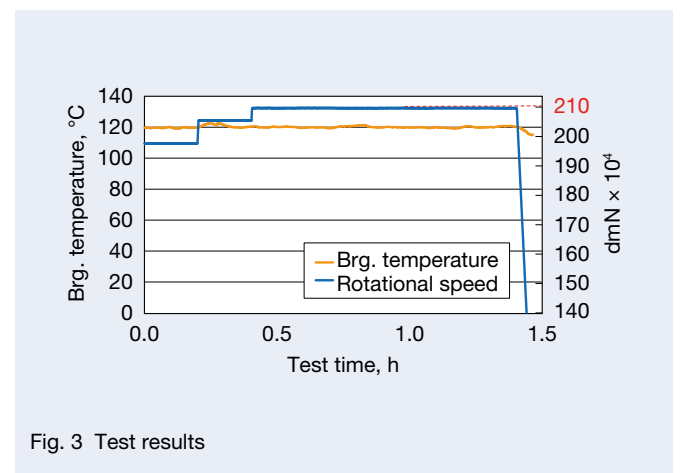


Fig. 3 Test results

Large-Size T-HUB 1 Bearings for Trucks

Introduction

Conventional wheel bearings for truck wheels are capable of supporting the vehicle's weight with a pair of single-row tapered roller bearings on the inside and outside of the truck. In recent years, there has been a demand for more efficient inspections, maintenance, and bearing replacement work, and double-row tapered hub unit bearings (large-size T-HUB 1), with integrated bearing outer rings on both sides, are increasingly being used.

When removing a general T-HUB 1 bearing from the vehicle body for maintenance, however, one of the inner rings will stick to the shaft, and this results in poor workability during replacement. It is therefore necessary to improve the workability and maintainability. Responding to these issues, NSK developed the large-size T-HUB 1 for wheels, which saves space while maintaining conventional bearing life.

1. Features

1.1 Functions of each component of the large-size T-HUB 1 for trucks

Compared to conventional tapered roller bearings, the new T-HUB 1 has a common double-row outer ring. It comprises various seals that are resistant to mud and differential oil, as well as a metal inner ring connecting ring. Figure 1 shows a schematic diagram.

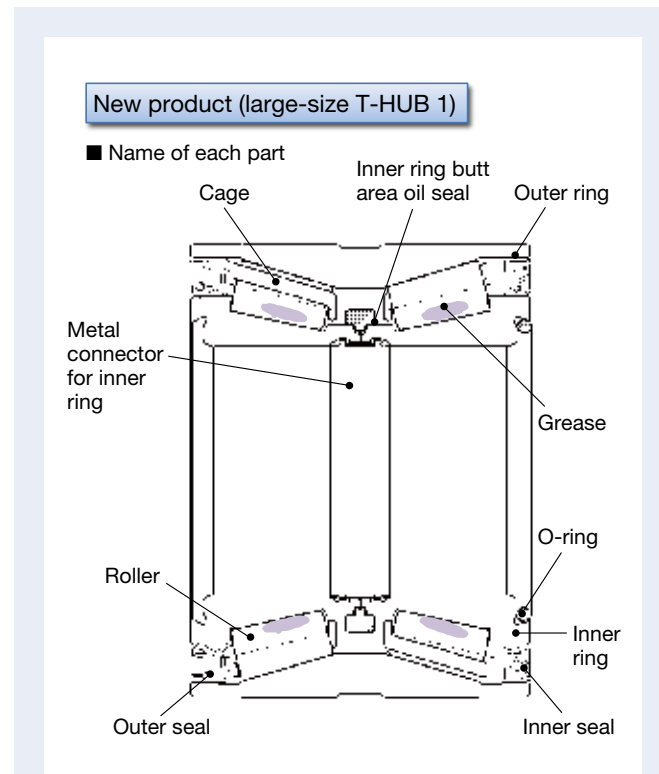


Fig. 1 Large-size T-HUB 1 bearing for trucks

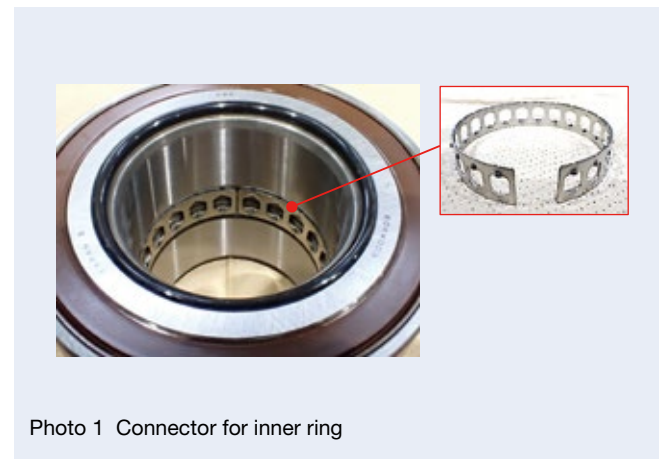


Photo 1 Connector for inner ring

The features of each component are described below.

Metal inner ring connecting ring

This connects the inner rings and makes them non-separable.

Three cases in which the inner rings must not be separated from each other are as follows.

- (1) When transferring bearings at the factory
- (2) When assembling bearings for vehicles
- (3) When disassembling bearings from the vehicle body

NSK has optimized the thickness and shape of the connecting ring to reduce weight and achieved non-separation in the above situations.

Mud-resistant seal

Truck hub unit bearings require high mud resistance performance. The new T-HUB 1 features a mud-resistant, high-integral seal with an additional garter spring. By setting a garter spring, the lip follows the spring, maintaining sealing performance even when the seal lip wears out.

Seals resistant to differential oil

This product is assumed to be used in a structure where differential oil flows from the differential gear through the drive shaft. If differential oil enters the bearing, there is concern that the properties of the internal grease will change.

- Route 1: From the bearing end face to the bearing interior (outer seal)
- Route 2: From the inner ring butt area to the inside of the bearing (oil seal in the inner ring butt area)
- Route 3: From the inner diameter of the inner ring to the brake disc (O-ring)

Cage

The cage aligns the rollers and maintains smooth rotation. The cage shape of the T-HUB 1 was optimized following strength analysis, during which turning acceleration loaded on the vehicle was considered. This optimization allows for the use of larger rollers compared to conventional single-row tapered roller bearings. Therefore, the T-HUB 1 is a space-saving bearing that maintains a life equal to or longer than that of conventional products.

Grease

In an environment where trucks are driven, the drivers use the foot brake frequently, causing heat to accumulate in the brake, which in turn results in high temperatures around the bearings. Because of this, heat-resistant grease is used to prevent oxidative deterioration and oil separation even at high temperatures.

2. Summary

Developing the large-size T-HUB 1 for trucks, NSK aimed to save space and improve reliability by utilizing its accumulated technologies and knowledge. The T-HUB 1, which European and American truck manufacturers have already been using, is now being introduced by Japanese manufacturers at an accelerated pace, and these bearings will increasingly satisfy market requirements in the future.

Next-Generation Long-Life Planetary Shafts (SHJ7)

Conventional engine-powered vehicles, as well as some EVs, which are becoming increasingly more common, have planetary gears that transmit engine or motor power to the tires.

Planetary gears must be more efficient, compact, and lightweight for better fuel efficiency (electric power consumption). The planetary gear consists of three gears (sun gear, ring gear, and pinion gear) and a planetary shaft, cage and roller, and carrier that support the pinion gear (Figure 1). Among these, the planetary shaft is fixed to the carrier as the support shaft for the pinion gear. Gear reaction forces and shaft bending subject the planetary shaft to complex and large loads, making high durability necessary. Improving the planetary shaft's durability allows for reductions of the size and weight by reducing the width of the pinion section and the number of pinions (Figure 2).

NSK offers a variety of long-life items for different types of planetary shaft. However, the most durable (SHX3)¹⁾ has a life factor of 4.5, which is excellent in terms of durability but is a factor in regard to such issues as material availability, workability, and cost. We developed the Next-Generation Long-Life Planetary Shafts (Photo 1) to resolve these issues. The product offers more optimal specifications and allows for downsizing the planetary gears and weight reduction.

1. Features

Manufacturing the new planetary shafts combines globally available materials and special induction hardening, which is advantageous in relation to durability and shaft deformation (Figure 3). The developed materials (SHJ7 materials)²⁾ are globally procurable and comply with ISO standards.



Photo 1 Next-Generation Long-Life Planetary Shafts

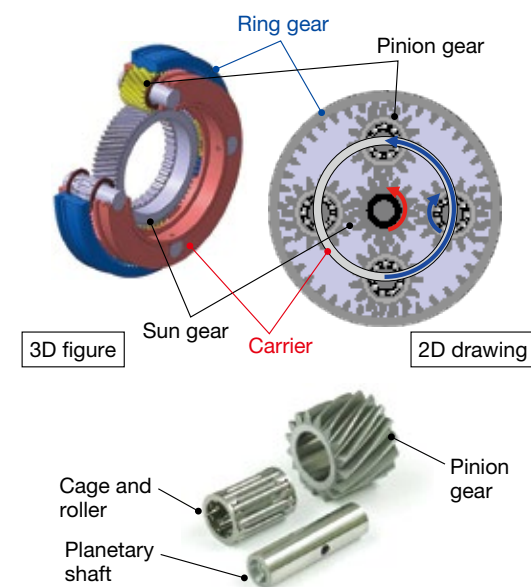


Fig. 1 Planetary gear structure

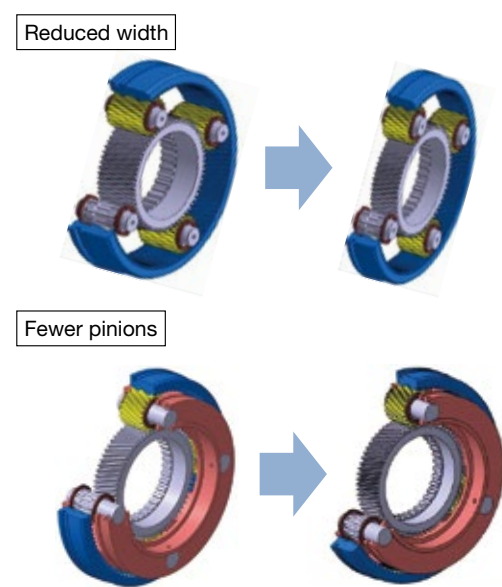


Fig. 2 Examples of smaller and lighter planetary gears

Special induction hardening is NSK's proprietary high-frequency technology used for conventional long-life products. Ensuring heat treatment quality provides a high endurance life in the load zone. Simultaneously, structural control applies to the ends and other parts of the shaft to withstand press-fit deformation, suppressing shaft deformation during use. This heat treatment enables the use of pinned and press-fastened types while improving durability.

2. Performance

Figure 4 shows the results of a planetary shaft durability test conducted on our radial testing machine using the new product. The test confirmed that the product has a longer life of three times more than that of the standard product.

Figure 5 shows the weight reduction effect of the bearing with the product. If we consider a cage and roller with a shaft diameter of 12 mm, roller diameter of 2.5 mm, and width of 20 mm, the new product, with the same bearing life as the standard product, can reduce the overall length by about 20%, and the weight by about 24%, including the shaft, cage, and roller. Reducing the shaft diameter in the radial direction is also possible, although the reduction ratio is different.

3. Applications

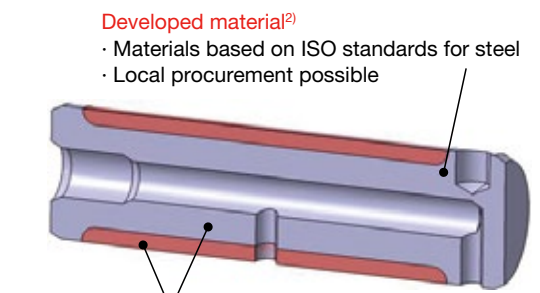
The new product applies not only to automatic transmissions, in which planetary gears have been conventionally used, but also to all-electric vehicles using planetary gears. It can also be used with various planetary gears other than those in vehicles.

4. Conclusion

We will add the Next-Generation Long-Life Planetary Shafts to our existing product lineup as a new product that combines long life with global procurability, and we will provide optimal proposals according to the particular usage environment and application of the planetary gear.

References

- 1) Kouichi Yamamoto and Hiromichi Takemura, "Development of Long-Life Planetary Shaft (SHX3 Steel) for Planetary Gears of Automotive Transmissions," *NSK Technical Journal Motion & Control*, No. 25 (2015) pp. 45–50.
- 2) "Long Life Material for Local Procurement (SHJ7)," *NSK Technical Journal Motion & Control*, No. 31 (2020) pp. 90–91.



- Developed material²⁾**
- Materials based on ISO standards for steel
 - Local procurement possible
- Special induction hardening**
- NSK's original high-frequency technology
 - High durability in areas subject to load. Structural control is applied to the edges, etc., to withstand crimping deformation while ensuring heat treatment quality.
 - Supports both the pinning type and the crimping type while improving durability life

Fig. 3 Features of the developed planetary shafts

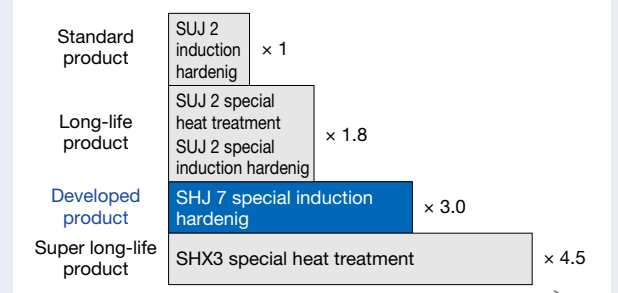


Fig. 4 Life comparison between planetary shaft models

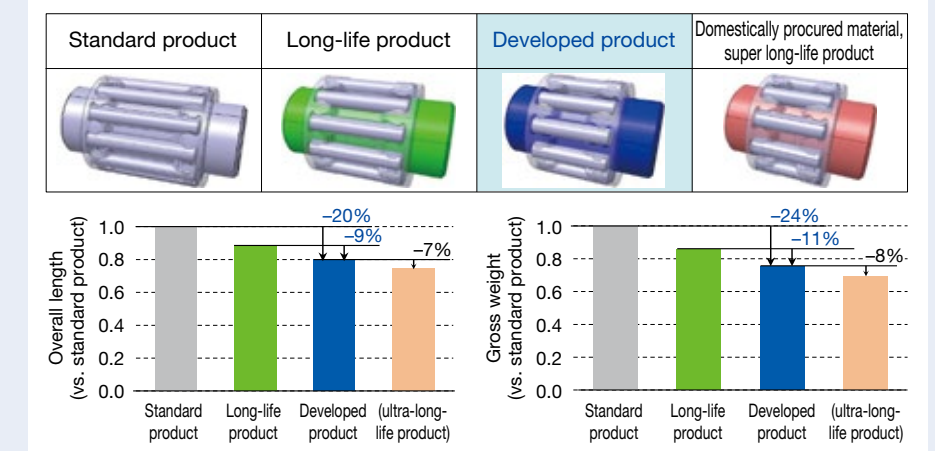


Fig. 5 Effects of downsizing the product

Drawn Cup Needle Roller Bearings with Large Diameter for Electric/Hybrid Vehicles

In recent years, electric vehicles such as EVs and HEVs are becoming increasingly common because they have less impact on the global environment in terms of reduced CO₂ emissions. Bearings used in the applications must have a broader range of sizes than those for conventional engine vehicles. NSK has developed large diameter drawn cup needle roller bearings (Photo 1) for these applications.

1. Background

Given the tight width constraints of vehicles, powertrains require an overall shorter length. The eAxle for EVs is available in 1-axis (co-axial) to 3-axis types. For example, the co-axial type arranges the motor, reduction/transmission, and differential on the same axis. Placed side by side, the overall length of the eAxle tends to increase. If the eAxle is not mountable on a vehicle, a layout has been devised to place the reduction/transmission above the differential to reduce the overall length (Figure 1).

On the other hand, many HEVs incorporate a clutch pack (module combining a motor and clutch) in the space that formerly housed the torque converter and other components. The clutch pack must therefore be less than or equal to the total length of the torque converter and other components. As shown in Figure 1, stacking several components, such as motors and clutches, in the radial direction shortens the overall length.

The above structure enlarges the diameter of some components of the powertrain and the bearings that support them. The components and bearings need to be as narrow and thin as possible to reduce the length and diameter of the eAxle and clutch packs. Considering this, keeping up with such trends is essential.

2. Composition, Structure, and Specifications

In conventional drawn cup needle roller bearings, after inserting the steel cage and roller into the heat-treated outer ring, one side edge of the outer ring is bent while being heated to form a brim. This product has a new specification: the outer ring is heat-treated after forming a brim and assembled with a single-split plastic cage and roller by shrinking in diameter (Figures 2 and 3). The features are listed here.

3. Features

3.1 Large diameter

In the conventional specifications, the brim of the heat-treated outer ring is reheated, and formed, so the outer ring dimensions are easily affected by the reheating



Photo 1 Drawn cup needle roller bearings with large diameter

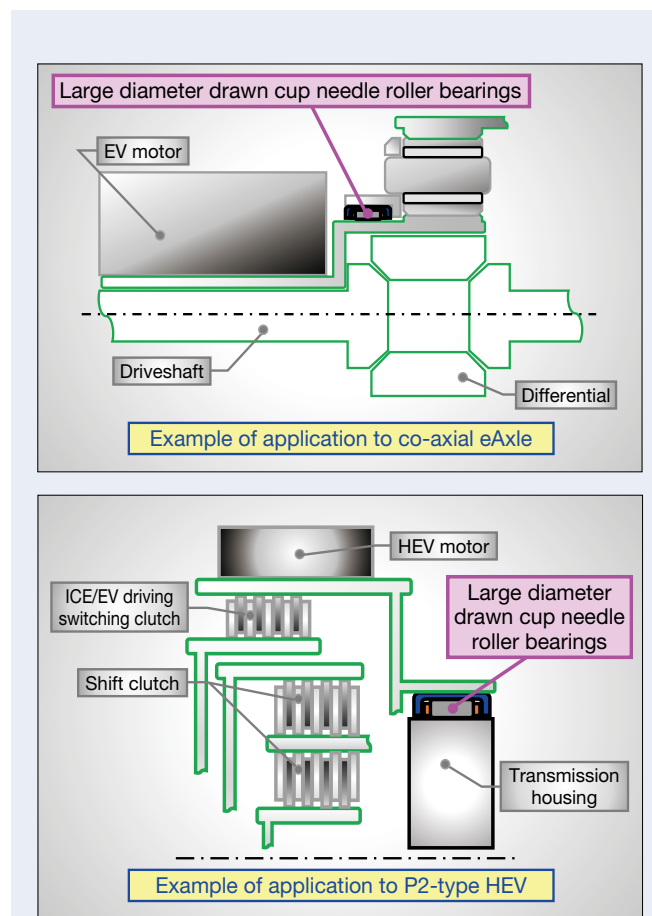


Fig. 1 Example applications in co-axial eAxle and P2 HEV

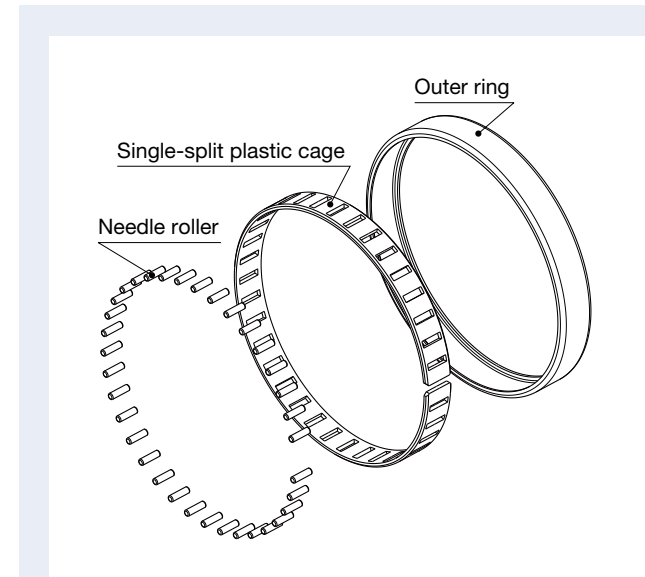


Fig. 2 Components of drawn cup needle roller bearings with large diameter

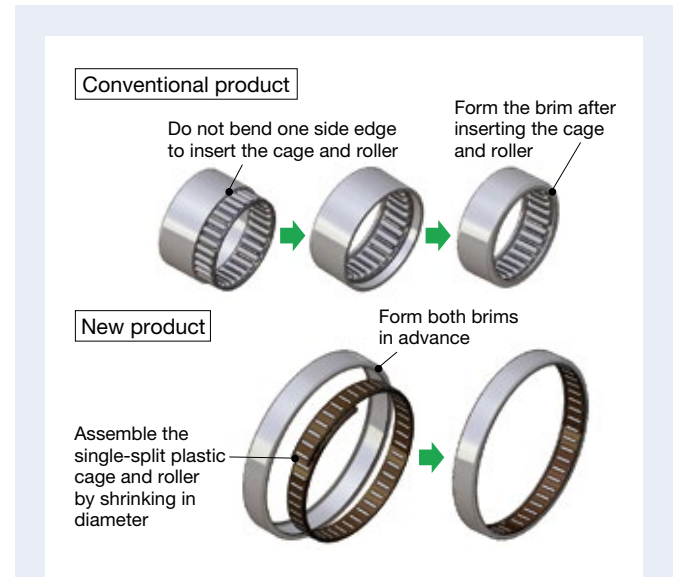


Fig. 3 Assembly of drawn cup needle roller bearings with large diameter

process. For the new product, forming the brim before heat treatment stabilized the outer ring dimensions, achieving a larger diameter. It can accommodate up to approximately $\phi 120$ mm in outer diameter, and further expansion development will be pursued (Figure 4).

3.2 Narrow width

One issue with the conventional specifications is that designing the roller length to be close to the outer ring width for narrow products reduces the hardness of the raceway surface near the heated outer ring brim, shortening the product life. To avoid this, forming the brims before heat treatment solved the problem of reduction in raceway surface hardness and the resulting reduction in life. The roller length is thereby not reduced, and the bearing life is ensured even with a narrow outer ring. Currently, the width can be as narrow as 10 mm, and even narrower specifications will be developed in the future (Figure 4).

3.3 Thin wall

Large diameter, thin-wall products were difficult to manufacture because the dimensions were unstable due to the reduced rigidity of the steel cage and increased heat treatment deformation. The new plastic cage solves this problem and allows for a thin wall. Currently, the cross-sectional thickness can be up to about 2.5 mm, and further thinning is planned (Figure 4).

4. Performance

The bearing life test assumed the EV and HEV operating environment confirmed the equal to or exceeding the rated fatigue life. A high-speed rotation test confirmed

that the product did not break even at 3.5 times the allowable rotation speed.

5. Summary

The larger diameter, narrower width, and thinner wall of the drawn cup needle roller bearing will contribute to electrification. NSK will continue to develop the technology in preparation for further changes related to bearing size requirements.

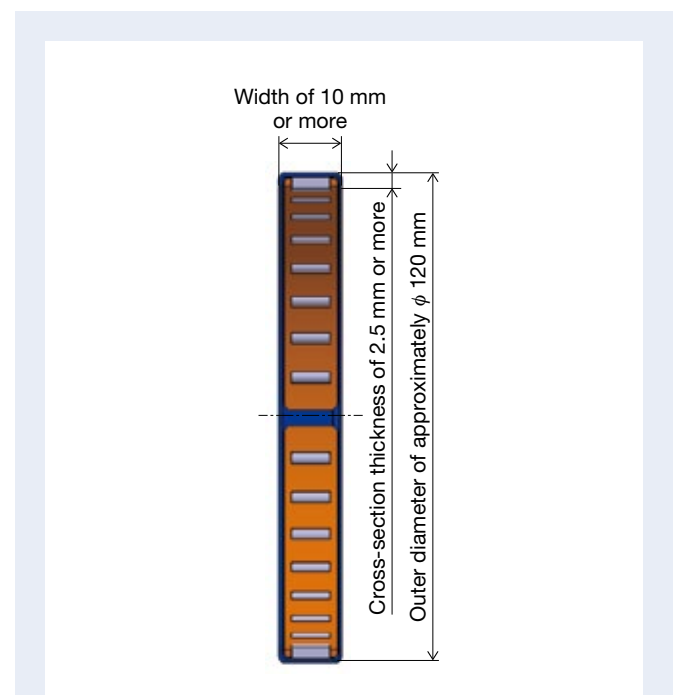


Fig. 4 Size of drawn cup needle roller bearings with large diameter

Column EPS with Steering Wheel Angle Detection

The recent expansion of vehicle advanced driver-assistance systems (ADAS) has increased the importance of steering wheel angle (steering angle) information in vehicles. Conventional systems with a dedicated steering angle sensor inside the steering wheel or in the electric power steering (EPS) (Figure 1) installed to sense the steering angle has led to such related issues as increasing the size, parts, and cost. We have developed and commercialized a unique function that calculates steering angle information essential for the spread of ADAS, utilized in OEM vehicle control and EPS (Figure 2). This function uses information from the motor angle sensor and steering torque sensor in the EPS system without having to install a steering angle sensor.

1. Composition, Structure, and Specifications

The steering angle is the absolute angle within approximately three revolutions between the right and left turn ends (lock to lock). The angle has a basis on the steering wheel's neutral angle when the vehicle is moving straight ahead. This detection is necessary for functional development. Conventional steering angle sensors have a built-in reduction gear or vernier mechanism to detect this multi-turn absolute angle. In this configuration, the sensors detect the steering angle even with the ignition turned on.

The EPS is equipped with a motor angle sensor to control the motor for assistance. The steering angle calculation function requires the following.

- Calculating the absolute steering angle
- Setting and storing the steering neutral angle
- Ensuring detection accuracy (resolution, precision, responsiveness, etc.)
- Securing and diagnosing signal reliability

Figure 3 shows the functional block of the new system. The steering angle is calculated by converting the angle information from the motor angle sensor to the steering shaft angle via the reduction gear. The neutral angle's initial position is calibrated when the vehicle is shipped. The angle is calculated as above during ignition. Utilizing the power supply, sensor, and angle counter for one of the two motor angle sensors maintains the angle detection function when ignition is off (dashed line in Figure 3). Diagnostics using two systems of angle information ensure the reliability of the steering angle information. The

calculated steering angle is used for control within the EPS. It is also transmitted to the vehicle in real time via communication for vehicle body control, such as ADAS.

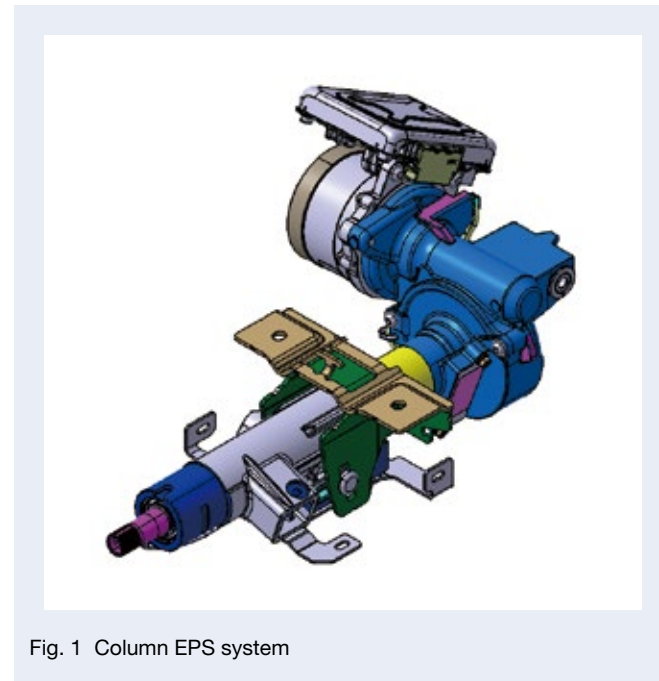


Fig. 1 Column EPS system

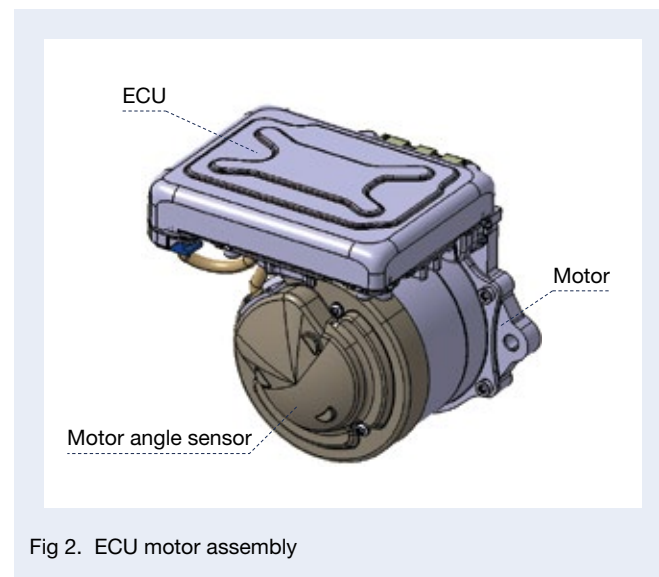


Fig. 2 ECU motor assembly

2. Features

The steering angle detection system has the following features.

- **Sensor saving:**
The EPS configuration enables multi-turn steering angle detection. It eliminates the need for a steering angle sensor, making it compact and low-cost.
- **High precision:**
Utilizes high-precision motor angle sensor signals to control the assist motor, ensuring sufficient accuracy, resolution, and responsiveness to control the ADAS functions.
- **High reliability:**
Sensor reduction reduces the risk of failure (reduced failure rate), and a mutual diagnosis of the sensors ensures functional reliability.
- **Continuous function of steering angle detection and low current consumption:**
Optimizing angle detection sampling operation when the ignition is off enables ultra-low battery current consumption.

- Calibration function for the steering angle neutral point:
A neutral point calibration function is associated with battery replacement.

3. Usage

EPS with a steering angle sensorless detection function:

- Increased demand for steering angle detection functionality is achieved without the need for a dedicated steering angle sensor
- Compact, low-cost configuration

4. Conclusion

With ADAS-equipped vehicles becoming mainstream and cost competition intensifying, NSK will make the steering wheel angle detection function a standard feature of NSK's EPS system, with plans to develop the series.

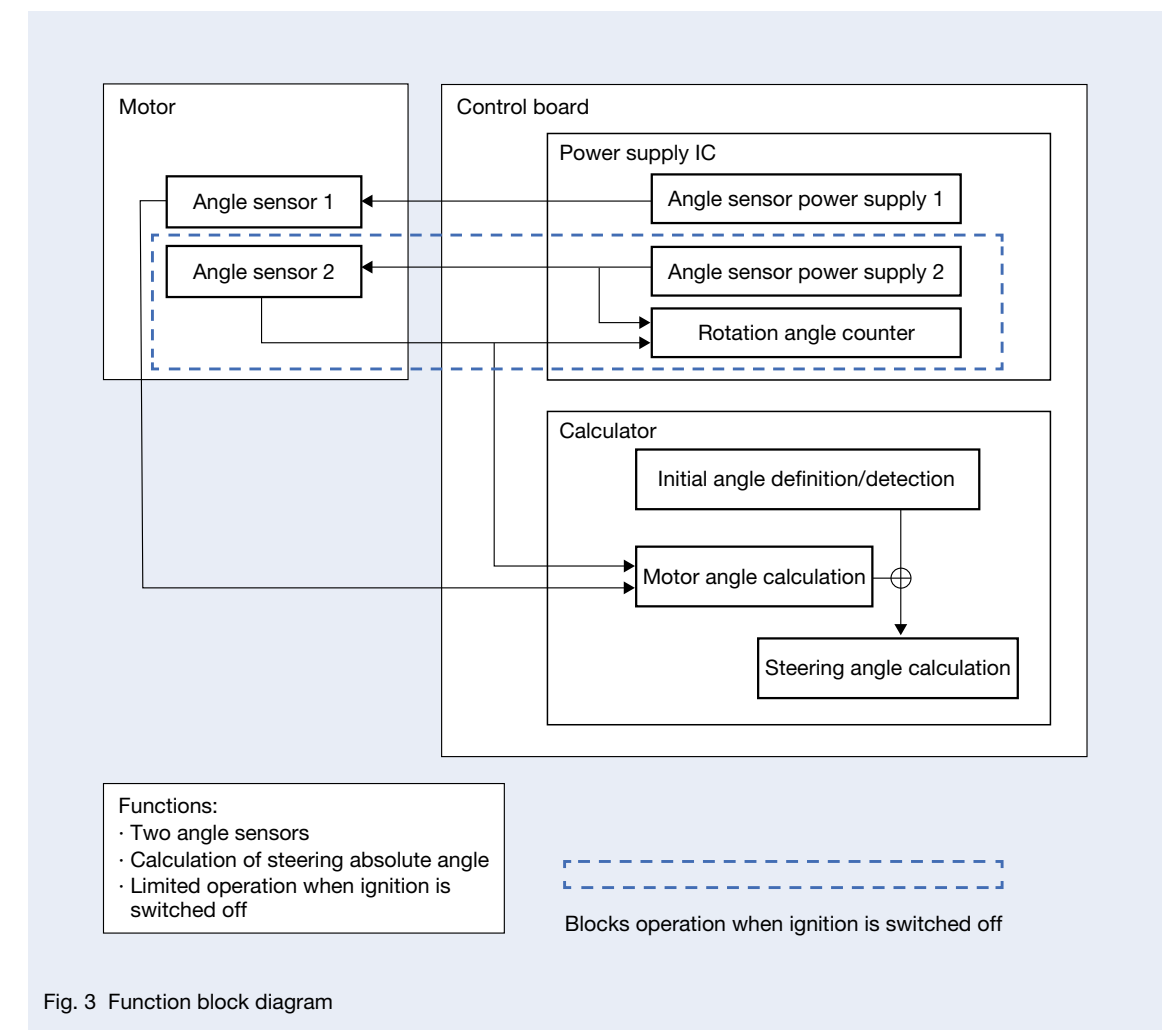


Fig. 3 Function block diagram

Trends in Bearings for Steelmaking Equipment

Tsuyoshi Nomura
 Industrial Machinery Bearing Technology Center,
 Industrial Machinery and Global Aftermarket Technology Department Steel Group

Abstract

Steel products are indispensable as basic materials that support economic activities and social life. Demand for steel is expected to continue to increase steadily due to economic growth and population growth in emerging countries. Due to growing environmental awareness in recent years, steelmakers are developing production methods and productivity improvements to lessen environmental impacts while offering high-value-added products aimed at carbon neutrality. Bearings for steelmaking equipment must improve production while offering long life and high reliability to reduce CO₂ emissions. Here, we summarize the problems facing bearings used in major steel production equipment and report on the latest technological trends.

1. Preface

Steel products are indispensable as basic materials that support economic activities and social life. For example, bridges and buildings form the foundation of infrastructure. Automobiles, vehicles, and ships are used for transport and transportation. Food containers such as beverage and food cans are also made of steel. World crude steel production reached 1.86 billion tons in 2020. High demand for steel products will continue due to economic growth and population increases in emerging economies. On the other hand, there is a strong demand for products with consideration for changes in social structure, especially in regard to the environment. Steelmakers are therefore working to reduce their environmental impact by reducing carbon dioxide emissions and saving energy, developing high-value-added products (such as high-tensile steel for automobiles¹⁾ and electromagnetic steel sheets²⁾). In addition, NSK is working to improve productivity through the stable operation of equipment and by reducing maintenance costs with advanced predictive maintenance, as well as by expanding and widening equipment to increase throughput and speed of operation.

The ironmaking process can be broadly divided into the pig ironmaking process (equipment that melts raw materials to produce molten steel), the steelmaking process (equipment that adjusts the composition of molten steel and hardens it), and the rolling process (equipment that rolls the hardened material into plates and bars) (Figure 1). The equipment uses various bearing types and sizes in each process, from standard and standardized by ISO to specialized bearings for specific applications. In addition, each process requires a different lubrication system and operating environment, and the functions required of the bearings also differ.

Table 1 summarizes these by process.

This article introduces the latest technological trends in bearings used in major equipment in the steelmaking process.

1: High tensile strength steel

Weight can be reduced while maintaining strength and workability.

2: Electromagnetic steel sheet used in iron cores for motors, generators, transformers, etc. Controlling the orientation of the crystal structure and other factors affect the efficiency of those devices.

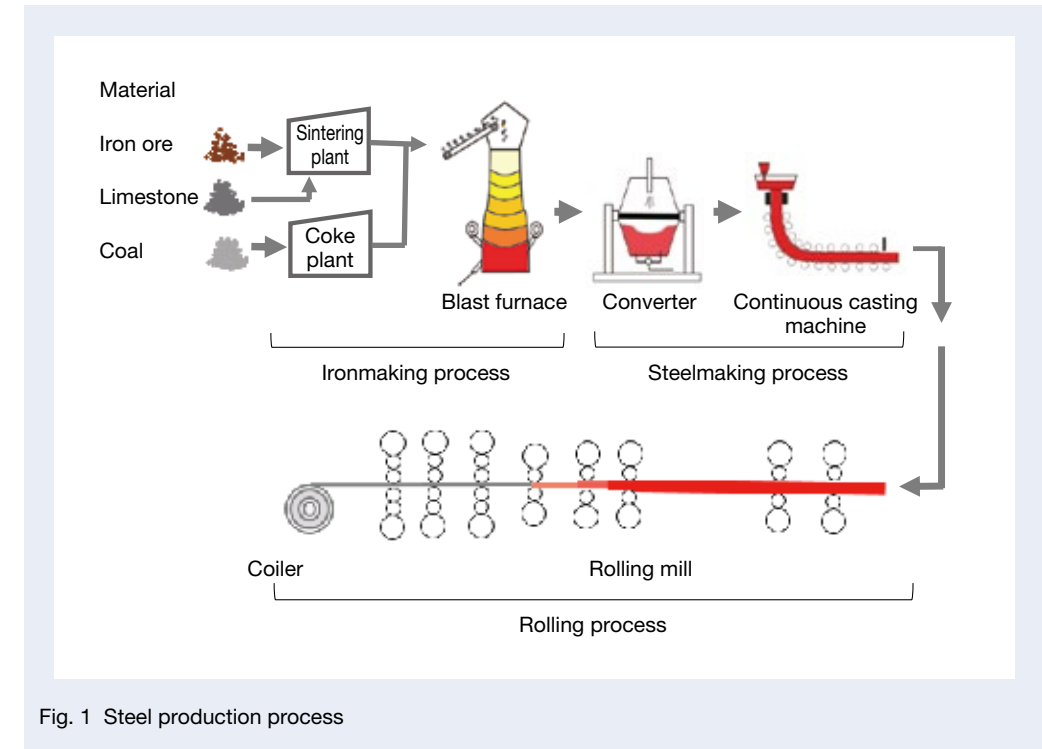


Fig. 1 Steel production process

Table 1 Bearing operating environments and needs by type of steelmaking equipment

Steelmaking process	Main equipment	Usage environment	Bearing needs
Ironmaking	Sintering	High temperature Low speed Shock load, unbalanced load Dust	Sealability Outer ring strength Load capacity (heavy load-resistant capacity)
Steelmaking	Converter	Handling the bearing is difficult due to the large size of the bearing and peripheral parts	Handling ability
	Continuous casting machine	High temperature (roll elongation) Very low speed Heavy load (roll deflection) Water (steam) Oxide scale	Eliminate roll elongation smoothly Wear resistance Alignment
Rolling	Rolling mill (4-high, 6-high, etc.)	Cycle operation (high speed ↔ low speed) Heavy load Cooling water (rolling water) Oxide scale Super fast	Sealability Foreign matter resistance (iron powder, water) High speed
	Cluster type rolling mill	High speed Heavy load Cooling water (rolling water)	Sealability Ease of seal installation/removal
	Special rolling mill	Low speed Eccentric load (heavy load)	Load capacity (heavy load-resistant capacity)

2. Pig Ironmaking Process

2.1 Sintering equipment

This equipment sinters powdered iron ore to an appropriate size in advance to produce pig iron from iron ore in a blast furnace (Figure 2). With blast furnaces becoming larger in recent years, efforts have increased sintering capacity by widening pallet trucks and extending machine lengths.

The bearings are used in the wheel section (where the pallet cart runs on rails) and in the middle roller section (where the sprockets mesh with the bearing outer ring outer diameter surface to drive the pallet cart) (Figure 3).

Among them, sliding bearings have been conventionally used for bearings for medium rollers. They used to suffer from early damage due to foreign matter (sintered dust) entering the bearing, frequent grease replenishment, contamination around the equipment due to grease leakage to the surroundings, and increased maintenance costs due to grease disposal costs. As a countermeasure, replacing sealed bearings with full roller-type cylindrical roller bearings led to improved equipment reliability, a better on-site environment, and reduced maintenance costs.

However, the larger sintering capacity described above has increased the loading capacity of pallet trucks, requiring a greater driving force for the sprockets. The impact load and unbalanced load have caused such problems as uneven wear on the outer ring outer diameter meshing surface of the sprocket and middle roller, outer ring cracks, and Brunel indentations on the raceway surface.

A review of the bearing design specifications addressed this problem. Increasing the outer ring wall thickness suppressed the cracking. Arranging many needle rollers significantly improved the static load capacity and reduced the risk of sudden failure (Figure 4). Stable operation of the bearings after the countermeasure has been confirmed in the actual equipment.

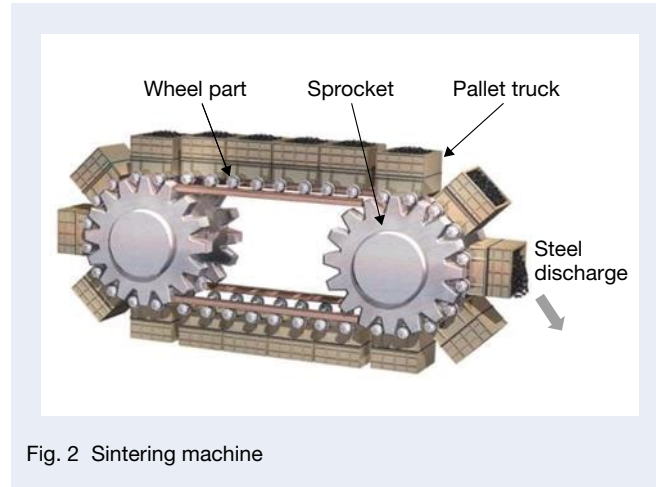


Fig. 2 Sintering machine

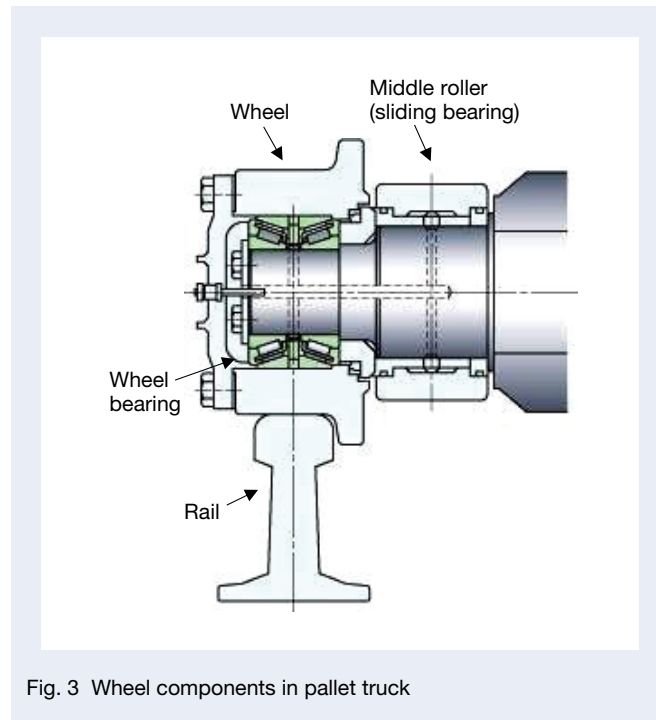


Fig. 3 Wheel components in pallet truck

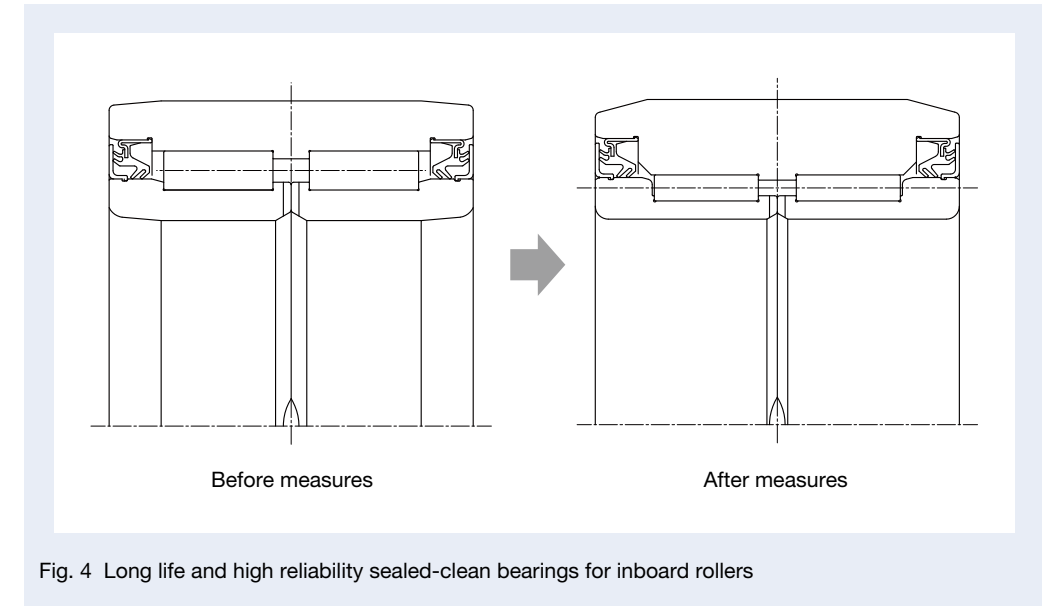


Fig. 4 Long life and high reliability sealed-clean bearings for inboard rollers

3. Steelmaking Process

3.1 Converter equipment

With this equipment, high-purity molten steel is produced by blowing oxygen onto pig iron to remove carbon from the molten pig iron, adjusting the composition, and floating impurities.

Figure 5 shows the structure of the converter. Large self-aligning roller bearings (integral bearings) with an outside diameter of approximately 1.5–2 m are installed in the trunnion on both sides of the converter.

Large bearings are difficult to handle due to their large mass. Maintenance, especially for the fixed side bearings, must remove the complete drive unit, including the vast bull gear (a large gear with a diameter of approximately 10 m), requiring considerable time and cost. In addition, there was a significant risk of production stoppage in the lower processes if a sudden accident necessitated the prompt replacement of a bearing.

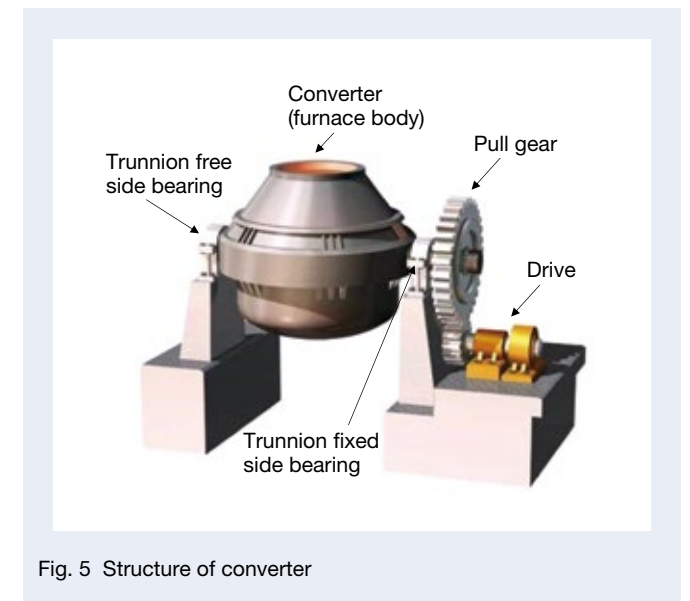


Fig. 5 Structure of converter

To solve this problem, a split self-aligning roller bearing (Figure 6: split bearing) was developed to replace the bearing without dismounting the bull gear.

This new bearing had to be interchangeable with the conventional integral-type bearing to enable replacement. All parts were divided into two parts in an annular shape. A pin-type cage was used to compensate for the reduced load rating within the restricted dimensions. The development of this split bearing eliminated the need to detach the bull gear and enabled replacement of the bearing.

On the other hand, assembling large, split parts with high precision requires expertise, and support from the bearing manufacturer is essential. NSK has been expanding its introduction of these systems in Japan. In recent years, it has expanded their use in China and other emerging economies while establishing on-site support systems. The replacement work with a conventional integral bearing required about two weeks. However, it has been confirmed that the work period is reduced by half with a split bearing.

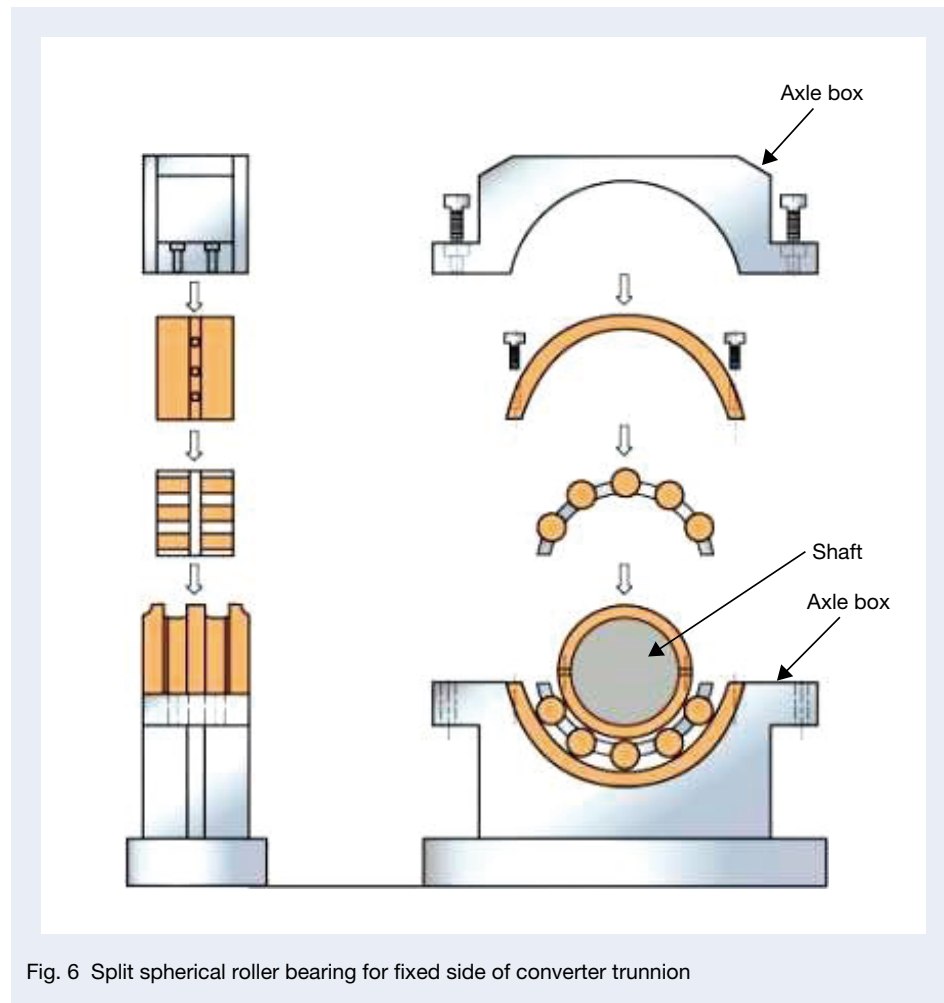


Fig. 6 Split spherical roller bearing for fixed side of converter trunnion

3.2 Continuous casting equipment (continuous casting machine)

This equipment continuously produces steel billets (slabs, blooms, and billets) by passing molten steel between guide rolls above the continuous casting machine and allowing the surface to solidify with cooling water. As a representative example, the structure of a slab continuous casting machine that produces wide billets is shown in Figure 7.

Guide rolls (Figure 8) must be capable of carrying heavy loads while allowing for deflection, so bearings with alignment properties are used in the inner ring rotation. Bearings are arranged on the fixed and free sides. In Japan, a self-aligning roller bearing capable of carrying radial and axial loads (Figure 9) is generally used on the fixed side. A cylindrical roller bearing with a separating-type aligning ring (Figure 9) is used on the free side. Outside of Japan, non-separating-type toroidal roller bearings (Figure 9) are often used on the free side due to differences in the structure of continuous casting machines.

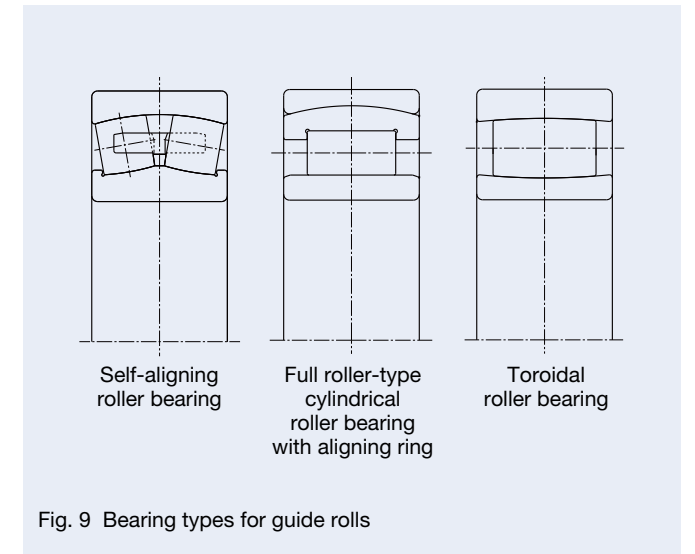


Fig. 9 Bearing types for guide rolls

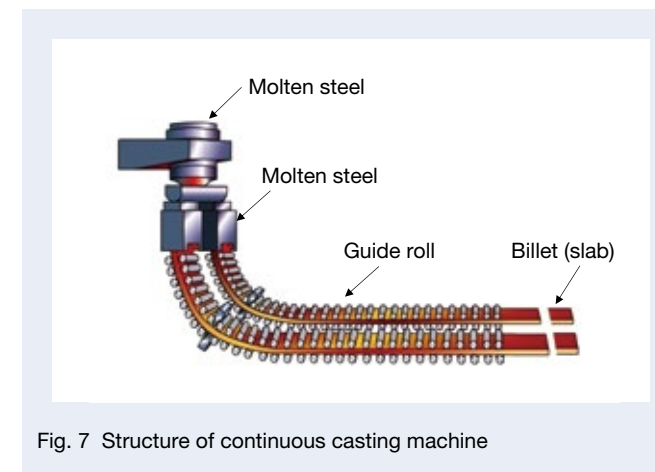


Fig. 7 Structure of continuous casting machine

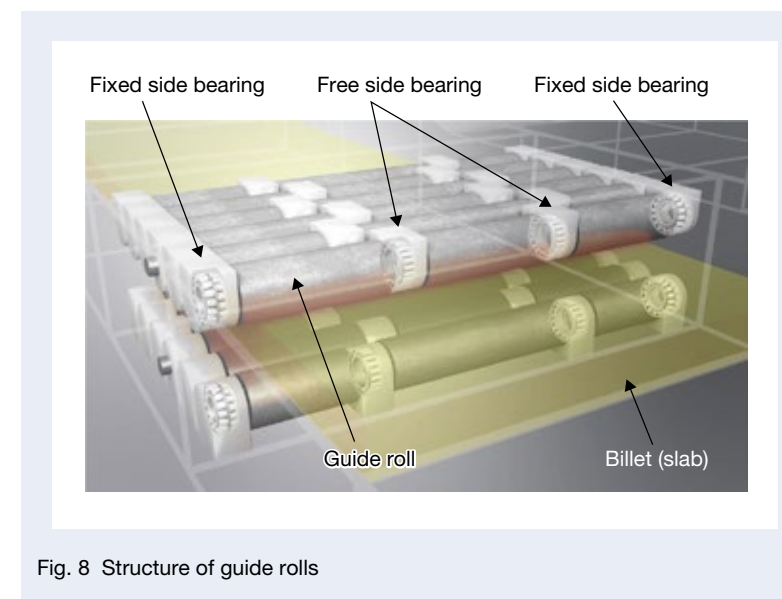


Fig. 8 Structure of guide rolls

Bearings for continuous casting machines are subjected to heavy loads of 30% or more of the basic dynamic load rating at extremely low speeds of several revolutions per minute, so it is difficult for a film of lubricant to form between the raceway rings and rollers. In addition, the area around the rolls is a harsh environment where the rolls are exposed to large amounts of cooling water, steam, and oxide scale (iron oxide powder peeled off from the surface of the steel billet), which can easily penetrate the bearing interior and cause lubrication failures. In addition, since spherical rollers are used in self-aligning roller bearings and toroidal roller bearings, the unique sliding wear between the raceways is accelerated due to the shape of the rollers, resulting in premature flaking and cracking that can cause sudden production stoppages and affect product quality, calling for improvements in the reliability of equipment by overcoming certain bearing challenges.

On the other hand, steelmakers are working to extend the service life of rolls and bearings to improve productivity and reduce maintenance costs by extending the equipment maintenance cycle.

As countermeasures for equipment, improving housing sealing performance and lubrication by changing the lubrication method from grease to oil-air have been promoted, and their effects have been confirmed.

As for bearing countermeasures, we have developed the following bearings to address the problems related to sliding wear inherent in bearings with the spherical rollers described above, and we are increasingly introducing them into the market.

The features of the developed bearings are described on the following pages.

3.2.1 Wear-resistant self-aligning roller bearings (SWR bearings)

SWR bearings are made by precipitating a large amount of fine, hard carbonitride of tens of nanometers in size (Figure 10), using NSK's proprietary vanadium-doped steel and state-of-the-art carburizing and nitriding technology to significantly improve wear resistance and flaking life characteristics. The surface hardening type also dramatically improves the toughness of the core compared to conventional steel (SUJ), which is a fully hardened type, thereby significantly reducing the risk of cracking. Compared with self-aligning roller bearings using SUJ in actual slab continuous casting machines, SWR bearings have been confirmed to extend maintenance cycles due to the life extension effect, reducing the number of scrapped bearings in maintenance and improving the reuse rate.

3.2.2 High-performance cylindrical roller bearings (NUB bearings)

NUB bearings are a new type of full roller-type cylindrical roller bearing consisting of four parts: an outer ring, inner ring, rollers, and retaining ring (Figure 11). The features of the bearings are as follows.

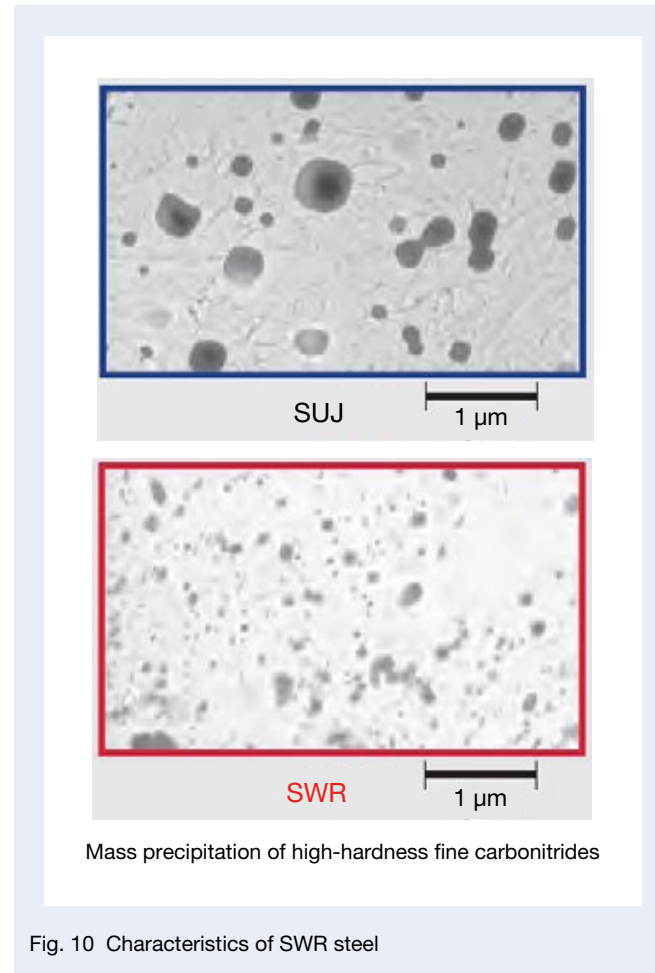


Fig. 10 Characteristics of SWR steel

1) Long life span

The full roller-type cylindrical roller bearing maximizes the load capacity and optimizes the internal design to suppress sliding contact on the raceway surface, which causes sliding wear. In-house endurance tests confirmed a longer service life of more than three times that of conventional bearings with spherical rollers (Figure 12).

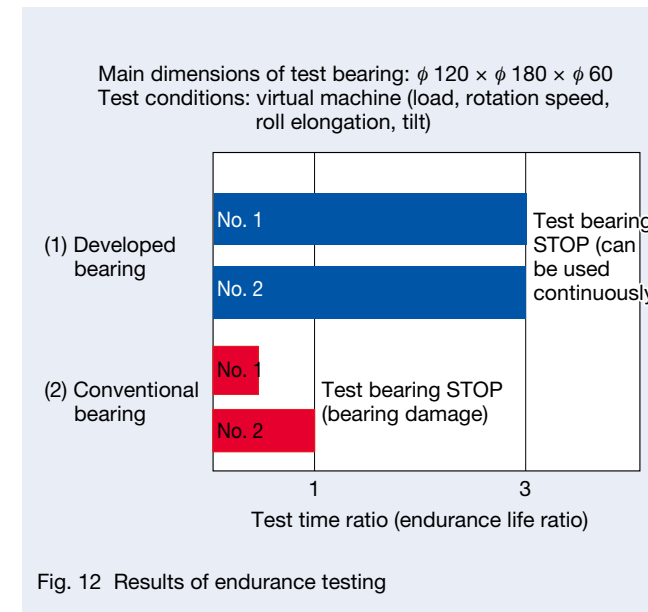


Fig. 12 Results of endurance testing

2) Alignment and roll elongation absorption

Optimum crowning geometry is applied between the roller and raceway rings to equalize the surface pressure distribution inside the bearing against the action of tilting (deflection) (Figure 13). Furthermore, the relative movement of the inner and outer rings smoothly releases roll elongation.

3) Improved handling

The non-separating structure eliminates the need for dedicated tools and significantly improves assembly workability (Figure 14).

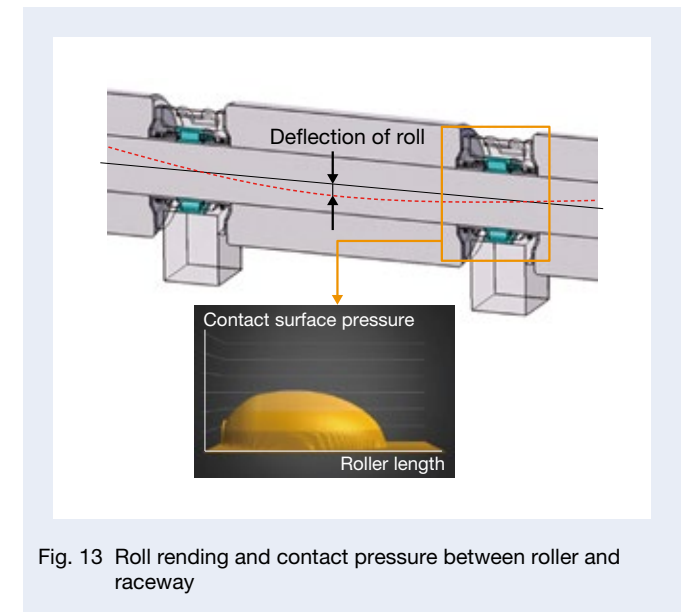


Fig. 13 Roll bending and contact pressure between roller and raceway

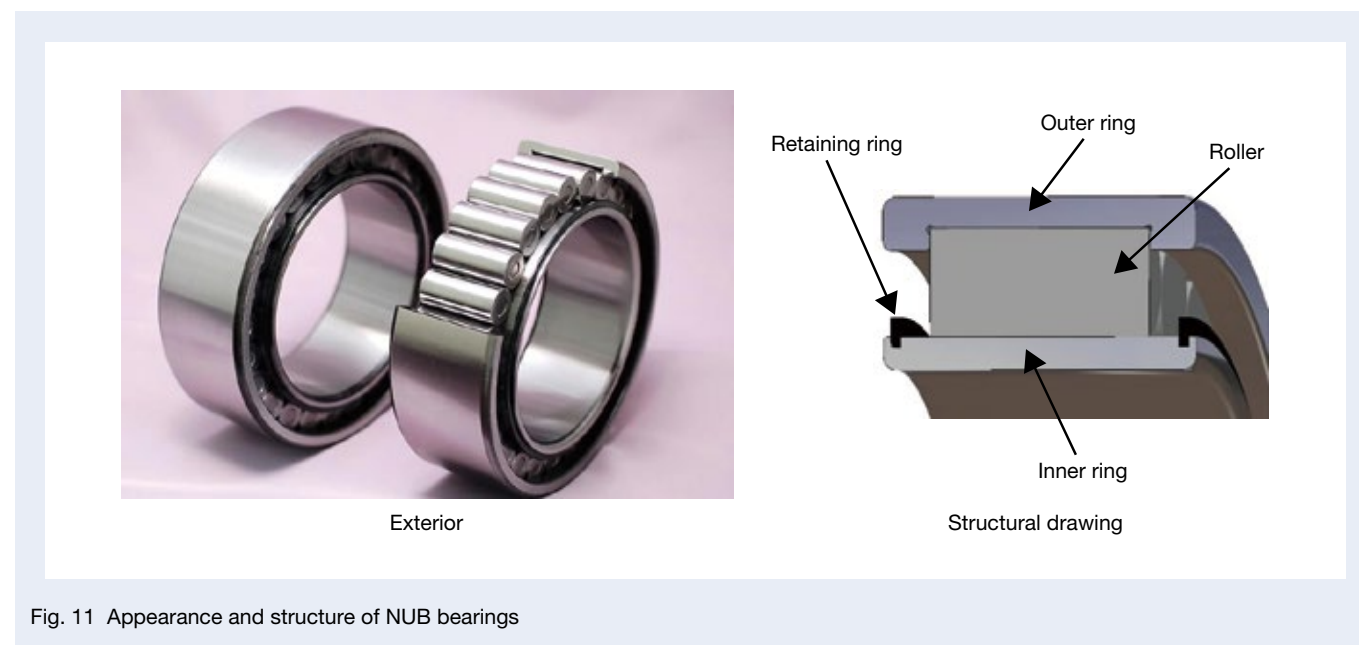


Fig. 11 Appearance and structure of NUB bearings

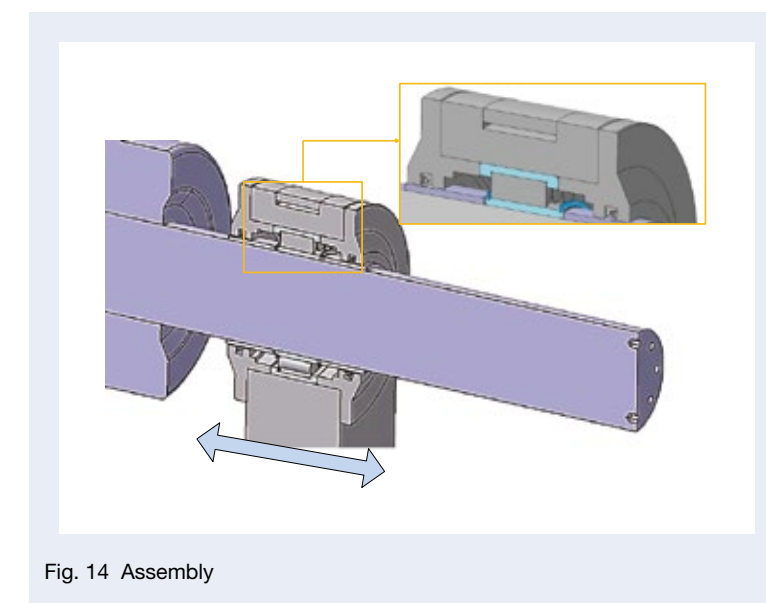


Fig. 14 Assembly

4. Rolling Process

4.1 Rolling mill

A rolling mill applies force to extend hot or room-temperature metal between two rotating rolls to finish it to a specified shape and accuracy. There are rolling mills for plate steel, bar steel, shaped steel, and wire rods. An example of a typical rolling mill structure for plate steel rolling is shown in Figure 15. The rolling mill consists of a work roll (WR) and the backup roll (BUR) that supports it. The bearings at both ends of each roll (journal section) are called roll neck bearings. Four-row tapered roller bearings are mainly used with grease lubrication for WR roller neck bearings (WR bearings). BUR roll neck bearings (BUR bearings) use four-row cylindrical roller bearings for radial loads and double-row tapered roller bearings for axial loads, with forced circulating lubrication, oil mist, or oil-air lubrication. The bearings are used under various conditions, from low to high rotational speeds, and are operated under heavy loads. The environment around the bearings is extremely harsh because of the large amount of cooling water (or rolling water) and foreign matter (oxide scale, etc.) scattered around the bearings.

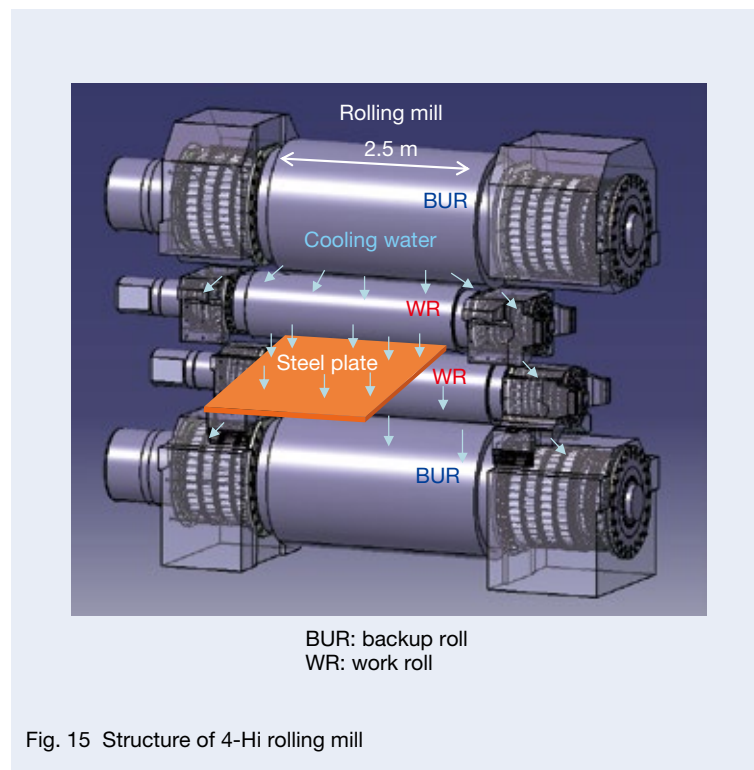


Fig. 15 Structure of 4-Hi rolling mill

Among them, WR bearings are particularly close to the rolling mill material. They are easily affected by cooling water and foreign matter, and premature bearing damage due to lubrication failure is common. We have determined that foreign material contamination is a factor in premature flaking. As a countermeasure, we have developed and expanded the market introduction of sealed WR bearings and long-life materials (Super TF)³⁾.

In recent years, there has been a strong demand for extended maintenance cycles by extending the WR bearings' service life and meeting the challenges of high-speed production.

3: Super TF is a long-life material in which the surface hardness is increased by dispersing a large amount of high-hardness fine carbides and nitrides through a special material heat treatment and optimizing the amount of residual austenite to alleviate stress concentration at the edge of indentations generated under foreign matter contamination.

4.1.1 Maximizing the design load capacity of sealed WR bearings

WR bearings are subjected to 30% or more loads of the basic dynamic load rating. They must be designed for a high load capacity in the sealed form to prevent premature damage due to lubrication failure factors caused by foreign matter or water intrusion into the bearing interior. The problem, however, was that the load capacity was much lower than that of an open-type bearing of the same dimensions to provide space for an oil seal. As a countermeasure, a high load capacity sealed four-row tapered roller bearing (Figure 16) was developed. Making the oil seal more compact and optimizing the internal design of the bearing extended the length of the rollers, allowing more rollers to be placed and achieving the same level of basic load rating as that of the open type.

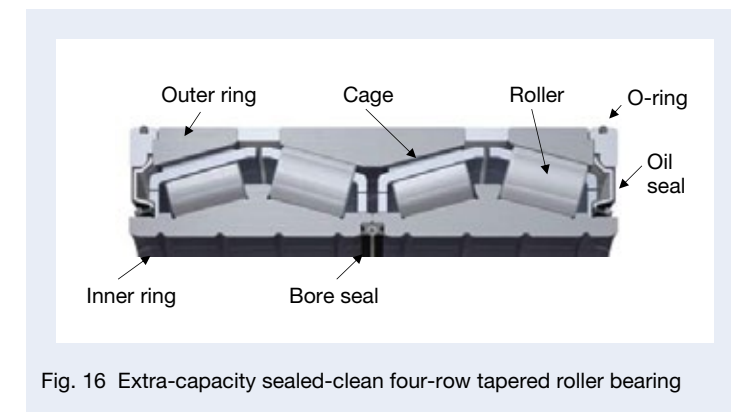


Fig. 16 Extra-capacity sealed-clean four-row tapered roller bearing

4.1.2 Development of water-resistant grease for sealing WR

As mentioned above, the factors that cause premature damage to WR bearings include the effects of lubrication failure due to the intrusion of foreign matter and water intrusion.

It has been confirmed that when water intrudes into the bearing, the oil film between the raceways and roller tends to wear out, causing metal contact, premature flaking, and rusting. As a countermeasure, we have developed a grease (Figure 17) that prevents premature flaking and rusting even when water penetrates the bearing. This grease has an optimized composition and special additives to produce a thick oil film and protective film on the raceway surface (Figure 18), preventing flaking and rusting due to lubrication failure, even when water gets into the grease. In-house underwater immersion tests using tapered roller bearings confirmed a significant life extension and high anti-rust effect. In addition, the grease-filled sealed WR bearings, developed for the actual machine tests, suppressed premature damage and extended the maintenance period.



Fig. 17 Grease to prevent premature damage from water entry

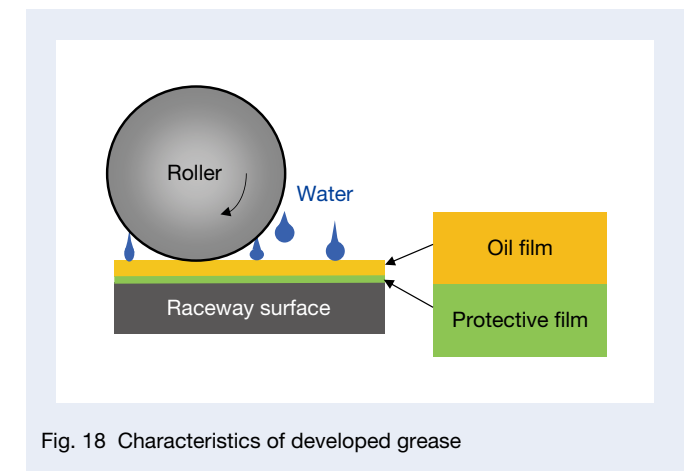


Fig. 18 Characteristics of developed grease

4.1.3 Development of WR bearings for high speeds

In recent years, companies have been working to increase the speed of rolling mills to improve productivity further. In particular, there is a need for ultra-high-speed rolling (2 200 m/min or higher) in rolling mills for thin plate products, such as tin steel plates.

Conventional oil seals for WR bearings for high-speed applications are made of heat-resistant fluorine rubber. However, under ultra-high-speed conditions, abnormal heat generation in the oil seal lip area causes premature lip deterioration, allowing rolling water to intrude into the bearing and causing seizure and other damage. A special oil seal (Figure 19) made of PTFE (polytetrafluoroethylene) resin integrated into the seal lip was adopted as a countermeasure. Furthermore, a sealed four-row tapered roller bearing for ultra-high-speed applications has been developed with low heat generation (reduction of rolling friction inside the bearing) by optimizing the bearing's internal design. This bearing has been tested in actual equipment, and temperature measurements have confirmed its effectiveness in reducing bearing heat generation and its high sealing performance over a long period, reducing the risk of sudden seizure.

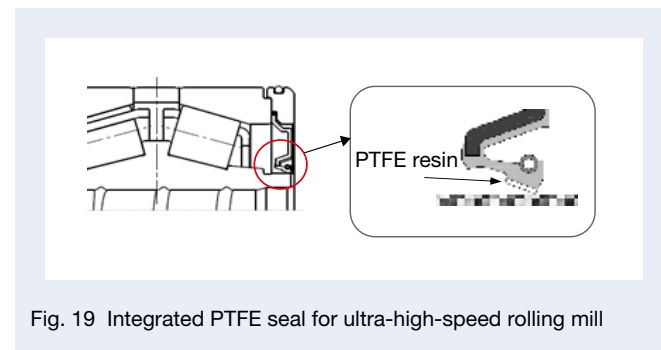


Fig. 19 Integrated PTFE seal for ultra-high-speed rolling mill

4.2 Development of backup roll bearings for cluster type rolling mills

Cluster type rolling mills are mainly used for rolling hard and hard-to-roll steel materials with uniform thickness, such as electromagnetic and stainless steel sheets. In recent years, with the emphasis on energy conservation and decarbonization, electrification of machinery and increased production of hybrid and electric vehicles have been promoted. In addition, demand for electromagnetic steel sheets has been increasing along with expanding power plants and substations due to infrastructure development in emerging regions. To increase the production capacity of high-value-added steel sheets, the rolling load has been increased, high-speed rolling has been promoted, and bearings are also required to respond.

Oil mist lubrication was used for the backup roll bearings to allow high-viscosity oil, and sealed bearings were used to prevent the ingress of rolling water into the bearings.

The bearing seal is a low-contact seal to meet high-speed specifications. However, a contradictory function was required to exhaust oil mist from the seal lip while maintaining a predetermined bearing inner pressure to prevent the ingress of rolling water.

To achieve this, seal specifications were established to optimize seal discharge pressure, and at the same time a structure was designed to facilitate seal replacement during maintenance. Furthermore, a sealed backup roll bearing for cluster type rolling mills was developed using the aforementioned Super TF material (Figure 20).

In actual use, the developed bearings contribute to improved equipment reliability through longer service life and reduced maintenance costs by reducing the number of scrapped bearings.

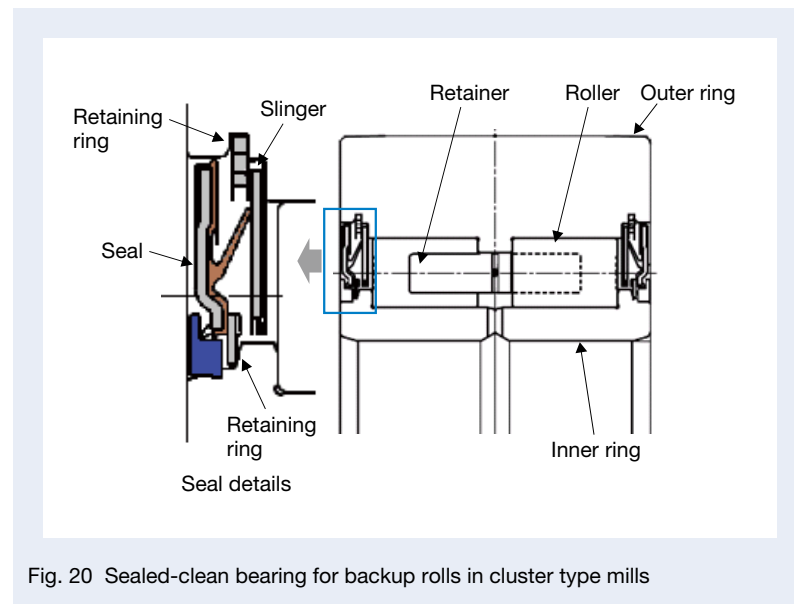


Fig. 20 Sealed-clean bearing for backup rolls in cluster type mills

4.3 Response to severe operating conditions of special rolling mills

Steel manufacturers are consolidating and integrating lines to streamline and improve the efficiency of their production equipment. One example is the increasing number of cases in which high-value-added products with dimensions and shapes utterly different from those of conventional products are manufactured using a common rolling mill. This results in a larger rolling load.

Since the dimensions of the equipment are standardized, and there are restrictions on the inner ring, outer ring, and width dimensions of the bearings, the load center of the equipment is misaligned with the bearing center. The heavy load is applied in an eccentric state (offset load action), and a concentrated load exceeding 100% of the basic load rating may be applied to one bearing row.

We have developed an asymmetric roller bearing structure to meet this requirement (Figure 21). Even under such severe load conditions, we have contributed to the stable operation of equipment by establishing specifications that satisfy user requirements through design, heat treatment, and analysis technologies.

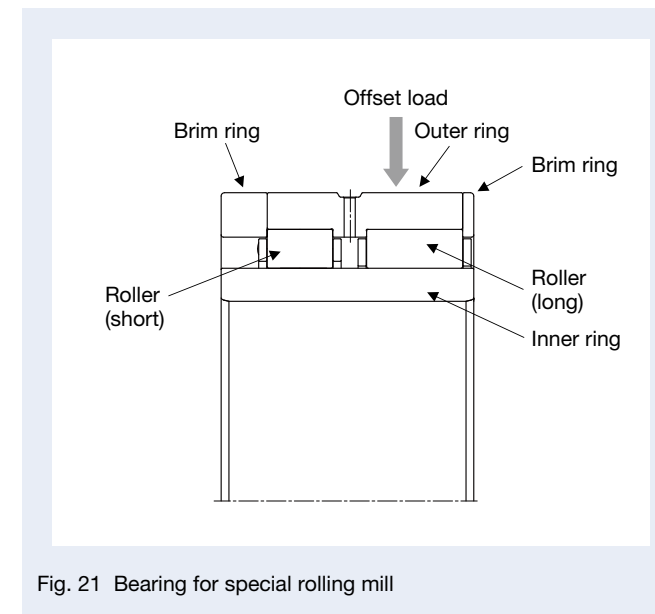


Fig. 21 Bearing for special rolling mill

5. Afterword

This paper reviews recent trends in bearing technology used in major equipment in the steelmaking process. Focusing on improving the productivity of steelmaking equipment, we have been developing highly reliable, long-life bearings to address the technical issues of each major piece of equipment.

In the future, we will work toward a carbon-neutral society by applying bearing diagnostic technology to meet the need for reuse and to reduce CO₂ emissions in bearing manufacturing.

References

- 1) *The Tribology*, No. 387 (Nov. 2019), pp. 16–19.
- 2) “Bearing Technology Trends in the Iron and Steel Industries,” *NSK Technical Journal*, No. 678.
- 3) “Optimized Long-life Cylindrical Roller Bearings for Continuous Casting Machines,” *NSK Technical Journal*, No. 691.



Tsuyoshi Nomura

QuickStopBearing™ for Dental Air Turbines

Yamato Okazaki, Mikiko Shirai
Electrical & Electrification Bearing Technology Center

Abstract

The Covid-19 pandemic has increased awareness of the risk of healthcare-associated infections and drawn focus to the handling of medical devices that may come into contact with the human body. Bearings support rotation in all kinds of medical devices, and post-use cleaning, disinfecting, and sterilizing create challenges for stable operation over the long term.

Here, we report on the QuickStopBearing for dental air turbines—handpieces used for drilling, cutting, and other dental treatments. Compared to conventional handpiece bearings, the new QuickStopBearing has a revised bearing seal structure and a significantly shorter duration of inertial rotation. These features help improve treatment efficiency, extend service life, and reduce the risk of nosocomial infections by reducing the entry of foreign matter into the bearing.

1. Preface

In recent years, the Covid-19 pandemic has raised concern about the risk of nosocomial infection. As a result, great care has especially been taken in the handling of medical devices that may come into contact with the human body. A wide range of medical devices have rotating components that require bearings as well as regular cleaning, disinfecting, and sterilizing after use.

In this article we focus on the new QuickStopBearing for air turbines (Photo 1) used by dental clinics to cut and treat teeth. The new QuickStopBearing has a different sealing structure from conventional bearings, which significantly reduces the inertia rotation stop time of the air turbine and thus allows for more efficient treatment while ensuring patient safety. Reducing the ingress of foreign matter into the bearing prevents nosocomial infection and prolongs the service life of the air turbine.

2. Characteristics of the QuickStopBearing

2.1 Structure of the air turbine

Bearings used in a typical air turbine are shown in Figure 1. These air turbines use deep groove ball bearings and angular contact ball bearings with an inner diameter of ϕ 3.175 mm and an outer diameter of ϕ 6.35 mm.

The inner and outer rings are made of highly corrosion-resistant stainless steel, the balls are made of ceramic, and the cage is made of polyamide-imide (PAI), polyether ether ketone (PEEK), and polyimide (PI), while the sealing plates are made of austenitic stainless steel to meet the cleaning, disinfection, and sterilization requirements of air turbines.

The structure of a typical air turbine head is shown in Figure 2. The air turbine is designed to rotate the impeller between the bearings at approximately 400 000 rpm by supplying air to cut teeth smoothly with a cutting bar attached to the end of the shaft. The supplied air that rotates the air turbine drives the impeller and then passes through the air turbine and is collected as exhaust air in the chair unit, while some air passes through the bearings and is discharged from the upper and lower parts of the head. (Figure 3)

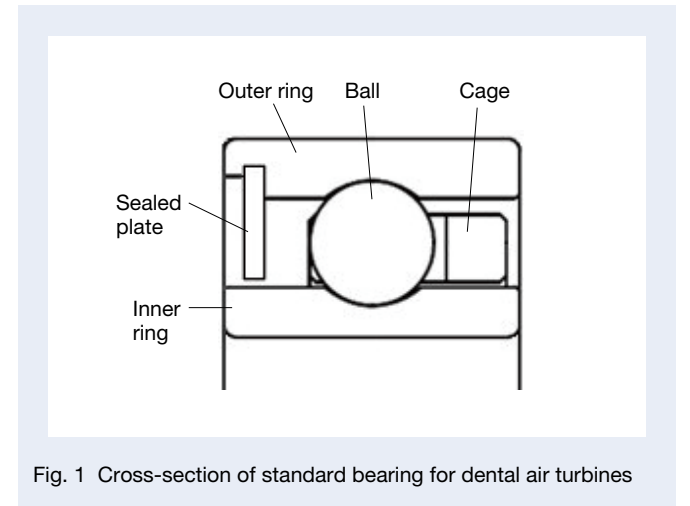


Fig. 1 Cross-section of standard bearing for dental air turbines

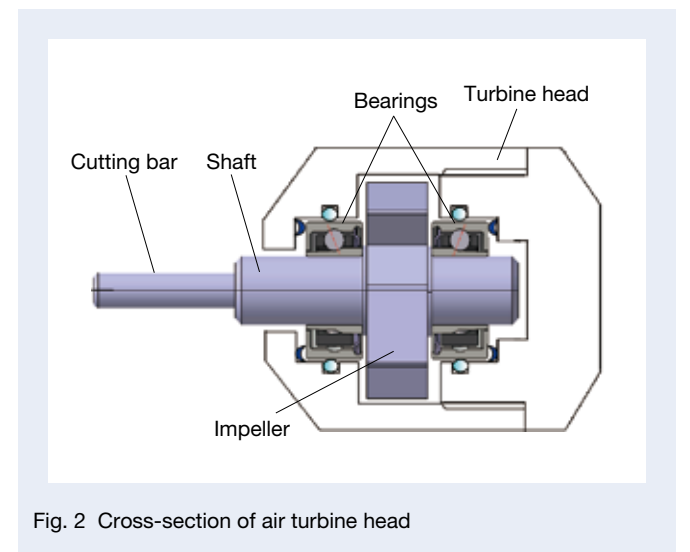


Fig. 2 Cross-section of air turbine head



Photo 1 Dental air turbine

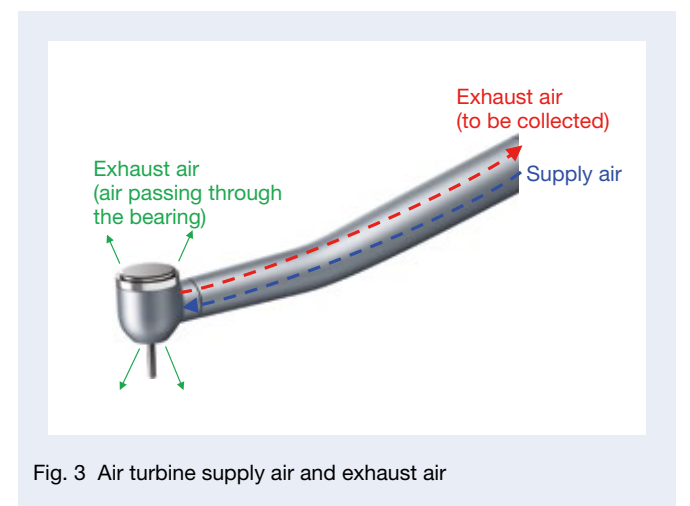


Fig. 3 Air turbine supply air and exhaust air

2.2 Structure of the QuickStopBearing

The appearance and structure of the QuickStopBearing are shown in Photo 2 and Figure 4.

With the QuickStopBearing, a rubber seal without a metal core is inserted into the seal groove of the bearing outer ring, and a metal retaining ring fixes the rubber seal. The rubber seal's inner diameter lightly contacts the inclined part of the inner ring's outer diameter. When the air from the air supply rotates the air turbine, the inner diameter of the rubber seal is raised by a certain amount by the air passing through the bearing to secure the specified rotation speed. However, when stopping the air supply, the rubber's elasticity causes the seal's inner diameter to instantly return to contact with the inclined part of the outer diameter of the inner ring, stopping inertia rotation in a short period. (Figure 5)

2.3 Rotational performance and inertia rotation stop time

To ensure patient safety, dentists should remove the air turbine from the mouth after it has completely stopped rotating. Conventional air turbines have an inertia period of 2 to 5 seconds after the air supply is stopped. During this time, the air turbine cannot be removed from the mouth, which affects treatment efficiency.



Photo 2 QuickStopBearing

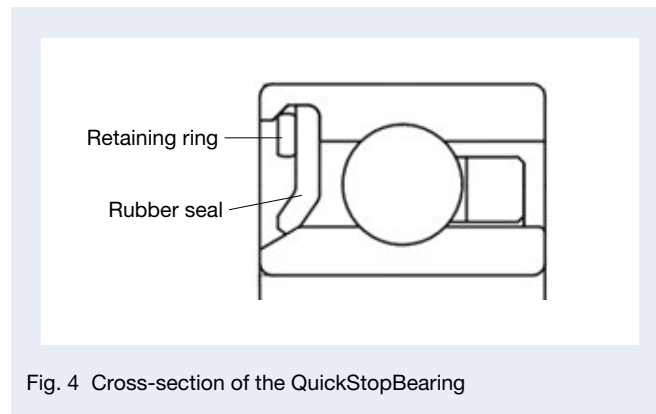


Fig. 4 Cross-section of the QuickStopBearing

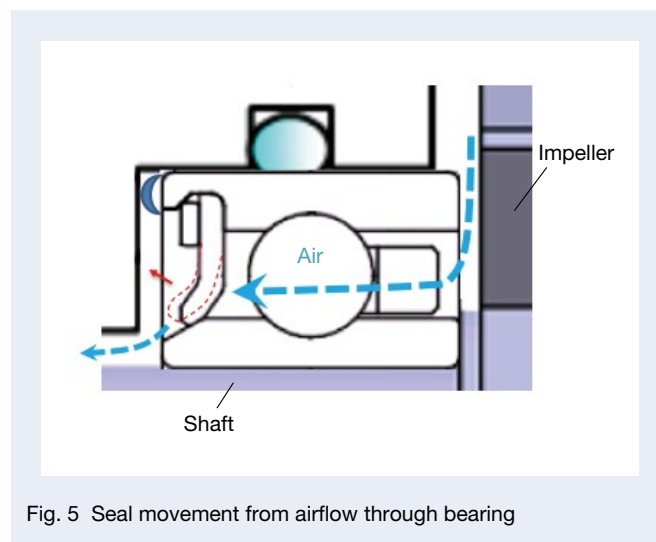


Fig. 5 Seal movement from airflow through bearing

Figure 6 shows the time data from the stop of the air supply to the stop of inertia rotation for an air turbine incorporating conventional bearings and the QuickStopBearing, respectively. The conventional bearings (red line) show a gradual decrease in speed (inertia rotation), whereas the QuickStopBearing (green line) shows a decrease in speed in a short time.

The QuickStopBearing achieves a rotation stop time of about one second or less after the air stops. Also, the rated speed of the air turbine, which affects treatment efficiency, is maintained at the specified speed.

2.4 Bearing sealing performance

2.4.1 Rotation stop time and suction prevention (suck-back prevention)

As shown in Figure 3, in a typical air turbine, a certain amount of air that passes through the bearings during rotation is discharged through the clearance between the top and bottom of the head. When the air supply is stopped, as shown in Figure 7, a phenomenon called “suck-back” occurs, in which intraoral foreign substances (saliva, tooth chips, blood, etc.) are sucked into the head through the clearance between the top and bottom of the head. This leads to concerns about nosocomial infection caused by infected substances entering the turbine head and reduced bearing life due to foreign substances entering the head.

Air turbine manufacturers have taken the following measures to reduce suck-back.

- Brake structure installed in the air turbine head to shorten the inertia rotation stop time
- Complex labyrinth structure
- Fine control of air supply from the chair unit when rotation is stopped

These measures have resulted in a complicated structure within the turbine head or control of the chair unit.

Figure 8 shows the structure of the test facility used to confirm suck-back. An air turbine is mounted inside an acrylic case, and a pressure sensor is placed to measure the air pressure inside the case. Pressure sensor signals can be checked over time with an oscilloscope. A tube extending into the water tank outside the case allows visual confirmation of water being sucked up through the tube when the pressure inside the case is lower than atmospheric pressure (negative pressure condition).

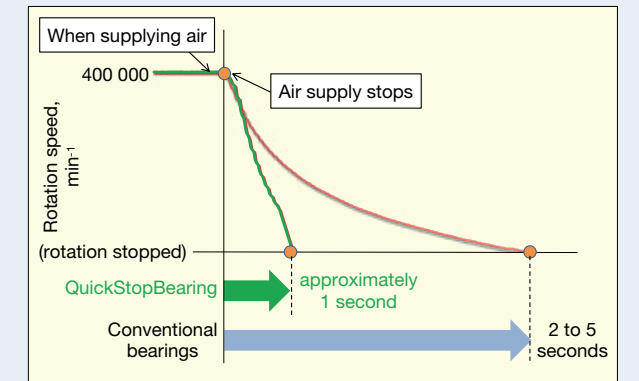


Fig. 6 Duration until inertial rotation stops in conventional bearings and the QuickStopBearing

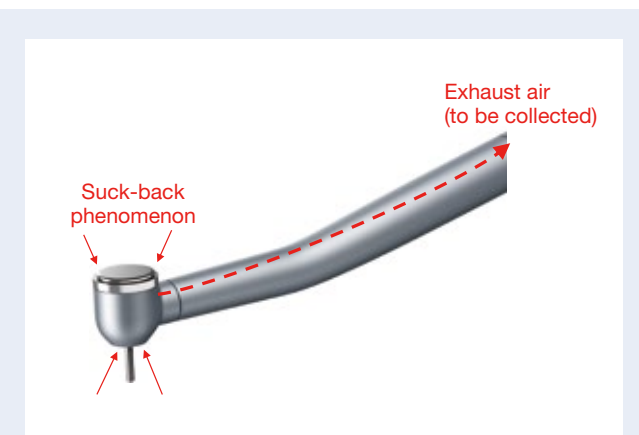


Fig. 7 Suck-back phenomenon in an air turbine

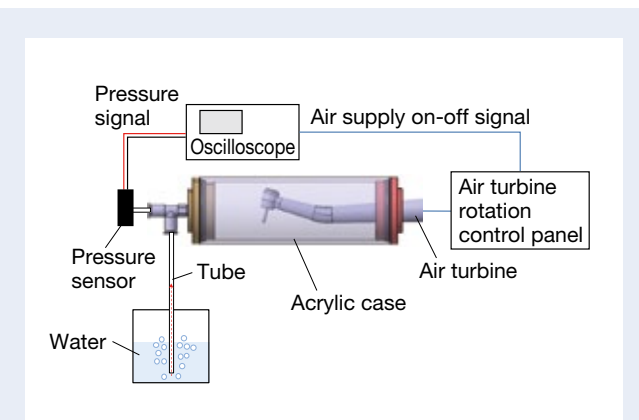


Fig. 8 Equipment to test air turbine suck-back

Figure 9 shows the test results comparing the change in air pressure inside the acrylic case of an air turbine with a conventional bearing and an air turbine with a QuickStopBearing. In an air turbine with general bearings (red line), after the air supply is stopped, the inside of the acrylic case rapidly enters a negative pressure state and gradually returns to atmospheric pressure. Remarkable water suction in the tube was also observed, confirming the occurrence of suck-back in the turbine head section.

In contrast, the air turbine with the QuickStopBearing (green line) does not experience negative pressure inside the acrylic case after the air supply is stopped and gradually returns to normal pressure. Therefore, no water uptake was observed in the tubes.

These results confirm the effectiveness of the QuickStopBearing in reducing and preventing suck-back when the air supply is stopped.

2.4.2 Wear-resistant performance of quick-stop rubber seals

The QuickStopBearing reduces the inertia rotation stop time and prevents suck-back by contacting the rubber seal inner diameter with the inclined part of the inner ring outer diameter.

Due to concerns about performance degradation caused by wear of the rubber seal's inner diameter over time, a rubber seal wear resistance test (rubber seal open/close test) was conducted, shown in Figure 10. The test was conducted by repeatedly rotating and stopping the air turbine and opening and closing the seal one million times. Still, no wear was observed on the rubber seal's inner diameter contact area. This is due to the extremely short contact time until the rotation stops and the optimum design of the rubber seal and inner ring contact area, which provides sufficient wear resistance.

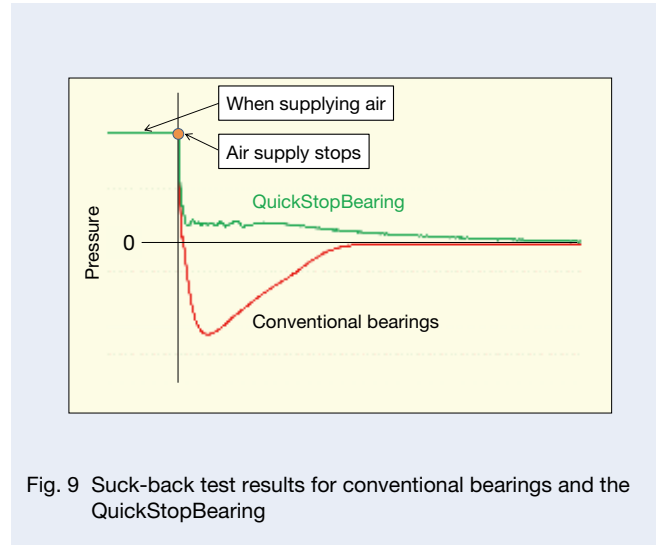


Fig. 9 Suck-back test results for conventional bearings and the QuickStopBearing

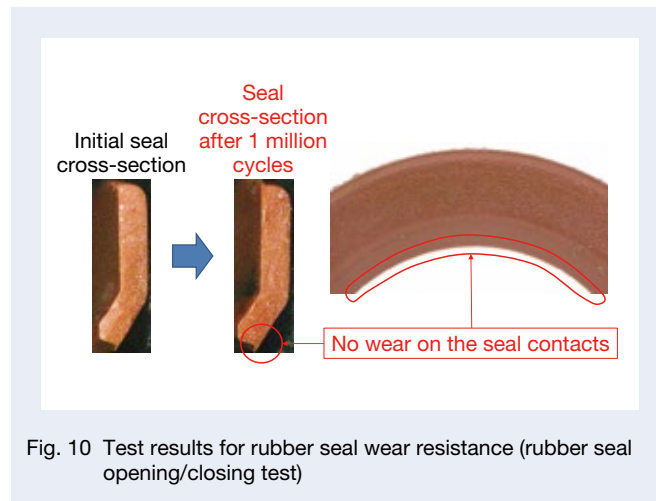


Fig. 10 Test results for rubber seal wear resistance (rubber seal opening/closing test)

2.5 Autoclave resistance

As shown in Figure 11, air turbines are cleaned, disinfected, lubricated, and sterilized after treatment before being used for the next treatment.

Among these, sterilization (autoclave) has been confirmed to degrade bearing performance due to the high temperature and high-pressure steam conditions.

In particular, rubber seals have been confirmed to deteriorate under high temperatures and high-pressure steam. There is concern that the performance of the QuickStopBearing may deteriorate in terms of inertia rotation stop time, securing rotation speed, and preventing suck-back. For this reason, we decided to use a high-performance rubber material with excellent heat and water resistance for the QuickStopBearing seal.

Figure 12 shows the changes in the number of rotations and rotation stop time for each sterilization frequency in the QuickStopBearing. The results of up to 250 sterilization cycles showed that the reduction in air turbine speed was less than 10% and the inertia rotation stop time was less than 2 seconds, confirming that autoclaving does not affect performance in actual use.

3. Afterword

In this article, we have reported on the structure and performance of the new QuickStopBearing for dental air turbines. The requirements for medical rotating equipment using bearings are expected to become increasingly demanding, and we will continue to develop bearings with higher functionality to meet the growing needs of users.

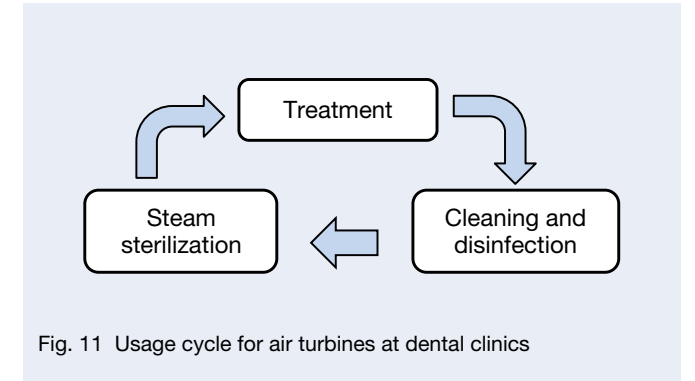


Fig. 11 Usage cycle for air turbines at dental clinics

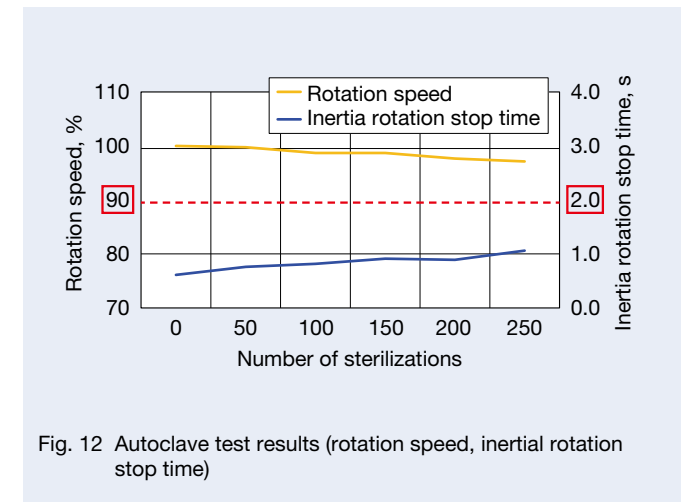


Fig. 12 Autoclave test results (rotation speed, inertial rotation stop time)



Yamato Okazaki



Mikiko Shirai

Evaluation of Lubrication Performance in Ball Screws and Linear Guides by the Electrical Impedance Method

Juri Aoyama, Akira Tsutsui

Industrial Machinery Linear Technology Center, Research Department

Abstract

Applying the electrical impedance method (EIM) to ball screws and linear guides allows for the measurement of oil film thickness and metal contact ratio along with broad evaluations of lubrication performance inside the actual product, a feat that was difficult until now. Wiring inductance is greatly influenced by the characteristics of reciprocating motion, but by correcting for these in calculations, we upgraded the conventional EIM and improved measurement accuracy. In addition, we propose a simple method to evaluate oil film thickness and metal contact ratio using the reciprocal of reactance and resistance per contact point. This helps to improve the EIM and makes it more convenient to use. Furthermore, we evaluated lubrication performance inside actual products with various lubricants, surface properties, and operating conditions and expect the improved EIM to be useful in extensive future applications.

1. Preface

Ball screws and linear guides are used as precision machine feed mechanisms for various applications. They are essential components for the manufacture of high-precision, high-quality products. For this purpose, proper internal lubrication is required. However, since measuring oil film thickness, an indicator of the lubrication state, is typically performed using optical interferometry of light-permeable materials, it has been difficult to measure the thickness of the oil film inside the actual product.

For ball screws and linear guides, there are simple methods for evaluating the state of lubrication, such as measuring dynamic torque and dynamic friction force to create a Stribeck curve. However, these are the sum representation of stirring resistance, rolling viscosity resistance, and sliding friction resistance. Consequently, quantitative determination of the lubrication state is challenging.

The electrical impedance method¹⁾, which applies a high-frequency AC voltage to actual machine elements composed of metal such as rolling bearings, enables measurement of oil film thickness and metal contact ratio in the EHD contact zone. The electrical impedance method, developed for bearings, has been applied to ball screws and linear guides, and its relation to lubrication characteristics has been extensively evaluated.

2. Measurement Methodology

A physical model diagram of a steel ball in contact with a raceway groove is shown in Figure 1. The figure also shows a model diagram in which a portion of the steel ball is in contact with the groove, i.e., in mixed lubrication. Here, r is the steel ball radius, a is the Hertzian contact radius, S is the Hertzian contact area, $h(x)$ is the oil film thickness at coordinate x , h_1 is the oil film thickness in the area where the oil film forms in the EHD contact zone, h_2 is maximum oil film thickness in the area surrounding the EHD contact zone, and α is the metal contact ratio (oil film breakdown ratio^{1, 2)}).

Figure 2 shows the equivalent circuit diagram inside the rolling bearing element. Here, R_1 is resistance that occurs in the area where the oil film is broken in the EHD contact zone, C_1 is a capacitor in the area where the oil film is formed in the EHD contact zone, and C_2 is a capacitor in the area outside the EHD contact zone²⁾. In addition, since ball screws and linear guides have long wiring to the measurement device due to their reciprocating characteristics, the inherent coil component was considered. L_E is the self-inductance of the wiring, which is approximately several μH .

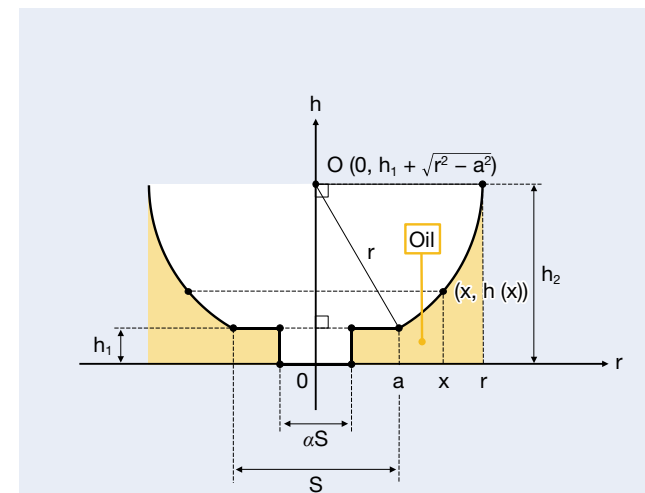


Fig. 1 Geometrical model of EHD point contact

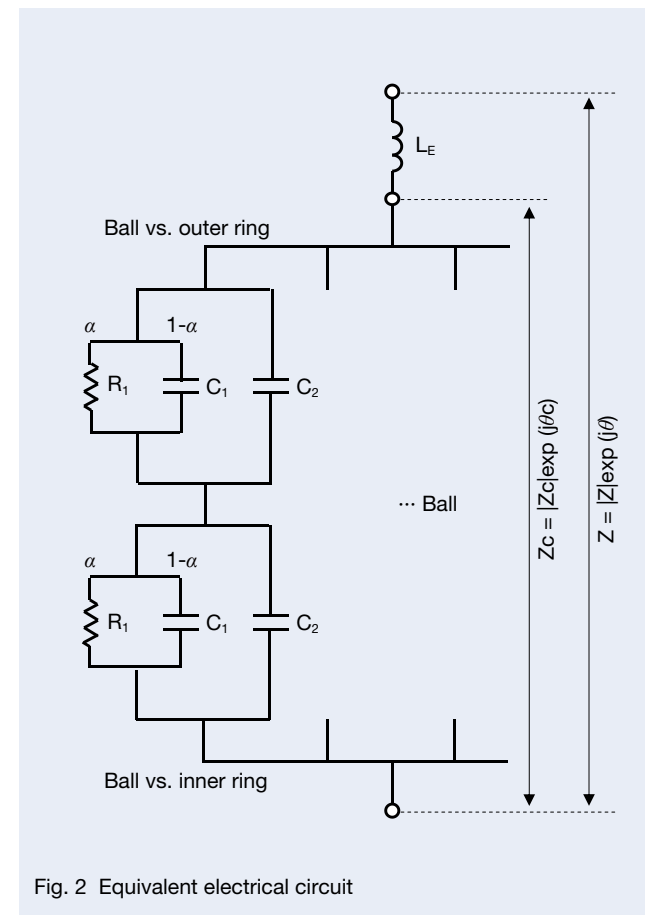


Fig. 2 Equivalent electrical circuit

3. Establishment of a Method for Evaluating Lubrication Conditions in Ball Screws

3.1 Test method

A schematic diagram of the ball screw testing machine used in this test is shown in Figure 3. The test used a ball screw with a screw shaft diameter of $\phi 25$ mm, a lead of 10 mm, and steel balls with a diameter of $\phi 3.175$ mm. The ball screw was connected to the drive motor and machine table via an insulating fixture using resin and similar material to configure an appropriate electrical circuit. The nut was wired directly to the LCR meter, and the screw shaft was connected to the LCR meter using a carbon brush. The test system's impedance Z and phase θ were measured at each operating speed, and the average oil film thickness and metal contact ratio were calculated.

Lubricants with the properties shown in Table 1 were used for comparative evaluation.

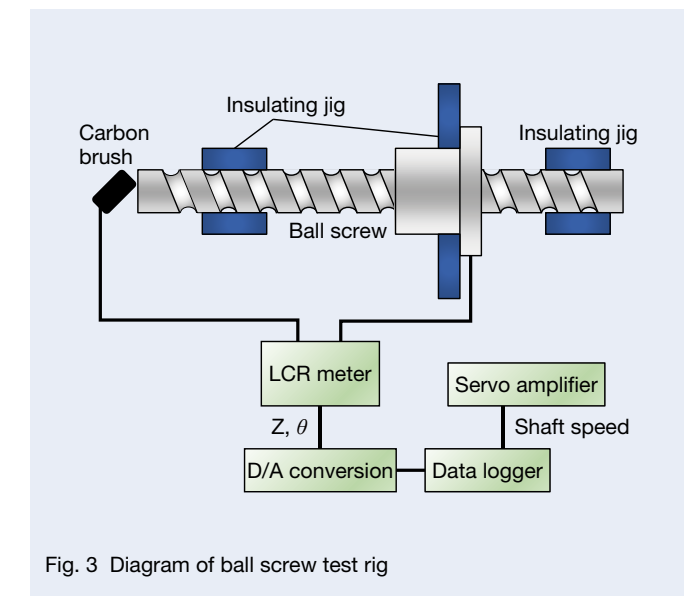


Fig. 3 Diagram of ball screw test rig

Table 1 Characteristics of lubricants

Lubricant	VG68 oil	A-grease	L-grease	N-grease
Usage	General multi-purpose	General purpose, for heavy loads	High speed, for medium loads	For fretting resistance
Thickener	—	Li soap	Li soap	Urea
Base oil	Paraffinic	Mineral oil	POE	PAO
Kinematic viscosity @40°C, mm ² /s	68	130	29	26

3.2 Measurement example

Figure 4 shows the results of complex impedance measurements at shaft speeds from 1 to 1 000 rpm for standard ball screws with VG68 oil lubrication. The higher the rotation speed, the larger Z becomes and the closer θ moves toward -90° . The results after converting these measurements to oil film thickness h and metal contact ratio α are shown in Figure 5. The dashed line is the approximate theoretical oil film thickness based on the Hamrock-Dowson equation. In both logarithmic graphs, the oil film thickness was very close to the slope of the theoretical value. However, its magnitude was about half the theoretical value, and the oil film thickness could not be converted below 50 rpm. The metal contact ratio was significantly above the upper limit of 1 at low speeds of less than 10 rpm, but such values are not logical.

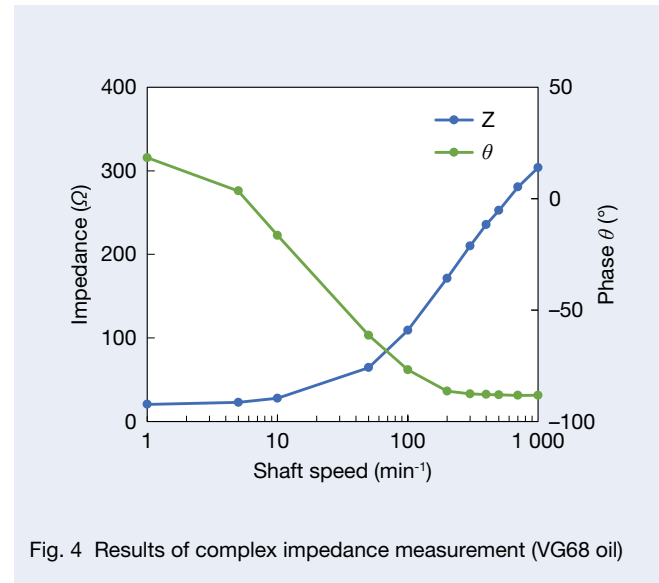


Fig. 4 Results of complex impedance measurement (VG68 oil)

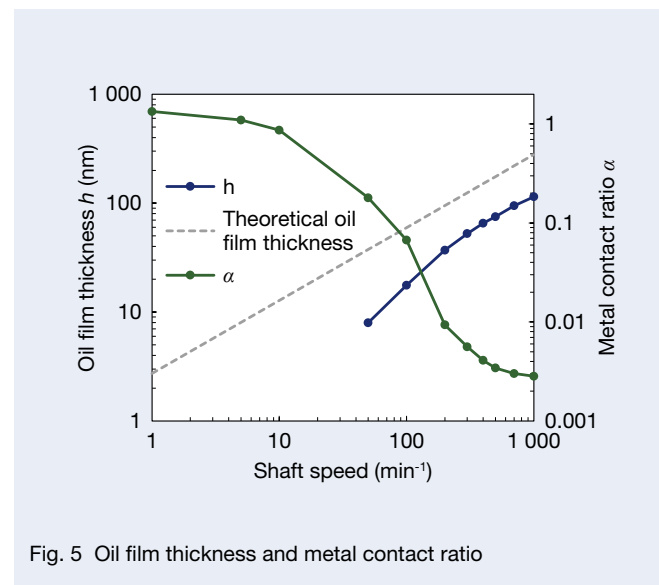


Fig. 5 Oil film thickness and metal contact ratio

3.3 Wiring inductance compensation and simplified evaluation method

We therefore focused on the effect of the coil component of the wiring. Although Z shown in Figure 2 includes the inductance of the wiring, Z_c is obtained by correcting for this based on Kirchhoff's laws, and the results for oil film thickness and metal contact ratio using Z_c and θ_c are shown in Figure 6. The oil film thickness could be calculated down to 1 rpm, and the highest metal contact ratio was about 0.6 with a logical range of values even under low-speed conditions.

The reactance C and resistance R per contact point were calculated based on Kirchhoff's laws, and their reciprocals $1/C$ and $1/R$ are shown in Figure 7 as a simple evaluation method. Parameter $1/R$ is proportional to the metal contact ratio and $1/C$ is a parameter that correlates well with oil film thickness. It is possible to perform a relative evaluation of lubrication conditions in cases where the oil film thickness cannot be calculated, such as when groove dimensions and lubricant properties are unknown. In fact, Figures 6 and 7 correspond well, indicating that $1/C$ and $1/R$ can, to some extent, substitute for oil film thickness and metal contact ratio.

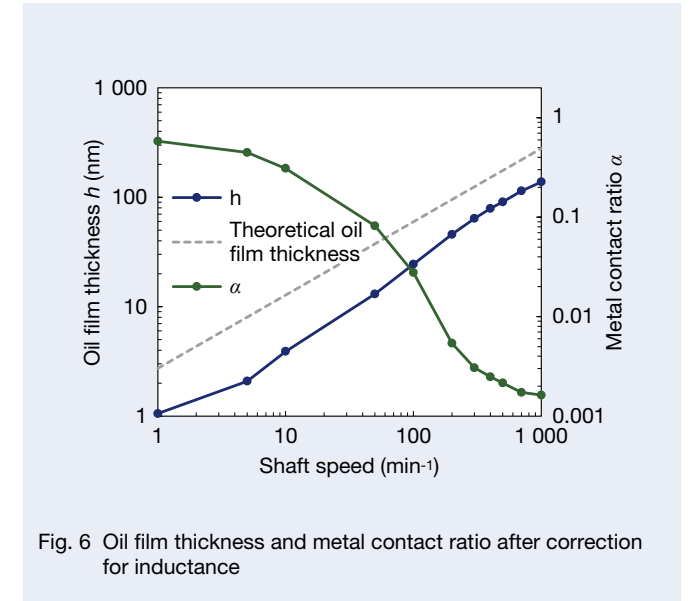


Fig. 6 Oil film thickness and metal contact ratio after correction for inductance

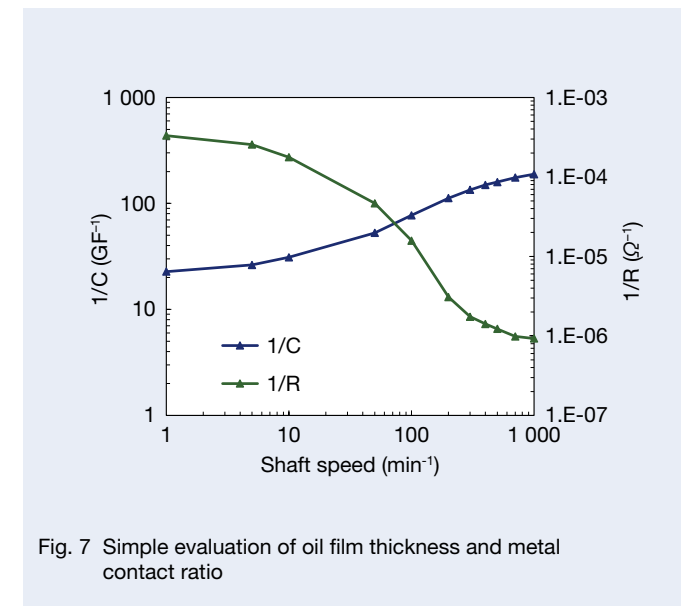


Fig. 7 Simple evaluation of oil film thickness and metal contact ratio

4. Ball Screw Evaluation Results

4.1 Grease varieties

The grease used for linear motion products is selected in consideration of operating temperature, speed, and load conditions. For example, high-base oil viscosity grease, such as A-grease in Table 1, is used for low-speed operation and high-load applications where oil film formation is difficult, and grease with low-base oil kinematic viscosity, such as L-grease, is used for high-speed operation where temperature rise is significant. Grease for special applications, such as oscillating operations, is also used.

In this study, the lubrication characteristics of A-grease for general-purpose high-load applications and L-grease for high-speed medium-load applications were compared and evaluated using the electrical impedance method to confirm actual lubrication conditions.

The results of the comparative evaluation of the two types of grease are shown in Figure 8 (oil film thickness) and Figure 9 (metal contact ratio). The dashed line in Figure 8 is the approximate theoretical oil film thickness based on the kinematic viscosity of the base oil at 25°C for each grease. At speeds of 100 rpm or higher, the oil film thicknesses of A-grease and L-grease were close to the theoretical values. However, at speeds under 100 rpm, L-grease shows an increase in oil film thickness with decreasing speed, which is far from the theoretical value, suggesting an interesting phenomenon regarding oil film retention under low-speed conditions. The metal contact ratio for A-grease was significantly higher at low speeds under 100 rpm, while L-grease maintained a low value even at a very low speed of 1 rpm.

The lubrication characteristics of L-grease at low speeds were significantly higher than the theoretical oil film thickness based on the Hamrock-Dowson equation. Previously, high-viscosity lubricants were generally applied to products used at low speeds to maintain an oil film, but oil film thickness was maintained at low speeds despite the low kinematic viscosity of the base oil. This result suggests the possibility of achieving low-torque products by applying L-grease to products used at low speeds.

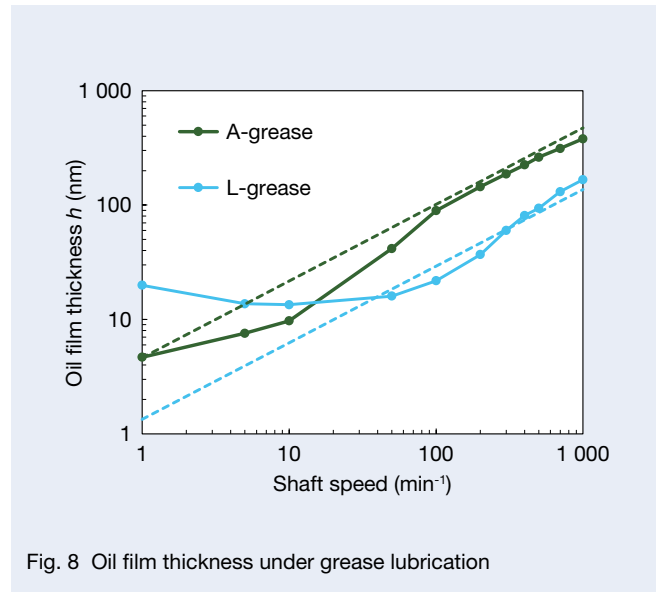


Fig. 8 Oil film thickness under grease lubrication

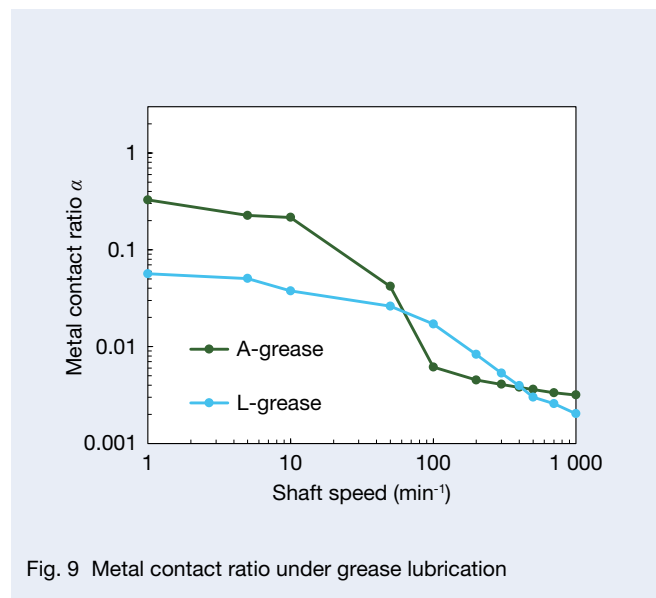


Fig. 9 Metal contact ratio under grease lubrication

4.2 High-durability precision ball screws

With ball screws used for long periods under low-speed conditions, wear of the raceway grooves causes a drop in preload, which tends to cause problems in maintaining feed accuracy. High-durability precision ball screws use NSK's original surface modification technology to suppress wear and maintain feed accuracy over the long term.

The raceway grooves of high-durability precision ball screws have numerous small dimples, which are thought to act as oil reservoirs and improve oil film formation capability. This study compared and evaluated lubrication characteristics by the electrical impedance method to verify the effectiveness of the lubrication. The oil film thickness of a high-durability precision ball screw under VG68 oil lubrication is shown in Figure 10, and the metal contact ratio is shown in Figure 11. The oil film thickness of the high-durability precision ball screw is equivalent to that of a conventional product under high-speed conditions. However, it is thicker under low-speed conditions of 100 rpm or less, and the metal contact ratio is lower, indicating its high oil film formation capability.

Figure 12 shows the results of comparative measurements of the increase in dynamic torque at 50 rpm with VG68 oil lubrication. The dynamic torque increase in the high-durability precision ball screw is less than that of the conventional product under low-speed conditions of 10 rpm or less. This indicates that the retention of the oil film under low-speed conditions kept the metal contact ratio low, confirming the effectiveness of the surface modification. In fact, the increase in dynamic torque in the high durability ball screw was less than that of the conventional product even under medium to high-speed conditions of 200 rpm or more. Since measurements of oil film thickness and metal contact ratio did not show any result indicating torque reduction, lubrication characteristics in this speed range may be due to other factors, a topic to explore in the future.

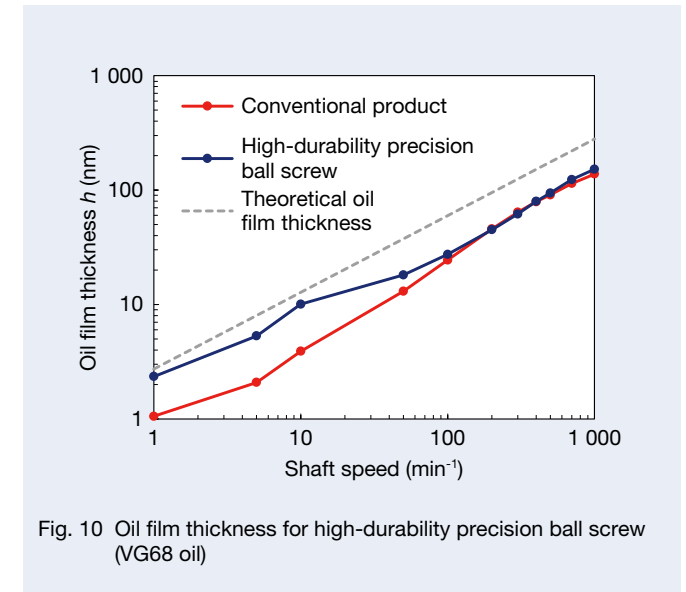


Fig. 10 Oil film thickness for high-durability precision ball screw (VG68 oil)

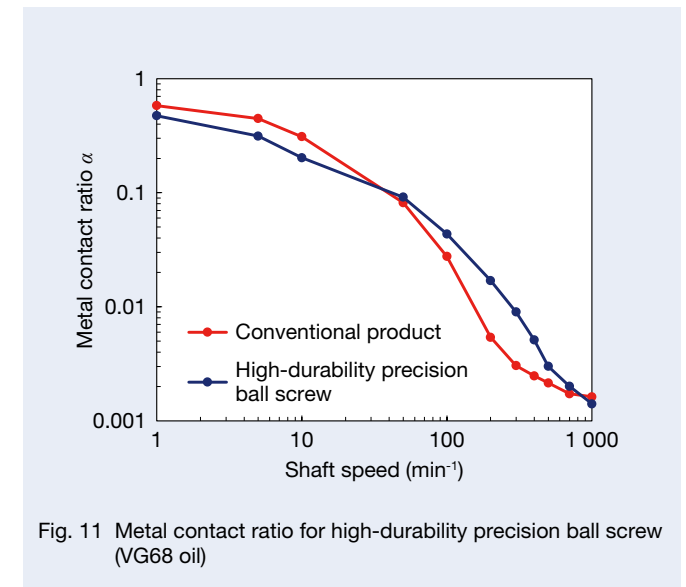


Fig. 11 Metal contact ratio for high-durability precision ball screw (VG68 oil)

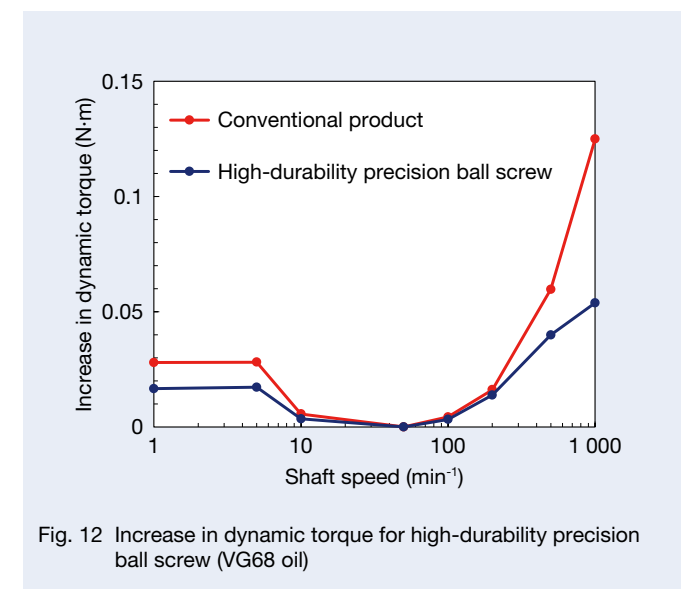


Fig. 12 Increase in dynamic torque for high-durability precision ball screw (VG68 oil)

5. Evaluation of Lubrication Conditions in Linear Guides

5.1 Test method

A schematic diagram of the linear guide testing machine used in this test is shown in Figure 13. A size 25 linear guide (steel ball diameter ϕ 4.76 mm) was used. The linear guide was connected to the drive system and machine table via an insulating fixture using resin and similar material to configure an appropriate electrical circuit. The LCR meter was connected to the rail and slider by direct wiring. The test system's impedance Z and phase θ were measured at each operating speed, and the average oil film thickness and metal contact ratio were calculated.

5.2 Measurement example

The results of the evaluation of oil film thickness and metal contact ratio for a linear guide in VG68 oil are shown in Figure 14. The simplified evaluations $1/C$ and $1/R$ are shown in Figure 15. The deviation from the theoretical oil film thickness increased at slide feed speeds of 40 m/min or less, and the oil film thickness became very thin under low-speed conditions, as shown by the change of $1/C$. Linear guides have a much slower ball speed relative to the feed speed than ball screws, which is presumably why it is difficult to form an oil film at low speeds.

Figure 16 shows the results of a comparative evaluation of $1/C$ for A-grease for general-purpose high-load applications and N-grease for fretting resistance. Although the base oil kinematic viscosity of N-grease is low, $1/C$ saturates at low-speed conditions of 20 m/min or less, indicating that the grease has high capabilities for oil film formation at low speeds.

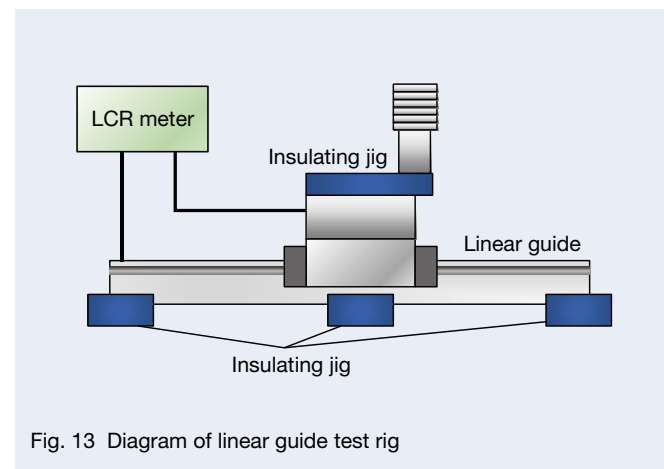


Fig. 13 Diagram of linear guide test rig

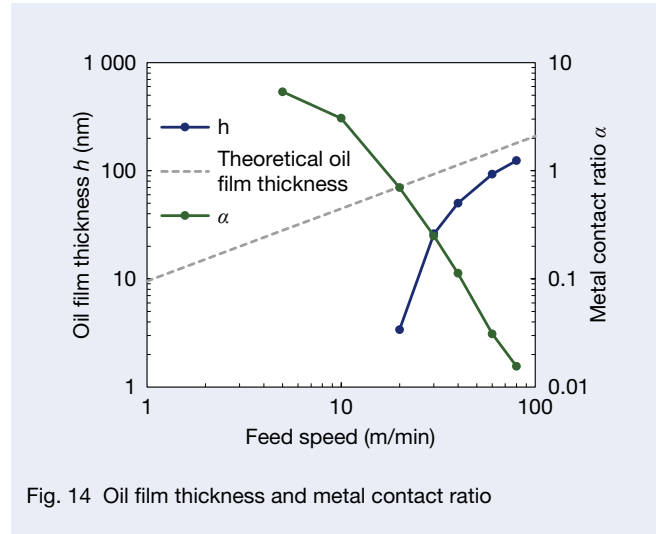


Fig. 14 Oil film thickness and metal contact ratio

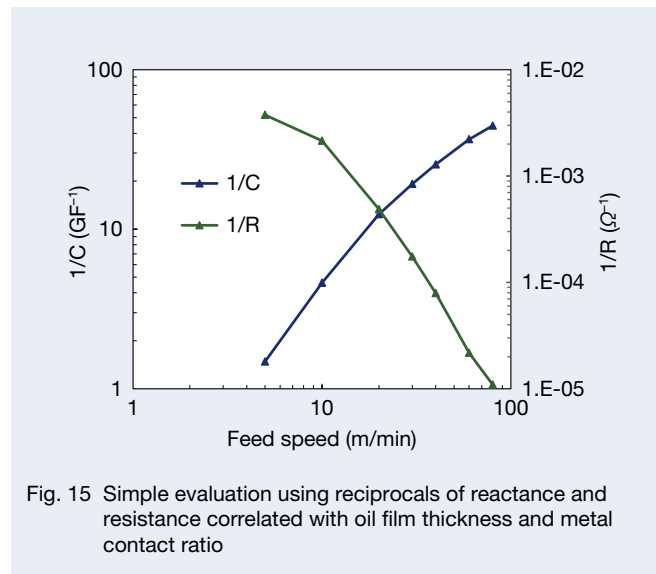


Fig. 15 Simple evaluation using reciprocals of reactance and resistance correlated with oil film thickness and metal contact ratio

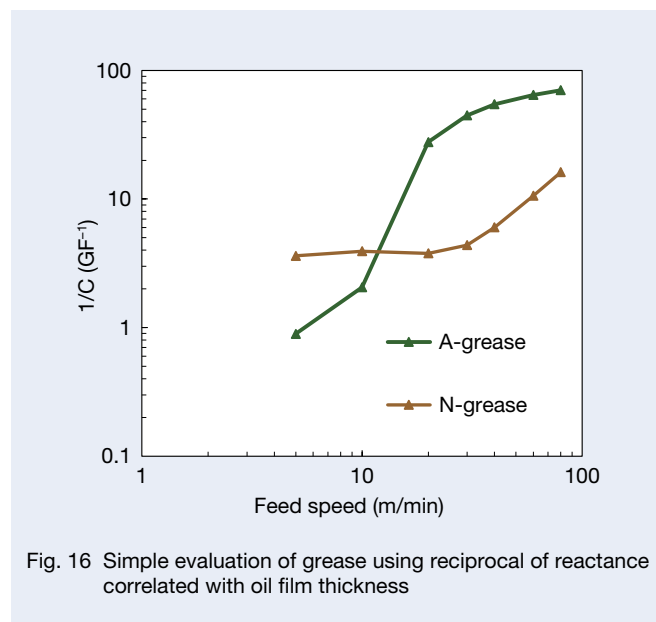


Fig. 16 Simple evaluation of grease using reciprocal of reactance correlated with oil film thickness

5.3 Micro-oscillation operation

Fretting tends to occur in the raceway grooves of linear guides under oscillating operation with small strokes, resulting in problems such as reduced feed accuracy and abnormal noise. Although the performance of N-grease for fretting resistance under oscillating operation is well established, oil film formation during oscillating operation was actually observed by utilizing the electrical impedance method.

Figure 17 shows the results of a simple evaluation of $1/C$ for the oil film thickness when the linear guide oscillates with short strokes. A-grease and N-grease were used as lubricants, with the X-axis showing the stroke divided by the diameter of the steel balls. Although the base oil kinematic viscosity of N-grease is much lower than that of A-grease, the oil film thickness of N-grease is equivalent to that of A-grease when the stroke is about ten times the steel ball diameter. For strokes less than five times the steel ball diameter, the simplified evaluation of oil film thickness $1/C$ for A-grease decreases as the stroke becomes shorter. In contrast, N-grease has the highest $1/C$ at a stroke four times the steel ball diameter, and maintains nearly the same level down to a stroke equal to the diameter of the steel balls.

Figure 18 shows the evolution of the simplified evaluation of oil film thickness $1/C$ during a micro-oscillation operation of 10 000 cycles at a stroke twice the steel ball diameter. The $1/C$ value of N-grease was stable at more than ten times that of A-grease, confirming the excellent lubricating characteristics of N-grease under micro-oscillation operation.

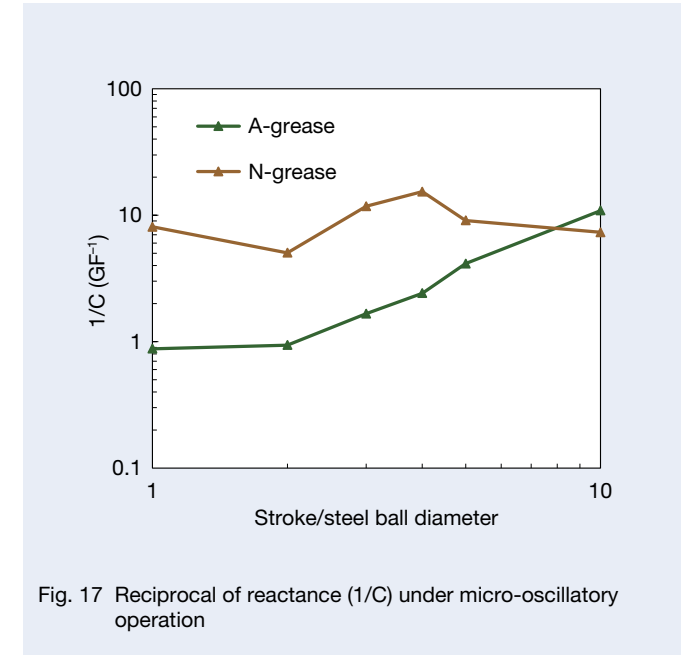


Fig. 17 Reciprocal of reactance ($1/C$) under micro-oscillatory operation

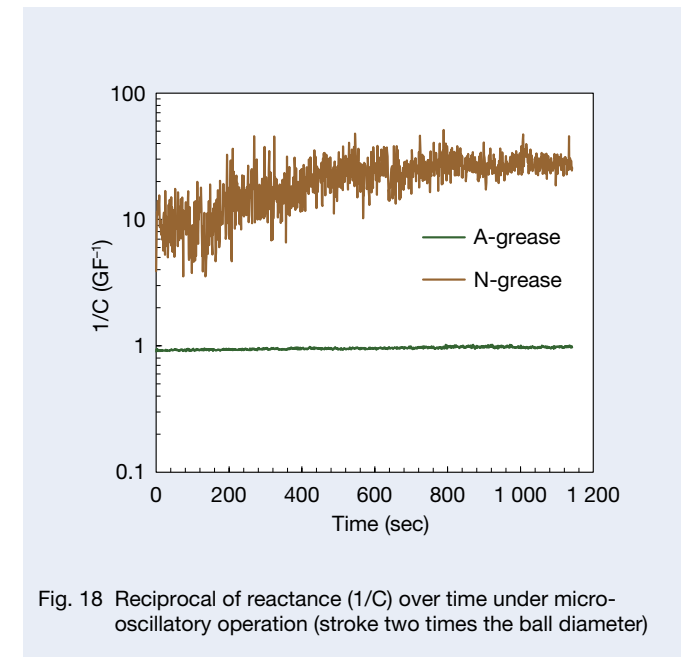


Fig. 18 Reciprocal of reactance ($1/C$) over time under micro-oscillatory operation (stroke two times the ball diameter)

6. Conclusion

Lubrication characteristics of ball screws and linear guides have been evaluated by substitutive methods such as dynamic torque and friction measurements. Applying the electrical impedance method allows for detailed evaluation of the lubrication state inside the product and obtaining new knowledge about lubrication characteristics under various lubricants, surface properties, and operating conditions.

By applying this knowledge, we will establish technology for monitoring the conditions of feed systems and the optimization of lubrication specifications to reduce environmental impact, thereby contributing to a carbon-neutral society.

References

- 1) T. Maruyama, "Study on Lubrication Condition Monitoring of Rolling Bearings—Development of the Electrical Impedance Method," doctoral dissertation.
- 2) M. Maeda, T. Maruyama, and K. Nakano, "Simultaneous Measurement of Oil Film Thickness and Breakdown Ratio in EHD Contacts—Verification of the Electrical Impedance Method," *NSK Motion & Control*, No. 30 (2019), pp. 73–75.



Juri Aoyama



Akira Tsutsui

NSK VIRTUAL EXPO

Yoshinori Yano

Industrial Machinery Technology Development Center, Linear Technology Center,
LG Technology Department

Abstract

In 2020, the Covid-19 pandemic made face-to-face business and technical exchanges difficult. We therefore held the NSK VIRTUAL EXPO in January 2021, which was a web exhibition to introduce new products and technologies from NSK to our customers. In addition to online seminars with chat capabilities, we posted videos, explanations, and technical data to detail the new products and technologies. After the expo, the site was revised and updated so that it could be used on a continual basis. We continue to hold online business and technical exchange meetings at the site that are equivalent to those held before the pandemic. In this article, we provide an overview of the NSK VIRTUAL EXPO site.

1. Preface

NSK held its first online exhibition, the NSK VIRTUAL EXPO, in January and February 2021. During the event, we posted videos, descriptions, and technical data on new products and technologies for machine tool sectors, held online seminars led by NSK engineers, and conducted Q&A sessions with customers in a real-time chat format.

Afterwards, the content was moved to the NSK website, where site visitors could continue to view it. This has led to online business meetings and technical exchanges with customers.

In this article, we provide an overview of the NSK VIRTUAL EXPO and how to use it. We hope you will make use of the site. Also, please be aware that the site's technical information will be continually updated.

2. What is the NSK VIRTUAL EXPO?

2.1 Overview

Figure 1 shows the NSK VIRTUAL EXPO site logo, top page URL, and QR code. Figure 2 shows the top page on a smartphone.

The NSK VIRTUAL EXPO is an online exhibition of new products and technologies developed by NSK, including bearings, spindles, ball screws, NSK linear guides, and condition monitoring technologies, for the machine tool



Fig. 1 NSK VIRTUAL EXPO site logo, URL and 2D barcode

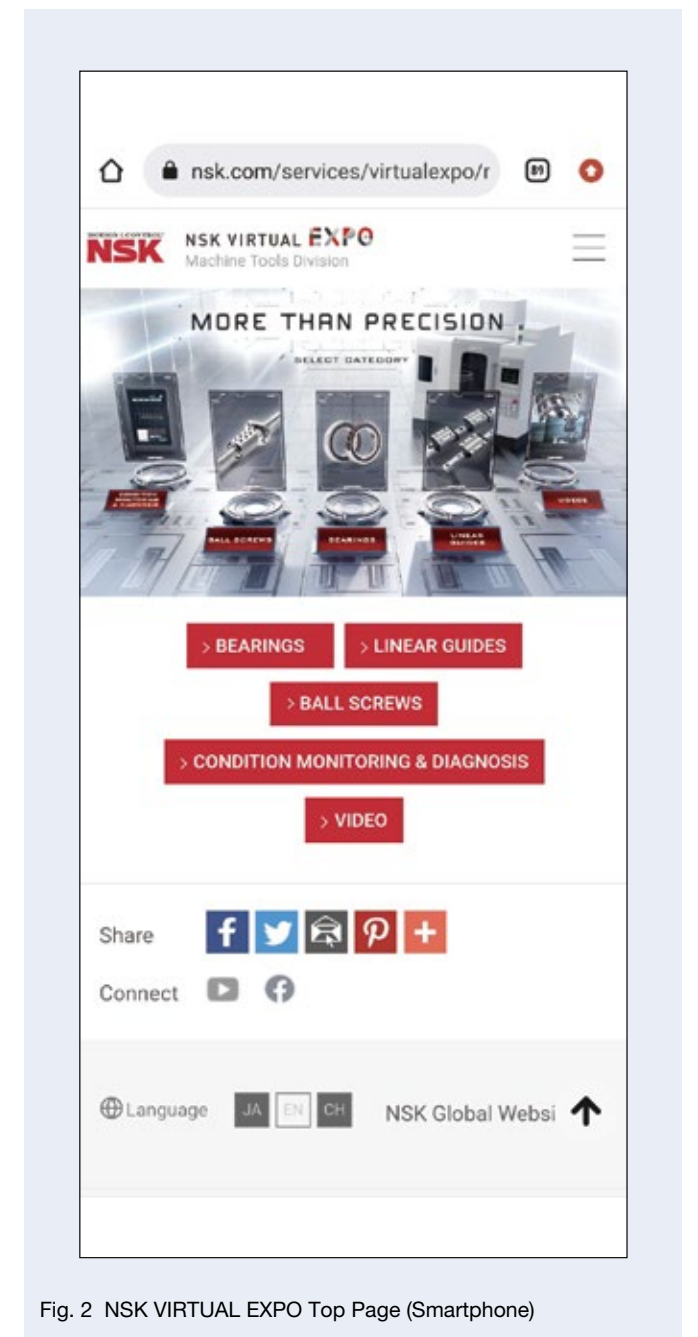


Fig. 2 NSK VIRTUAL EXPO Top Page (Smartphone)

sector. As shown in Figure 3, a technical demonstration that brings together NSK's four core technologies: tribology, material technology, analysis technology, and mechatronics technology. The production technology that gives form to these core technologies is explained in an easy-to-understand manner through videos. It also includes a video introducing NSK's business and links to the NSK Motion And Control channel on YouTube, as shown in Figure 4.

This is a permanent exhibit, and registration is not required. The system is available in three languages: Japanese, English, and Chinese.

2.2 Categories

Figure 5 shows the NSK VIRTUAL EXPO category selection page. From left to right, the five categories are Condition Monitoring & Diagnosis, Ball Screws, Bearings, Linear Guides, and Videos. Selecting any of these will take

you to the page for that particular category.

Figure 6 shows a product line of precision roller bearings and ball screws (excerpts) as examples.

2.3 New product and technology introduction page

By clicking an option on the category selection page shown in Figure 5, the user is redirected to a page that introduces the new product, technology, or videos. This page offers a one-minute video with an overview of the product and its features, a narrated description, and figures and tables so that visitors can develop an understanding of the new products and technologies in a short period of time.

Figure 7 shows an example of one of the new product introduction pages.



Fig. 3 Technology demonstration video

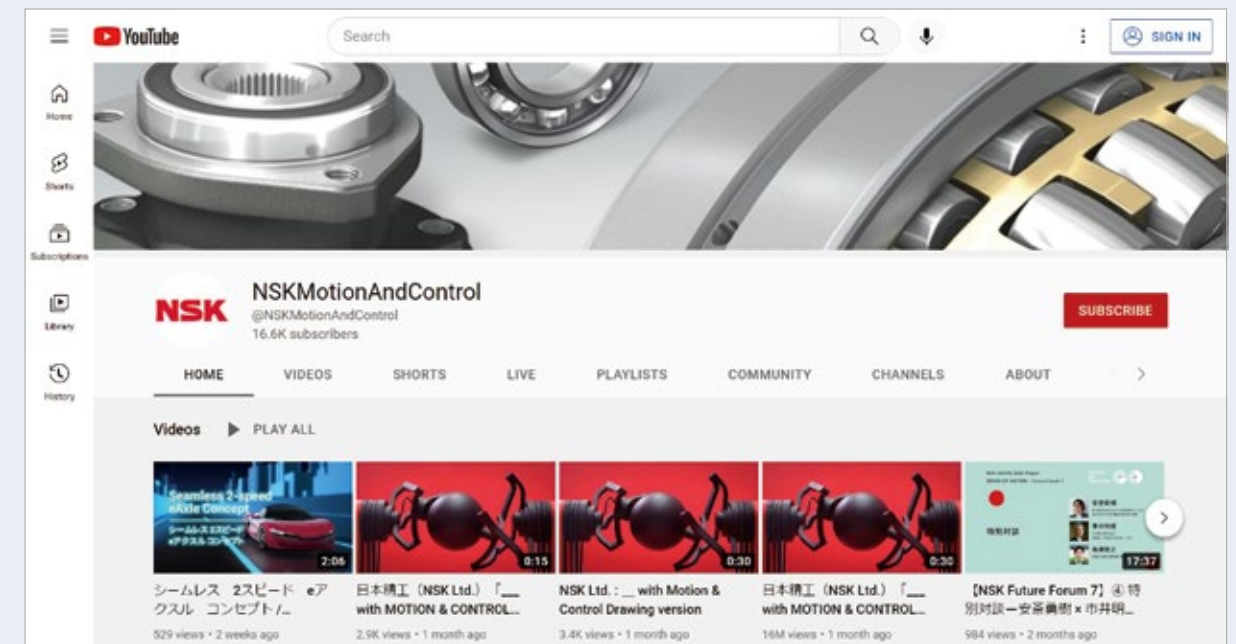


Fig. 4 YouTube NSK Motion and Control Channel



Fig. 5 Category selection page

3. Afterword

In April 2020, a state of emergency was declared due to the spread of Covid-19. The Tokyo 2020 Olympics was postponed to the following year, and JIMTOF 2020, Japan's largest machine tool trade fair, was instead held in November 2020 as an online exhibition, or JIMTOF 2020 Online. In an environment where face-to-face business meetings and technical exchanges have become difficult, NSK is seeking new ways to interact with customers and established the NSK VIRTUAL

EXPO to introduce and accurately explain new products and technologies to customers. While the surrounding environment continues to change, at times even beyond our expectations, we will continue to update the NSK VIRTUAL EXPO and publish informative articles for our customers on the site while also providing a forum through which we can identify their needs and challenges in a timely manner, find solutions in terms of new products and technologies, and hold discussions for future developments.

The grid contains the following product listings:

- Ball Screw Technology of Reducing Machine Tool Quadrant Glitches:** Reduced frictional variation when the ball screw reverses direction of motion thereby enabling higher surface finish quality.
- High Durability Precision Ball Screw:** Surface processing technology reduces wear. Maintenance-free for longer periods.
- ROBUSTDYNA™ High Load Capacity Ultra High Speed Angular Contact Ball Bearings:** ROBUSTDYNA bearings support both heavy cutting and ultra-high speed rotation, helping spindles operate stably over long periods.
- Pneumatic Shaft Deflection Sensor System:** Non-contact, high-accuracy shaft deflection sensor system. Compressed air is used for measurement, requiring no wiring in the spindle.
- High-Speed Low-Noise Ball Screws:** NSK technology achieves high speed, low noise performance with a compact design.
- Ball Screw with X1 Seal:** Achieves both high dust resistance and high grease retention thereby improving machinery reliability.
- Ultra High Speed Angular Contact Ball Bearings with SURSAVE™ Cage:** Reduced NRR0 by optimizing guide and pocket clearance. Reduced torque by optimizing cage design.
- High-Load Capacity Spindle with Built-in Motor:** Delivers both high speed operation and high load capacity. Grease lubricated design reduces energy consumption.

Fig. 6 Excerpt of product listings for super precision bearings and ball screws

Ball Screws for Next-Generation High-Accuracy Machine Tools

NSK Ball Screw Quadrant Glitch Reduction Technology

NSK developed a new ball screw design to address quadrant glitch motion errors.

MORE THAN PRECISION

Reduced frictional variation when the ball screw reverses direction of motion thereby enabling higher surface finish quality.

All new NSK technology reduces frictional variation when the ball screw reverses direction of motion. This significantly reduces motion errors called quadrant glitches thereby increasing surface finish quality.

Press Release

Features

- 1 Stable torque when the ball screw reverses direction nearly eliminates the peak 2 from quadrant glitches.
- 2 Up to 20% less dynamic frictional torque allows for better correction of the peak 1.
- 3 Mounting dimensions fully interchangeable with conventional products make for an easy upgrade in existing equipment.
- 4 Improved surface quality shortens finishing time and saves energy.

Effect of new technology

Motion error and torque changes when reversing direction

Conventional vs. New Product comparison showing reduced motion error and torque peaks.

Motion error during circulation interpolation machining

Enlarged view of machined surface (simulated)

Conventional vs. New Product comparison showing improved surface finish.

Fig. 7 Overview of ball screws for next-generation high-accuracy machine tools



Yoshinori Yano

Study on Simple Vibration Prediction Method for Permanent Magnet Synchronous Motors and Applications

Isamu Nitta

Technology Research and Development Office 3, Core Technology R&D Center

Abstract

Permanent magnet synchronous motors (PMSMs) are widely used across industries. In many applications, vibration must be suppressed to improve processing accuracy and comfort. Currently, magnetic-structural coupled analysis is used to reproduce vibration phenomena, but this is often used only as a countermeasure for defects. Therefore, we devised a simple vibration prediction method using a 1D vibration model.

Here, we explain the mechanism for this method and offer an applied example of vibration suppression through current control and adjustment of the magnetic circuit.

1. Preface

Due to their high-power density, permanent magnet synchronous motors (PMSMs) are widely used in automotive, home appliance, and industrial applications. PMSMs are also excellent in terms of sound and vibration. The actuator, combined with a PMSM and the mechanism, is used to manufacture devices and equipment that operate around people, such as service robots. Further vibration suppression has become a focus in these applications in the pursuit of improved machining accuracy and comfort.

Currently, magnetic field-structure coupled analysis is used to reproduce vibration phenomena. However, while these methods provide vibration values, they do not address why such vibrations occur. Therefore, the analysis mentioned above is often used only for addressing defects.

Accordingly, a simple vibration prediction method using a 1D vibration model was devised. Here, we explain the mechanism revealed by the method and its application to control design and magnetic circuit design.

2. Motor Vibration and Previous Means of Examination

2.1 Forced vibration

There are two types of vibration generated by motors. One is caused by uneven rotation of the rotation axis, a phenomenon that excites an object connected to the rotation axis by accelerating or decelerating rotation. This phenomenon has been extensively studied and will not be covered in this article.

The other is vibration, in which the motor is deformed largely in the radial direction, as shown in Figure 1, and is behind the research discussed in this article.

This phenomenon in a PMSM is called forced vibration because the excitation force changes periodically as the motor rotates, and the amount of deformation changes accordingly. This forced vibration shakes the actuator by vibrating the object to which the motor case is fixed and the surrounding air, which generates noise that must be suppressed.

In the time dimension, periodicity appears at the rotation angle of one revolution or two poles of a permanent magnet. The former is called the rotation order, and the latter is called the electric angular order.

Periodicity also appears in spatial dimensions. For example, the deformation in Figure 1 shows that the motor cylindrical cross-section is deformed into a star shape with four ridges and two ridges (visually a quadrilateral and an ellipse). This periodicity is called the deformation mode, and since motors are generally circular in shape, it

is known as the circular mode. Note that the circular mode also has an order corresponding to the number of ridges (the 0th order, however, is a deformation of similarity, and the first order is a deformation of translation). Furthermore, since the deformation rotates spatially, we define the case of transitions in the rotor's rotation direction as a positive circular mode order and the opposite transition as a negative circular mode order.

Defining the circular mode order in this way, the forced vibrations of a PMSM can be understood to be deformations of multiple circular mode order orders co-occurring at each time frequency.

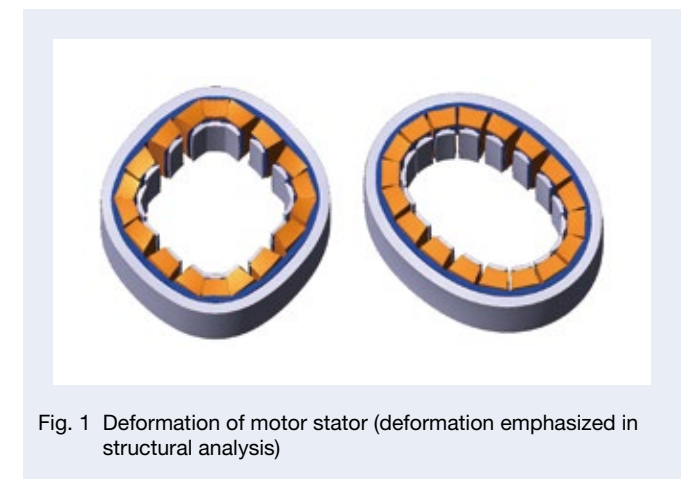


Fig. 1 Deformation of motor stator (deformation emphasized in structural analysis)

2.2 Excitation forces acting on the PMSM stator core

With a few exceptions, PMSMs are of the adduction type with the rotor on the inner circumference. In these forms, the cause of motor case deformation is the electromagnetic excitation force acting on the stator core. Figure 2 shows the cross-section of a PMSM and the distribution of excitation forces acting on the stator core. As shown on the right side of Figure 2, the excitation force is distributed at the tip of the salient pole protruding from the inner circumference of the core. Since there is no exact solution for vibration in a system where the excitation force is distributed in three dimensions, it is customary to calculate vibration by structural analysis using the finite element method, which is a numerical analysis.

2.3 Advantages and disadvantages of structural analysis

Structural analysis software is widely available on the market, and highly accurate results can be expected if the data for physical properties, constraints, and other conditions can be prepared. An additional advantage is that there are no restrictions on shape. There are two significant drawbacks. The first is that it does not show the intermediate stage between the input stage of the distribution of the excitation force and the output stage of the vibration values such as acceleration and displacement. This makes it difficult for users to understand the vibration mechanism and

leads them to rely on their experience and intuition when formulating improvement plans. The second is that the analysis process demands a substantial amount of time. For example, it takes more than one hour in our environment, even when limited to one design proposal and one rotational speed. This is because, in addition to treating three dimensions as space, the vibration must also be treated in terms of time, and hundreds of vibration frequencies must be addressed. This required time is acceptable to predict the vibration value of one narrowed-down case. However, it becomes a significant problem when control of hundreds or thousands of iterations is required using the current waveform as a parameter or to optimize the magnetic circuit for better design. Therefore, structural analysis is unsuitable for many trials and often not used for the application.

3. Simplified Vibration Prediction Method

3.1 Previous simplified prediction methods for vibration

Considering the structural analysis described in the second section of this article, simple methods¹⁾ have been proposed to study vibration. These methods use a 1D model of excitation force density, in which the magnetic flux density of the void surface is used to create a ring distribution in 3D space with no cross-sectional area.

As a precondition for these methods, the circumferential stiffness of the structure should be uniform. For example, if the outer shape of the motor case is rectangular, an error will occur.

Now, in the conventional method, the equation of motion of the motor core is defined as in equation (1) for each frequency component in the time and circular mode dimensions.

$$m \left(\frac{d^2 r_i}{dt^2} + \omega_i^2 r_i \right) = \pi (B_{ci} - h_j B_{si}) g \quad \dots\dots\dots (1)$$

$$h = \begin{cases} 1 : \left(0 < i \leq \frac{u}{2} \right) \\ -1 : \left(i = 0, \frac{u}{2} < i \leq u \right) \end{cases}$$

$$g = \cos \omega' t \text{ (in the case of harmonic excitation)}$$

Where u is the number of salient poles, i is the order of the circular mode, m is the total weight of the stator, r is the radial displacement of the stator circumference, the subscript is the circular mode order, ω is the eigenvalue angular velocity (2π times the frequency) of the subscript circular mode order, ω' is the angular velocity of the excitation force, B is the amplitude of the radial component of the excitation force density, subscript c is the cos component, s is the sin component, and j is the imaginary unit. The excitation force is defined as a periodic function whose fundamental wave is one cycle of the electric angle (the angle of rotation of two magnetic poles) in the time dimension and one revolution of the machine angle in the circular mode (spatial) dimension.

Equation (1) shows that vibration values such as displacement and acceleration are affected by the excitation force distribution in the circular mode dimension but are not interfered with when broken down into frequency components.

The frequency component of the excitation force density is calculated from the void magnetic flux density. However, there is a high hurdle to overcome with this model in terms of applying the void surface's excitation force density to vibration calculations. This is because the circular mode order of the void excitation force density differs from that of the excitation force distribution acting on the yoke portion of the stator core and the motor case, where the deformation occurs and a transformation is required. Details are described in 3.3.

3.2 Overview of original methodology (VMFS)

To avoid the problems of the conventional method, our original method regards the stator core as an assembly of blocks divided into one per salient pole, as shown in Figure 3. The excitation force is not the excitation force density of the void but rather the electromagnetic

force acting on the block itself. We therefore call it the "vibration prediction method using excitation force acting on salient poles" (VMFS).

Using sampled electromagnetic forces, which are vector composites of the electromagnetic forces acting on the blocks, enabled eliminating the influence of the salient pole shape. The number of spatial data is drastically reduced to the number of salient poles. This offers two advantages. The first is that treating only low circular mode order components as excitation forces makes them easy to grasp. The second advantage is the remarkably small computational workload.

To illustrate this, the VMFS system overview and data flow are shown in the figure. Roughly speaking, the sampled electromagnetic force is transformed into an excitation force matrix in the frequency domain by a complex 2D Fourier transform to rotational and circular mode orders. The vibration value matrix is obtained by the Hadamard product of the excitation force matrix and the transformation coefficient matrix obtained in advance. This is converted back to vibration values in the time domain by a real 2D inverse Fourier transform.

In Hadamard products, other terms in the matrix do not interfere. Forward and inverse Fourier transforms involve iterative calculations. However, the amount of data is very small because it is the product of the number of salient poles and the time resolution. The number of calculations can thus be dramatically reduced compared to the solution of simultaneous equations with millions of unknowns used in structural analysis. A comparison of actual computation times is presented in section 4.

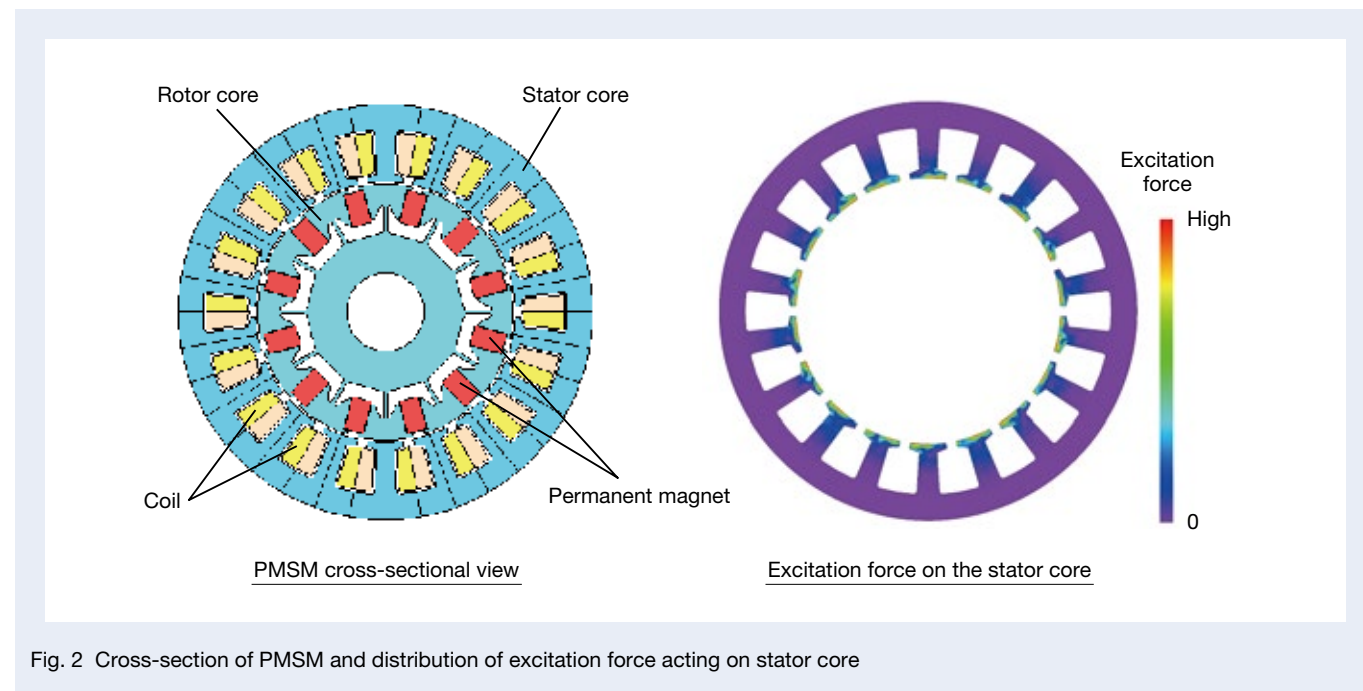


Fig. 2 Cross-section of PMSM and distribution of excitation force acting on stator core

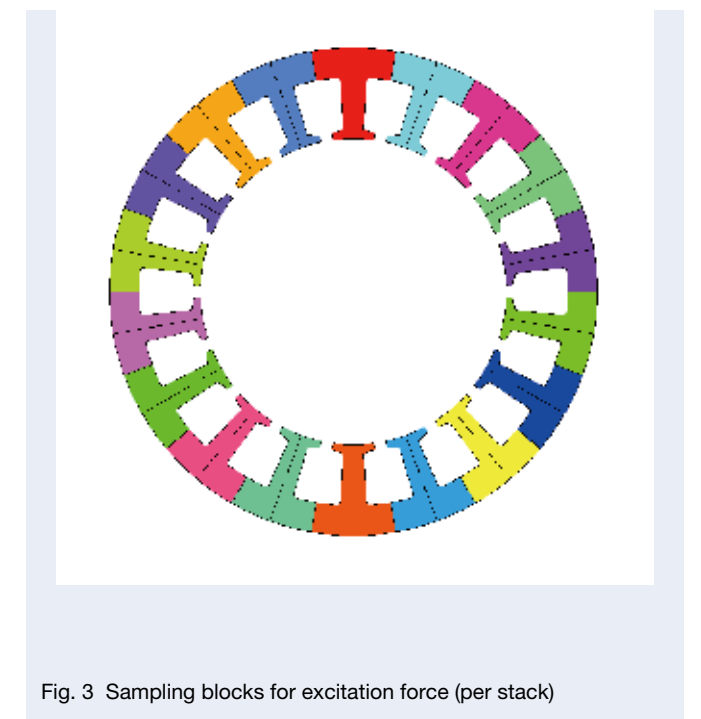


Fig. 3 Sampling blocks for excitation force (per stack)

3.3 Pros and cons of using the excitation force sampled per block

As shown in the previous section, VMFS uses sampled values for each block as the excitation force. Therefore, the range of possible circular mode orders i exists only in the equation (2) range from the sampling theorem, assuming that the number of salient poles is u .

$$-u/2 \leq i < u/2 \quad \dots\dots\dots (2)$$

So then, what about the real phenomenon? The magnetomotive force distribution of permanent magnets and coils, which determines the electromagnetic force of a PMSM, has a circular mode 9th-order component outside the range of equation (2). However, since the excitation force is concentrated at the salient stator pole, it is transformed according to equation (3). The circular mode order of the excitation force is still within the range of equation (2).

$$i = \begin{cases} n \bmod u : (n \bmod u < u/2) \\ (n \bmod u) - u : (n \bmod u \geq u/2) \end{cases} \quad \dots\dots\dots (3)$$

Here, mod is the modulo operator.

Equation (3) is the same as the aliasing phenomenon in communications engineering (generating a folded imaginary image due to a low sampling rate). The magnetomotive and excitation forces are also called alias transformations.

Here, $i < 0$ for the case below equation (3), which indicates that the excitation force distribution rotates in the opposite direction.

To illustrate with an actual example, Figure 4 shows the magnetic field analysis results of a 12-magnetic pole, 18-salient pole motor, where the colors in the figure indicate the absolute value distribution of the magnetic flux density. The square distribution of the magnetomotive force is the smallest, with a circular mode order of $n = 12$,

because of the 12 magnetic poles. The circular mode period of the excitation force distribution is six cycles, as seen in the color distribution in Figure 4, indicating that the circular mode order is -6 because it rotates in the opposite direction to the rotor. This corresponds to the case below in equation (3) and is calculated as follows.

$$i = (n \bmod u) - u = (12 \bmod 18) - 18 = 12 - 18 = -6$$

Therefore, at least on circular mode order surfaces, it is acceptable to use excitation forces that sample one salient pole as a block. Furthermore, the excitation force distribution is consistent with n cycles of excitation force variation per rotor revolution since there are $|n/i|$ rotations per rotor revolution.

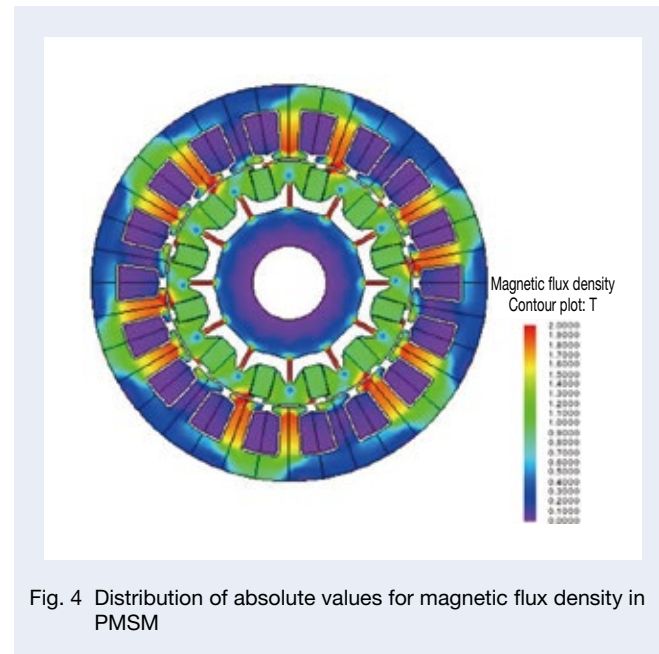


Fig. 4 Distribution of absolute values for magnetic flux density in PMSM

3.4 Equations of motion and conversion coefficients for VMFS

The VMFS system and data flow are shown in Figure 5. The figure shows that the main processing is the forward and inverse Fourier transform and Hadamard product, allowing for the use of the existing general computation algorithms. The calculation method of the conversion coefficients is explained in steps, starting with the equation of motion.

In VMFS, instead of the excitation force density, F is used, which is the value obtained by frequency-decomposing the excitation force for each salient pole by time frequency and by circular mode order, so equation (1) is rewritten as equation (4). Since the circular mode order i is folded back into the range of equation (2) due to the aliasing phenomenon, there is no need to separate the case by h .

$$\begin{aligned} \delta_{im} \left(\frac{d^2 r_i}{dt^2} + \omega_{0i}^2 r_i \right) &= \pi F \\ &= \pi (F_{ci} - jF_{si}) g \quad \dots\dots\dots (4) \end{aligned}$$

Here, the subscript c denotes the cos component, and s is the sin component. To use the excitation force for each salient pole, a different coefficient δ is introduced into the left-hand side for each circular mode order i for correction.

The displacement, which is a special solution of equation (4) after sufficient time has elapsed, becomes equation (5), and the acceleration becomes equation (6). To avoid singularities in the vibration values of the eigenvalues ω_{0i} , D and phase ϕ derived from the damping coefficient ζ are introduced.

$$r_i = \text{Special solution} = \frac{\pi F}{\delta_{im} \omega_{0i}^2} D e^{j\phi} \quad \dots\dots\dots (5)$$

$$\frac{d^2 r_i}{dt^2} = \frac{\pi \omega'^2 F}{\delta_{im} \omega_{0i}^2} D e^{j\phi} \quad \dots\dots\dots (6)$$

$$D_i = \frac{1}{\sqrt{\left(1 - \frac{\omega'^2}{\omega_{0i}^2}\right)^2 + \left\{2\zeta \frac{\omega'}{\omega_{0i}}\right\}^2}}$$

$$\phi_i = \tan^{-1} \frac{2\zeta \frac{\omega'}{\omega_{0i}}}{1 - \frac{\omega'^2}{\omega_{0i}^2}}$$

The compliance and inertance, the conversion coefficients, are equations (7) and (8), respectively.

$$\text{Compliance}_i = \frac{r_i}{F} = \frac{\pi}{\delta_{im} \omega_{0i}^2} D_i e^{j\phi_i} \quad \dots\dots\dots (7)$$

$$\text{Inertance}_i = \frac{d^2 r_i}{F dt^2} = \frac{\pi \omega'^2}{\delta_{im} \omega_{0i}^2} D_i e^{j\phi_i} \quad \dots\dots\dots (8)$$

Note that δ_{im} is generally unknown but can be transformed, as in equation (9), by taking the low-frequency limit $\lim_{\omega' \rightarrow 0} r$ of the displacement r .

$$\begin{aligned} \lim_{\omega' \rightarrow 0} r_i &= - \lim_{\omega' \rightarrow 0} \frac{\pi F}{\delta_{im} \omega_{0i}^2} D_i e^{j\phi_i} = \frac{\pi F}{\delta_{im} \omega_{0i}^2} \\ \delta_{im} &= \frac{\pi F}{\omega_{0i}^2 \lim_{\omega' \rightarrow 0} r_i} \quad \dots\dots\dots (9) \end{aligned}$$

Since the $\lim_{\omega' \rightarrow 0} r_i$ can be substituted with the results of structural analysis at frequencies sufficiently smaller than the eigenvalues (frequency response analysis), δ_{im} can be calculated backward with a very small amount of calculation. The results of structural analysis (eigenvalue analysis) are used for each eigenvalue frequency.

The compliance and inertance obtained by this procedure are shown in Figures 6 and 7, respectively.

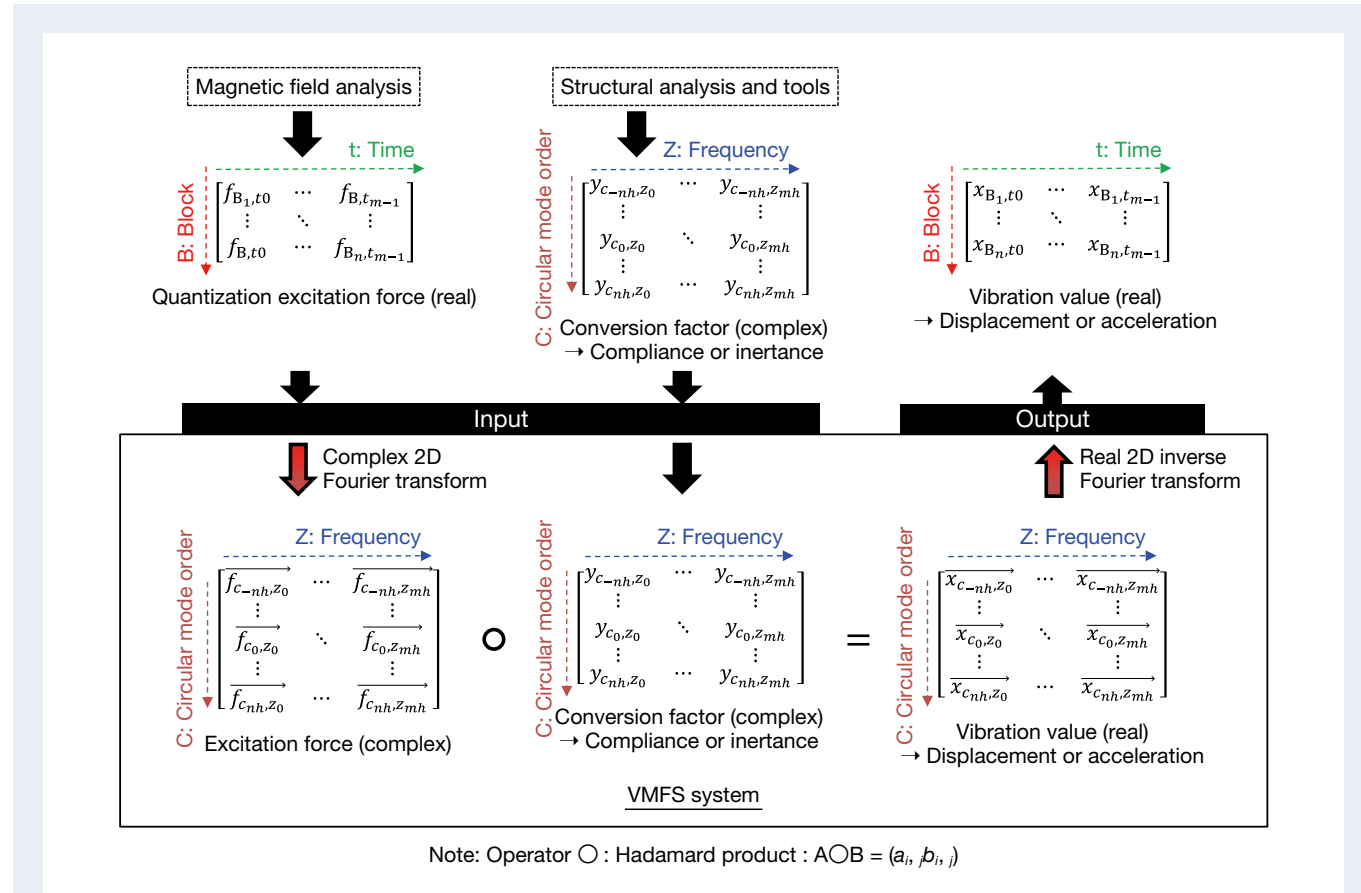


Fig. 5 VMFS system and data flow

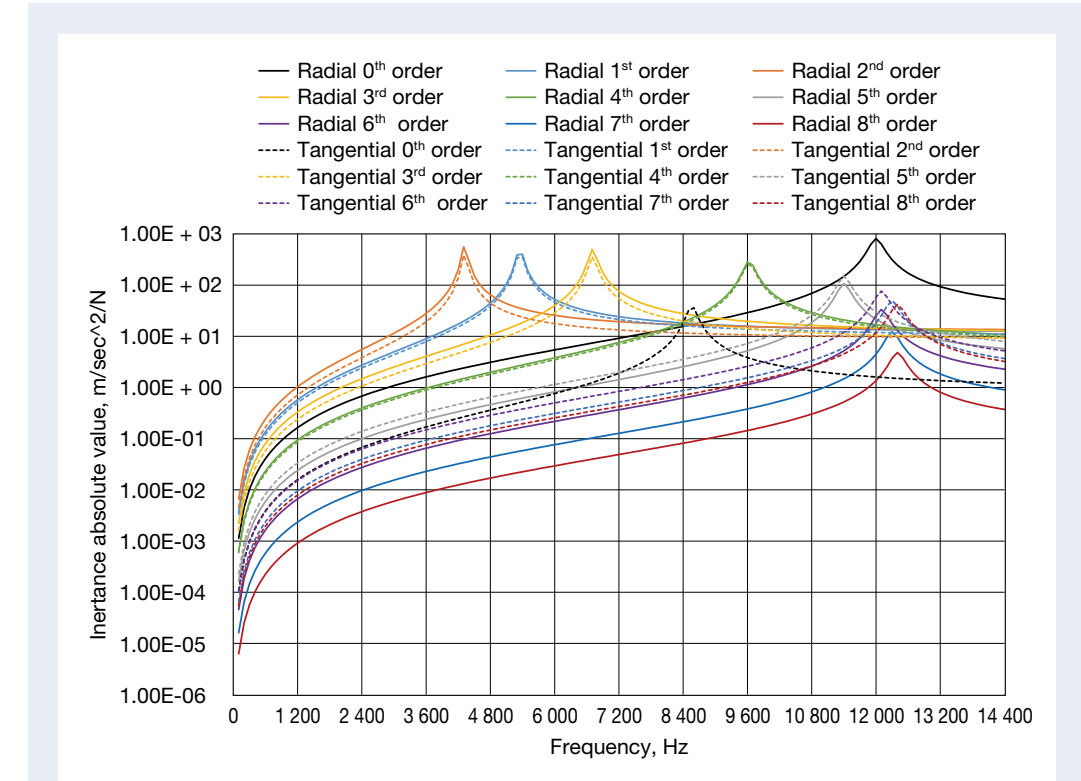


Fig. 7 Example of vibration conversion coefficient (inertance)

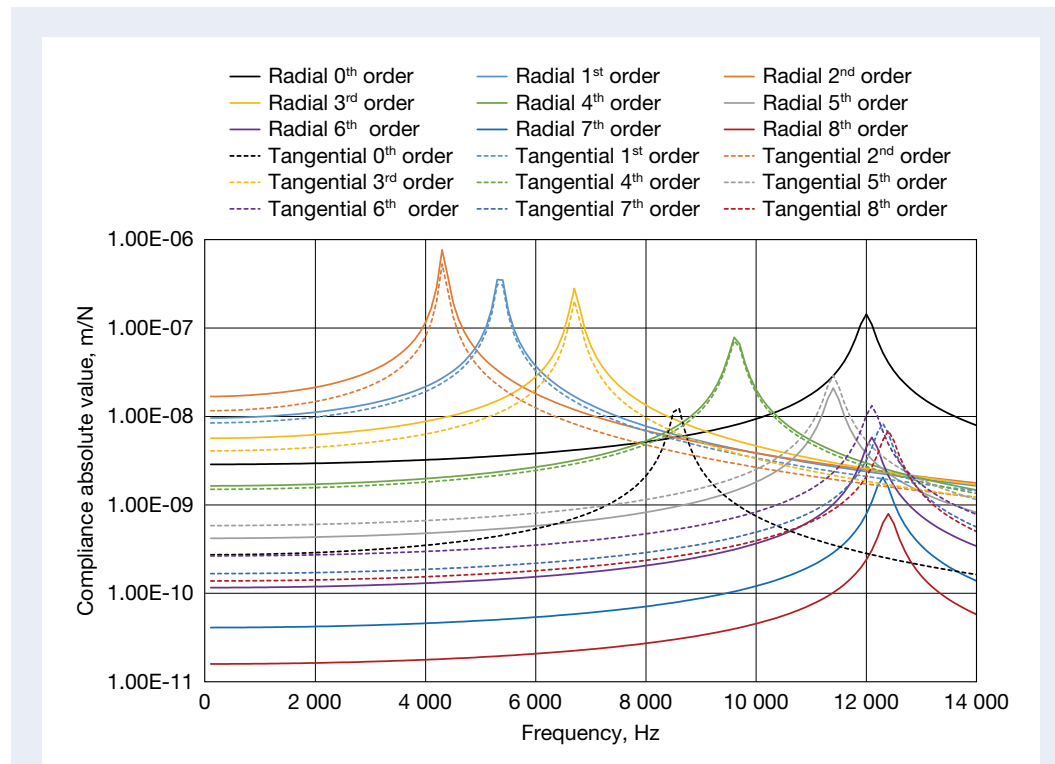


Fig. 6 Example of vibration conversion coefficient (compliance)

4 Accuracy of VMFS Calculations and Examples of Optimization

4.1 Accuracy of VMFS calculations

As a calculation result of VMFS, an example of the application to PMSM with 12 magnetic poles and 18 salient poles, shown in Figure 2, is provided. Figure 8 shows the time-domain excitation force for each block, Figure 9 shows the frequency decomposition results for each circular mode order, and Figure 10 shows the radial component circular mode maximum and time rms of the acceleration. The inertance is the value shown in Figure 7. The rotor speed is 1 000 rpm.

The motor has multiple configurations of two magnetic poles and three salient poles. The excitation force is

dominated by multiple-order components of the 0th and 12th orders of rotation (time frequency every 200 Hz). Circular mode orders correspond to the 0th, -6th, and 6th orders. The excitation force at every 200 Hz decreases gradually, as shown in the figure. The figure also shows that the vibration acceleration is outstanding every 600 Hz because the inertance of the circular mode 0th order is more than ten times greater than that of the 6th circular mode order and the circular mode -6th order. Thus, with VMFS, the excitation force, conversion factor, and vibration values are all available as quantitative values in a 1D model, facilitating an understanding of the vibration mechanism.

Figure 10 compares the results of the acceleration calculations with VMFS with those of the structural analysis. The overall accuracy is good, proving the effectiveness of VMFS.

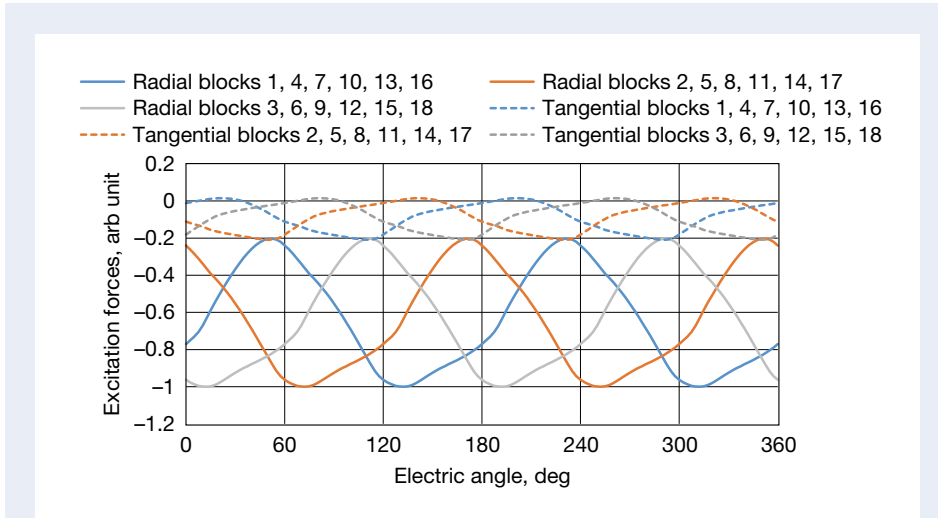


Fig. 8 Excitation force of block samples

4.2 Examples of design optimization by VMFS

An example of optimizing the current control and rotor pole shape to suppress the torque ripple of the vibration value using VMFS is also provided in this article. The motor configuration is the same as in the previous section. The optimization parameters are summarized in Table 1.

The resulting overall trend of optimization, which converged at 25 generations and 570 individuals, is shown in Figure 11. A comparison of the initial and post-optimization vibration acceleration is shown in Figure 12. A clean response surface is shown, indicating that good optimization was achieved. At the selected optimized values, the 600 Hz vibration acceleration decreased from 1 to 0.183, as calculated by the structural analysis, and the torque ripple from 40% to 2.5%.

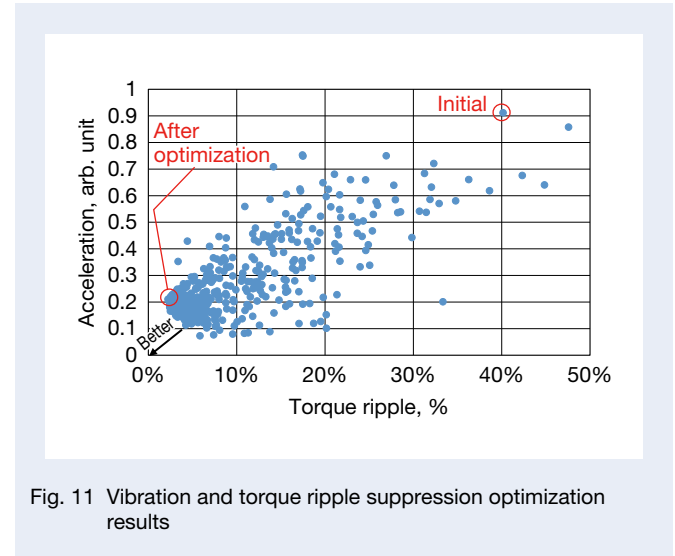


Fig. 11 Vibration and torque ripple suppression optimization results

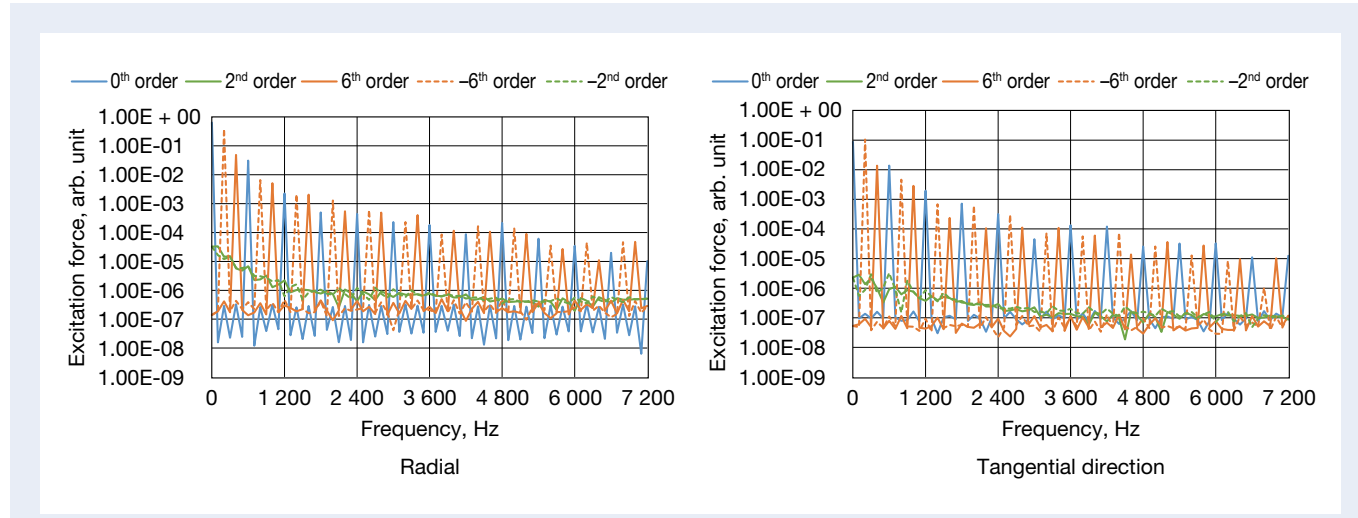


Fig. 9 2D Fourier transform results for excitation force of block samples

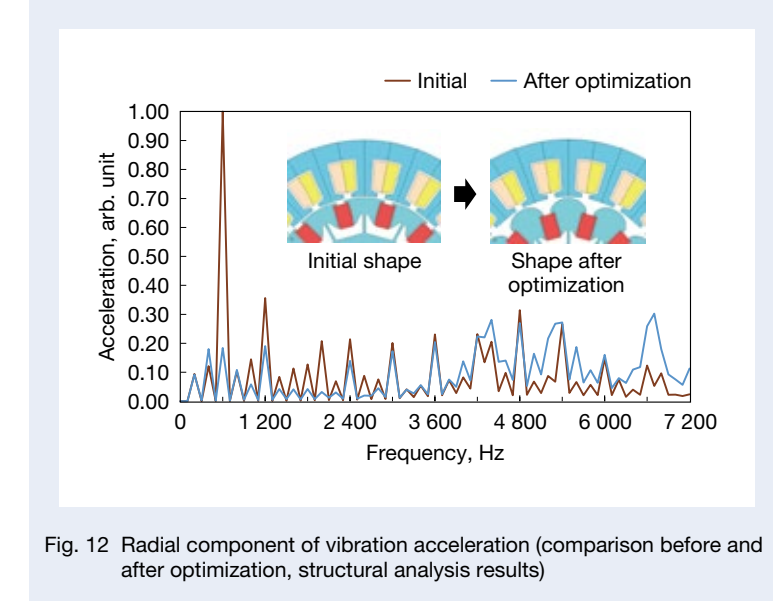


Fig. 12 Radial component of vibration acceleration (comparison before and after optimization, structural analysis results)

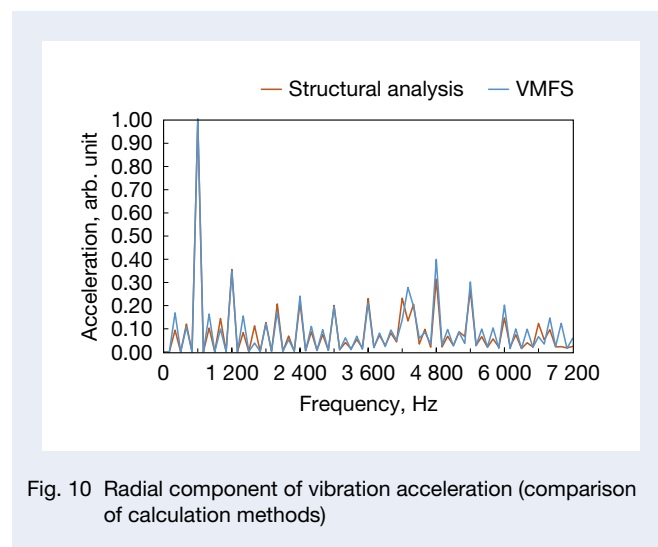


Fig. 10 Radial component of vibration acceleration (comparison of calculation methods)

Table 1 Specifications after optimization

Item	Description
Optimization algorithm	Multipurpose genetic algorithm (JMAG) Population: 20, Offspring: 15
Optimization objective function	Torque ripple value (desirably small item) 600 Hz vibration acceleration (desirably small item)
Optimization criteria	4 300 Hz (circular mode 2 nd order eigenvalue) vibration acceleration Multiple frequency vibration acceleration of 600 Hz Do not increase as much as possible from the initial value state
Optimization parameters	dq axis 6 th -order current (less than or equal to 10% of fundamental) Rotor salient shape (3 tangent cylindrical surface curvature)

4.3 Calculation time for VMFS

The computing environment in the previous section is an Intel(R) Xeon(R) CPU E5-2690 v4 @ 2.60 GHz with 14 cores. JMAG V20.2 was used for magnetic field analysis, structural analysis, and the optimization engine. VMFS is called from the JMAG response value script. The angular increments for magnetic field analysis are 144 divisions of one magnetic pole pair (machine angle of 60 degrees). The computation time for one case is about 180 seconds for magnetic field analysis and less than 2 seconds for VMFS with script turnaround. The optimization of the previous section was completed in approximately 29 hours.

For reference, a structural analysis similar to VMFS took about 4 800 seconds.

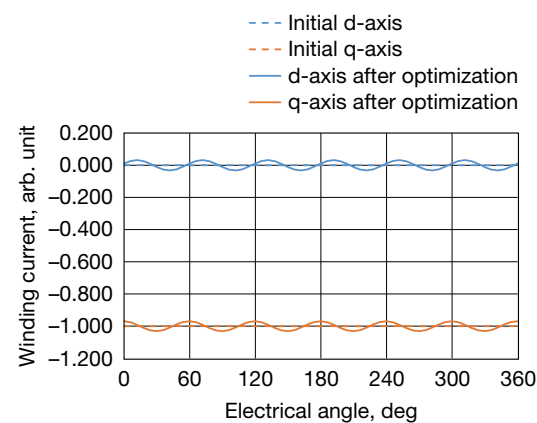


Fig. 13 Winding current dq axis waveform (before and after optimization)

5. Afterword

In this article, we have shown that, in regard to VMFS, a simple calculation method for forced vibration that can be used in a PMSM, it is easy to understand the concept and features of the vibration mechanism and also that it is effective in practical use for design optimization. In the optimization examples, we introduced examples of the combined use of control design and magnetic circuit design. It is also possible to use it, for example, for current control alone, and it can be applied in a wide range of development stages. We will further promote the use of this technology and enhance our design knowledge to break through the situation in which motor sound and vibration design are postponed to other processes or considered as a verification of the results of actual equipment measurements.

Reference

- 1) Suzuki Shohei, et al., "Study of Electromagnetic Resonance Conditions in Interior Permanent Magnet Synchronous Motor (IPMSM)," *Meiden Review*, Series No. 182, No. 2 (2021), pp. 2–7.



Isamu Nitta

Establishment of an Integrated Automated Embryonic Manipulation System for Producing Genetically Modified Mice

Hiroki Ueda

New Field Products Development Center, Technology Development Department 1

Tomoo Eto

Central Institute for Experimental Animals

Nobuaki Tanaka

New Field Products Development Center, Technology Development Department 1

Abstract

Genetically modified mice are commonly used in biologic, medical, and drug discovery research, but conventional microinjection methods used for genetic modification require extensive training and practical experience. Here we present a fully automated system for microinjection into the pronucleus to facilitate genetic modification. We first developed software that automatically controls the microinjection system hardware. The software permits automatic rotation of the zygote to move the pronucleus to the injection pipette insertion position. We also developed software that recognizes the pronucleus in three-dimensional coordinates so that the injection pipette can be automatically inserted into the pronucleus, and achieved a 94% insertion rate by linking the two pieces of software. Next, we determined the optimal solution injection conditions (30 hPa, 0.8–2.0 s) by examining the survival rate of injected zygotes. Finally, we produced transgenic (traditional DNA injection and piggyBac Transposon system) and knock-in (genomic editing) mice using our newly developed Integrated Automated Embryo Manipulation System (IAEMS). We propose that the IAEMS will simplify highly reproducible pronuclear stage zygote microinjection procedures.

Reprinted with permission from Springer Nature and the Central Institute for Experimental Animals, from *Scientific Reports*, 11 (2021) 11770.

1. Introduction

Genetically modified mice are widely used in broad areas of biologic, medical, and drug discovery research^{1–4}. Genetic modification of mammals was first reported in 1980 using mice⁵. Since then, several methods, such as transposon methods^{6, 7}, have been developed to improve the efficiency of producing transgenic mice. The advent of genome-editing technologies has additionally revolutionized the generation of genetically engineered mice. For example, gene targeting⁸ and knock-in^{9, 10} methods previously performed in embryonic stem cells are now performed in zygotes via genome editing. Various methods are used for genetic modification in mice, such as manual injection of a solution into the pronucleus of the mouse zygote. This method was used to perform the first

genetic modification⁵ of mammals and is widely applied in many laboratories. Current microinjection techniques, however, require extensive training because the hardware must be manually operated in a complicated manner, even when injecting a solution into only one zygote¹¹. In addition, mastering microinjection techniques requires years of experience¹². Although electric injectors and electric joysticks have been developed to assist with the manual operations^{13, 14}, the most critical steps of the microinjection still depend on manual operation (i.e., determining the zygote holding site, adjusting the focus on the zygote, selecting the injection site, and injecting the correct volume). Therefore, microinjection is a painstaking technique that is applied to one zygote at a time by only highly skilled microinjectionists¹².

In the present study, we designed a fully automated method for injecting a solution into the zygote pronucleus that makes genetic modifications by microinjection easy and highly reproducible. First, we identified the sequence of actions required for fully automated operation and developed hardware that combines multiple machines. We then designed new software to operate the hardware. Finally, we developed the Integrated Automated Embryonic Manipulation System (IAEMS), which integrates the newly developed hardware and software, and demonstrated the usefulness of the IAEMS for producing genetically modified mice.

2. Results

2.1 Sequences, hardware, basic software for automated injection

In this study, we first designed the sequence required to achieve fully automated solution injection (Figure. 1). The sequence comprises a series of operations, such as immobilizing the zygote, focusing on the pronucleus, injecting the solution, and releasing the zygote. Thus, injection is performed automatically after manually transferring several zygotes to the injection medium drop. Next, to realize the sequence, we developed hardware that incorporates the electric manipulation system (EMS) and electric injector that we previously developed into a microscope (Figure. 2). Currently existing manual microinjection systems are equipped with a manipulator that moves the pipette in three dimensions, a sample stage that moves the zygote in two dimensions, and a pump for solution injection. For the microinjection system to be fully automatic, all devices must be driven electrically and in tandem. The currently existing manual microinjection devices cannot support full automation; for automation, all devices must be powered and the EMS is used to control the devices with the controller and electric distribution board. Further, for accuracy, each device needs to make the fine movements required to perform microinjection; all EMS devices have the ability to perform the necessary fine movements (Table. 1). In addition, the software installed in the EMS automatically detects the zygote position (Figure. 3), moves the pipette near the non-injected zygote, and moves the injected zygote to the release area (Figure. 4).

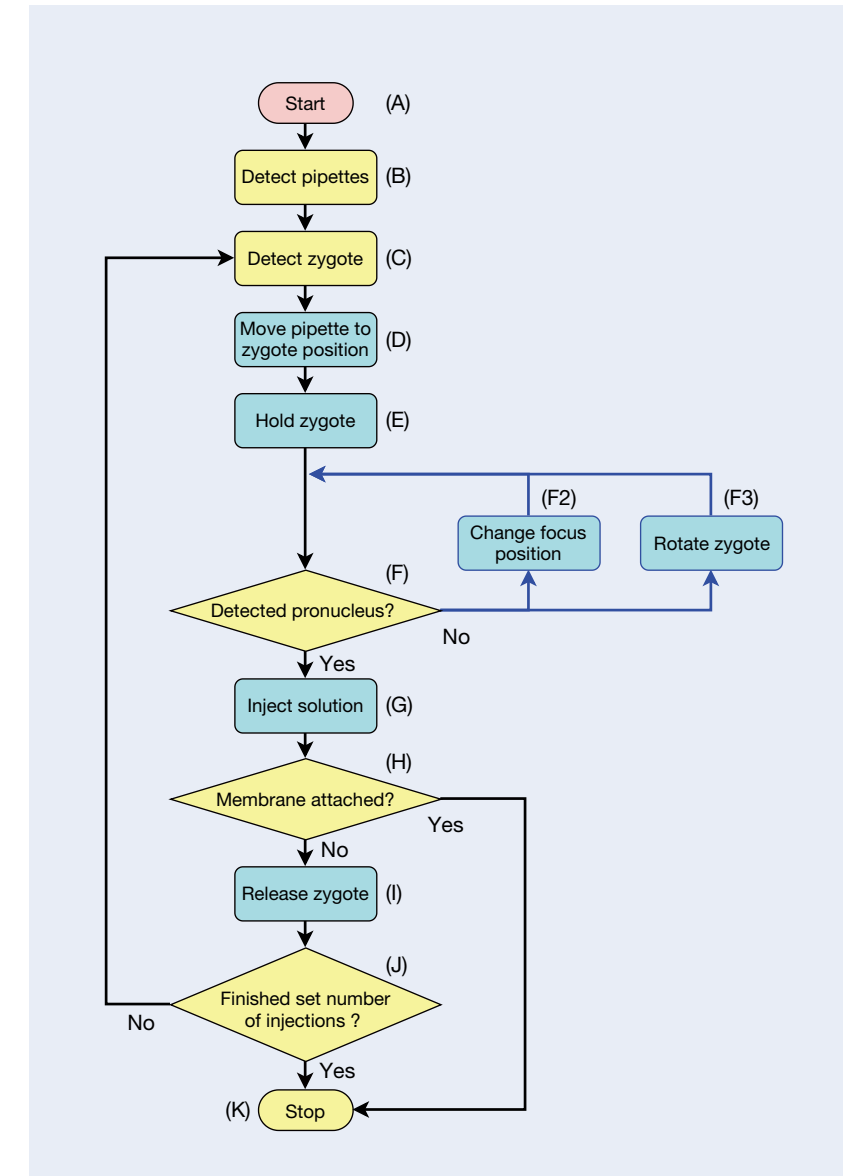


Fig. 1 Flowchart required for fully automated solution injection

The sequence involves detection of the injection target and judgment of the work at each step (yellow), and then execution of the work (blue). (A) Command the controller (Computer) to start the fully automated operation. (B) Detect the coordinates of the current positions of the pipettes. (C) Detect the zygote position. (D) Move the pipette to the zygote position. (E) Hold the zygote in the holding pipette and release the zygote once to adjust the holding pressure. (F) Detect the current position of the pronucleus. If the pronucleus cannot be detected, change the height of the holding pipette while holding the zygote (F2), and then re-detect the pronucleus (F). If the pronucleus is not detected after performing sequence F2 multiple times, use an injection pipette to rotate the zygote vertically (F3) and then re-detect the pronucleus (F). (G) Insert the injection pipette into the pronucleus. (H) If, after injection of the solution, the nuclear membrane adheres to the injection pipette and does not come off, then stop the procedure (K). Remove the nuclear membrane from the injection pipette and restart (A). (I) Move the zygote to the release area and release the zygote. (J) Check whether the injection has been performed on all zygotes. If an injection zygote remains that has not been injected, return to sequence C and continue injecting. (K) After injecting the solution into all available zygotes, stop the fully automated injection process.

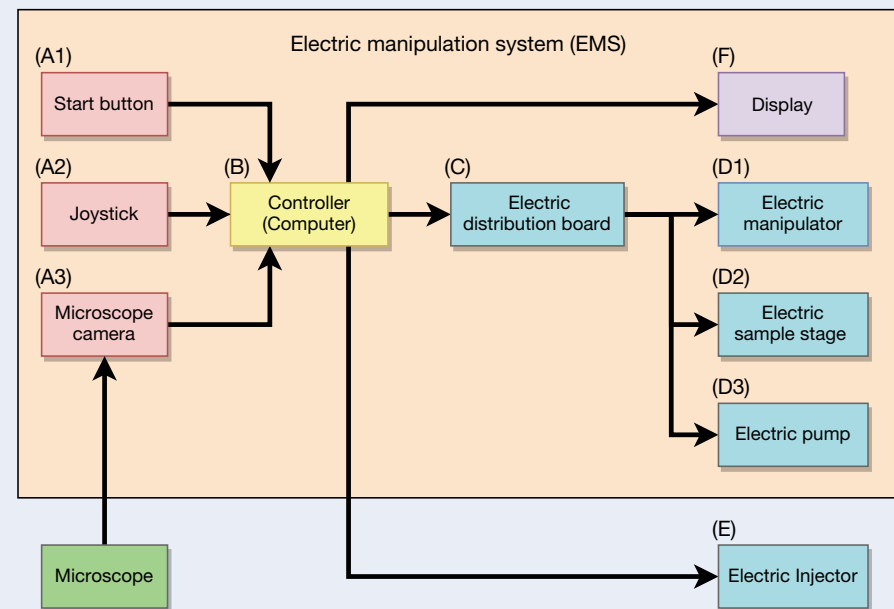


Fig. 2 Hardware

The hardware was created by connecting an electric injector to an electric manipulation system, and comprises 3 main elements: input device (red), controller (yellow), and output device (blue). In the hardware, when the signal is input from the outside (A), the controller analyzes the signal (B), the electric distribution board controls multiple machines according to the analyzed data (C) and operates multiple electric machines (D, E). (D) The electric manipulator moves the pipettes 3-dimensionally (D1), the electric sample stage moves the dish containing the zygotes 2-dimensionally (D2), and the electric pump increases or decreases the holding pressure in the holding pipette (D3). (E) The electric injector injects the solution by applying the injection pressure for the amount of time that was previously set in the controller. Only the electric injector (E) operates with a serial communication from the controller (B). In a fully automated operation, when the start button (A1) signal is input to the controller, multiple machines (D, E) operate electrically based on the microscope image acquired by the microscope camera (A3). In manual mode, the operator manually operates the joystick (A2) while looking at the display (F) to enter operational commands into the controller (B) to electrically operate multiple machines (manipulator (D1), sample stage (D2), and pump (D3)). In addition, in solution injection, the operator manually inputs the operation signal directly to the electric injector (E).

Table 1 Specifications of the electric manipulation system (EMS) device

Specifications	Electric manipulator	Electric sample stage	Electric pump
Stroke	20 mm		1 179.09 μl
Resolution	0.1 μm		0.0039 $\mu\text{l}/\text{step}$
Maximum velocity	5 mm/s		5 s^{-1}
Driving method	5-phase stepping motor		

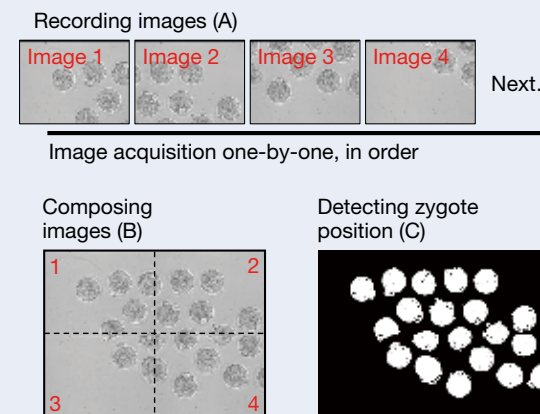


Fig. 3 Zygote position detection by the image processing function in the EMS software

(A) Record the microscopic images of the predefined area where the zygotes are placed in the order shown (red numbers). (B) Combine the acquired images to generate image data that enables detection over a wide area. (In this case, 4 images are combined.) (C) Binarize the generated image and detect a particle object as a zygote.

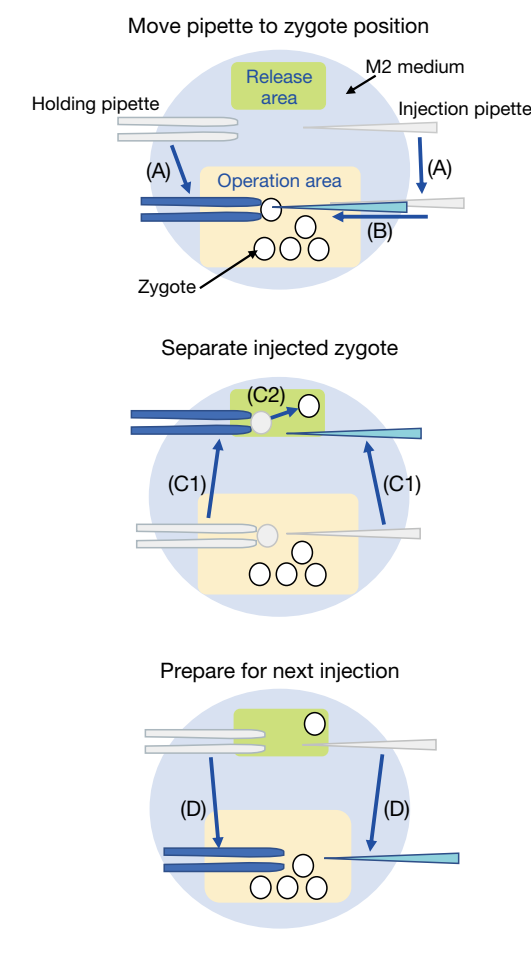


Fig. 4 Sequencing functions in the EMS software

The EMS can perform any sequence of operations by sending movement commands to the electric manipulators. This function can be used to move the pipette near the zygote, or to set up operation and release areas, and automatically move between each area to prevent mixing of injected and non-injected zygotes. (A) Move the pipette near to the non-injected zygote in the operation area based on detection of the zygote position. (B) Injection operation using the newly developed software. (C1, C2) While holding the injected zygote with the holding pipette, move to the release area 3 000 μm away and release the injected zygote. (D) Return to the operation area and move the pipette to the next zygote to be injected.

2.2 Automated pipette insertion into the pronucleus

In conventional manual injection procedures, the operator visually confirms the position of the pronucleus, moves the pronucleus to a position where the pipette can be inserted by rotating the zygote, and then inserts the pipette into the pronucleus. To our knowledge, no software exists to perform this operation automatically, so we developed two new software programs in LabVIEW. First, we developed software that automatically rotates the zygote to correctly position the pronucleus for insertion of the injection pipette (Figure. 5). Rotation of the zygote is achieved by changing the holding pressure of the holding pipette and moving the zygote to contact the injection pipette. We then developed software that recognizes the pronucleus location with two dimensional (2D) coordinates so that the injection pipette can be automatically inserted into the nucleus. With this software, however, the success rate of pipette insertion into the pronucleus was only 70.0% (n = 50). Therefore, we next developed software that recognizes the pronucleus location with three dimensional (3D) coordinates, which has the ability to correct the height position of the pipette. Using this software, the success rate of automated pipette insertion was significantly improved to 94% (n = 50) (Figure. 6). In subsequent experiments, the zygote rotation software was combined with the 3D software to automatically insert an injection pipette into the nucleus.

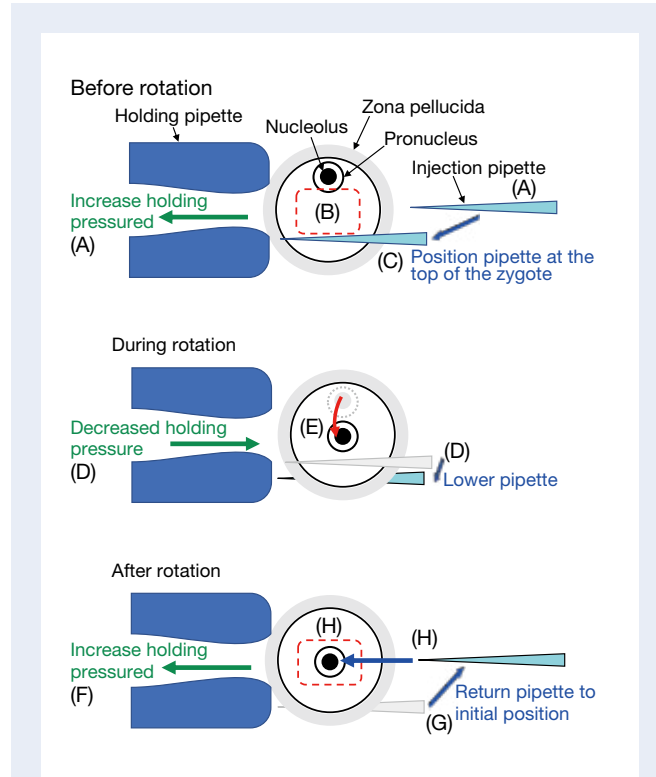


Fig. 5 Procedure to fully rotate the zygote to move the pronucleus to the injection pipette insertion position

(A) Before rotation, the zygote is held in the holding pipette under a state of increased holding pressure. The injection pipette is held stationary at the middle height position of the zygote. (B) If the pronucleus inside the zygote is outside the range (red dotted square) where automated solution injection is possible. (C) The injection pipette automatically moves to the upper part of the zygote opposite the pronucleus. (D) Due to the decreased holding pressure, the zygote disengages from the holding pipette, and immediately lowering the injection pipette causes the zygote to rotate. (E) With the rotation, the pronucleus moves from the corner of the zygote to the center (red arrow). (F) Immediately after rotation, the holding pressure is increased to hold the zygote. (G) The injection pipette is returned to its initial position (A). (H) When the pronucleus is within the range for automated solution injection (red dotted square), the injection pipette is inserted into the pronucleus.

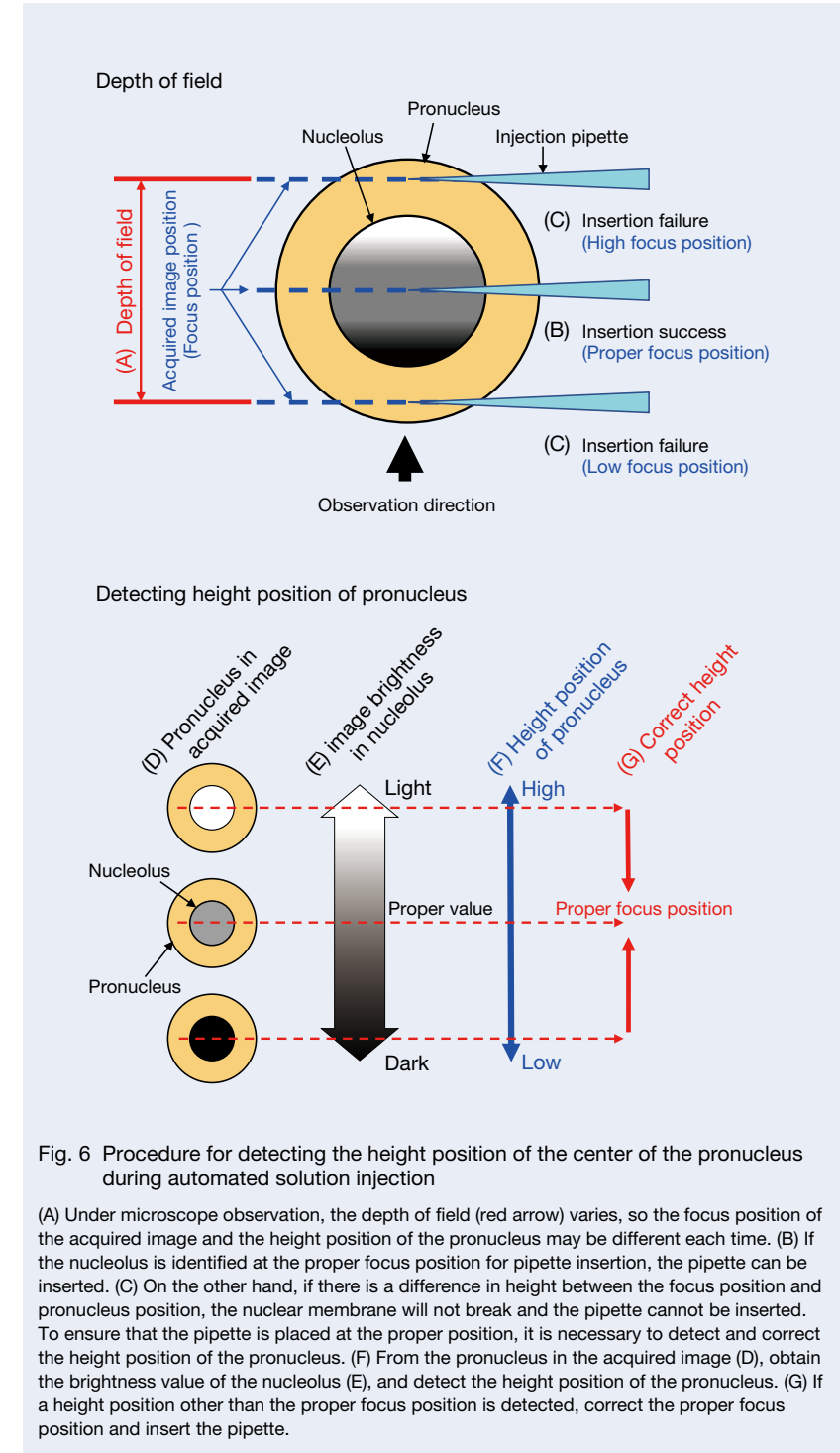


Fig. 6 Procedure for detecting the height position of the center of the pronucleus during automated solution injection

(A) Under microscope observation, the depth of field (red arrow) varies, so the focus position of the acquired image and the height position of the pronucleus may be different each time. (B) If the nucleolus is identified at the proper focus position for pipette insertion, the pipette can be inserted. (C) On the other hand, if there is a difference in height between the focus position and pronucleus position, the nuclear membrane will not break and the pipette cannot be inserted. To ensure that the pipette is placed at the proper position, it is necessary to detect and correct the height position of the pronucleus. (F) From the pronucleus in the acquired image (D), obtain the brightness value of the nucleolus (E), and detect the height position of the pronucleus. (G) If a height position other than the proper focus position is detected, correct the proper focus position and insert the pipette.

2.3 Establishment of automated pronuclear injection conditions

Injecting a large volume of solution into the pronucleus adversely affects the zygote¹¹. Therefore, it is important to determine the proper settings for both the injection pressure and injection time, which determine the injection volume¹⁵. In this experiment, optimization of the injection pressure and injection time was aimed at injecting as much volume as possible without decreasing the zygote survival rate. Zygote survival was determined by observing the oocyte morphology 1 h after injection.

First, the appropriate injection pressure was determined. The injection time was fixed at 0.8 s and the solution was injected at 30, 35, or 45 hPa (n = 188, 191, and 200 zygotes, respectively, for each injection pressure). The zygote survival rate was nearly 100% at 30 hPa (Figure. 7A), but the survival rate decreased significantly when the injection pressure exceeded 35 hPa. We then examined the solution injection time. The injection pressure was fixed at 30 hPa, and the solution was injected over 0.8, 1.2, 1.6, 2.0, or 2.4 s (n = 100/injection time). Zygote viability after the solution injection decreased significantly when the injection time exceeded 2.0 s (Figure. 7B). In this range, the volume of the pronucleus expanded linearly with the injection time (Figure. 7C). The volume achieved at 45 hPa for 0.8 s was similar to that at 30 hPa for 1.6 s, suggesting that the injected volume is not simply determined by the product of the injection time and injection pressure. In the following experiments, the injection pressure was fixed to 30 hPa, because the volume of the injection solution is finely adjustable by changing the time.

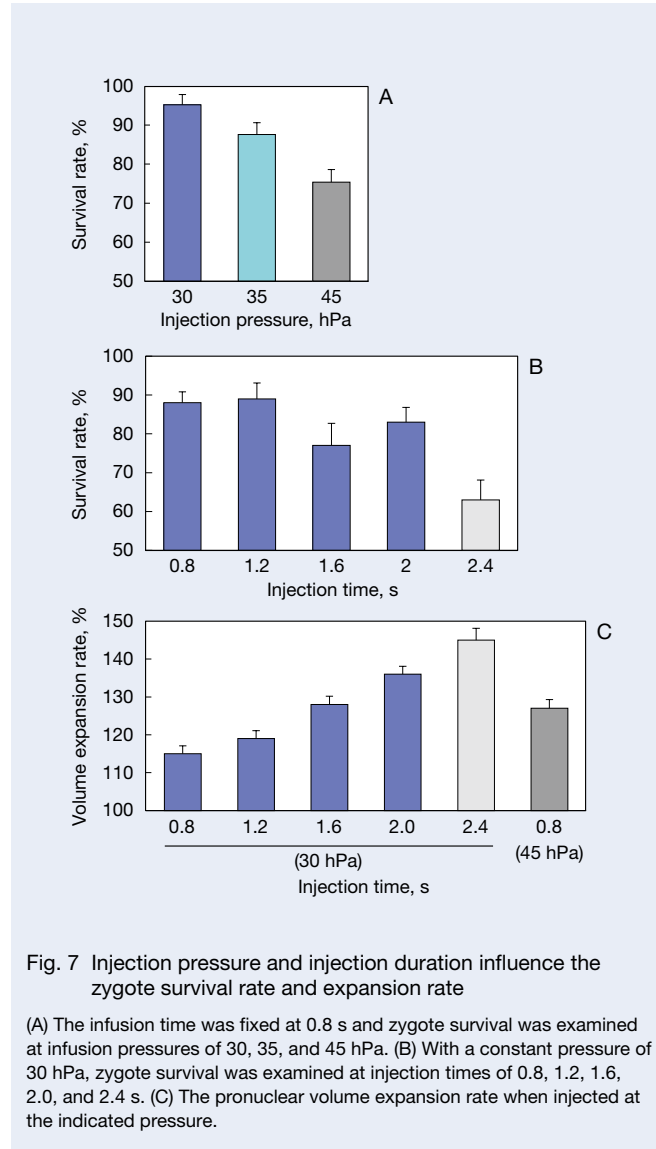


Fig. 7 Injection pressure and injection duration influence the zygote survival rate and expansion rate

(A) The infusion time was fixed at 0.8 s and zygote survival was examined at infusion pressures of 30, 35, and 45 hPa. (B) With a constant pressure of 30 hPa, zygote survival was examined at injection times of 0.8, 1.2, 1.6, 2.0, and 2.4 s. (C) The pronuclear volume expansion rate when injected at the indicated pressure.

2.4 Production of genetically modified mice

When producing genetically modified mice by injecting a solution, the type and concentration of the nucleic acids and proteins added to the solution differ depending on the method. Therefore, it is necessary to fully automatically inject multiple types of solutions into zygotes to confirm whether genetically modified mice can be produced in

each case. In this study, we produced genetically modified mice using three different methods: traditional DNA injection (traditional DI) using linearized plasmid DNA; a piggyBac Transposon system (piggyBac TS) using circular plasmid DNA and transposase mRNA; and a CRISPR-Cas9 system (knock-in) using single-stranded DNA, guide RNA, and Cas9 nuclease protein (Figure. 8). In all of the experiments, the mouse was judged to be genetically

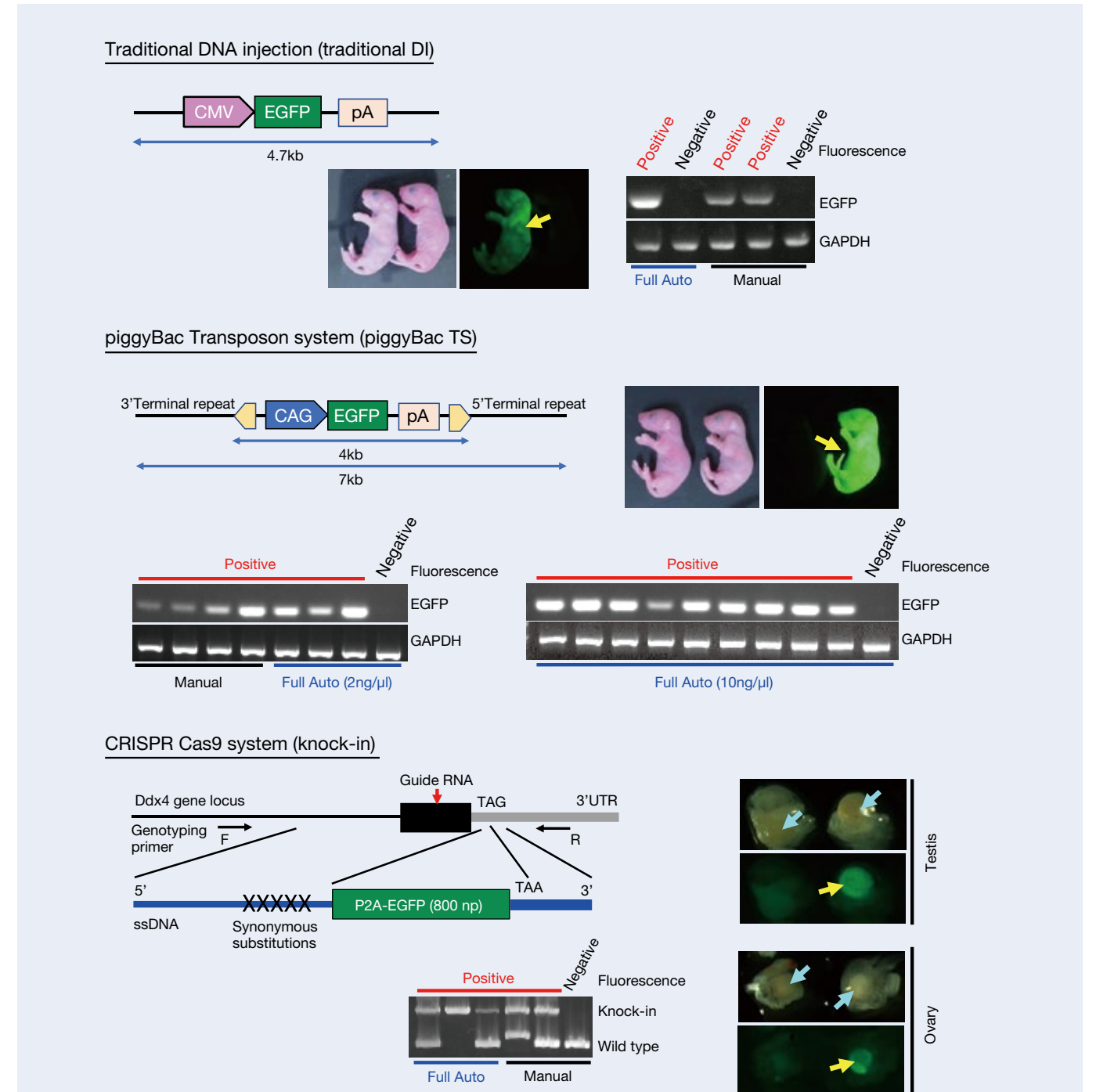


Fig. 8 EGFP expression and gene transfer in genetically modified mice produced by three different methods

Different DNA constructs were used to produce the three types of genetically modified mice. Mice produced by fully automated or manual injection were examined for EGFP expression by UV irradiation and for gene modification by genomic DNA PCR. Yellow arrows indicate typical examples of testes and ovaries containing germ cells with confirmed EGFP fluorescence. Blue arrows indicate typical examples of ovaries or testes before UV irradiation. EGFP fluorescence-positive mice were always positive on PCR examination.

modified when positive results were obtained in both enhanced green fluorescent protein (EGFP) fluorescence analyses and genotyping polymerase chain reaction (PCR) analyses (Figure. 8, Figure. 9). In contrast to the ubiquitous expression of EGFP in mice generated by traditional DI and piggyBac TS experiments, the reporter gene expression was restricted to germ cells in mice generated by knock-in, because EGFP is knocked into the germ cell-specific gene (*Ddx4*) locus.

First, a traditional DI experiment was performed under three conditions (automated injection for 0.8 s, automated injection for 1.6 s, and manual injection). We injected 151 (0.8 s), 199 (1.6 s), and 148 (manual) embryos using plasmid DNA at a concentration of 1.5 ng/ μ l. The survival rate of the zygotes was 87.4%, 79.4%, and 86.5%, respectively, and the in vitro development

rate to two cell embryos was 88.6%, 89.2%, and 82.8%, respectively (Figure. 10). The results did not differ significantly between the automated and manual injection methods with regard to survival or development rates. Importantly, the percentage of pups obtained from transplanted embryos injected automatically was 19.7% (0.8 s) and 19.1% (1.6 s), and tended to be higher than the percentage of pups obtained from manual injection (5.7%; Table 2). The number of genetically modified mice obtained from embryos injected using the automated injection system, however, was 0 (0.8 s) and 1 (1.6 s), and manual injection generated two genetically modified mice. Thus, in these conditions, the manual injection produced genetically modified animals more efficiently than the automated injection method. The higher survival rate and lower modification rate in the automated injection

method suggests that the amount of injected DNA in the automated injection should be increased to achieve maximum efficiency.

Next, the piggyBac TS experiment was conducted using automated (injection time 1.6 s) and manual injection. Two different plasmid DNA concentrations were tested for automated injection (2 and 10 ng/ μ l). In the manual condition, 2 ng/ μ l plasmid DNA was injected. The survival rate (2 ng/ μ l automated; 80.0%, 10 ng/ μ l automated; 82.7%, manual; 82.7%) and development rate to two cell stage embryos (2 ng/ μ l automated; 91.7%, 10 ng/ μ l automated; 87.1%, manual; 91.9%) did not differ significantly among the three conditions (Figure. 10). In addition, using 2 ng/ μ l DNA, the fully automated and manual results were similar (2.7% and 3.5%, respectively; Table 2). Furthermore, we demonstrated that even piggyBac¹⁶⁾ transgenesis can be reproduced fully automatically because the transgenic mouse production rate improved when the DNA concentration was increased (10 ng/ μ l; 8.3%). Experimental results of traditional DI and piggyBac TS suggest that transgenic mice can be produced even with fully automated solution injection.

In the knock-in experiment, automated solution injection was performed in 1.6 s using 2 ng/ μ l of single-stranded DNA. The automated injection and manual injection methods were not significantly different with regard to the survival rate (80.9% and 84.0%, respectively) and the development rate to two cell stage embryos (88.8% and 80.4%, respectively; Figure. 10). In addition, the offspring production rate was higher for the automated injection method (25.9%) than the manual injection method (11.1%), and the gene modification rates were comparable (2.1 and 1.5%, respectively; Table 2). These results suggested that knock-in mice produced by genome editing can be produced with fully automated solution injection.

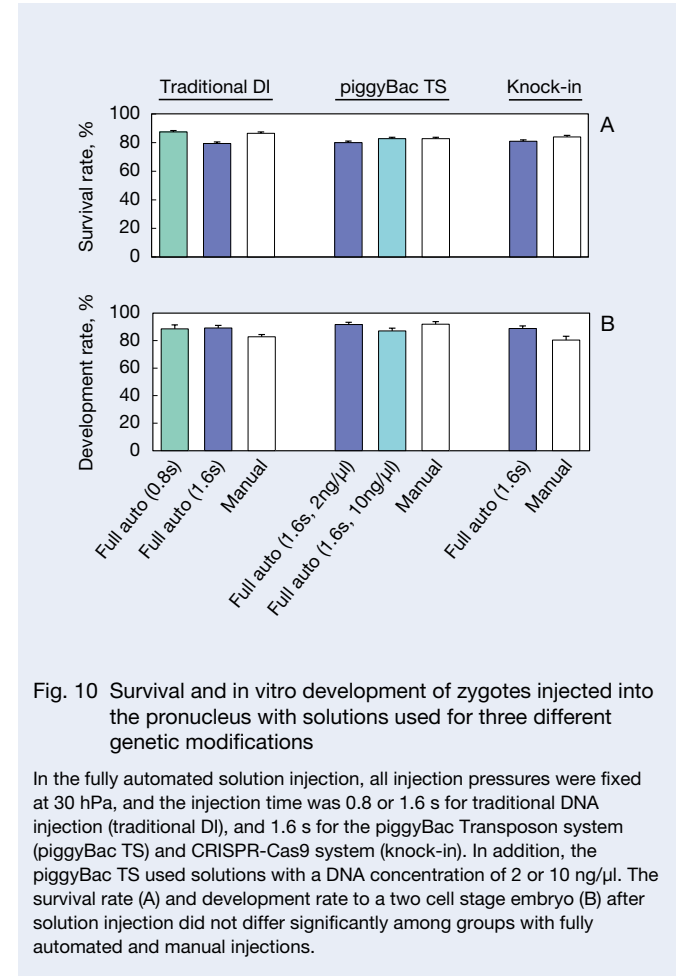


Fig. 10 Survival and in vitro development of zygotes injected into the pronucleus with solutions used for three different genetic modifications

In the fully automated solution injection, all injection pressures were fixed at 30 hPa, and the injection time was 0.8 or 1.6 s for traditional DNA injection (traditional DI), and 1.6 s for the piggyBac Transposon system (piggyBac TS) and CRISPR-Cas9 system (knock-in). In addition, the piggyBac TS used solutions with a DNA concentration of 2 or 10 ng/ μ l. The survival rate (A) and development rate to a two cell stage embryo (B) after solution injection did not differ significantly among groups with fully automated and manual injections.

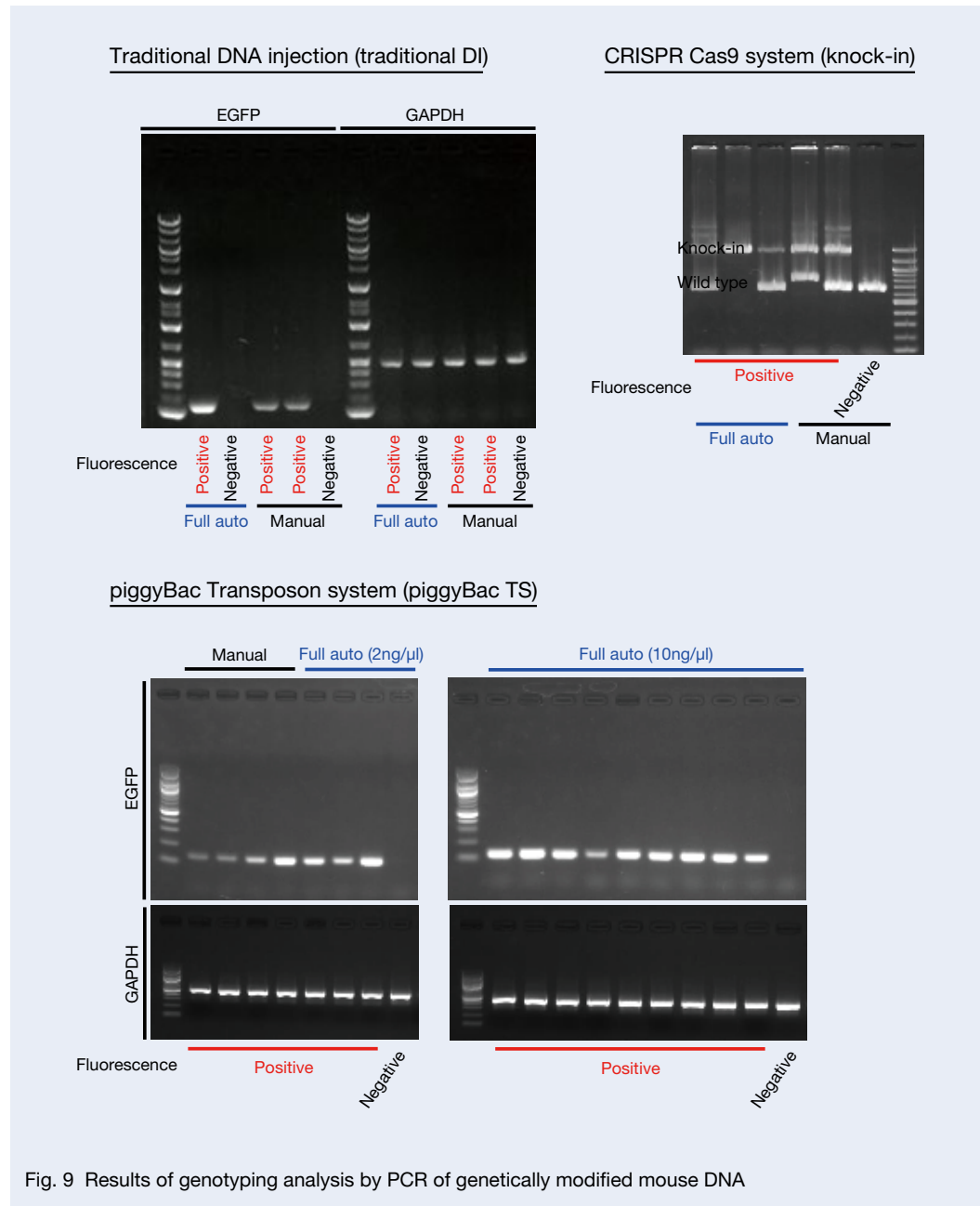


Fig. 9 Results of genotyping analysis by PCR of genetically modified mouse DNA

3. Discussion

This study reports for the first time (1) automated nuclear injection and (2) production of genetically modified animals using fully automated injection. Rapid production of new genetically modified mice will accelerate medical,

Table 2 Offspring and genetic modification of zygotes injected into the pronucleus with solutions used for 3 different genetic modifications

Genetic modification method	Injection method	Injection time (s)	DNA concentration (ng/ μ l)	Number of embryos transferred	Offspring (%)	Genetically modified (%)
Traditional DI	Full auto	0.8	1.5	117	23 (19.7)	0 (0.0)
		1.6	1.5	141	27 (19.1)	1 (0.7)
	Manual	—	1.5	106	6 (5.7)	2 (1.9)
piggyBac TS	Full auto	1.6	2	110	20 (18.2)	3 (2.7)
		1.6	10	108	24 (22.2)	9 (8.3)
	Manual	—	2	114	26 (22.8)	4 (3.5)
Knock-in	Full auto	1.6	2	143	37 (25.9)	3 (2.1)
	Manual	—	2	135	15 (11.1)	2 (1.5)

pharmaceutical, and biology research.

Multiple methods currently exist for genetically modifying zygotes. One genetic modification method is electroporation¹⁷⁾, but the generation of transgenic mice is difficult using traditional DI⁵⁾, piggyBac TS¹⁸⁾, and artificial chromosomes (YACs, BACs, and PACs)¹⁹⁾. Furthermore, in genome editing, gene knock-in tends to be a less efficient method for producing genetically modified mice than gene knock-out²⁰⁾. Although a method has been developed for injecting DNA solutions into the cytoplasm, the types of genes that can be introduced are limited compared with those that can be directly injected into the pronucleus^{18, 20)}. Injecting the solution into the pronucleus is considered suitable for various genetic modifications, but the conventional method is a complicated procedure that requires highly skilled microinjectionists. The conventional method cannot likely be sufficiently modified to more rapidly provide genetically modified mice. Therefore, we developed a fully automated injection system for producing genetically modified mice.

We considered the injection site of the solution before designing the sequence for the fully automated solution injection. The potential sites for solution injection into zygotes are the cytoplasm^{21–23)} and pronucleus, but in the first reports of traditional DI⁵⁾, piggyBac TS¹⁸⁾, and knock-in genome editing^{9, 10)}, the solution was injected into the pronucleus. In addition, in traditional DI, intracellular injection significantly reduces the efficiency of transgenic mouse production compared with intranuclear injection²⁰⁾. Furthermore, in genome editing using CRISPR Cas9, the concentration of vector DNA contained in the injection solution must be 20 times higher when injected into the cytoplasm than when injected into the pronucleus²⁴⁾. Therefore, in the present study, the solution was injected into the pronucleus.

For manual injection, an injection pipette is appropriately inserted into the pronucleus by a microinjectionist, which requires many years of experience. Because it is difficult to automatically reproduce extensive experience, however, we developed software to determine the optimal insertion site. For automated insertion of the injection pipette into the pronucleus, the controller must accurately recognize the position of the pronucleus in the cytoplasm. Therefore, we also developed software that recognizes the pronucleus in two dimensions utilizing a generalized Hough transform²⁵⁾ of the obtained digital image. To accurately detect an object using the generalized Hough transform, the outline of the object in the image must be sharp. In this study, nucleoli whose contours were clearly confirmed in many pronuclei were targeted for acquiring the position coordinates. The injection success rate using the 2D system, however, was only 70%. In a digital image, while the 2D coordinates of the nucleolus can be obtained, the 3D solid coordinates, including the height direction, cannot be obtained. When observing a 3D structure with an inverted microscope, the depth of field that appears to be in focus on the object varies (Figure. 6). Therefore, even if

the nucleolus is displayed in the acquired image, the focal position and the actual height of the nucleolus may not match. It is likely that the height of the actual nucleolus will not match that of the injection pipette and thus the injection pipette will miss the pronucleus. Therefore, in addition to the 2D coordinates obtained by the Hough transform, we developed software that recognizes the pronucleus in three dimensions by correcting the distance in the height direction between the position of the nucleolus and the focal position from the image brightness value of the nucleolus in the image (Figure. 6). Using the 3D coordinate software, we obtained an insertion success rate of 94%, which was significantly higher than that using the 2D coordinate software. In the following experiments, we therefore used the software that provides the pronucleus location in 3D coordinates.

When manually injecting a solution into the pronucleus, the nucleus tends to swell within 1 s at an injection pressure of 30–40 hPa²⁰⁾. Therefore, to examine the injection pressure, the injection time was fixed at 0.8 s and the pressure was increased stepwise from 30 to 45 hPa. The results of the experiment indicated that the survival rate was the same at 30 hPa and 35 hPa, and significantly decreased at 45 hPa. Because increasing the injection pressure above 35 hPa decreased the survival rate, the injection pressure was fixed at 30 hPa and the injection time was examined. Survival rates were similar for infusion times ranging from 0.8 to 2.0 s, but significantly decreased at 2.4 s. A 2.0-s injection at 30 hPa, resulting in an expansion of the pronucleus to 136% of the original volume, had little effect on the zygote survival rate (Figure. 7). Although the expansion rates at 30 hPa for 1.6 s and 45 hPa for 0.8 s were equivalent, the survival rate at 45 hPa and 0.8 s was lower. If the injection pressure is too high, the zygote may be damaged even if the injection amount is equivalent to that produced at a lower injection pressure²⁰⁾. These findings suggested that performing the solution injection at the lowest possible pressure over a longer time should improve the survival rate. Therefore, the injection pressure was fixed at 30 hPa and the injection time was extended stepwise from 0.8 s in the experimental production of genetically modified mice.

The automated and manual injection methods did not differ significantly with respect to zygote survival and development to two cell stage embryos in the traditional DI, piggyBac TS, and knock-in experiments after injecting a solution at 30 hPa over 1.6 s (Figure. 10). The solutions used in each experiment had different contents. Thus, injection settings rather than the injection method (i.e., automated or manual) or injected solution were likely the major determinants of zygote survival and development rates. In traditional DI, only a small number of transgenic mice was obtained using a 1.5-ng/ μ L DNA solution, both manually and automatically. In traditional DI, however, the gene modification rate fluctuates depending on the increase or decrease in the DNA concentration²⁰⁾. In the future, we would like to evaluate the effect of the DNA concentration on the production of transgenic mice by

traditional DI using fully automated solution infusion.

On the basis of the experiments using the IAEMS, we found that genetically modified mice can be produced even by fully automated injection of multiple types of solutions (Table 2). Several methods of automatically injecting a solution into zygotes have been reported. For example, while automated injection into the cytoplasm has been reported in zebrafish²¹⁾ and drosophila²²⁾, genetic modification has not been achieved. In mammals, automated injection into the cytoplasm has been reported in mice²³⁾, but its effect on genetic modification was not examined.

4. Methods

4.1 Animals

Jcl:BDF1 mice were used to collect zygotes at the pronuclear stage (female: 8–16 weeks old, male: 12–20 weeks old). Jcl:MCH (ICR) female mice 10–16 weeks of age were used as recipients for embryo transfer. All mice were purchased from CLEA Japan Inc. (Tokyo, Japan). The mice were reared under the following conditions: room temperature 22°C \pm 0.5°C, humidity 55% \pm 5%; lights on 08:00–20:00. Food (CA-1; CLEA Japan) and water were provided ad libitum.

All animal experiments were approved by the Animal Committee of Central Institute for Experimental Animals, and the study was performed in accordance with ARRIVE guidelines (Animal Research: Reporting of In Vivo Experiments) and with Central Institute for Experimental Animals guidelines.

4.2 Collection, cryopreservation, and embryo transfer of zygotes

Zygotes were collected by in vitro fertilization²⁶⁾. Approximately 8 h after insemination by the sperm, the pronuclear zygotes were cryopreserved using the vitrification method of Eto et al²⁶⁾. Vitrified pronuclear oocytes were used for injection of the solution 1 h after warming. The pronuclear oocytes injected with the solution were cultured in vitro in KSOM medium²⁷⁾, and two cell stage embryos were transplanted to recipient females in the morning of the next day (10:00–12:00). The solutions used for these embryo manipulations were purchased from ARK Resource (Kumamoto, Japan).

4.3 Solution injection into pronuclear zygotes

The hardware was made by mounting an EMS (XY-MC0202-701-001; NSK Ltd., Tokyo, Japan) and an electric injector (Femtojet 4i, Eppendorf AG, Hamburg, Germany) onto a microscope (ECLIPSE Ti2-U; Nikon Co. Ltd., Tokyo, Japan; Figure. 2, Photo 1). The EMS is pre-installed with software for electric operation and control of electronic devices such as an electric injector

via serial communication. The software also includes an image-processing function that automatically detects the position of the zygote (Figure. 3) and a sequence function that automatically moves the pipette to near the non-injected zygote or moves the injected zygote to the release area (Figure. 4). In the experiment for producing genetically modified mice, we used IAEMS, which was newly developed in LabVIEW 2017 for Windows (National Instruments, Austin, TX, USA) for fully automated insertion of the injection pipette into the pronucleus and integrated into the existing software (Figures 1, 5, and 6). Fully automatic injection was performed under the solution injection conditions (injection time and injection pressure) experimentally derived for IAEMS. The solution injection in the control experiment was all performed manually using hardware that combined the EMS and electric injectors¹¹⁾.

All microinjections were performed using a holding pipette (outer diameter ϕ 100 μ m, inner diameter ϕ 40 μ m, bending angle 30°. HD052010040; Sankyo Medic Co., Ltd., Shizuoka, Japan) that holds the zygote and an injection pipette (tip angle 45°, inner diameter of the opening ϕ 1 μ m, bending angle 20°, and the volume of liquid in the pipette 3 μ L. DNA-102001; Sankyo Medic) that injects the solution. The injection chamber was prepared by dropping 20 μ L of M2 medium (M7167, Millipore Sigma, St. Louis, MO, USA) on a plastic dish (351,006, Corning Inc., Corning, NY, USA) and covering it with mineral oil (M8410, Millipore Sigma). The experiments were repeated using 15–30 zygotes for each solution infusion. Successful insertion of the injection pipette was confirmed by observing pronucleus swelling upon injection of the solution.

4.4 Preparation of the injection solution for transgenic mice

For the traditional DI, the pEGFP-N1 vector (Clontech, Mountain View, CA, USA) containing the cytomegalovirus (CMV) promoter was digested with an AseI restriction enzyme (NEB, Ipswich, MA, USA) to generate a 4.7-kb linearized fragment (Figure. 8). The prepared fragment was diluted to 1.5 ng/ μ L with nuclease-free water (Promega, Madison, WI, USA) and injected into the pronucleus.

For piggyBac TS, piggyBac vector (1.33 ng/ μ L or 6.66 ng/ μ L), and transposase mRNA (0.66 ng/ μ L or 3.33 ng/ μ L) were dissolved in saline for total concentrations of 2 ng/ μ L and 10 ng/ μ L, respectively, and injected into the pronucleus.

To generate knock-in mice, in which the P2A-EGFP sequence was inserted into the C-terminus of the Ddx4 gene, a targeting vector (Vasa-P2A-EGFP) was constructed.

4.5 Analysis of transgenic mice

Traditional DI and piggyBac TS were analyzed by the same method. Expression of EGFP fluorescence

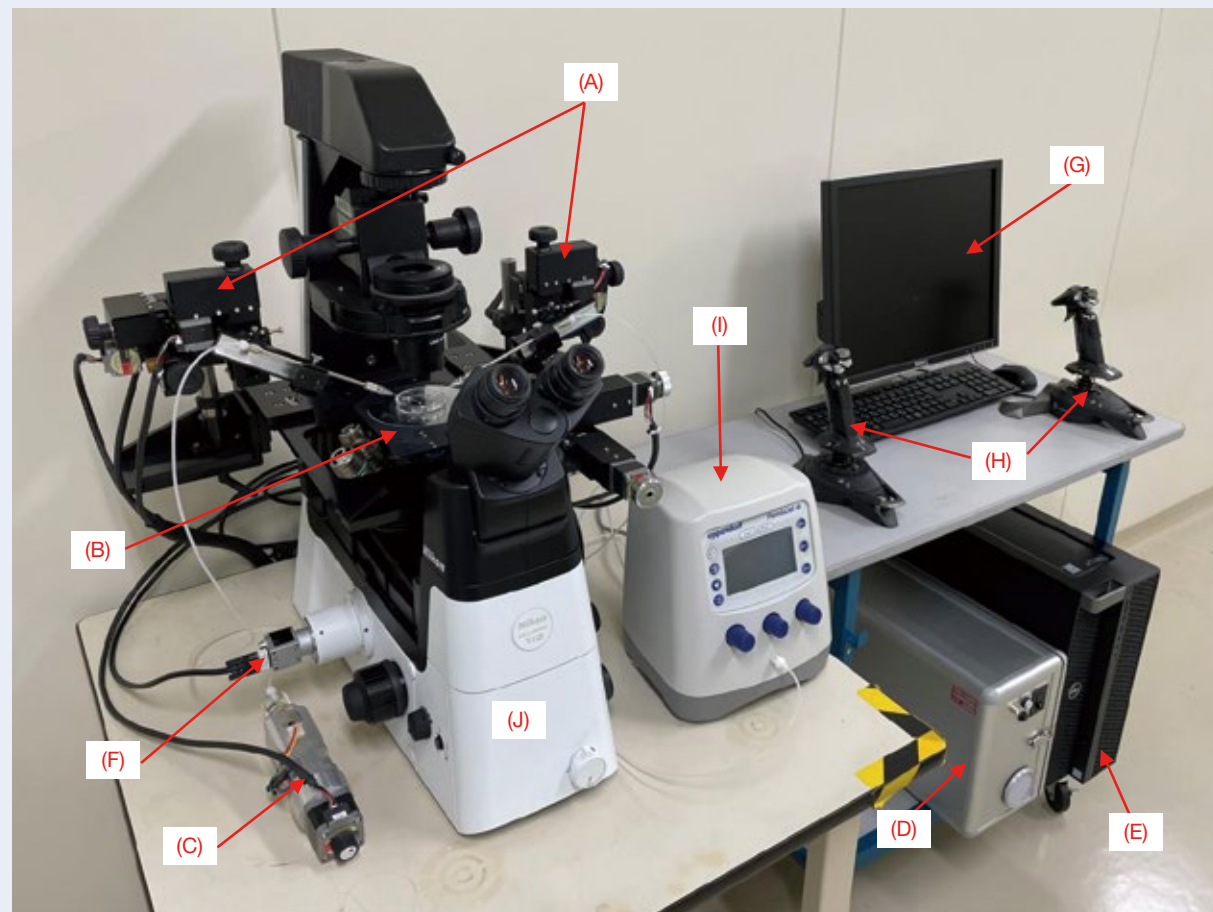


Photo 1 Integrated Automated Embryo Manipulation System (IAEMS)

The IAEMS consists of an EMS [(A) electric manipulator, (B) electric sample stage, (C) electric pump, (D) electronic distribution board, (E) controller (computer), (F) microscope camera, (G) display, (H) joystick, (I) electric injector, and (J) microscope]. LabVIEW software for Windows is installed on the controller and is used to control each electronic device.

in newborn transgenic mice was visualized by UV microscopy (VB-6000; KEYENCE Inc., Osaka, Japan). PCR genotyping of offspring was performed using a crude lysate of the tail tips. Genomic DNA was extracted from the mouse tail using Direct PCR Lysis Reagent (Viagen Biotech Inc., Los Angeles, CA, US) containing 0.2 mg/ml proteinase K (Nacalai Tesque Inc., Kyoto, Japan). Knock-in were analyzed by irradiating the ovary or testis with UV light because the EGFP protein is expressed in germ cells. PCR genotyping of offspring was performed using a crude lysate of the tail tips. For PCR analysis, the same method as for guide RNA preparation was used.

4.6 Statistical analysis

Experimental results of zygote survival and development into two cell stage embryos are expressed as mean \pm standard error of the mean and statistical analysis was performed using the Student t-test after confirming a normal distribution. In all analyses, $P < 0.01$ was

considered to indicate statistical significance. For analyses of the experimental data, Statcel 4 (OMS Publishing, Saitama, Japan) automated analysis software was used.

5. Conclusion

Through this research, we were able to develop an IAEMS that can easily and reproducibly microinject solutions into the pronucleus of a zygote without extensive training or experience. We believe that the use of the IAEMS will make it easier to produce genetically modified mice for research in biology, medicine, and pharmaceutical sciences. The development of software and hardware for automated micromanipulation will be an important research topic for future progress in the natural sciences for humans and animals.

Note: This article is a revised version of a paper submitted for publication in *Scientific Reports*, an electronic journal published by Springer Nature²⁸.

References

- 1) K. Kersten, K. E. de Visser, M. H. van Miltenburg, and J. Jonkers, "Genetically engineered mouse models in oncology research and cancer medicine," *EMBO Mol. Med.*, 9 (2017), pp. 137–153.
- 2) R. A. Davey and H. E. MacLean, "Current and future approaches using genetically modified mice in endocrine research," *Am. J. Physiol. Endocrinol. Metab.* 291 (2006) E429–438.
- 3) S. B. Liggett, "Genetically modified mouse models for pharmacogenomic research," *Nat. Rev. Genet.*, 5 (2004), pp. 657–663.
- 4) C. Babinet, "Transgenic mice: an irreplaceable tool for the study of mammalian development and biology," *J. Am. Soc. Nephrol.*, 11 (2000) S88–S94.
- 5) J. W. Gordon, G. A. Scangos, D. J. Plotkin, J. A. Barbosa, and F. H. Ruddle, "Genetic transformation of mouse embryos by microinjection of purified DNA," *Proc. Natl. Acad. Sci. U.S.A.*, 77 (1980), pp. 7 380–7 384.
- 6) Z. Ivics et al., "Transposon-mediated genome manipulation in vertebrates," *Nat. Methods*, 6 (2009), pp. 415–422.
- 7) D. A. Largaespada, "Transposon mutagenesis in mice," *Methods Mol. Biol.*, 530 (2009), pp. 379–390.
- 8) M. Meyer, M. H. de Angelis, W. Wurst, and R. Kühn, "Gene targeting by homologous recombination in mouse zygotes mediated by zinc-finger nucleases," *Proc. Natl. Acad. Sci. U.S.A.*, 107 (2010), pp. 15 022–15 026.
- 9) B. Wefers, B et al., "Direct production of mouse disease models by embryo microinjection of TALENs and oligodeoxynucleotides," *Proc. Natl. Acad. Sci. U.S.A.*, 110 (2013), pp. 3 782–3 787.
- 10) B. Shen et al., "Efficient knockin mouse generation by ssDNA oligonucleotides and zinc-finger nuclease assisted homologous recombination in zygotes," *PLoS One*, 8 (2013), e77696.
- 11) R. Behringer, M. Gertsenstein, A. Nagy, and K. Nagy, "Manipulating the Mouse Embryo: A Laboratory Manual," Fourth edition (2014), pp. 237–319, CSH Press.
- 12) W. Xu, "Microinjection and Micromanipulation: A Historical Perspective," *Methods Mol. Biol.*, 1874 (2019), pp. 1–16.
- 13) D. Murphy, "Microinjection of cloned DNA fragments into fertilized one-cell mouse eggs: II. Automatic injection," *Methods Mol. Biol.*, 18 (1993), pp. 163–167.
- 14) A. Nagy, M. Gertsenstein, K. Vintersten, and R. Behringer, "Manipulating the Mouse Embryo: A Laboratory Manual," Third edition (2003), pp. 289–358, CSH Press.
- 15) X. A. Pu, A. P. Young, and H. M. Kubisch, "Production of Transgenic Mice by Pronuclear Microinjection," *Methods Mol. Biol.*, 1874 (2019), pp. 17–41.
- 16) J. Marh et al., "Hyperactive self-inactivating piggyBac for transposase-enhanced pronuclear microinjection transgenesis," *Proc. Natl. Acad. Sci. U.S.A.*, 109 (2012), pp. 19 184–19 189.
- 17) T. Kaneko and T. Mashimo, "Simple Genome Editing of Rodent Intact Embryos by Electroporation," *PLoS One*, 10 (2015), e0142755.
- 18) S. Ding et al., "Efficient transposition of the piggyBac (PB) transposon in mammalian cells and mice," *Cell*, 122 (2005), pp. 473–483.
- 19) P. Giraldo and L. Montoliu, "Size matters: use of YACs, BACs and PACs in transgenic animals," *Transgenic Res.*, 10 (2001), pp. 83–103.
- 20) R. L. Brinster, H. Y. Chen, M. E. Trumbauer, M. K. Yagle, and R. D. Palmiter, "Factors affecting the efficiency of introducing foreign DNA into mice by microinjecting eggs," *Proc. Natl. Acad. Sci. U.S.A.*, 82 (1985), pp. 4 438–4 442.
- 21) W. Wang, X. Liu, D. Gelinas, B. Ciruna, and Y. Sun, "A fully automated robotic system for microinjection of zebrafish embryos," *PLoS One*, 2 (2007), e862.
- 22) E. Cornell et al., "Automating fruit fly *Drosophila* embryo injection for high throughput transgenic studies," *Rev. Sci. Instrum.*, 79 (2008), 013705.
- 23) X. Liu et al., "Automated microinjection of recombinant BCL-X into mouse zygotes enhances embryo development," *PLoS One*, 6 (2011), e21687.
- 24) H. Yang et al., "One-step generation of mice carrying reporter and conditional alleles by CRISPR/Cas-mediated genome engineering," *Cell*, 154 (2013), pp. 1 370–1 379.
- 25) D. H. Ballard, "Generalizing the Hough transform to detect arbitrary shapes," *Pattern Recognition*, 13 (1981), pp. 111–122.
- 26) T. Eto, R. Takahashi, and T. Kamisako, "Strain preservation of experimental animals: vitrification of two-cell stage embryos for multiple mouse strains," *Cryobiology*, 70 (2015), pp. 150–155.
- 27) Y. Ho, K. Wigglesworth, J. J. Eppig, and R. M. Schultz, "Preimplantation development of mouse embryos in KSOM: augmentation by amino acids and analysis of gene expression," *Mol. Reprod. Dev.*, 41 (1995), pp. 232–238.
- 28) T. Eto, H. Ueda, N. Tanaka et al., "Establishment of an integrated automated embryonic manipulation system for producing genetically modified mice," *Sci. Rep.*, 11 (2021), pp. 11 770.



Hiroki Ueda



Nobuaki Tanaka

NSK Verify (Bearing Information Acquisition Service Using 2D Barcode)

In recent years, there has been a rapid acceleration in the implementation of information technology in manufacturing, exemplified by Industry 4.0. Realizing a smart factory based on communication and sharing information at the production site requires digitizing information on manufacturing processes and producer goods while also enabling prompt access to such information.

This article introduces a service NSK provides to facilitate the obtaining of bearing information so that it can be efficiently used in the production and design of products in which a particular bearing is used.

1. Composition, Structure, and Specifications

To use the service, simply install the free NSK application on a mobile device and use the application to scan the 2D barcode on the NSK bearing box. (Photo 1)

Supported devices: iOS and Android

Supported languages: English, Japanese, and Chinese

Note: The service is available for products marked with "N" in the lower right corner of the 2D barcode.

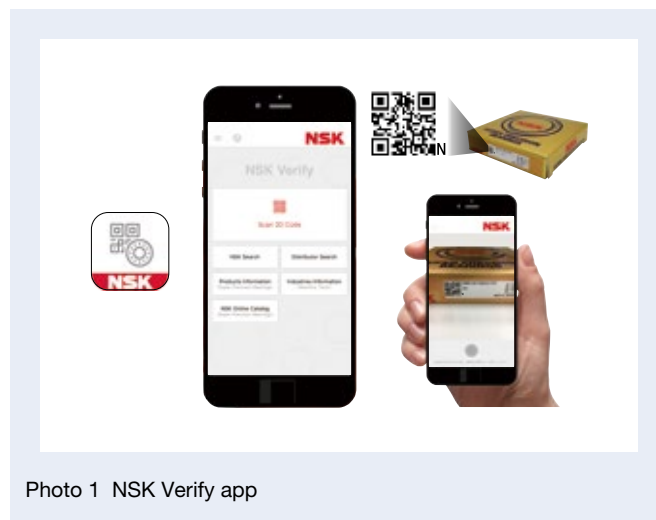


Photo 1 NSK Verify app

2. Features

(1) Provision of bearing inspection results in the form of electronic data

Information on bearing inspection results for each bearing, such as identification number, bearing number, grease code, and various dimensional and rotational accuracy details (Photo 2), can be obtained in the electronic data. The data can be retrieved in CSV and PDF format, allowing for transfer of the data to other devices and electronic data management to, for example, automate bearing sorting, manage bearing use history, and improve traceability (Figure 1).

Note: Products for which electronic data of bearing inspection results are provided. Angular contact ball bearings, cylindrical roller bearings, and thrust angular contact ball bearings of precision bearings (bearing accuracy ISO Class 5 or higher).

(2) Support for determining authenticity

The information in the 2D barcode is matched with NSK's database to provide any relevant information pertaining to genuine/fraudulent products (Photo 3). It is also possible to infer the possibility of imitations based on the number of readings.

(3) Search for offices and dealers

The identification number obtained from the 2D barcode allows for the quick placement of orders and inquiries.

(4) Other services

With the application, users can access useful content on the NSK website, including product details, catalogs, maintenance information such as how to handle bearings, and various technical calculations.

3. Usage

The service is particularly suitable for information management of precision bearings used in machine tool spindles, where bearings are selected for use based on dimensional accuracy.

4. Afterword

In this article, we have introduced our new service for obtaining bearing information through 2D barcodes and mobile terminal applications. Through this service, users can obtain bearing information instead of having to open the NSK bearing box.

Our commitment to further facilitating the provision and use of information in the manufacturing industry will remain as we also strive to broaden our product offerings and their sizes and applications.

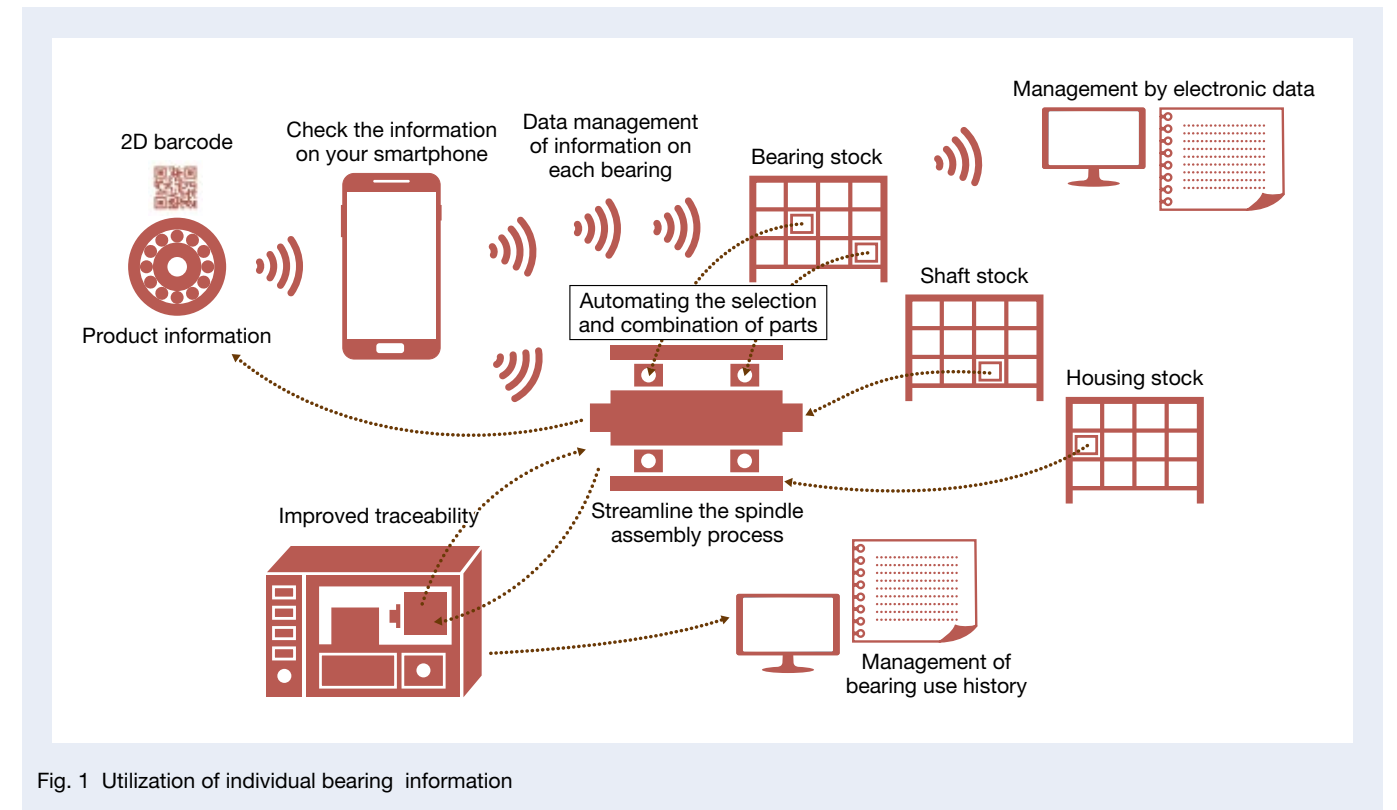


Fig. 1 Utilization of individual bearing information

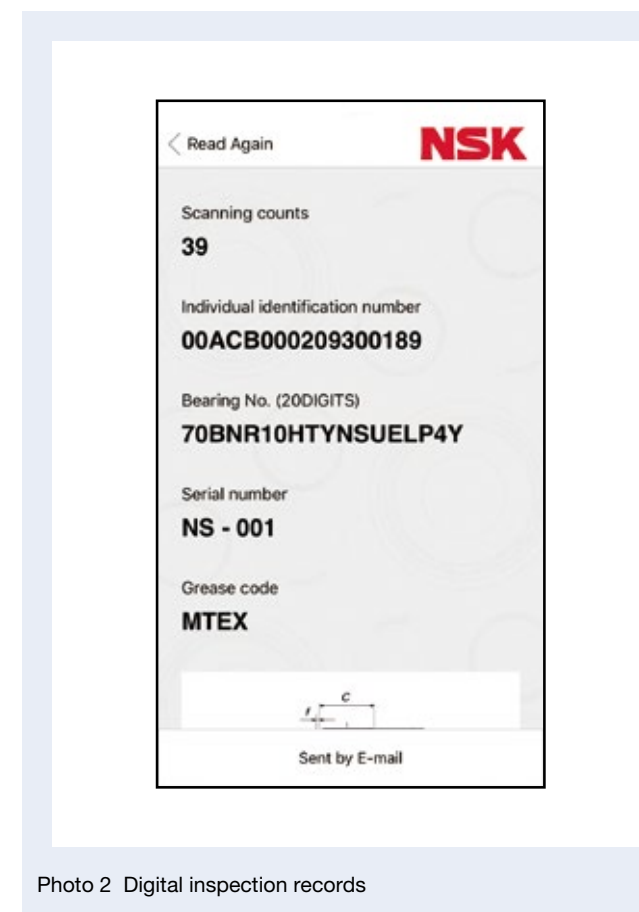


Photo 2 Digital inspection records

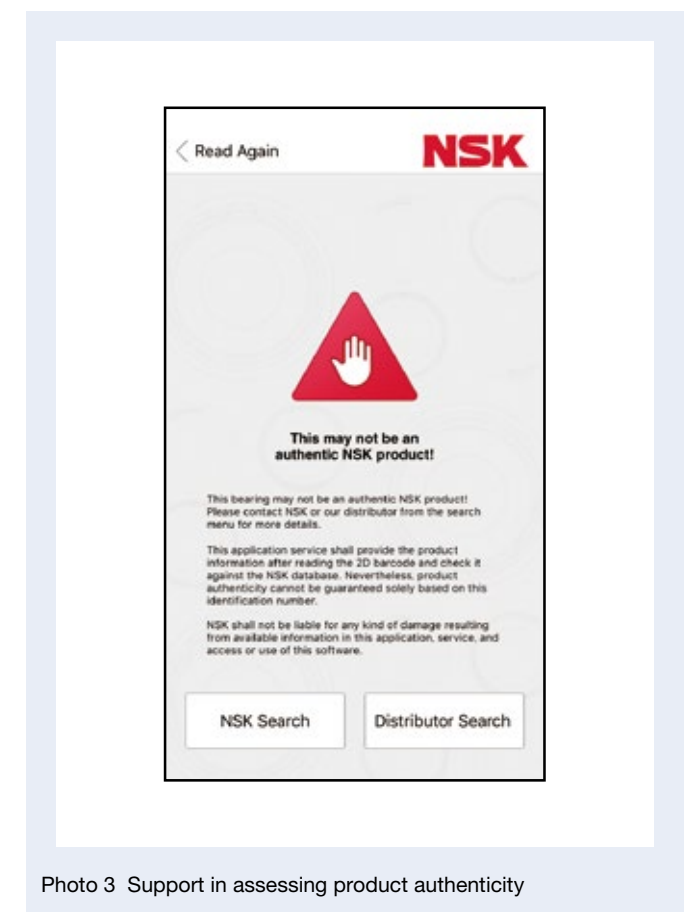


Photo 3 Support in assessing product authenticity

Bioplastic Cage for Deep Groove Ball Bearings

As the global push toward carbon neutrality gains momentum, NSK is actively taking steps to reduce CO₂ emissions in the supply chain not only in the production process (Scope 1 and 2) but also by minimizing energy loss due to bearing rolling resistance (downstream of Scope 3). Additionally, we are developing products (example in Photo 1) that use biomass plastic as a cage material to promote carbon neutrality (upstream of Scope 3). (Photo 1)

- Scope 1: Emissions from in-house fuel consumption, etc.
- Scope 2: Emissions from in-house electricity use, etc.
- Scope 3 (upstream): Emissions from raw materials, transportation, etc.
- Scope 3 (downstream): Product use and discharge

1. Composition, Structure, and Specifications

Using 100% plant-derived heat-resistant biomass plastic in the cage reduces CO₂ emissions compared to conventional petroleum-derived plastics.



Photo 1 Deep groove ball bearing with bioplastic cage

2. Features

(1) Reduction of CO₂ emissions

Compared to traditional petroleum-based plastic cages, use of a biomass plastic cage will result in approximately 90% less CO₂ emissions.

(2) Utilization of real digital twins

Predicting dimensions, shape/deformation, defects/molding failure, and strength using Real Digital Twin* could shorten the development period (Figure 1).

*NSK's development method for observing the inside of a phenomenon in detail, deducing how it works, and understanding its essence through modeling to come up with solutions that break through conventional thinking.

(3) Bearing performance

Compared to conventional petroleum-derived plastic cages, the new cage offers new value in the form of a significant reduction in CO₂ emissions while maintaining the same bearing performance (Figure 2).

3. Usage

The product suits small motors, such as fan motors for air conditioners.

4. Afterword

NSK will remain committed to achieving a carbon-neutral society. As part of this commitment, we will expand the use of biomass plastics, which are more effective in reducing CO₂ emissions than conventional petroleum-based plastics. In addition, NSK is aiming to achieve JPY800 million in sales of this product in 2024.

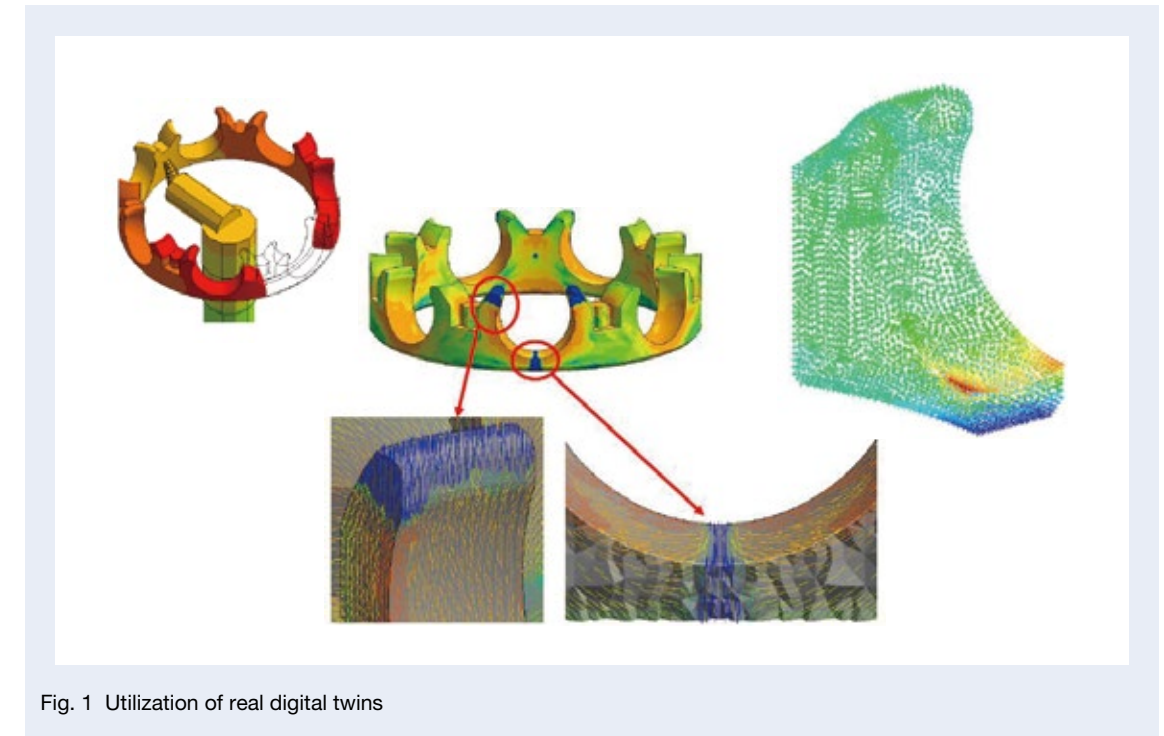
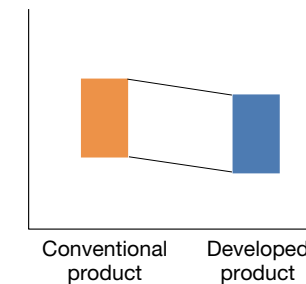


Fig. 1 Utilization of real digital twins

Quiet performance

- Test bearing: 608
- Axial preload: 30 N.
- Rotation speed: 1 800 rpm
- Temperature: Room temperature

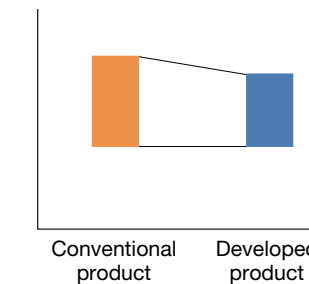
Vibration level



Long life performance

- Test bearing: 608
- Axial preload: 30 N.
- Rotation speed: 1 800 rpm
- Temperature: 80°C
- Test time: 3 000 hrs

Vibration level



Friction loss performance

- Test bearing: 608
- Axial preload: 30 N.
- Rotation speed: 1 800 rpm
- Temperature: Room temperature

Torque

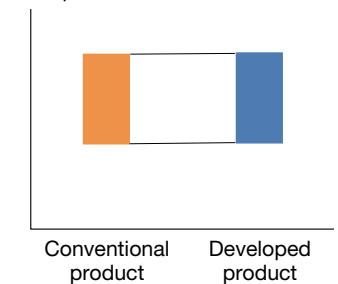


Fig. 2 Evaluation results for bearing function

High Load Capacity Angular Contact Ball Bearings with Pressed Steel Cage (BEAW)

Industrial machines are generally required to be highly reliable, easy to maintain, and environmentally friendly while also allowing for reduced operational costs and energy savings. Because of this, the bearings used in such machinery need to be more advanced in terms of performance. NSK has therefore developed and has commercialized a new type of angular contact ball bearings with pressed steel cage, which are widely used in industrial machinery such as general pumps and injection molding machines. This angular contact ball bearing (BEAW type, Photo 1) achieves an even higher load capacity than our conventional specification (BW type).



Photo 1 High load capacity angular contact ball bearings with pressed steel cage (BEAW)

1. Composition, Structure, and Specifications

The high load capacity angular contact ball bearings with pressed steel cage that we developed have a larger ball diameter (Figure 1) and longer life compared to our conventional products. They also improve the fluidity of lubricating oil, thereby contributing to higher efficiency and reliability of mounted products.

2. Features

The features of the new bearings are as follows.

- (1) Service life: 1.2 to 1.6 times longer than our conventional products

Increasing the ball diameter has achieved a longer life of 1.2–1.6 times that of our conventional products. Figure 2 shows the L10 life (fatigue life) for each size in the lineup compared to conventional products. Figure 3 shows the life calculation results for the new and conventional products.

- (2) Improved oil fluidity

Increasing the clearance between the inner ring and cage (Photo 2) has improved the penetration speed of lubricating oil by 1.4 times compared to our conventional product (Figure 4). This is expected to improve the fluidity and cooling effect of the lubricating oil, contributing to improved efficiency and reliability of mounted products.

3. Usage

The new bearings can be widely applied to general industrial machinery such as general pumps and injection molding machines. Additionally, the series has inner diameters from 35–80 mm (Table 1).

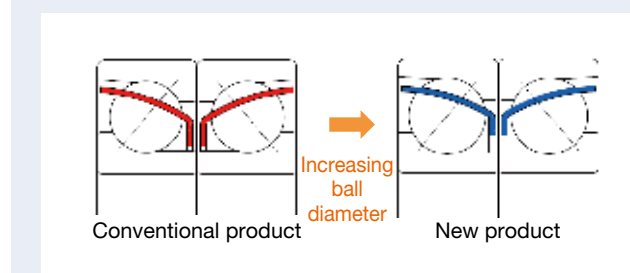


Fig. 1 Cross-sectional view of conventional product and new product

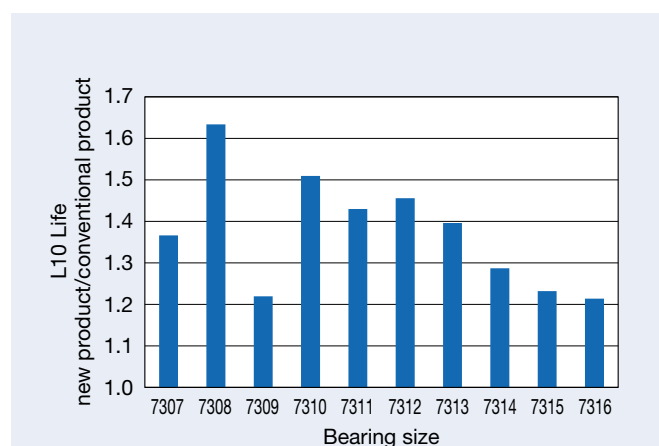


Fig. 2 L10 life comparison by bearing size

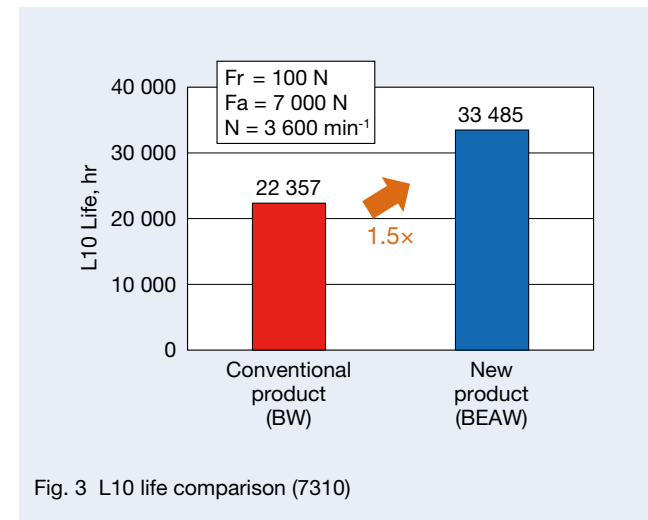


Fig. 3 L10 life comparison (7310)

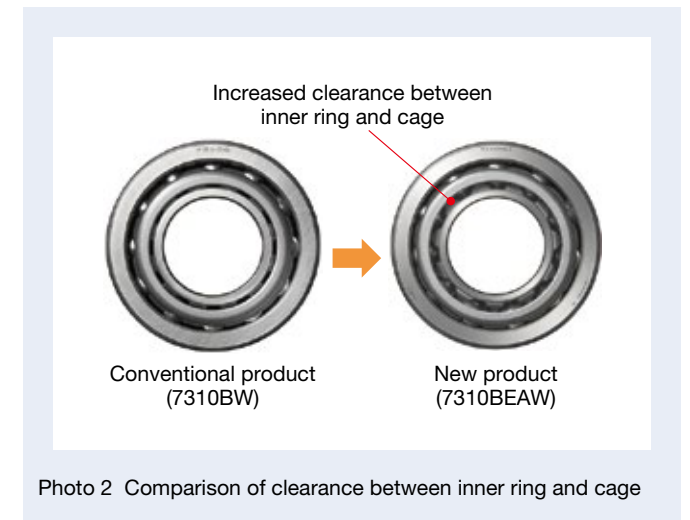


Photo 2 Comparison of clearance between inner ring and cage

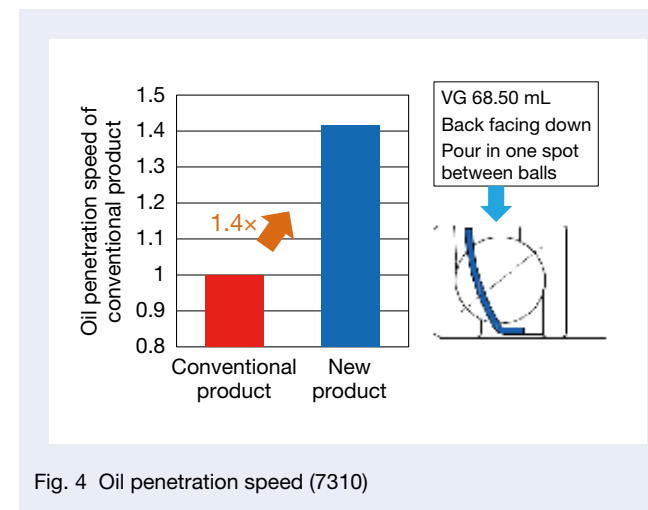


Fig. 4 Oil penetration speed (7310)

4. Afterword

The new bearings (BEAW) are expected to improve economic efficiency by extending maintenance periods and reducing running costs through longer service life. The increased fluidity of the lubricating oil has also improved the reliability of the lubrication function.

This product can be widely applied to general industrial machinery and supports the market's increasingly demanding environment.

Table 1 New product (BEAW) lineup and specifications

	Boundary dimensions, mm					Load Ratings Single, N		Limiting Speeds Single, min ⁻¹		Basic Load Rating Matched, N		Limiting Speeds Matched, min ⁻¹	
	d	D	B	r min.	r1 min.	Cr	C0r	Oil	Grease	Cr	C0r	Oil	Grease
7307BEAW	35	80	21	1.5	1	40 500	24 400	7 500	5 600	65 500	49 000	6 000	4 500
7308BEAW	40	90	23	1.5	1	53 000	33 000	6 700	5 000	86 500	65 500	5 300	4 000
7309BEAW	45	100	25	1.5	1	62 500	39 500	6 000	4 500	102 000	79 500	4 800	3 600
7310BEAW	50	110	27	2	1	78 000	50 500	5 600	4 000	127 000	101 000	4 500	3 200
7311BEAW	55	120	29	2	1	89 000	58 500	5 000	3 600	145 000	117 000	4 000	3 000
7312BEAW	60	130	31	2.1	1.1	102 000	68 500	4 500	3 400	166 000	137 000	3 800	2 600
7313BEAW	65	140	33	2.1	1.1	114 000	77 000	4 300	3 200	184 000	154 000	3 400	2 400
7314BEAW	70	150	35	2.1	1.1	124 000	87 500	4 000	2 800	201 000	175 000	3 200	2 400
7315BEAW	75	160	37	2.1	1.1	134 000	98 500	3 800	2 800	217 000	197 000	3 000	2 200
7316BEAW	80	170	39	2.1	1.1	144 000	110 000	3 400	2 600	235 000	220 000	2 800	2 000

Worldwide Sales Offices

P: Phone F: Fax ☆: Head Office

NSK LTD.-HEADQUARTERS, TOKYO, JAPAN

Nissel Bldg., 1-6-3 Ohsaki, Shinagawa-ku, Tokyo 141-8560, Japan

INDUSTRIAL MACHINERY BUSINESS DIVISION-HEADQUARTERS

P: +81-3-3779-7227 F: +81-3-3779-7433

AUTOMOTIVE BUSINESS DIVISION-HEADQUARTERS

P: +81-3-3779-7189 F: +81-3-3779-7917

●Africa

South Africa:

NSK SOUTH AFRICA (PTY) LTD.

SANDTON 25 Galaxy Avenue, Linbro Business Park, Sandton 2146, South Africa

P: +27-011-458-3600 F: +27-011-458-3608

●Asia and Oceania

Australia:

NSK AUSTRALIA PTY. LTD.

MELBOURNE 100 Logis Boulevard, Dandenong South, Victoria, 3175, Australia

P: +61-3-9765-4400 F: +61-3-9765-4466

New Zealand:

NSK NEW ZEALAND LTD.

AUCKLAND Unit F, 70 Business Parade South, Highbrook, Business Park Auckland 2013, New Zealand

P: +64-9-276-4992 F: +64-9-276-4082

China:

NSK (SHANGHAI) TRADING CO., LTD.

JIANGSU No.8 NSK Rd., Huaqiao Economic Development Zone, Kunshan, Jiangsu, China (215332)

P: +86-512-5796-3000 F: +86-512-5796-3300

NSK (CHINA) INVESTMENT CO., LTD.

JIANGSU ☆ No.8 NSK Rd., Huaqiao Economic Development Zone, Kunshan, Jiangsu, China (215332)

P: +86-512-5796-3000 F: +86-512-5796-3300

BEIJING Room 1906, Beijing Fortune Bldg., No.5 Dong San Huan Bei Lu, Chao Yang District, Beijing, China (100004)

P: +86-10-6590-8161 F: +86-10-6590-8166

TIAN JIN Unit 4604, 46/F., Metropolitan Tower, 183 Nanjing Road, Heping District, Tianjin, China (300051)

P: +86-22-8319-5030 F: +86-22-8319-5033

CHANGCHUN Room 902-03, Changchun Hongwell International Plaza, No.3299 Renmin Street, Changchun, Jilin, China (130061)

P: +86-431-8898-8682 F: +86-431-8898-8670

SHENYANG No.7, 15 Street, Shenyang Economic & Technological Development Area, Shenyang, Liaoning, China (110141)

P: +86-24-2550-5017 F: +86-24-2334-2058

DALIAN Room 1805 Xiwang Tower, No.136 Zhongshan Road, Zhongshan District, Dalian, Liaoning, China (116001)

P: +86-411-8800-8168 F: +86-411-8800-8160

NANJING Room A1 22F, Golden Eagle International Plaza, No.89 Hanzhong Road, Nanjing, Jiangsu, China (210029)

P: +86-25-8472-6671 F: +86-25-8472-6687

FUZHOU Room 1801-1811, B1#1A Class Office Building, Wanda Plaza, No.8 Aojiang Road, Fuzhou, China (350009)

P: +86-591-8380-1030 F: +86-591-8380-1225

WUHAN Room 1512, No.198Yunca Road, Office Building, Oceanwide City Square, JiangHan, District, WuHan, China (400039)

P: +86-27-8556-9630 F: +86-27-8556-9615

QINGDAO Room 802, Farglory International Plaza, No.26 Xianggang Zhong Road, Shinan District, Qingdao, Shandong, China (266071)

P: +86-532-5568-3877 F: +86-532-5568-3876

GUANGZHOU Room 1011-16, Yuexiu Financial Tower, No.28 Zhujiang Road East, Zhujiang New Town, Guangzhou, Guangdong, China (510627)

P: +86-20-3817-7800 F: +86-20-3786-4501

CHANGSHA Room 3209, Huayuan International Center, No.36, Section 2, Xiangjiang Middle Road, Tianxin District, Changsha, Hunan, China (410002)

P: +86-731-8571-3100 F: +86-731-8571-3255

LUOYANG Room 955, HUA-YANG PLAZA HOTEL, NO.88 Kaixuan W.Rd., Jian Xi District, Luoyang,Henan Province, China (471003)

P: +86-379-6069-6188 F: +86-379-6069-6180

XI'AN Room 1007, B Changan Metropolis Center, No.88 Nanguanzheng Steet, Xi'an, Shanxi, China (710068)

P: +86-29-8765-1896 F: +86-29-8765-1895

CHONGQING Room 612, Commercial Apartment, Athestel Hotel, No.288, Keyuan Rd.4, Jiulongpo District, Chongqing, China (400039)

P: +86-23-6806-5310 F: +86-23-6806-5292

CHENGDU Room1117, Lippo Tower, No.62 North Kehua Road, Chengdu, Sichuan, China (610041)

P: +86-28-8528-3680 F: +86-28-8528-3690

NSK CHINA SALES CO., LTD.

JIANGSU No.8 NSK Rd., Huaqiao Economic Development Zone, Kunshan, Jiangsu, China (215332)

P: +86-512-5796-3000 F: +86-512-5796-3300

NSK HONG KONG LTD.

HONG KONG ☆ Suite 705, 7th Floor, South Tower, World Finance Centre, Harbour City, T.S.T., Kowloon, Hong Kong, China

P: +852-2739-9933 F: +852-2739-9323

SHENZHEN Room 624-626, 6/F, Kerry Center, Renminnan Road, Shenzhen, Guangdong, China

P: +86-755-25904886 F: +86-755-25904883

Taiwan:

TAIWAN NSK PRECISION CO., LTD.

TAIPEI ☆ 10F-A6, No.168, Sec.3, Nanjing East Rd., Zhongshan Dist., Taipei City 104, Taiwan

P: +886-2-2772-3355 F: +886-2-2772-3300

TAICHUNG 3F. -2, No. 540, Sec. 3, Taiwan Blvd., Xitun Dist., Taichung City 407, Taiwan

P: +886-4-2708-3393 F: +886-4-2708-3395

TAINAN Rm. A1, 9F., No.189, Sec. 1, Yongfu Rd., West Central Dist., Tainan City 700, Taiwan

P: +886-6-215-6058 F: +886-6-215-5518

India:

NSK BEARINGS INDIA PRIVATE LTD.

CHENNAI ☆ TVH Beliciaa Towers, 2nd Floor, Block I, No.71/1, MRC Nagar Main Road, MRC Nagar, Chennai, Tamil Nadu, India - 600028

P: +91-44-28479600

GURGAON Unit No. 202, 2nd Floor, 'A' Block, Iris Tech Park, Sector-48, Sohna Road, Gurgaon, Haryana, India-122018

P: +91-124-4838000

MUMBAI No.321, A Wing, Ahura Centre, 82, Mahakali Caves Road, Andheri East, Mumbai, Maharashtra, India-400093

P: +91-22-28387787

JAMSHEDPUR 36, Maharani Mansion Ground Floor, Circuit House Area P.O.- Bistupur, East Singhbhum, Jamshedpur, Jharkhand, India-831011

P: +91-657-2421144

Indonesia:

PT. NSK INDONESIA

JAKARTA Summitmas II, 4th Floor, Jl. Jend Sudirman Kav. 61-62, Jakarta 12190, Indonesia

P: +62-21-252-3458 F: +62-21-252-3223

Korea:

NSK KOREA CO., LTD.

SEOUL Posco Center (West Wing) 9F, 440, Teheran-ro, Gangnam-gu, Seoul, 06194, Korea

P: +82-2-3287-0300 F: +82-2-3287-0345

Malaysia:

NSK BEARINGS (MALAYSIA) SDN. BHD.

SHAH ALAM ☆ No. 12A, Jalan Subang 7/4, Taman Perindustrian Subang USJ 1, 47600 Subang Jaya, Selangor D.E., Malaysia.

P: +60-3-5886-3388

PRAI No.24, Jalan kikik, Taman Inderawasih, 13600 Prai, Penang, Malaysia

P: +60-4-3902275 F: +60-4-3991830

JOHOR BAHRU 88 Jalan Ros Merah 2/17, Taman Johor Jaya, 81100 Johor Bahru, Johor, Malaysia

P: +60-7-3546290 F: +60-7-3546291

Philippines:

NSK INTERNATIONAL (SINGAPORE) PTE LTD.

PHILIPPINES REPRESENTATIVE OFFICE (MANILA)

MANILA 8th Floor The Salcedo Towers 169 H.V. Dela Costa St.,Salcedo Villege Makati City, Philippines 1227

P: +63-2-893-9543 F: +63-2-893-9173

Singapore:

NSK INTERNATIONAL (SINGAPORE) PTE LTD.

SINGAPORE 238A, Thomson Road, #24-01/02, Novena Square Tower A, Singapore 307684

P: +65-6496-8000 F: +65-6250-5845

Thailand:

NSK BEARINGS (THAILAND) CO.,LTD.

BANGKOK 26 Soi Onnuch 55/1 Pravet Subdistrict, Pravet District, Bangkok 10250, Thailand

P: +66-2320-2555 F: +66-2320-2826

Vietnam:

NSK VIETNAM CO., LTD.

HANOI Techno Center, Room 204-205, Thang Long Industrial Park, Dong Anh District, Hanoi, Vietnam

P: +84-24-3955-0159 F: +84-24-3955-0158

HO CHI MINH CITY Unit 609, The Landmark Building, 5B Ton Duc Thang Street,District 1, Ho Chi Minh City, Vietnam

OFFICE P: +84-28-3822-7907 F: +84-28-3822-7910

Worldwide Sales Offices

P: Phone F: Fax ☆: Head Office

●Europe

United Kingdom:

NSK EUROPE LTD. (EUROPEAN HEADQUARTERS)

MAIDENHEAD The Place, Bridge Avenue, Maidenhead, Berkshire SL6 1AF, U.K.

P: +44-1628-509-800

NSK UK LTD.

NEWARK Northern Road, Newark, Nottinghamshire NG24 2JF, U.K.

P: +44-1636-605-123 F: +44-1636-605-000

France:

NSK FRANCE S.A.S.

PARIS Quartier de l'Europe, 2 Rue Georges Guynemer, 78283 Guyancourt, France

P: +33-1-30-57-39-39 F: +33-1-30-57-00-01

Germany:

NSK DEUTSCHLAND GMBH

DUSSELDORF ☆ Harkortstrasse 15, D-40880 Ratingen, Germany

P: +49-2102-4810 F: +49-2102-4812-290

STUTTGART Liebknechtstrasse 33, D-70565 Stuttgart-Vaihingen, Germany

P: +49-711-79082-0 F: +49-711-79082-289

WOLFSBURG Tischlerstrasse 3, D-38440 Wolfsburg, Germany

P: +49-5361-27647-10 F: +49-5361-27647-70

Italy:

NSK ITALIA S.P.A.

MILANO Via Garibaldi 215, Garbagnate Milanese (Milano) 20024, Italy

P: +39-299-5191 F: +39-299-025778

Netherlands:

NSK EUROPEAN DISTRIBUTION CENTRE B.V.

TILBURG Brakman 54, 5047 SW Tilburg, Netherlands

P: +31-13-4647647 F: +31-13-4641082

Poland:

NSK POLSKA SP.Z O.O.

WARSAW Ul. Migdalowa 4/73, 02-796, Warsaw, Poland

P: +48-22-645-1525 F: +48-22-645-1529

Spain:

NSK SPAIN S.A.

BARCELONA C/Tarragona, 161 Cuerpo Bajo, 2a Planta, 08014, Barcelona, Spain

P: +34-93-289-2763 F: +34-93-433-5776

Turkey:

NSK RULMANLARI ORTA DOGU TIC. LTD. STI.

ISTANBUL Cevizli Mahallesi, D-100 Güney Yanyolu, Kuriş Kule İş Merkezi No:2 Kat:4, P.K.: 34846, Cevizli-Kartal-Istanbul, Turkey

P: +90-216-5000-675 F: +90-216-5000-676

United Arab Emirates:

NSK BEARINGS GULF TRADING CO.

DUBAI JAFZA View 19, Floor 24 Office LB192402/3, PO Box 262163, Downtown Jebel Ali,

Dubai, U.A.E

P: +971-(0)4-804-8200 F: +971-(0)4-884-7227

●North and South America

United States of America:

NSK AMERICAS, INC. (AMERICAN HEADQUARTERS)

ANN ARBOR 4200 Goss Road, Ann Arbor, Michigan 48105, U.S.A.

P: +1-734-913-7500 F: +1-734-913-7511

NSK CORPORATION

ANN ARBOR 4200 Goss Road, Ann Arbor, Michigan 48105, U.S.A.

P: +1-734-913-7500 F: +1-734-913-7511

NSK PRECISION AMERICA, INC.

FRANKLIN ☆ 3450 Bearing Drive, Franklin, Indiana 46131, U.S.A.

P: +1-317-738-5000 F: +1-317-738-5050

SAN JOSE 780 Montague Expressway, Suite 505, San Jose, California, 95131, U.S.A.

P: +1-408-944-9400 F: +1-408-944-9405

NSK LATIN AMERICA, INC.

MIAMI 11601 NW 107 Street, Suite 200, Miami Florida, 33178, U.S.A.

P: +1-305-477-0605 F: +1-305-477-0377

Canada:

NSK CANADA INC.

TORONTO ☆ 317 Rutherford Road South, Brampton, Ontario, L6W 3R5, Canada

P: +1-888-603-7667 F: +1-905-890-1938

MONTREAL 2150-32E Avenue Lachine, Quebec, Canada H8T 3H7

P: +1-514-633-1220 F: +1-800-800-2788

Argentina:

NSK ARGENTINA SRL

BUENOS AIRES Garcia del Rio 2477 Piso 7 Oficina "A" (1429) Buenos Aires-Argentina

P: +54-11-4704-5100 F: +54-11-4704-0033

<As of June 2023>

For the latest information, please refer to the NSK website.

www.nsk.com

Every care has been taken to ensure the accuracy of data in this publication, but NSK Ltd. accepts no liability for any loss or damage incurred from errors or omissions. As we pursue continuous improvement, all content (text, images, product appearances, specifications, etc.) contained in this publication is subject to change without notice. Unauthorized copying and/or use of the contents of this publication is strictly prohibited. Please investigate and follow the latest product export laws, regulations, and permit procedures when exporting to other countries.

Motion & Control

No. 34 June 2023

Published by NSK Ltd.



NSK used environmentally friendly printing methods for this publication.

CAT. No. ETJ-0034 2023 X-6 Printed in Japan ©NSK Ltd. 2023